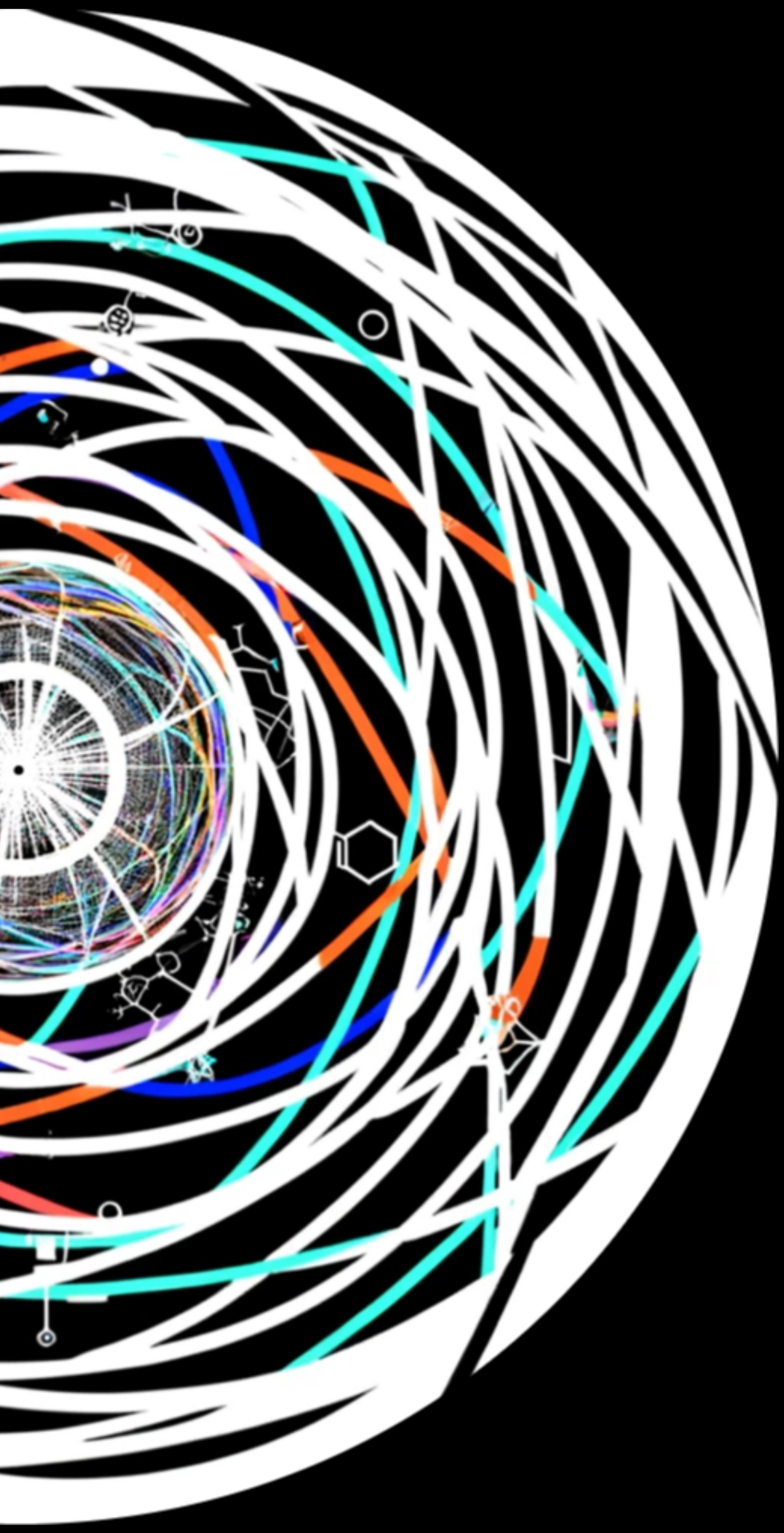

THE SEARCH FOR THE CHIRAL MAGNETIC EFFECT WITH ALICE AT THE LHC

Shi Qiu

The Search for the Chiral Magnetic Effect with ALICE at the LHC

Shi Qiu

Promotor:	Prof. dr. R.J.M. Snellings
Copromotoren:	Dr. P.G. Kuijer Dr. P. Christakoglou
Beoordelingscommissie:	Prof. dr. C.F.F. Van Den Broeck Dr. U. Gursoy Prof. dr. T. Peitzmann Prof. dr. J. Rojo Prof. E. Pallante

DOI: https://doi.org/10.33540/2205
Printed by Gildeprint
Cover design by Shi Qiu

This work is part of the research programme "*A new state of matter: The Quark Gluon Plasma*" with project number 680-47-608, which is financed by the Dutch Research Council (NWO). This work has been carried out at Nikhef.

The Search for the Chiral Magnetic Effect with ALICE at the LHC

De Zoektocht naar het Chirale Magnetische Effect met ALICE bij de LHC

(met een samenvatting in het Nederlands)

Proefschrift

ter verkrijging van de graad van doctor aan de
Universiteit Utrecht
op gezag van de
rector magnificus, prof. dr. H.R.B.M. Kummeling,
ingevolge het besluit van het college voor promoties
in het openbaar te verdedigen op
woensdag 17 april 2024 des ochtends te 10.15 uur

door

Shi Qiu

geboren op 7 maart 1993
te Anhui, China

Promotor:	Prof. dr. R.J.M. Snellings
Copromotoren:	Dr. P.G. Kuijer Dr. P. Christakoglou
Beoordelingscommissie:	Prof. dr. C.F.F. Van Den Broeck Dr. U. Gursoy Prof. dr. T. Peitzmann Prof. dr. J. Rojo Prof. E. Pallante

Contents

Preface **v**

1 Theory and background **1**
1.1 Quantum Chromodynamics . . . 1
1.2 Towards chirality imbalance in QCD vacuum . . . 3
1.2.1 QCD Lagrangian . . . 3
1.2.2 Axial Anomaly in the QCD Lagrangian . . . 3
1.2.3 The QCD Vacuum Structure . . . 5
1.2.4 Transitioning Between Vacuum States . . . 8
1.2.5 Connection between the axial anomaly and P (or CP) violation in QCD 10
1.3 Heavy-ion physics . . . 11
1.3.1 Evolution of a heavy-ion collision . . . 11
1.3.2 Anisotropic flow . . . 14
1.3.3 Electromagnetic fields in heavy-ion collisions . . . 17
1.4 Chiral Magnetic Effect . . . 21
1.4.1 Status of the experimental search of the chiral magnetic effect . . . 23

2 Experimental Setup **27**
2.1 The Large Hadron Collider . . . 27
2.2 A Large Ion Collider Experiment (ALICE) . . . 29
2.2.1 Inner Tracking System (ITS) . . . 31
2.2.2 Time-Projection Chamber (TPC) . . . 31
2.2.3 VZERO (V0) system . . . 32
2.2.4 Zero Degree Calorimeter (ZDC) . . . 34

3 Data Analysis **37**
3.1 Data Set . . . 37
3.2 Event selection . . . 37
3.3 Centrality determination . . . 40
3.4 Track selection . . . 40
3.5 Q-vector . . . 41
3.6 TPC Reconstruction Efficiency . . . 42
3.7 ZDC calibration . . . 45
3.7.1 Standard ZDC calibration procedure . . . 45

3.7.2 New ZDC calibration procedure . . . 50
3.7.3 ZNA-ZNC cross-terms . . . 54
3.7.4 Construction of the 1st Order Event Plane . . . 56
3.8 V0 calibration . . . 59

4 Chiral Magnetic Effect measured relative to the participant and spectator flow planes 63
4.1 Charge-dependent azimuthal correlators . . . 64
4.1.1 Introduction . . . 64
4.1.2 Calculation of δ and γ correlators . . . 67
4.2 Spectator-participant plane method . . . 70
4.2.1 Introduction . . . 70
4.2.2 Obtaining the statistical uncertainty with subsampling method . . . 74
4.3 Systematic uncertainties . . . 76
4.3.1 Systematic uncertainty of the double ratio . . . 76
4.3.2 Systematic uncertainty in the fraction of CME . . . 80
4.4 Results . . . 81
4.4.1 Measurements of γ/v_2 . . . 81
4.4.2 Double ratio . . . 81
4.4.3 Constraint on the fraction of CME . . . 84
4.4.4 Discussion . . . 86

5 Studying Pb-Pb and Xe-Xe measurements with AVFD 89
5.1 AVFD framework . . . 89
5.1.1 Introduction . . . 89
5.1.2 Key parameters in AVFD . . . 92
5.2 Model calibration and parametrisation . . . 93
5.3 Results . . . 98
5.4 Discussion . . . 102

6 Outlook 105

7 Summary 109

8 Appendix 111
8.1 Additional plots demonstrating the effect of the new gain equalisation method . 111
8.2 Additional correlation plots for $\Psi_1^{\text{ZNC-ZNA}}$ vs. Ψ_2^{V0C} and Ψ_1^{ZNC} vs. Ψ_1^{ZNA} . . . 113
8.3 Systematic uncertainty of other two choices of double ratio: ZDC/V0A and ZDC/TPC . . . 117

Bibliography 119

Public Summary 133

Openbare Samenvatting 139

Acknowledgements 145

Preface

Experience without theory is blind, but theory without experience is mere intellectual play.
Thoughts without content are empty, intuitions without concepts are blind.

Immanuel Kant

Chapter 1

Theory and background

In this opening chapter, I establish the conceptual groundwork within which the chiral magnetic effect can be comprehensively explored and understood, and elucidate the intricacies of the theory of the chiral magnetic effect from the perspective of an experimentalist. In Sec. 1.1, the theory of QCD will be introduced based on [1–3]. In Sec. 1.2, the origin of the chirality imbalance in the QCD vacuum, which is a crucial ingredient in the chiral magnetic effect, will be explained. This involves a few concepts: the axial anomaly in the QCD Lagrangian, the topological structure of the QCD vacuum, and the pseudoparticle instantons and sphalerons. In addition, we will discuss the connection between the axial anomaly and parity violation, as the frequent interchange of chirality and helicity can sometimes lead to confusion between these two concepts. Heavy-ion collisions create the perfect environment to search for the chiral magnetic effect as a result of the interplay between the local imbalance of the chirality of quarks and the presence of an external magnetic field. Sec. 1.3 will be dedicated to introducing heavy-ion physics, with a focus on the most relevant concepts related to the chiral magnetic effect including anisotropic flow and the early magnetic field. We will conclude this chapter by introducing the mechanism of the chiral magnetic effect and the current status of its experimental search in Sec. 1.4.

1.1 Quantum Chromodynamics

Deep inelastic scattering experiments have shown that quarks serve as fundamental constituents of hadrons like baryons (which consist of three valence quarks) and mesons (made up of a quark and an antiquark) [4, 5]. The binding of quarks is facilitated by the strong force, conveyed through strong force carriers: gluons. The Pauli Exclusion Principle states that no two or more identical particles with half-integer spins can simultaneously occupy the same quantum state within a quantum system. To create, for instance, a Δ^{++} composed of three up quarks, the introduction of a new quantum attribute is necessary to ensure that the overall wave function is antisymmetric. This property, known as "*colour*", prevents breaking the Pauli Exclusion Principle in the same energy state. Consequently, the theory for the strong force is aptly named Quantum Chromodynamics (QCD). The current description of colour in the Standard Model manifests in three kinds: red, blue, and green, along with their respective opposites: anti-red, anti-blue, and anti-green. Quarks and antiquarks possess a solitary positive or negative colour charge, while gluons exhibit a dual colour charge, encompassing both a colour and a different anticolour charge. When quarks interact through the strong force, gluons are exchanged between

them. This means that the interacting quarks via exchanges of gluons change the colour states of quarks by a discrete amount.

Physically, there exists no distinction between various colour states, making it impossible to distinguish different colour states through experimentation. For instance, we can represent the state of a quark of colour red as the vector: $\psi_{\text{q,red}} = (1, 0, 0)^{\text{T}}$, where T denotes the transpose of a matrix. The strong force interaction between quarks through exchanging gluons is described as the transformation under some representation of the gauge group SU(3), which stands for the Special Unitary group in 3 dimensions (represented by 3×3 unitary matrices with determinant one). What this means is that the states of quarks, column vectors, are acted on by the generators of SU(3) 3×3 matrices, as matrix multiplication. The generators, a subset of the group that can express all the group elements under the group operation (or more technically, the basis of the Lie algebra), of SU(3) are the set of eight traceless Hermitian matrices, known as the Gell-Mann matrices. These matrices can be considered as representations of gluons within colour space, specifically denoting the gauge transformations conducted by gluons. Consequently, this arrangement yields a total of eight distinct gluons. Physically, were the ninth colourless gluon (or the colour singlet state) to exist, colour-neutral baryons could emit these gluons (analogous to photons in the electromagnetic force) and participate in long-distance interactions through the strong force, which is clearly not the case for the strong interaction. Since the gluons are Lie algebra-valued, it transforms in the adjoint representation of the gauge group. Without digging into the mathematical definition, the adjoint representation is well-suited to describe gluon self-interactions and their interactions with other gluons, making it a natural choice within the context of QCD.

The coupling of gluons to themselves is a crucial factor that leads to QCD being a non-Abelian gauge theory, which is reflected in the generators of SU(3) exhibiting non-commutativity. In addition, it is the basic reason for one of the most distinct features of QCD: *asymptotic freedom*, where the strong force, equivalently the QCD coupling, becomes weaker at shorter distances or higher energies. As discussed in Sec. 1.4 of [1], the negative (*anti-screening*) impact of the leading-order gluon loop (representing gluon self-interaction) surpasses the positive (*screening*) impact of the leading-order quark loop. This leads to the negative overall sign of Eq. 19 in [1] (recognised as the beta function), characterising the "slope" of the energy dependence of the strong coupling. A negative slope translates to the effective decrease of the QCD coupling with increasing energy, and the quarks and gluons become asymptotically free. As discussed in Sec. 2.3 of [3], there is no straightforward and intuitive interpretation for this property, but one can imagine that the emission of virtual gluons from stationary colour sources leads to a dispersion of their colour charges into the neighbouring vacuum. The interaction between distributed charges is weaker when "examined" closely or at high interaction energies, compared to the interaction between point charges "observed" from a distance or at low interaction energies where the charge distributions overlap. This results in a decrease in the strength of the colour force at short distances. Conversely, the strong force becomes stronger at longer distances, and it increases very quickly near the energy (or distance) scale at which quarks and gluons are bound into hadrons. This leads to another unique feature of QCD referred to as *colour confinement*, which states that quarks and gluons are never found as free particles, and they are always confined within colourless hadrons forming bound states. It should be noted that the relationship between asymptotic freedom and confinement is rooted in the running of the strong coupling constant, rather than being a direct causal relationship between the two phenomena. Their coexistence is a remarkable property of QCD.

1.2 Towards chirality imbalance in QCD vacuum

The chiral magnetic effect originates from the interplay between the chirality imbalance in the QCD vacuum and the strong magnetic field produced in heavy-ion collisions. It is commonly described in an experimental paper that the mechanism of the CME is "*the interaction of quarks with gluonic fields describing transitions between topologically different (nontrivial) QCD vacuum states changes the quark chirality and leads to a local chiral imbalance*" [6]. However, it is not possible to grasp exactly what it means, as there are many terminologies unexplained. In this section, I will explain how chirality imbalance appears in the QCD vacuum using more intuitive language that is more understandable to an experimentalist, and I will skip many detailed derivations.

1.2.1 QCD Lagrangian

The general Lagrangian density for QCD in the Standard Model can be written in the following form[1]:

$$\mathcal{L} = \sum_q \bar{\psi}_q^i (i\gamma^\mu D_\mu - m_q)_{ij} \psi_q^j - \frac{1}{4} G^a_{\mu\nu} G^{\mu\nu a}, \tag{1.2.1}$$

where ψ_q^i denotes a quark field with the indices q and i running over all quark flavours (1-6) and the quark colour indices from 1-3 respectively, γ^μ and D_μ are the Dirac matrix and the covariant derivative respectively with spacetime index μ, m_q is the quark mass, and $G^a_{\mu\nu}$ is the gluon field strength tensor with (adjoint) colour index a running over all eight gluons. The first term in the QCD Lagrangian captures kinetic energy and mass terms for quarks, and their interaction with gluons (through the gluon fields in the covariant derivative). The second term, also known as the Yang-Mills part, describes how gluon fields (A_μ) interact with themselves.

1.2.2 Axial Anomaly in the QCD Lagrangian

The famous Noether's theorem reveals that for every symmetry (transformation of the field by a certain amount leading to no change in the Lagrangian), there corresponds a conserved current ($\partial_\mu J^\mu = 0$, where J denotes a current). Consider the so-called vector $U(1)_V$ and axial $U(1)_A$ rotation on the quark field ψ in the QCD Lagrangian and the corresponding infinitesimal action ($\delta\psi$) and current (j^μ):

$$\begin{aligned} &\text{vector rotation:} \quad \psi \to e^{i\alpha}\psi,\ \delta\psi = i\epsilon\psi,\ j_V^\mu = j_L^\mu + j_R^\mu = \bar{\psi}\gamma^\mu\psi; \\ &\text{axial rotation:} \quad \psi \to e^{i\alpha\gamma^5}\psi,\ \delta\psi = i\epsilon\gamma^5\psi,\ j_A^\mu = j_L^\mu - j_R^\mu = i\bar{\psi}\gamma^\mu\gamma^5\psi, \end{aligned} \tag{1.2.2}$$

where α is a scalar, γ^5 is the fifth gamma matrix related to the chirality of the quark, $\epsilon = \delta\alpha$ is an infinitesimally small parameter and the indices L and R refer to the left- and right-handedness, respectively. The anomaly arises here is called the *axial anomaly* as it turns out that:

$$\partial_\mu J_V^\mu = 0, \quad \partial_\mu J_A^\mu \neq 0. \tag{1.2.3}$$

The form of symmetry breaking addressed here is of a more nuanced nature. More specifically, the axial symmetry that seems to remain intact in the classical theory, as observed by examining

[1] You may also see it written like $\mathrm{Tr}\{G^{\mu\nu}G_{\mu\nu}\}$. A useful relation is $\mathrm{Tr}\{G^{\mu\nu}G_{\mu\nu}\} = \mathrm{Tr}\{t_a t_b\}G^a_{\mu\nu}G^{\mu\nu b} = T(R)G^a_{\mu\nu}G^{\mu\nu a}$, where $T(R) = 1/2$ in the fundamental representation of SU(N). See e.g. Eq. 1.8 in [7] and Table 1. in [1].

the Lagrangian alone, ceases to be a true symmetry when the Lagrangian is applied within a quantum theory. Historically, this insight was initially uncovered by means of a rather intricate calculation involving a Feynman diagram referred to as the triangle diagram. The triangle diagram is calculated as a three-point correlation function containing e.g. two vector currents and a single axial current. The level of detail required for this calculation is beyond the scope of this dissertation. However, for those interested in delving into this topic further, please refer to e.g. Sec. 3.2.3 in [8] for a comprehensive explanation. The identical result can be derived by computing the fermionic measure (namely the path integral of a free massless fermion coupled to a U(1) gauge field, $\bar{\psi}\not{D}\psi$) under the axial rotation (known as the *Fujikawa method*), which must remain invariant if axial rotation is indeed a true symmetry (see e.g. Sec. 3.2.2 in [8]). All of these calculations point to the same conclusion that the axial current is not conserved

$$\partial_\mu j_A^\mu = \frac{N_f g^2}{16\pi^2} G^a_{\mu\nu} \tilde{G}^{\mu\nu a}, \tag{1.2.4}$$

where g is the coupling constant, N_f denotes the number of flavours and the notation

$$\tilde{G}^{\mu\nu a} = \frac{1}{2}\epsilon^{\mu\nu\rho\sigma} G^a_{\rho\sigma}. \tag{1.2.5}$$

It is not too surprising that these two calculations give the same conclusion as the path integral approach incorporates all possible gauge field configurations, which contribute to the anomaly, while the triangle diagram approach captures the anomaly through loop diagrams involving the axial and vector currents. Note that the contribution from the quark mass term $2m_q i\bar{\psi}_q\gamma^5\psi_q$ (a "classical" contribution to the divergence, arising from the mass term explicitly breaking the chiral symmetry) is neglected in $\partial_\mu j_A^\mu$ because, in hot QCD, the quark mass can be treated as zero. This approximation is adopted by Kharzeev in the original papers on the chiral magnetic effect [9, 10]. The anomaly means the corresponding Noether charge $Q_A = \int dx^3 j_A^0$ is not conserved, where dx^3 represents the spatial 3-manifold. The integrated anomaly equation yields the change in the charge (scaled by a factor of $1/(2N_f)$)

$$\Delta Q_A = Q_A|_{t=+\infty} - Q_A|_{t=-\infty} = \int d^4x \frac{g^2}{32\pi^2} G^a_{\mu\nu}\tilde{G}^{\mu\nu a} \neq 0. \tag{1.2.6}$$

Note that the left side is a not just a quantity, but also an integer (known as the topological charge). A detailed explanation requires a solid understanding of the *Atiyah-Singer Index Theorem* (see e.g. Sec. 3.3.1 in [8] or Sec. 3.2.2 in [11] for details) and familiarity with the detailed calculation process of the axial anomaly. Briefly, the calculation of the measure of the path integral tells us that

$$\frac{g^2}{32\pi^2}\int d^4x G^a_{\mu\nu}\tilde{G}^{\mu\nu a} = \sum_n \int d^4x \bar{\psi}_n \gamma^5 \psi_n. \tag{1.2.7}$$

Given that the eigenfunctions ψ_n and $\gamma_5\psi_n$ of $i\not{D}$ (known as the Dirac operator, where the slashed notation is the abbreviation of $\not{D} = \gamma^\mu D_\mu$) possess distinct eigenvalues (λ_n and $-\lambda_n$ correspondingly), with the exception of $\lambda_n = 0$ (zero mode), it follows that ψ_n and $\gamma_5\psi_n$ are orthogonal to each other for $\lambda_n \neq 0$ and consequently only zero modes contribute to the integral. In addition, γ^5 has possible eigenvalues of ± 1 ($\gamma^5\psi = \pm\psi$, with $+$ and $-$ corresponding to right- and left-handedness, respectively). Therefore, we get

$$\begin{aligned}\Delta Q_A &= \sum_{m=1}^{n_-}\int d^4x \bar{\psi}_{0-,m}\psi_{0-,m} - \sum_{m=1}^{n_+}\int d^4x \bar{\psi}_{0+,m}\psi_{0+,m} \\ &= n_- - n_+,\end{aligned} \tag{1.2.8}$$

where the integral is a unity due to normalisation condition and $n_\pm$ represents the number of zero modes of $i\not{D}$ with γ^5 eigenvalue $\pm$. When there is a positive ΔQ_A of 1, it results in the emergence of $2N_f$ units of axial charge (see Eq. 3.60-3.63 in [11] for derivation of the relation $2N_f\Delta Q_A = N_L - N_R$, where N_L and N_R are left- and right-handed fermions[2]), which can occur either through creation and annihilation of N_f left-handed quarks and N_f right-handed antiquarks in zero-mode states, respectively, or by flipping the helicity of quarks propagating in the zero-mode state [11–13].

On the other hand, the integer nature of the right-hand side of Eq. 1.2.6 is not obvious, and this is attributed to topology, a concept currently left unaddressed. This necessitates an understanding of the QCD vacuum structure and related concepts, which will be elaborated on in subsequent sections. At the moment, it is not hard to guess that the right-hand side is related to the gluon field. The fact that it must be equal to an integer means that ΔQ_A cannot change when the background gluon field undergoes smooth variations. This is precisely the essence of the term "topologically nontrivial" mentioned at the beginning of Sec. 1.2.

1.2.3 The QCD Vacuum Structure

The vacuum of a theory is characterised as the state possessing the least amount of energy on which the Fock space[3] is built. Since QCD is strongly coupled at low energies, the QCD vacuum can be viewed as a very dense state of matter, composed of complex interactions between quarks and gluons, along with their vacuum fluctuations. The strength of the QCD vacuum can be measured from the trace anomaly, which connects the expectation value of the vacuum energy density to the expectation value of the strength of squared quark fields (quark condensate $\langle\psi_q\bar{\psi}_q\rangle$) and squared gluon fields (gluon condensate $\langle G^a_{\mu\nu}G^{\mu\nu a}\rangle$) in the QCD vacuum [14]. The quark condensate has its role in the story of the spontaneous chiral symmetry breaking (similar to the Higgs mechanism), where the quark condensate spontaneously breaks the chiral symmetry $SU(N_f)_L \times SU(N_f)_R$ with N_f denoting the number of light flavours, usually including u, d, s (similar to the vacuum state of the Higgs field spontaneously breaking $U(1)$ symmetry). Here, the focus is on the gluon condensate as it is relevant to our story of the axial anomaly. This means that the vacuum is achieved by minimising the Yang-Mills energy coming from the Yang-Mills part of the QCD Lagrangian, which further implies that the gluon field strength tensor is zero. This does not mean that the gluon field is zero, but it constrains the gluon field to be "pure gauge"

$$A_\mu = -\frac{i}{g}U\partial_\mu U^\dagger, \tag{1.2.9}$$

where g is the coupling constant and U encompasses all possible gauge transformations into the gauge group SU(3). Another way of seeing it is that as the gluon field transforms as

$$A'_\mu \to UA_\mu U^\dagger - \frac{i}{g}U\partial_\mu U^\dagger, \tag{1.2.10}$$

putting $A_\mu = 0$ yields all configurations of the vacuum configurations with zero energy. For convenience, it is usually chosen to make use of the gauge redundancy to set the temporal gauge

[2]Fermions refer to quarks and antiquarks in this context. The total count of right(left)-handed fermions encompasses both right(left)-handed particles and right(left)-handed antiparticles.

[3]The Fock space is defined as the direct sum of a set of Hilbert spaces encompassing all possible particle numbers. In other words, it is a way to represent all possible states of the quantum system, from having no particles (the vacuum state) to having many identical particles.

(time-independent)

$$A_0 = 0. \tag{1.2.11}$$

So U just represents gauge transformations on spatial coordinates, $U(\vec{x})$. The key message here is that there are infinitely many possible vacuum configurations. Superficially, it may seem that all these configurations are connected by U and are equivalent. However, it is not the case. The temporal gauge does not completely fix the gauge freedom. Other constraint(s) are required to fully determine the gauge for the quantisation of the theory. As assumed by Jackiw in one of the earliest papers on QCD vacuum [15] and argued by e.g. Huang in Sec. 8.6 of [16], the gauge transformation U is assumed to be restricted to approach unity at spatial infinity

$$U(\vec{x}) \to 1 \quad \text{for} \quad |\vec{x}| \to \infty \tag{1.2.12}$$

to satisfy that the boundary conditions at the surface of infinity have no effect on local phenomena. This requirement is explained further in e.g. Sec. 2.2.1 of [8] by Tong and Sec. 10.4 of [17] by Rajaraman, based on Gauss' law in Yang–Mills theories, which is an analogy to Maxwell's electromagnetism theory, as a constraint on the physical states (see Eq. 2.27, 2.29, and 2.30 in [8] and Eq. 10.85-10.88 in [17]).

To illustrate that this crucial condition makes it impossible to deform one configuration continuously into another one (to be explained more clearly later), let us look at a simplified but equivalent scenario in SU(2). Any element in SU(2) can be written as

$$U_{\text{SU(2)}}(\vec{x}) = e^{i\omega(\vec{x})\hat{x}\cdot\vec{\sigma}}, \tag{1.2.13}$$

where $\omega(\vec{x})$ is some monotonic function equalling to 0 at $|\vec{x}| = 0$, $\hat{x}$ is the unit vector and $\vec{\sigma}$ represents Pauli matrices. The condition Eq. 1.2.12 directly translates to

$$\omega(\vec{x}) \to 2n\pi \quad \text{for} \quad |\vec{x}| \to \infty, \tag{1.2.14}$$

where n is called the winding number (or topological charge[4], topological quantum number, Pontryagin index, second Chern class number). The boundary condition described by Eq. 1.2.12 implies that the appearance of spatial infinity is the same everywhere, effectively allowing it to be "stitched" down to a single point. For a line, it compactifies to a circle (U(1) symmetry) and the winding number can be easily understood as the number of times that the domain space wraps (counterclockwise) around the circle. In the case of SU(2), the three spatial dimensions are compactified to a 2-dimensional sphere (refer to Fig. 4.1 in [18] for visualisation). Visualising SU(3) is more difficult as it is compactified into a 3-sphere. Nevertheless, the fundamental concept persists: the winding number in SU(N), where N is 3 in the context of QCD, denotes the number of times that one gets the SU(N) manifold, when integrating over the $\vec{x}$ spanning all points on the spatial N-sphere or equivalently integrating over the volume element of SU(N).

Assuming that we have two gauge transformations with winding number $n = 0$ ($U^{(0)}_{\text{SU(2)}}(\vec{x})$) and $n = 1$ ($U^{(1)}_{\text{SU(2)}}(\vec{x})$). The function $\omega(\vec{x})$ goes to $\omega^{(0)}(\vec{x}) = 0$ and $\omega^{(1)}(\vec{x}) = 2\pi$ at spatial infinity, respectively. It becomes evident that one cannot smoothly transition $\omega^{(0)}(\vec{x})$ into $\omega^{(1)}(\vec{x})$, while maintaining the endpoint fixed at one of the permissible values. Putting everything together, the pure gauge fields characterising the QCD vacuum for the gluon fields are

[4]This may be very confusing to the previous definition in Eq. 1.2.6. The topological charge is a more general term used in gauge theories like QCD to describe the presence of topological invariants, while the winding number is a topological invariant.

constructed from gauge transformations $U^{(n)}$ that satisfy the boundary condition and belong to distinct topological categories characterised by an integer winding number n. Though we cannot continuously deform $U^{(n)}$ into $U^{(m)}$ ($m \neq n$), it is possible to continuously go from a pure gauge field of class n to another class m. However, the process requires leaving the form of pure gauge, meaning that we inevitably encounter field configurations with non-minimal Yang-Mills energy. Each distinct topological class (different winding number) corresponds to an unequivocal minimum in Yang-Mills energy, and these minima are separated by finite barriers referred to as the "sphaleron barrier". The ground state possessing a certain winding number is not gauge invariant, as different winding numbers are topologically different. Fig. 1.1 illustrates the vacuum structure of the gluon field as a function of the winding number. It is worth mentioning that the standard story of the QCD vacuum choosing the temporal gauge and the constraint in Eq. 1.2.12 gives the special periodic structure. Working in other gauges gives different pictures (e.g. only one non-degenerate ground state if choosing the axial gauge or the Coulomb gauge), while the discussion on the consistency between those situations and the standard picture is way out of the scope of this thesis. At this point, the meaning of the phrase "nontrivial topological configurations in the gluon field" is really clear, and the gauge transformation between different gauge configurations is topologically nontrivial if the winding number is not zero.

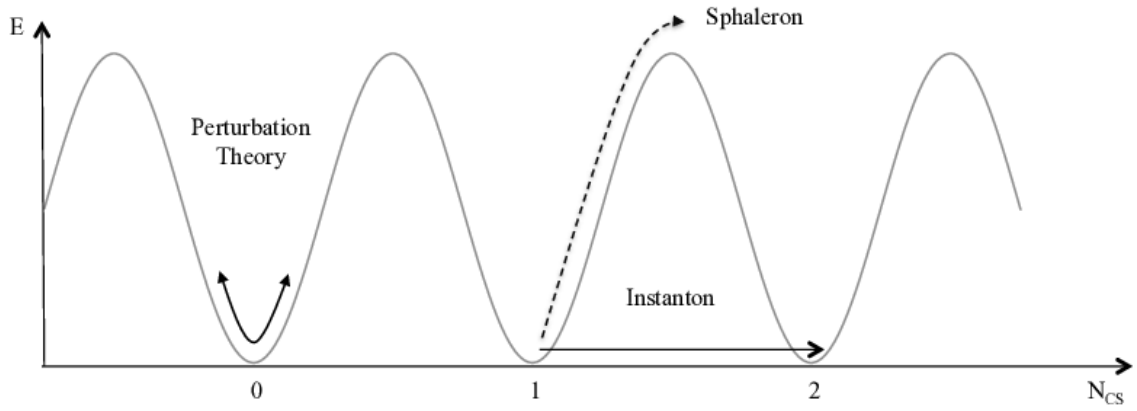

Figure 1.1: *Illustration of the vacuum structure of the gluon field as a function of the winding number (a.k.a. Chern-Simons number N_{CS}). The processes of instanton tunnelling through the potential barrier and sphaleron crossover the barrier are also shown. Figure adopted from [19].*

It is desired to construct a gauge-invariant ground state. To start, it is natural to write each configuration (Eq. 1.2.9) with its winding number as $|n\rangle$, and the gauge transformation $U^{(n')}$ transforms it as $U^{(n')}|n\rangle = |n + n'\rangle$. In analogy to Bloch's theorem (used to describe the electronic states in a crystal lattice with a periodic potential), the physical ground state of the system can be constructed as a coherent sum over (or a superposition of) all the states $|n\rangle$, denoted as

$$|\theta\rangle = \sum_{n=-\infty}^{\infty} e^{in\theta}|n\rangle. \tag{1.2.15}$$

This superposition of state $|\theta\rangle$ is also known as the *theta vacuum*. It is trivial to see that $|\theta\rangle$ is gauge invariant, as a gauge transformation, e.g. with winding number 1, would change $|\theta\rangle$ by

only a phase:

$$U^{(1)}|\theta\rangle = \sum_{n=-\infty}^{\infty} e^{in\theta} U^{(1)}|n\rangle = \sum_{n=-\infty}^{\infty} e^{in\theta}|n+1\rangle = e^{-i\theta} \sum_{n'=-\infty}^{\infty} e^{in'\theta}|n'\rangle = e^{-i\theta}|\theta\rangle. \quad (1.2.16)$$

Instead of viewing $|\theta\rangle$ as the ground state, θ can be considered as a parameter in the Lagrangian, with its value naturally chosen to be within the range of $0 \leq \theta < 2\pi$. In contrast to Bloch's theorem, where $\theta = 0$ corresponds to the ground state (the lowest-energy state) and higher-θ corresponds to excited states, in Yang-Mills theory, each value of θ characterises a distinct quantum theory encompassing a Hilbert space of states, with the associated vacuum state given by $|\theta\rangle$. Importantly, no gauge-invariant operator can establish a connection between states belonging to different θ sectors. The θ term, which is added to the standard QCD Lagrangian, is determined by considering the transitions between vacuum states using the path integral formalism. The detailed derivation can be found in e.g. Eq. 10.70-10.74 and 10.98-10.99 in [17] or Eq. 3.105-3.123 in [11], but it is crucial to demonstrate the steps that establish the connection between the transition of the winding number and the θ term:

$$\begin{aligned} \langle\theta|e^{-iH\tau}|\theta\rangle &= \sum_{n,Q} e^{-iQ\theta}\langle n+Q|e^{-H\tau}|n\rangle = ... \\ &= 2\pi\delta(0)\int D[A_\mu]_{\text{all Q}} \exp\left(-S_E + \frac{i\theta}{32\pi^2} g^2 \int G^a_{\mu\nu}\tilde{G}^{\mu\nu a} d^4x\right), \end{aligned} \quad (1.2.17)$$

where Q is the change of the winding number and S_E denotes the Euclidean action. This means that (in Minkowski space) an extra amount of

$$\Delta\mathcal{L}_\theta = \frac{\theta}{32\pi^2} g^2 G^a \mu\nu \tilde{G}^{\mu\nu a} \quad (1.2.18)$$

needs to be added to the QCD Lagrangian[5]. It is readily apparent that this term shares the same form as the anomalous axial current in Eq. 1.2.4. This implies that the alteration (topological fluctuations) of the winding number of gluon fields is linked to an imbalance in the chirality of quarks. While this process is more intricate, I will provide a brief overview of how the change in winding numbers occurs in the next section.

1.2.4 Transitioning Between Vacuum States

As shown in Figure 1.1, the QCD vacuum exhibits a periodic structure. There are two distinct processes responsible for inducing transitions between vacuum states characterised by different winding numbers: quantum tunnelling facilitated by instantons [27] and classical thermal activation processes (crossover of the potential well) involving sphalerons [28,29], respectively.

[5] It is often mentioned in the literature that the motivation for adding the θ term is that there is no fundamental obstruction to introducing a P- and CP-violating term into the QCD Lagrangian. While this is indeed the correct motivation, I would like to elucidate a bit more details that lead to this particular form. This term can be expressed in terms of the colour electric and magnetic fields (see definitions in e.g. Eq. 3.80 in [11]) as $F^a_{\mu\nu}\tilde{F}^{\mu\nu a} \propto E_i B_i$. Now, it becomes more apparent that this term breaks P and CP symmetry, drawing an analogy to the standard electric and magnetic fields. Under parity, E_i changes sign and B_i remains the same. Similarly, while E_i remains invariant under the time-reversal transformation (equivalent to the CP transformation), B_i changes sign. The value of θ is constrained by the measurement of the electric dipole moment of the neutron to be $|\theta| < 10^{-10}$ [20]. The temperature-dependent nature of the θ parameter has yet to be experimentally observed. However, it is argued in [21] that θ may have had a significantly non-zero value during the QCD phase transition in the early universe, while it vanishes in the current universe [22–26].

The term "instanton" was introduced by 't Hooft [30]. The "-on" suffix is used to highlight its mathematical similarity to solitons, which are self-reinforcing, stable, particle-like solutions found in classical field theories and maintain their shape and energy as they propagate through a medium, without dispersing or dissipating. However, the "instant-" prefix distinguishes instantons as structures in time[6], setting them apart from solitons. Determining the solution for QCD instantons is a complicated process and involves many subtleties, but, at its core, the process shares similarities with an electron encountering a potential barrier. Before encountering the potential barrier, the electron is expressed by an ordinary oscillating wavefunction $e^{i\omega t}$. Yet, once the electron resides within the potential barrier, the wavefunction takes on a form proportional to $e^{-\omega\tau}$. This implies an exponential decrease in the probability of locating the electron within the barrier. Comparing the wavefunction inside the barrier to the original wavefunction, the key distinction is the substitution: $t \to i\tau$ (known as the Wick rotation). From another perspective, the effect of the Wick rotation is essentially akin to inverting the potential, turning the barrier into a valley, thereby establishing a classical pathway across this. The tunnelling amplitude for instantons transition between QCD vacuum states is exponentially suppressed as $\exp\left(-S_E/\hbar\right)$ (see e.g. Sec. 2.3.3 in [8], Sec. 2.2.1 in [11] or Eq. 2.40 in [31] for details). Here, S_E signifies the (Euclidean) action associated with the instanton solution, which is linearly related to the energy of the potential barrier, E_{sph} (as detailed in Eq. 2.58 in [11]). While the precise energy of this potential barrier remains uncertain, it has been approximated to be on the order of Λ_{QCD} [32,33]. Consequently, this leads to an extremely significant suppression in the likelihood of quantum tunnelling through instantons[7].

On the other hand, sphalerons induce a change in winding number when they hop over the potential barrier. Sphalerons correspond to saddle-point configurations of the potential, which implies that lowering their energy makes them unstable. Nevertheless, if left undisturbed, they remain static because they still represent critical-point configurations. These sphalerons are typically located on potential energy barriers that separate the classical vacua of the theory. The transition rate of sphalerons can be intuitively connected to the Boltzmann factor[8] in statistical mechanics as $\exp\left(-E_{\text{sph}}/T\right)$, which implies that, at high temperature $T \gg E_{\text{sph}}$, the transition rate is unsuppressed. The lattice calculations have yielded the sphaleron transition rate for SU(2) Yang-Mills at high temperatures [35–37]. By extrapolating this outcome to SU(3), the transition rate is given by

$$\Gamma = \frac{dN}{d^3x dt} \approx 386\alpha_s^5 T^4, \tag{1.2.19}$$

where α_s is the strong coupling constant [32]. As shown in Fig. 1.2, a dynamic rate is calculated on the lattice showing that the transition rate drops as the temporal evolution of the dense gluonic matter, called the Glasma [38].

[6] As shown in e.g. Fig. 4 (based on Eq. 2.21) in [31], the solution of instantons for double well is sketched as a function of time, where the tunnelling transition occurs nearly instantaneously.

[7] The level of suppression in QCD is not well-known, but drawing insight from the electroweak theory, which can also exhibit tunnelling between degenerate vacua featuring distinct winding numbers, ultimately resulting in baryon (B) and lepton (L) violation, this tunnelling process is highly suppressed by a factor of 10^{-170} at zero temperature [34].

[8] The Boltzmann factor represents the probability of a system being in a particular state at a given temperature.

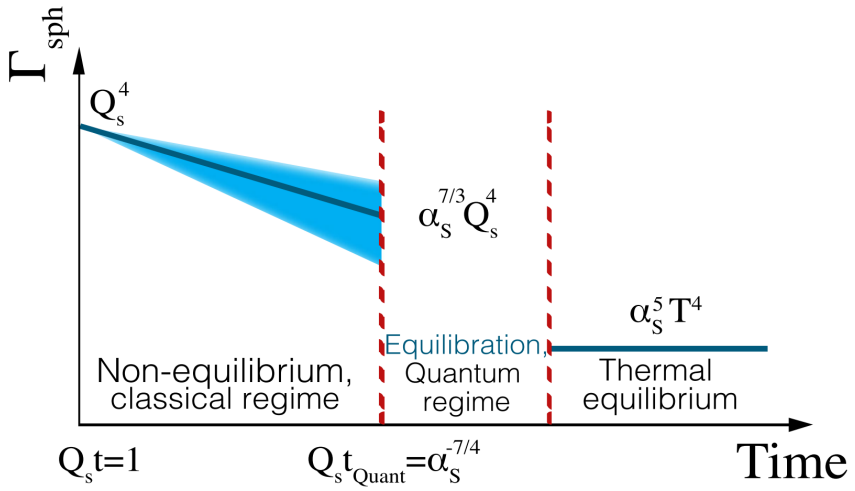

Figure 1.2: *Illustration of the temporal evolution of the sphaleron transition rate in the Glasma. The uncertainty band is represented by the blue shaded area. Figure adopted from [38].*

Consequently, it is predicted that in a thermalised quark-gluon plasma, numerous sphaleron transitions are anticipated to occur, approximately at a rate of several transitions per fm^3 per fm/c[9] [32].

At this point, the narrative regarding the local domain of chirality imbalance, resulting from the transition in the nontrivial topology of gluon field configurations induced by instantons and sphalerons, should be relatively clear.

1.2.5 Connection between the axial anomaly and P (or CP) violation in QCD

It has been introduced previously that the calculation of the transition amplitude between different vacuum states can lead to the introduction of a P- and CP-violating θ term in the QCD Lagrangian. Here, the P and CP violation are the breaking of P and CP symmetry in the strong interaction. However, despite the theoretical possibility, such violations have never been experimentally observed. The only constraint, as mentioned earlier, comes from the measurement of the electric dipole moment of the neutron, which imposes a limit of $|\theta| < 10^{-10}$ [20]. It is argued in [21] that θ may have had a significantly non-zero value during the QCD phase transition in the early universe, while it vanishes in the current universe [22–26].

In the description of the chiral magnetic effect, it is common to encounter sentences like "(vacuum) configurations with nonzero Q_w break the P (and CP) symmetry of QCD" [12], which may require some further clarifications. In this context, P and CP violation refer to a local symmetry breaking caused by the imbalance between left- and right-handed quarks within a local domain, originated from the axial anomaly and the transition in the nontrivial topology of gluon field configurations.

Under parity transformation ($\mathcal{P}$), the sign of one of the spatial coordinates is inverted: $x^i \to -x^i$. However, the chirality of a particle is a Lorentz-invariant property defined through the eigenvalues (± 1) of the Dirac fermion Ψ for the operator γ^5, where +1 represents right-handed and -1 represents left-handed. The connection between parity and chirality is actually through helicity, which is defined as the projection of spin (angular momentum) along the direction of

[9] When quark density is low, the massless quarks are not expected to significantly alter the rate.

momentum. Based on this definition, the right- and left-handed helicity states are mirror images of each other. It is easy to see that helicity is not an intrinsic property of a massive particle because one can always boost to another frame where the momentum changes sign. In the massless limit, helicity becomes the same as chirality, implying that a right(left)-handed helicity state is exactly the same as a right(left)-handed chiral state. In the language of high-energy particle physicists, helicity is usually replaced by chirality if the mass can be neglected. The effect of the parity transformation on helicity is simply the reversal of the direction of momentum, resulting in a change in the helicity state. In heavy-ion collisions, the temperature of the system is much higher than the mass of light quarks. Therefore, the local imbalance of chirality is treated in the same way as an imbalance of helicity, which is not symmetric under a parity transformation.

1.3 Heavy-ion physics

In this section, heavy-ion collisions, which create the perfect environment for the chiral magnetic effect to happen due to the interplay between the chirality imbalance in QCD and the strong magnetic field, will be introduced. First, it is necessary to present the overall evolution of heavy-ion collisions, which is a very complicated process and encompasses a wide range of physics topics. Then, the most relevant concepts to the chiral magnetic effect will be introduced, including anisotropic flow and the early magnetic field.

1.3.1 Evolution of a heavy-ion collision

At the Large Hadron Collider (LHC), ions like Pb and Xe[10] are accelerated to nearly the speed of light, reaching a total collision energy per nucleon-nucleon pair in the centre-of-mass frame of $\sqrt{s_{\mathrm{NN}}} = 5.02$ TeV[11] for Pb-Pb collisions and 5.44 TeV for Xe-Xe collisions. The evolution of a heavy-ion collision can be factorised into four stages: initial state, quark gluon plasma (QGP) formation, hadronisation, (chemical and then kinetic) freeze-out, in chronological order as shown in Fig. 1.3. The dynamics to connect each stage from the modelling perspective is labelled below the diagram: pre-equilibrium, viscous hydrodynamics, hadronic rescattering. Before the actual collision, each incident nucleus is Lorentz contracted to a disc in the laboratory frame with a diameter of about 14 fm for large nuclei like Pb and a corresponding thickness of $14/\gamma$ fm, where the relativistic γ factor is approximately 2500 for LHC energies [40]. The impact parameter b represents the distance separating the centres of the colliding discs, which governs the size of the collision zone. It is closely related to two quantities: the number of participating nucleons, denoted as N_{part}, and the number of binary nucleon-nucleon collisions, denoted by N_{coll}. For N_{part}, it is the count of nucleons involved in the inelastic collision process at least once (with a maximum of $2A$ for colliding nuclei of the same nucleon number A). The latter represents the total number of individual inelastic nucleon-nucleon collisions, which is proportional to $A^{4/3}$ and can reach approximately 2000 for Pb–Pb collisions at LHC energies [41].

[10] The LHC is capable of accelerating different ions. For example, there is an intention to have a short programme of oxygen-oxygen collisions in Run 3 [39].

[11] In 2022 (start of the Run 3), the Pb-Pb collisions at LHC reached a new record energy of $\sqrt{s_{\mathrm{NN}}} = 5.36$ TeV.

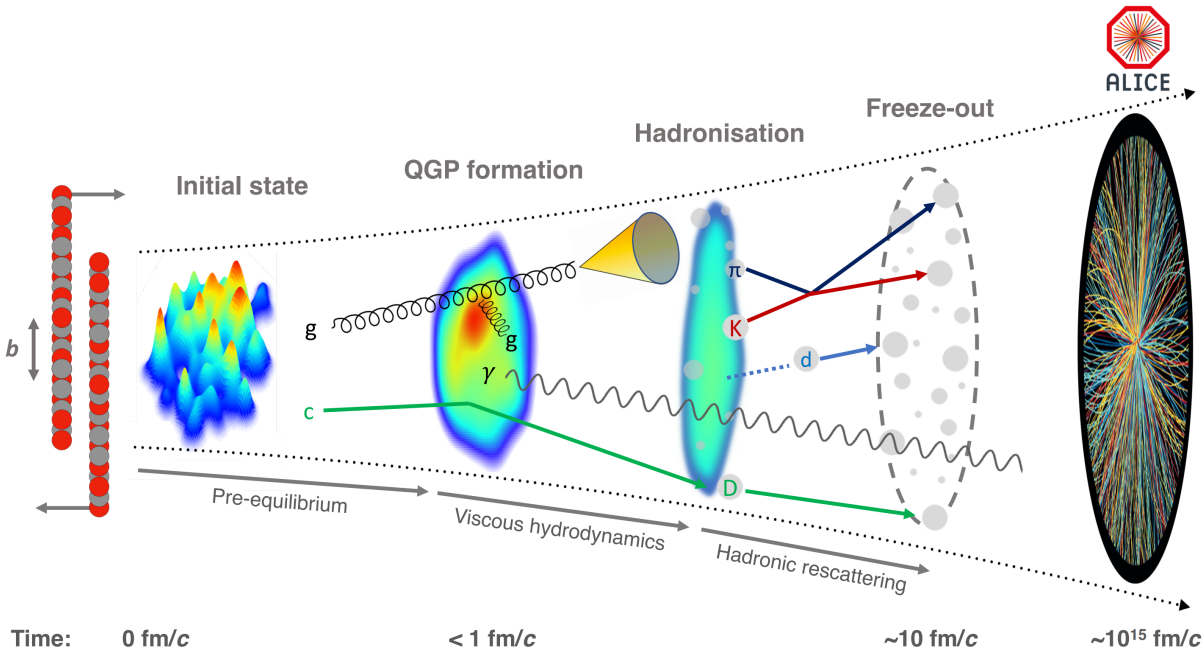

Figure 1.3: *Various phases in the spacetime evolution of a heavy-ion collision. Figure adopted from [41].*

Initial state

The initial state refers to the characteristics of colliding partons (e.g. the spatial and momentum distributions of the partons contained within the incoming nuclei) and the resultant system formed (a pre-equilibrium parton gas) after their initial interactions, predominantly involving gluons. Each incoming nucleus is a highly complex system, where the spatial variation of the partons is primarily a reflection of the instantaneous distribution of nucleons within the nuclei and the distribution of partons within those nucleons. Each nucleon is composed of three valence quarks and $q\bar{q}$ pairs from quantum fluctuations, while the dominant composition is low-x gluons, as clearly demonstrated in the nuclear parton distribution function [42]. Here, "x" represents the longitudinal momentum fraction carried by the gluon. Importantly, these gluons play an important role in shaping the spatial distribution of energy within the initial system and contribute a significant proportion of the colliding partons at first contact of two discs. Both small- and large-Q^2 interactions[12] happen during the first interaction of two discs, where the former one forms a pre-equilibrium[13] parton gas with its interaction rate driven by N_{part} and the latter one comes from the hard scattering of high momentum gluons and quarks with its interaction rate driven by N_{coll}. The process from initial state to the formation of the quark-gluon plasma is thought to last less than 1 fm/c.

There are several methods for modelling the initial state [43–47]. One commonly used approach is to represent the initial state as a superposition of independent nucleons, based on the Monte Carlo (MC) Glauber model, which works by sampling the nucleon density typically from a Woods-Saxon distribution [43]. Despite its simplicity, which does not involve assumptions

[12] Q^2 is the Mandelstam variable t, which is the square of the four-momentum difference (or four-momentum transfer) of two incoming particles.

[13] This implies that the system reaches equilibrium at a later time, but it is crucial to note that equilibrium, specifically thermal equilibrium, is considered to be achieved only locally based on our current understanding.

about the sub-structure and neglects nucleon binding, it has proven highly effective in describing common observables such as charged-particle yields and elliptic flow (v_2) at different impact parameters that are sensitive to the initial state. It is used to relate the impact parameter, N_{part} and N_{col}, which is intuitively calculable from the distribution of nucleons inside the nuclei, to the event centrality (defined in Sec. 3.3) in experiment.

The Impact Parameter Glasma (IP-Glasma) model goes beyond the assumptions of the MC Glauber model, which relies on simple nucleon superposition, by including the dynamics of gluons. This is particularly important in high-energy heavy-ion collisions due to nuclear saturation effects, where the partons interact strongly with each other, leading to a saturation of the parton densities at small x values. The saturation is modelled by the colour-glass condensate (CGC) effective field theory to describe the initial state as a coherent sheet of gluon field [44]. In this way, it includes quantum fluctuations in both nucleon positions within the nucleus and the colour charge distribution in the nucleus. This additional feature leads to a superior description of the v_n distributions (anisotropic flow coefficients). In addition, this model is excellent in describing charged particle multiplicity distributions in agreement with experimental data. The distributions of the initial energy densities in the transverse plane for the MC Glauber model and IP-Glasma model are shown in Fig. 1.4.

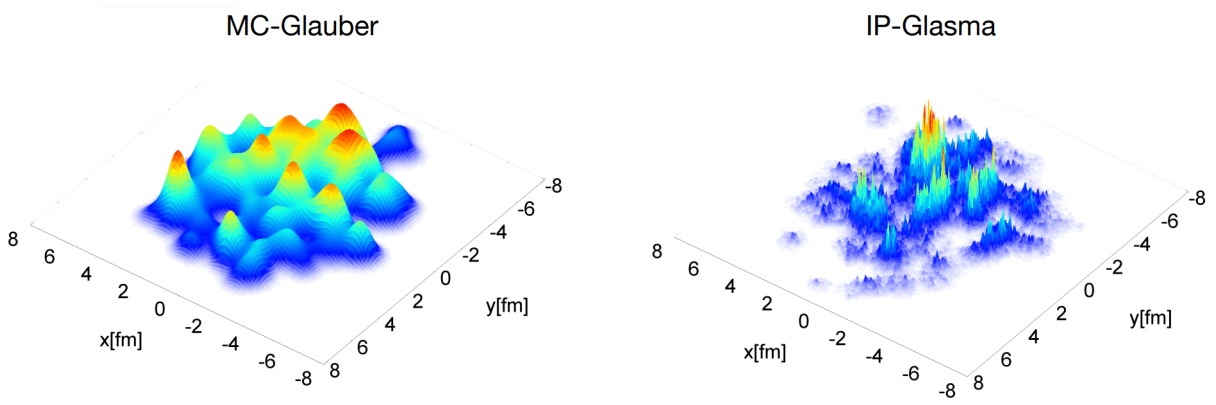

Figure 1.4: *The distributions of the initial energy density (in arbitrary units) in the xy-plane from the MC Glauber model (left) and IP-Glasma model (right) for a heavy-ion collision. Figure originally from [44].*

QGP formation

Around 1 fm/c after the initial collision, the system is thermalised and reaches an extremely high temperature exceeding the crossover temperature range ($T_c \sim 150$ MeV as predicted by lattice calculations [48]), which is a range of temperature when the confined QCD matter undergoes a crossover phase transition into deconfined quarks. This new state of matter is known as the quark gluon plasma. Given that the mean free path of the main constituents inside QGP is anticipated to be shorter than the size of the formed QGP, the expansion of the QGP is primarily driven by multiple interactions. The interactions sustain local thermodynamic equilibrium throughout the subsequent expansion, after which the system cools down sufficiently for hadronisation to take place.

The QGP exhibits properties like a perfect fluid, such as a very low specific shear viscosity, which is a measure of the resistance of a fluid to flow under the influence of shear forces [49,50]. Its evolution can be described by the laws of fluid dynamics, also referred to as relativistic vis-

cous hydrodynamics [51–53]. This approach effectively characterises the system using macroscopic variables like local energy density, pressure, temperature, and flow velocity. During the time evolution of the QGP, the equation of state (which describes the relationship between various thermodynamic variables, such as temperature, pressure, energy density, and entropy density, in QGP) is based on lattice calculations to evolve the system. In this picture, the non-uniform spatial energy distribution in the initial state give rise to directional-dependent pressure gradients, which play an important role in driving the expansion leading to the so called anisotropic flow. The level of observed anisotropy is suppressed by the shear viscosity of the QGP. The bulk viscosity of the QGP, representing its resistance to expansion, governs the rate of the expansion process, which affects the radial flow driven by a higher pressure at the centre of the QGP medium compared to outer layers.

Hadronisation

Hadronisation occurs at the end of the QGP expansion when the system or parts of the QGP cool down, leading to the confinement of quarks. Primarily pions (π), kaons (K), and protons (p) are formed out of quarks and gluons. Since the temperature and the energy density of the QGP medium are expected to gradually decrease with increasing distance from the collision centre, and the phase transition from QGP phase to normal hadronic matter is a smooth cross-over, as suggested by lattice QCD calculations (see e.g. [54]), the position and time that hadronisation takes place may vary in phase space. The process of hadronisation can be modelled by statistical hadronisation models [55, 56], where statistical mechanics is used to calculate the probabilities of forming various hadrons, or by coalescence (a.k.a. recombination) models [57, 58], where partons at low momenta are recombined into hadrons if they are nearby in phase space. In general, these models successfully describe several properties (e.g. hadron yields, momentum distributions) of the final-state hadrons as recorded by the experiments, validating their ability to capture key features in the hadronisation process. However, the exact mechanism, e.g. to which extent the quarks coalesce, is still under debate.

Freeze-out

The temperature gradually decreases during the hadronisation process. Two distinct types of freeze-out occur: chemical freeze-out and kinetic freeze-out. Typically, chemical freeze-out occurs first when the energy density of the system drops to a point where inelastic interactions cease, resulting in a stable "chemical" composition of the medium. As shown in Fig. 1.3, loosely bound states, such as deuterons, are particularly sensitive to the chemical freeze-out temperature, given their ease of formation and destruction. The kinetic freeze-out occurs at a later stage when elastic interactions (energy and momentum exchange) cease, typically around 10 fm/c after the initial collision [40, 41]. At this point, the system has become dilute enough for particles to stream outward freely.

1.3.2 Anisotropic flow

It is important to give a more detailed introduction to anisotropic flow because it is not only used in the analysis using the spectator-participant plane method (Sec. 4.2), but also drives the backgrounds in the chiral magnetic effect. The term "flow" in anisotropic flow refers to the hydrodynamic description of the collective expansion of the QGP, while the term "anisotropic"

refers to the non-uniformity in the spatial energy distribution in the initial state, resulting in particles accelerated proportionally to different pressure gradients in different directions and therefore momentum anisotropies in the azimuthal distribution of final-state particles. This is particularly important in non-central heavy-ion collisions. As shown in Fig. 1.5 (a), the initial cross section of the interaction area is an almond shape, so that the pressure gradient, indicated by the arrow lengths, increases with the decrease of the angle between the direction of emission projected onto the transverse plane (x-y plane) and the reaction plane. The goal of the anisotropic flow analysis is to quantify momentum anisotropies through the measurement of different flow coefficients denoted as v_n, which are essentially the Fourier coefficients of the harmonic expansion of the azimuthal distribution of particles [14]. The sub-index n represents the specific order of the harmonic expansion of the anisotropic flow being under consideration. The expansion is given by

$$\frac{dN}{d[\varphi - \Psi_n]} \propto 1 + 2\sum_{n=1}^{\infty} v_n \cos\left[n(\varphi - \Psi_n)\right], \tag{1.3.1}$$

where the azimuthal distribution of particles is defined with respect to its associated global plane angle Ψ_n. Compared to a standard Fourier expansion, the sine terms are absent here because the anisotropic flow is by definition symmetric with respect to the global plane. The Fourier series (flow) coefficients can be calculated as

$$v_n = \frac{1}{2\pi}\int_0^{2\pi} \frac{dN}{d[\varphi - \Psi_n]} \cos\left(n[\varphi - \Psi_n]d\varphi \approx \langle \cos\left(n[\varphi - \Psi_n]\right\rangle, \right. \tag{1.3.2}$$

where the angular brackets denote an average over all particles in one collision. Based on the geometry of each expansion (see Fig. 1.6), different orders of flow coefficients are referred to as directed flow (v_1), elliptic flow (v_2), triangular flow (v_3), etc.

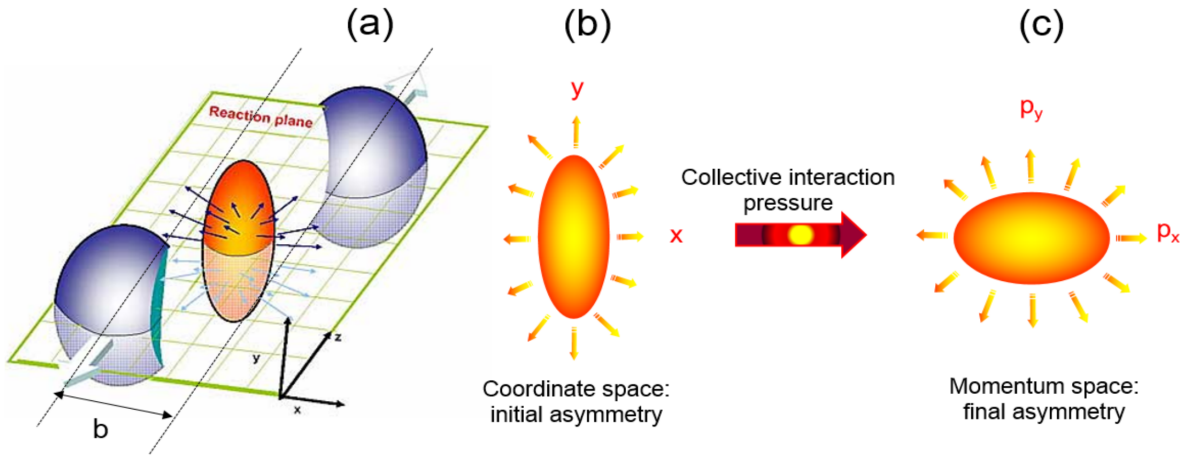

Figure 1.5: *(a) A non-central heavy-ion collision leads to an almond-shaped interaction volume, where the magnitude of the pressure gradient, represented by the length of arrows, is larger in the direction along the reaction plane; (b) the initial spatial anisotropy translates via collective expansion under pressure gradients into (c) a momentum anisotropy of the final-state particles. Figure originally from [59].*

[14] Particularly, charged particles with low transverse momenta are of interest here, as particles with high momenta may originate from hard scatterings rather than soft emissions from the QGP and only charged particles can be easily detected by the detector.

Figure 1.6: *Harmonic expansion of the momentum anisotropy of the final-state particles as a result of the anisotropic flow of the initial spatial anisotropy.*

As shown in Fig. 1.7, there are a few different choices of the global plane:

- **Reaction plane** Ψ_{RP}
  It is defined as the azimuthal angle of the plane spanned by the vector of the impact parameter and the beam axis. There is no experimental technique to precisely determine this plane's orientation event by event.

- **Participant planes (a.k.a. symmetry planes or event planes)** Ψ_n
  Participant planes are defined by the plane spanned by the minor axis of the overlap region of two colliding nuclei (participant zone) and the beam axis. At a fixed impact parameter, the orientation of the plane fluctuates due to the fluctuations in the initial energy density of the participant zone. It is also known as the symmetry plane, as it has a simple geometric interpretation: the probability for particles to be emitted either above or below the plane is symmetric. Each harmonic possesses a distinct symmetry plane, and these distinct symmetry planes do not necessarily exhibit correlations with each other [60].

  The participant plane Ψ_n is defined as

  $$\Psi_n = \frac{1}{n}\mathrm{atan}\left(\frac{\mathrm{Im}Q_n}{\mathrm{Re}Q_n}\right) \tag{1.3.3}$$

  where the Q-vector is defined as

  $$Q_n = \sum_{j=1}^{M} e^{in\varphi_j}, \tag{1.3.4}$$

  where M is the multiplicity of particles in one collision event, and φ_j represents the azimuthal angle of the j^{th} particle.

- **Spectator plane** Ψ_{SP}
  Nucleons that do not participate in collisions and continue their direction of motion without deflection, essentially remaining close to the beam direction after the nuclei fragment, are referred to as spectators. The spectator plane is defined by the deflection direction of spectators.

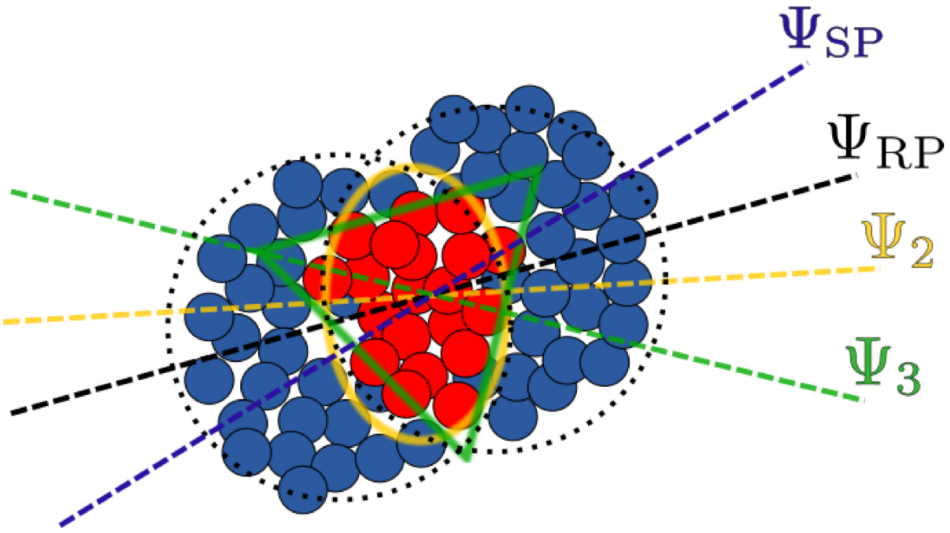

Figure 1.7: *Illustration of various choices of the global plane, including the reaction plane Ψ_{RP} in black, the second (Ψ_2 in yellow ellipse) and the third order participant plane (Ψ_3 in green triangle), and the spectator plane Ψ_{SP} in blue. The participant nucleons and the spectator nucleons are depicted in red and blue, respectively.*

Different flow harmonics have been studied extensively, but the only harmonic used in this dissertation is the elliptic flow v_2, which is the dominant flow coefficient in non-central heavy-ion collisions. Intuitively, it can be seen in Fig. 1.7 that the overlap region of two colliding nuclei has an ellipsoidal shape. If the value of v_2 reaches a value of 0.1, it indicates that the value of Eq. 1.3.1 (to first order) varies between 0.8 and 1.2, corresponding to the out-of-plane ($\varphi - \Psi_2 = \pi/2$) and in-plane ($\varphi - \Psi_2 = 0$) directions, respectively. This implies that there are about 1.5 times more particles emitted in the reaction plane than in the direction orthogonal to it. This azimuthal asymmetry, driven by the elliptic flow coupled with the conservation of electric charge in local phase space (local charge conservation), leads to a dominant source of the charge-dependent background in the measurement of the CME-sensitive observables. The explanation of why it constitutes the dominant charge-dependent background will be provided in Sec. 4.1.1. The higher-order harmonics originate from initial-state fluctuations. The measurements of different flow coefficients are sensitive to multiple properties of heavy-ion collisions, including initial-state anisotropies, the transport coefficients (such as specific shear[15] and bulk viscosity) and the equation of state of the system [41]. It is challenging to simultaneously constrain multiple properties of the heavy-ion collision and the QGP solely using anisotropic flow. However, in recent years, it has become an active field to perform a Bayesian analysis using measurements of flow coefficients with other experimental observables to constrain multiple properties at the same time [61–63].

1.3.3 Electromagnetic fields in heavy-ion collisions

In the earliest moments after non-central heavy-ion collisions, an extremely strong magnetic field is created by the spectator protons. The magnitude of the initial magnetic field is estimated

[15] In comparing to the shear viscosity η, the specific shear viscosity is normalised by the entropy, η/s. It is intuitive that a lower η/s results in a larger anisotropic flow because it suggests a lower resistance to the layers of fluid sliding past each other, thereby facilitating a greater velocity gradient.

to reach up to an order of $eB \sim 10^{15}$ T $= 10^{19}$ Gauss (or $eB \approx 10 m_\pi^2$) in Pb–Pb collisions at the LHC energy $\sqrt{s_{\rm NN}} = 4.5$ TeV with the impact parameter $b = 4$ fm through the application of the Biot-Savart law

$$eB \sim \gamma \alpha_{\rm EM} \frac{Z}{b^2}, \tag{1.3.5}$$

where γ is the Lorentz factor, $\alpha_{\rm EM} \simeq 1/137$ and Z is the charge number [64–67]. This magnetic field is expected to influence the charge dynamics with a complicated interplay of the Faraday effect, and Lorentz and Coulomb forces in the QGP, which leads to potential characteristic imprints on experimental observables [68–70]. As shown in Fig. 1.8, two incident nuclei moving in the $-z$ and $+z$ direction are chosen to be located at positive and negative x, which produces a magnetic field pointing in the $+y$ direction.

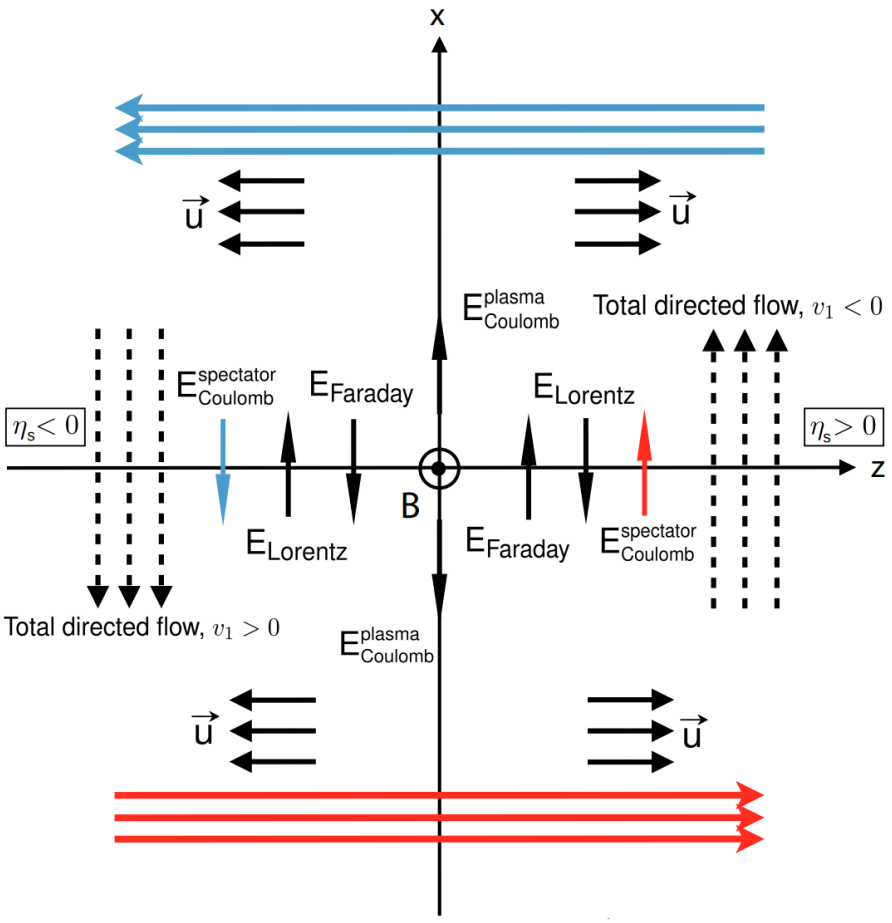

Figure 1.8: *Schematic illustration of the interplay of the Faraday effect, and Lorentz and Coulomb forces due to the initial magnetic field created by the spectator protons. The collision takes place along the z-direction, leading to a longitudinal expansion velocity $-\vec{u}$ and $\vec{u}$ of the produced QGP in the $-z$ and $+z$ direction, respectively. The impact parameter vector is chosen to align with the $+x$ direction, meaning that two incident nuclei moving in the $-z$ and $+z$ direction are located at positive and negative x, respectively. The motions of two nuclei are also indicated by blue arrows at the top and red arrows at the bottom of the diagram. This configuration produces a magnetic field pointing in the $+y$ direction as labelled by the $\odot$ at the origin. The directions of the electric fields (and, consequently, the currents) resulting from the Faraday, Lorentz, and Coulomb effects are also indicated. Figure adopted from [68].*

This leads to four types of currents:

- **Faraday current**
  It is generated as a consequence of the decreasing magnetic field over time, leading to the induction of an electric current in accordance with Faraday's law;

- **Lorentz current**
  The charged particles inside the expanding QGP experience a Lorentz force exerted by the initial magnetic field. In the longitudinal direction, the QGP expands with a velocity of $-\vec{u}$ and $\vec{u}$ in the $-z$ and $+z$ direction, respectively. An electric current perpendicular to both the velocity and the magnetic field, represented as E_{Lorentz} in Fig. 1.8, is induced by the Lorentz force, akin to the classical Hall effect;

- **Coulomb current** It arises from the Coulomb force, denoted as $E_{\text{Coulomb}}^{\text{spectator}}$ in Fig. 1.8, exerted by positively charged spectators passing the collision zone. Spectators moving in the $-z$ (z) direction create a Coulomb force directed downward (upward) in the negative (positive) z region, respectively;

- **Plasma current**
  It refers to an outward component of the electric field, denoted by $E_{\text{Coulomb}}^{\text{plasma}}$ in Fig. 1.8, which arises due to the net positive charge within the plasma. This, in turn, gives rise to a Coulomb force.

It has been shown in [69] that the interplay of the first three effects leads to a charge-odd contribution to the rapidity dependence of the directed flow coefficient, meaning that $\Delta v_1 = v_1^+ - v_1^-$ is odd in rapidity. The charge-odd triangular flow Δv_3 is also predicted to be odd in rapidity, arising from a similar physical origin as Δv_1. The last effect leads to a rapidity-even charge-odd elliptic flow Δv_2. The major unknown in the estimation of the effects is the treatment of the nontrivial electric conductivity of the QGP medium. Lattice QCD calculations suggest that the electric conductivity can be treated as a constant due to its weak dependence on the temperature [71–75]. However, it is important to note that during the initial pre-equilibrium phase, the electric conductivity should rapidly transition from zero to its equilibrium value, and this transition has not been accounted for in previous studies [68, 69].

Therefore, it is of great experimental interest to probe the magnitude of the early magnetic field especially through Δv_1, but only ambiguous evidence has been collected from the experimental side. The main difficulties arise from the fact that, despite its immense strength, this magnetic field has an exceptionally short lifetime, typically well below 1 fm/c, which may not be long enough to leave a significant impact on anisotropic flow in ultra-relativistic heavy-ion collisions [67]. Nevertheless, the electromagnetically induced directed flow is expected to be several orders of magnitude larger for heavy-flavour particles, e.g. D^0 and $\bar{D}^0$ mesons, in comparison to light-flavour particles [76], because heavy-flavour quarks, due to their heavier masses, are produced mainly through hard binary collisions when the magnetic field is maximal. In addition, the equilibration time is longer for heavy-flavour quarks, which enables them to better retain the initial momentum received from the electromagnetic force until the freeze-out stage. Both the ALICE collaboration at LHC and the STAR collaboration at RHIC have performed the measurement of Δv_1 for inclusive charged particles and D mesons in Pb-Pb collisions at $\sqrt{s_{NN}} = 5.02$ TeV [77] and in Au-Au collisions at various low energies (eight in total) ranging from 7.7 GeV up to the top RHIC energies of $\sqrt{s_{NN}} = 200$ GeV [78, 79]. As shown in Fig. 1.9, the Δv_1 of D mesons measured at midrapidity ($|\eta| < 0.8$) in the 10–80% centrality interval

in Au–Au collisions at $\sqrt{s_{NN}} = 200$ GeV gives a negative slope, but the similar measurement in the 10–40% centrality interval in Pb-Pb collisions leads to a positive slope. The observation of opposite and large slopes at the LHC might indicate a stronger effect of the magnetic field (Lorentz force) in comparison to the induced electric field (Coulomb force) and the initial tilt of the source in the reaction plane [68]. Overall, these results provide the experimental hint of the existence of the early electromagnetic fields in heavy-ion collisions, while high precision and differential measurements are required to draw strong conclusions on the charge transport both for the light- and the heavy-flavour particles.

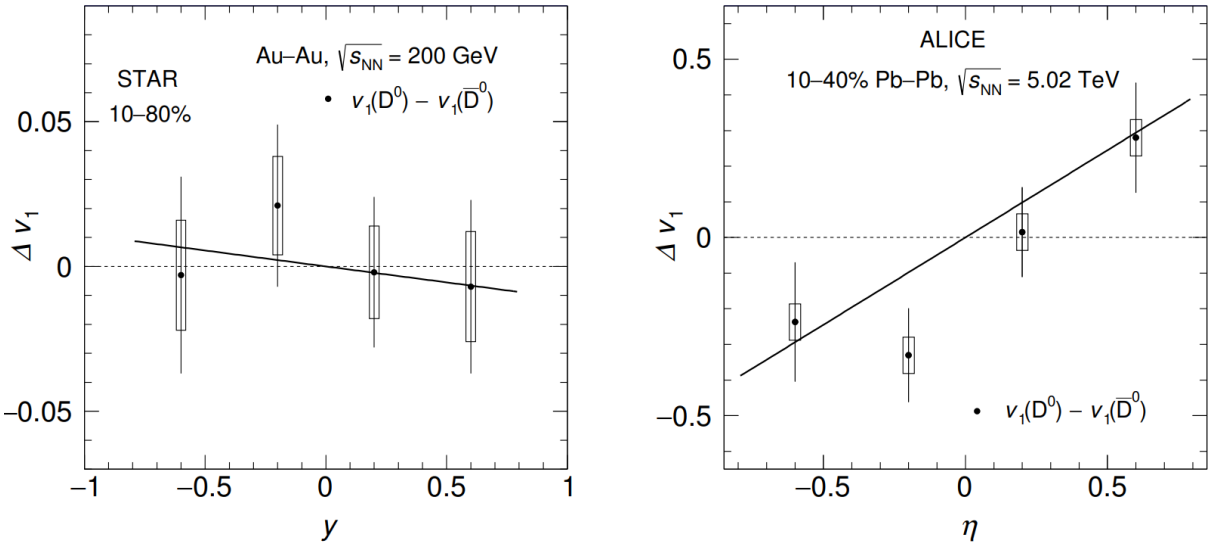

Figure 1.9: *The rapidity dependence of Δv_1 for D mesons measured by STAR in Au-Au collisions at $\sqrt{s_{NN}} = 200$ GeV (left) and by ALICE in Pb-Pb collisions at $\sqrt{s_{NN}} = 5.02$ TeV (right), respectively. Data points are fitted with a linear function to show the rapidity slope $d\Delta v_1/d\eta$. Figure adopted from [68].*

The early magnetic field can be probed from a completely different perspective: the hyperon–anti-hyperon ($\Lambda - \bar{\Lambda}$) global spin polarisation asymmetry, which is a measurement of the degree of alignment of hyperons' or anti-hyperons' spin with a given direction, in this case the spectator plane, which is strongly correlated to the direction of the magnetic field [80]. The Λ and $\bar{\Lambda}$ are experimentally favourable because the protons emitted from their dominant decay channel, ($\Lambda(\bar{\Lambda}) \to p(\bar{p}) + \pi^-(\pi^+)$), align preferentially to the direction of the $\Lambda(\bar{\Lambda})$ spin. The main mechanism for the global polarisation effect comes from the large fluid vorticity, ω, generated from two colliding heavy ions moving in opposite directions with velocity close to the speed of light. Orbital angular momentum is transferred to particle spin equally for particles and antiparticles. The magnetic field, as a secondary effect, pointing in the same direction as the average vorticity, aligns particles' and antiparticles' spin oppositely due to the opposite sign of the magnetic moment. The relationship can be written in the following approximate forms:

$$P_\Lambda \approx \frac{\omega}{2T} + |\mu_\Lambda|\frac{B}{T}, \quad \text{and} \quad P_\Lambda \approx \frac{\omega}{2T} - |\mu_\Lambda|\frac{B}{T}, \tag{1.3.6}$$

where μ_Λ is the Λ magnetic moment and T is the system temperature. Therefore, taking the difference between the global polarisation of Λ and $\bar{\Lambda}$ largely cancels out the effect of fluid vorticity and provides an alternative way to probe the magnetic field at freeze-out.

The global polarisation of Λ and $\bar{\Lambda}$ have been reported by both the ALICE and STAR collaborations. The ALICE collaboration studied such polarisation at mid-rapidity in mid-central Pb-Pb collisions at $\sqrt{s_{NN}} = 2.76$ and 5.02 TeV [81]. The magnitudes of the average global polarisation at LHC energies are consistent with the expectation based on the decreasing trend with the increase of collision energies seen from the same measurements by the STAR collaboration at RHIC in Au-Au collisions at various lower energies ranging from 7.7 GeV up to $\sqrt{s_{NN}} = 200$ GeV [82, 83]. No significant splitting between the polarisation of Λ and $\bar{\Lambda}$ was found at LHC energies, but an upper limit of the magnitude of the magnetic field $eB/m_{\pi}^2 = 0.017$ (equivalent to 5.7×10^{16} Gauss) and 0.044 (or 14.4×10^{16} Gauss) at a 95% confidence level was determined for Pb-Pb collisions at $\sqrt{s_{NN}} = 2.76$ and 5.02 TeV, respectively. The same upper limits have been determined by the STAR collaboration at RHIC in Au-Au collisions at centre-of-mass energies varying from $\sqrt{s_{NN}} = 7.7$ GeV to 200 GeV. Fig. 1.10 shows the collision energy dependence of the upper limits of the magnetic field at freeze-out based on the splitting of Λ and $\bar{\Lambda}$ polarisation measured at the LHC and RHIC.

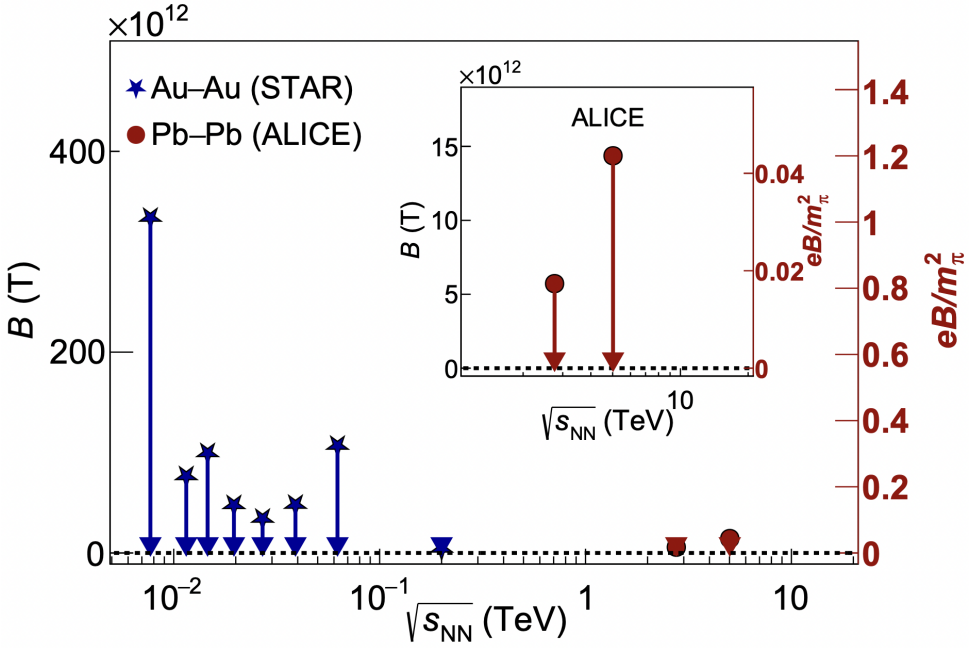

Figure 1.10: *The upper limit of the magnetic field at kinetic freeze-out relative to collision energies determined from the global Λ and $\bar{\Lambda}$ hyperon polarisation measured at the LHC and RHIC [81, 82]. This figure is adopted from [41].*

In conclusion, the complicated interplay of different currents induced by the electromagnetic fields and vorticity is not well understood due to limited constraints from experimental data. The major unknown is the lifetime of the magnetic field in different collision systems at different energies. This is also closely related to the lack of knowledge of the evolution of the electric conductivity in the heavy-ion collisions.

1.4 Chiral Magnetic Effect

The Chiral Magnetic Effect (CME) is the interplay between the local imbalance of the chirality (or helicity to be precise, since $T \gg m_{\text{quark}}$) of quarks and the presence of an external strong

magnetic field. The particle's spin tends to align either parallel or anti-parallel to the magnetic field depending on its charge, as it is a more energetically favourable state. This can be easily seen from the expression of the potential energy U of a particle with magnetic momentum $\vec{\mu} \propto q\vec{S}$ in an external magnetic field $\vec{B}$:

$$U = -\vec{\mu} \cdot \vec{B} \propto -q\vec{S} \cdot \vec{B}, \tag{1.4.1}$$

where the lowest energy happens when the angle between $\vec{S}$ and $\vec{B}$ is either 0 for positive q or π for negative q. For example, the spin of u (+2/3 charge) and d (-1/3 charge) quarks align in the same and opposite directions as the magnetic field, respectively. Consider only positively charged quarks for simplicity, as depicted in the left part of Fig. 1.11. The transition in the gluon field with nontrivial topological configurations leads to a change of the winding number, resulting in an imbalance between left- and right-handed quarks within a local domain. More specifically, the change of the winding number by $Q_{\mathrm{W}} = -1$ flips the left-handed quarks to right-handed quarks, and vice versa. This is depicted in the middle part of Fig. 1.11, where the system exhibits a surplus of right-handed positively-charged quarks, labelled with a non-zero chiral chemical potential $\mu_5 \neq 0$. In particular, a system with more right-handed quarks corresponds to a positive chiral chemical potential μ_5. Quarks can change their chirality (helicity) only by reversing their momenta in the presence of a strong magnetic field, as a spin flip is energetically suppressed. This implies that the momenta of positively-charged right-handed quarks and negatively-charged left-handed quarks align in the same direction as $\vec{B}$, while the momenta of positively-charged left-handed quarks and negatively-charged right-handed quarks align anti-parallel to $\vec{B}$. Consequently, in the case of an excess of right-handed quarks, an electric current forms with a net quantity of positively-charged right-handed quarks moving in the same direction as the magnetic field, as shown in the right part of Fig. 1.11. This phenomenon is called the Chiral Magnetic Effect.

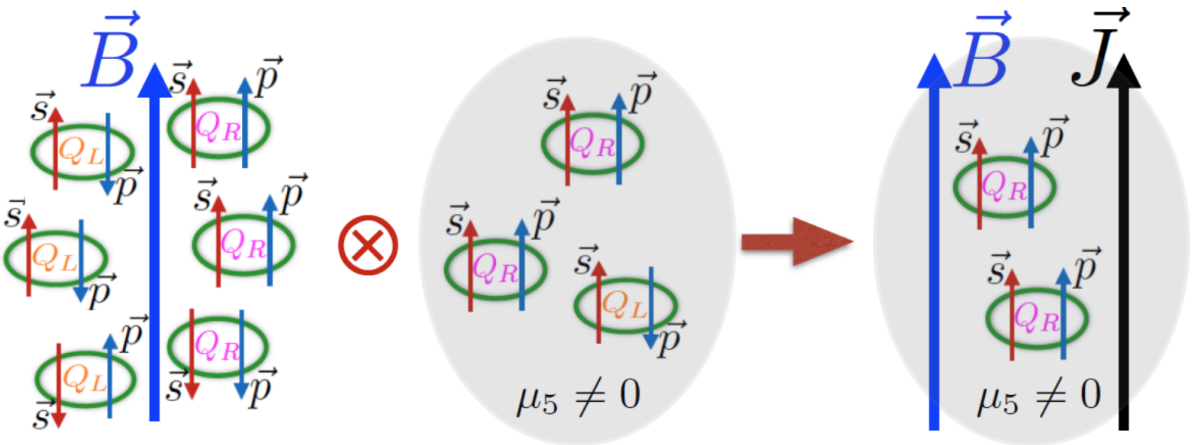

Figure 1.11: *Qualitative illustration of the mechanism of the Chiral Magnetic Effect. The direction of momentum and the spin of quarks are denoted by the blue and red arrows, respectively. With the presence of an external strong homogeneous magnetic field, the spin of quarks is polarised, as shown in the left panel. Then, in the middle panel, the interaction with gluon fields with non-zero winding number induces a local imbalance of the chirality (or helicity, as explained previously, since $|\vec{p}_{quark}| \gg m_{quark}$) of quarks. Lastly, in the right panel, the interplay of the strong external magnetic field and the chirality imbalance leads to a net electric current along the direction of $\vec{B}$. Figure adopted from [32].*

Heavy-ion collisions create a perfect environment to search for it. The magnitude of the electric current can be obtained based on the energy balance argument, which states that the total cost of the energy required to flip the handedness of quarks equals the power delivered by the current, assuming no energy losses [84]. This leads to

$$\vec{J} = \frac{e^2 \mu_5}{2\pi^2} \int d^3x \vec{B}, \tag{1.4.2}$$

where μ_5 denotes the chiral chemical potential, which quantifies the net chirality imbalance $N_5 = N_R - N_L$ (see Sec. IV in [84] for details).

The interplay of charge, local chirality imbalance, electromagnetic fields, and local angular momentum (vorticity) of the system can also give rise to a diverse range of phenomena akin to the Chiral Magnetic Effect, including the Chiral (Electric) Separation Effect, Chiral Vortical Effect, Chiral Magnetic Wave, Chiral Vortical Wave. A comprehensive description of these phenomena is beyond the scope of this dissertation. Interested readers can refer to [85] for a detailed review and discussion.

1.4.1 Status of the experimental search of the chiral magnetic effect

The experimental signature of the CME is a charge separation across the plane perpendicular to the magnetic field (Ψ_{B}). Here, we assume that Ψ_{B} is equivalent to the reaction plane Ψ_{RP}. Note that both Ψ_{B} and Ψ_{RP} are not experimentally accessible. In Sec. 4.2, we will see that the reaction plane can be replaced by either the second-order symmetry plane Ψ_2 or the spectator plane Ψ_{SP} in the CME analysis. The CME signal introduces an asymmetry with respect to Ψ_{B}, leading to a sine term in the azimuthal expansion

$$\begin{aligned} \frac{dN}{d[\varphi - \Psi_n]} &\propto 1 + 2a_{1,\alpha} \sin(\varphi - \Psi_{\mathrm{B}}) + 2\sum_{n=1}^{\infty} v_{n,\alpha} \cos[n(\varphi - \Psi_n)] \\ &= 1 + 2a_{1,\alpha} \sin(\varphi - \Psi_{\mathrm{RP}}) + 2\sum_{n=1}^{\infty} v_{n,\alpha} \cos[n(\varphi - \Psi_n)], \end{aligned} \tag{1.4.3}$$

where $\alpha = \pm$ denotes the charge.

At an early time, Voloshin proposed that a way to probe the leading order P-odd coefficient in CME is by measuring charge-dependent three-particle ($\gamma_{1,1}$) azimuthal correlations [86], defined as

$$\gamma_{1,1} = \langle \cos(\varphi_\alpha + \varphi_\beta - 2\Psi_{\mathrm{RP}}) \rangle, \tag{1.4.4}$$

where the angular brackets indicate an average over all events and particles, and sub-indices α and β refer again to charge. The final observable for CME is constructed by taking the difference between opposite-sign combinations and same-sign combinations, denoted as $\Delta\gamma$. The two-particle azimuthal correlator (δ_1) has also been proposed to help disentangle the contributions from correlations in- and out-of-plane (see Sec. 4.1.1 for details)

$$\delta_1 = \langle \cos(\varphi_\alpha - \varphi_\beta) \rangle. \tag{1.4.5}$$

For now, it is sufficient to mention that a charge separation with respect to the reaction plane leads to $\Delta\gamma > 0$. In Sec. 4.1.1, the potential and constraints of these observables will be further discussed in detail.

Since then, experimental searches have been firstly performed at the STAR Collaboration in Au–Au collisions [87, 88], in which the results were aligned with the initial expectation of $\Delta\gamma > 0$ for a charge separation with respect to the reaction plane due to the CME. Soon after the operation of the LHC, the ALICE collaboration reported the measurements of the same correlations for Pb–Pb collisions at $\sqrt{s_{NN}} = 2.76$ TeV [89] and showed a quantitatively similar effect. This is followed by more measurements in Pb-Pb collisions at $\sqrt{s_{NN}} = 5.02$ TeV by both ALICE and CMS collaboration [90, 91]. Recently, the measurements in Xe-Xe collisions were also reported in [6, 92]. However, the observation of quantitative agreement between the same charge-dependent correlation in the LHC and RHIC [87, 88], despite different collision energies and collision systems leading to different multiplicity densities and magnetic fields, hints that these correlations are heavily contaminated by background effects. The sources of contamination were identified to be mainly from local charge conservation coupled to the anisotropic expansion of the system in noncentral collisions [93–95].

Several new methods were developed to disentangle the signal and the background in the charge-dependent correlators. For conciseness, all the upper limits presented below represent the percentage of contribution from CME to the $\Delta\gamma$ at 95% confidence level. The ALICE and CMS collaboration presented the upper limit of 26–33% [96] and 7% [97], respectively, using an event shape engineering (ESE) technique proposed in [98]. The main idea of ESE is that at each centrality interval (events with similar impact parameters), the initial geometry of each collision (i.e., the position of participating nucleons) exhibits strong fluctuations, which allows one to select events with different initial system shapes. The dominant component of the background, the elliptic flow coefficient v_2, which is correlated to the initial system shape, can be minimised accordingly. The STAR collaboration combined ESE with cuts on pair invariant mass to also reduce strong resonance background contributions, concluding an upper limit of 15% in Au-Au collisions at $\sqrt{s_{NN}} = 200$ GeV [99].

The higher harmonic method is another approach attempted by ALICE collaboration. This method constrains the fraction of CME by disentangling the background through modified charged azimuthal correlators and provides an upper limit of 15-18% for mid-central collisions in Pb-Pb collisions [90]. The original three-particle charged azimuthal correlator is modified by correlating the charged particles with respect to the third order symmetry plane (Ψ_3) of the form $\gamma_{1,2} = \langle \cos(\varphi_\alpha + 2\varphi_\beta - 3\Psi_3)\rangle$, where Ψ_3 is very weakly correlated with $\Psi_2 \approx \Psi_{\mathrm{RP}}$. The correlator $\gamma_{1,2}$ is expected to contain negligible CME signal (charge separation relative to the reaction plane), but it mainly reflects the background effects. In the background-only scenario, $\Delta\gamma_{1,1}$ and $\Delta\gamma_{1,2}$ can be approximated according to $\Delta\gamma_{1,1} \propto \kappa_2 \Delta\delta_1 v_2$ and $\Delta\gamma_{1,2} \propto \kappa_3 \Delta\delta_1 v_3$, where κ_2 and κ_3 are proportionality constants assumed to be approximately the same. This assumption is backed up by the study from the CMS collaboration at the LHC on charge-dependent azimuthal correlations in p-Pb and Pb-Pb collisions [97].

More recently, the idea of using isobar collisions (two ions with the same nucleon number but different proton numbers) was proposed to verify the CME [100]. The STAR Collaboration performed dedicated isobar collisions (Ru-Ru and Zr-Zr) and compared the CME sensitive observables among these two systems which are thought to have the same level of background (same nucleon number in Ru and Zr) but different strengths of CME owing to Ru and Zr having different proton numbers and thus magnetic fields [101]. The original STAR paper reported that no CME signature was observed. It was also noted that v_2 and multiplicity distribution from Ru and Zr were noticeably different, resulting in more difficulties for direct extraction of the upper limit as the background effects may be different enough to overwhelm the small signal of CME. Later, a model-dependent upper limit was provided as $6.8 \pm 2.6\%$ by [102]. The LHC

has not performed any isobar collisions, but inspired by the idea of isobar collisions, the ALICE collaboration studied the Xe-Xe collisions at $\sqrt{s_{NN}} = 5.44$ TeV and Pb-Pb collisions at $\sqrt{s_{NN}} = 5.02$ TeV together using a two-component model [6]. The study resulted in an upper limit of around 2% and 25% for the 0–70% centrality interval in Xe–Xe and Pb–Pb collisions, respectively.

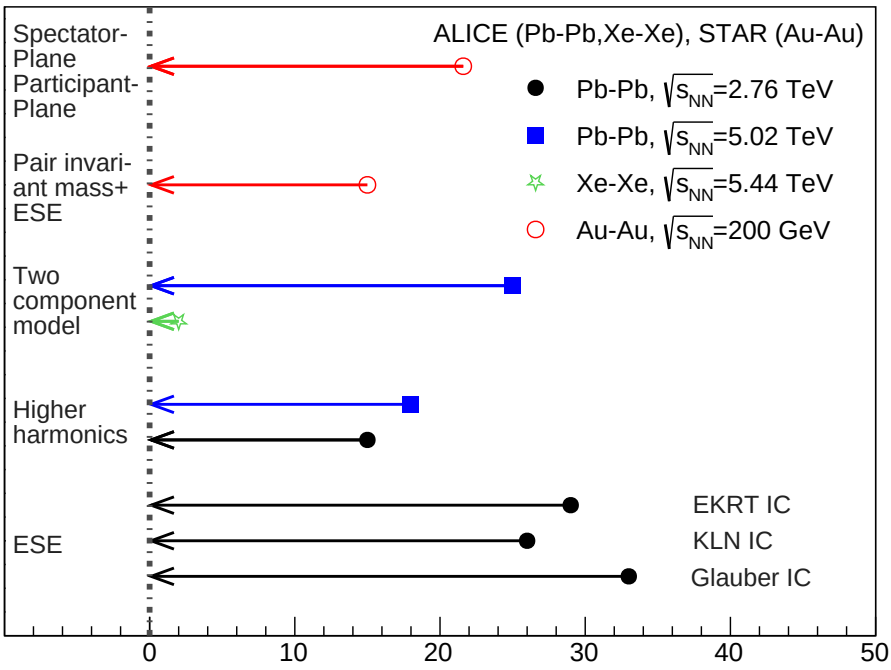

Figure 1.12: *Summary of the results for the upper limit of the CME contribution to the $\Delta\gamma$ correlator at 95% confidence level obtained from different methods performed at various LHC and RHIC energies and colliding systems integrated over centralities. For the event shape engineering method (ESE), three model-dependent upper limits are obtained using different initial conditions (IC): EKRT [45], KLN [46, 47] and Galuber [43]. Data points are from [6, 90, 96, 99, 103].*

In this dissertation, another method known as the spectator-participant-plane method, proposed in [104, 105], is used to search for CME in Pb-Pb collisions at $\sqrt{s_{NN}} = 5.02$ TeV collected by the ALICE detector. During the work of this project, the same method utilised by the STAR collaboration in Au-Au collisions at $\sqrt{s_{NN}} = 200$ GeV has been published [103]. In peripheral collisions, the analysis yields a signal consistent with zero. However, a hint of finite positive signal with a 1-3σ (depending on different centrality intervals) significance was found in mid-central Au-Au collisions. A final upper limit of the percentage of CME signal for full data within the centrality interval 20-50% and $0.2 < p_T < 2$ GeV/c is given as $14.7 \pm 4.3(\text{stat.}) \pm 2.6(\text{syst.})\%$.

The upper limits of CME from all ALICE studies at various collision energies and systems are summarised in Fig. 1.12. Overall, the current upper limits in Pb-Pb and Xe-Xe collisions suggest a higher potential to reveal CME in large collision systems (e.g. Pb–Pb) than in their small collision counterparts, mainly due to the higher early magnetic field created by a larger number of protons in large collision systems. Considering the strong connections previously

introduced between the CME and fundamental, yet unexplored aspects of QCD, as well as its connection to the θ term in the QCD Lagrangian, it is an imperative question to be answered by the heavy-ion community.

Chapter 2

Experimental Setup

2.1 The Large Hadron Collider

The Large Hadron Collider (LHC) is the world's largest and most powerful particle accelerator. It is situated approximately 100 meters beneath the Earth's surface within a circular tunnel measuring 27 kilometres in circumference, in the vicinity of Geneva, Switzerland, and is operated by the European Organization for Nuclear Research, known as CERN. The LHC is designed to accelerate beams of protons and of heavy ions (e.g. lead and xenon ions) up to nominal energies of $\sqrt{s} = 14$ TeV and $\sqrt{s_{\mathrm{NN}}} = 5.5$ TeV, respectively. In addition, the LHC can perform collisions with asymmetric beam configurations such as proton-lead collisions.

The acceleration of lead ions is achieved through a complex process prior to their final acceleration to their top energy at the LHC. This process starts with heating a 2-centimetre-long piece of pure lead weighing 500 milligrams to approximately 500 degrees Celsius to vaporise a small number of atoms. Each atom's electrons are then removed using an electrical current, and the newly created ions commence their journey through the particle accelerator. The ions receive a slight amount of energy (up to an energy of $\sqrt{s_{\mathrm{NN}}} = 50$ MeV) as they travel through a linear accelerator called Linac3 before undergoing another round of electron removal. In the next stage, the Low Energy Ion Ring (LEIR) is used to accumulate and accelerate the ions, segregating them into bunches of around 2.2×10^8 ions per bunch. Although vaporisation and acceleration in Linac3 and LEIR are specific to ions, the ions travel the same path as protons once they leave the LEIR. The Proton Synchrotron (PS) and the Super Proton Synchrotron (SPS) are utilised to accelerate heavy ions in the subsequent stages, where an energy of 450 GeV per nucleon is finally reached and the last of their electrons stripped away before injecting them into the Large Hadron Collider in two directions. A schematic representation of the accelerator complex is shown in Fig. 2.1.

The particles undergo collision at four distinct junctures around the LHC ring, specifically where the beam pipes intersect. At each of these points, a detector is placed, namely, ATLAS [106] and CMS [107], both of which are general-purpose detectors, LHCb [108], designed solely for the purpose of studying CP violation in B-decays, and ALICE, intended for the study of heavy-ion collisions. A comprehensive account of the LHC's technical specifications and characteristics can be found in [109].

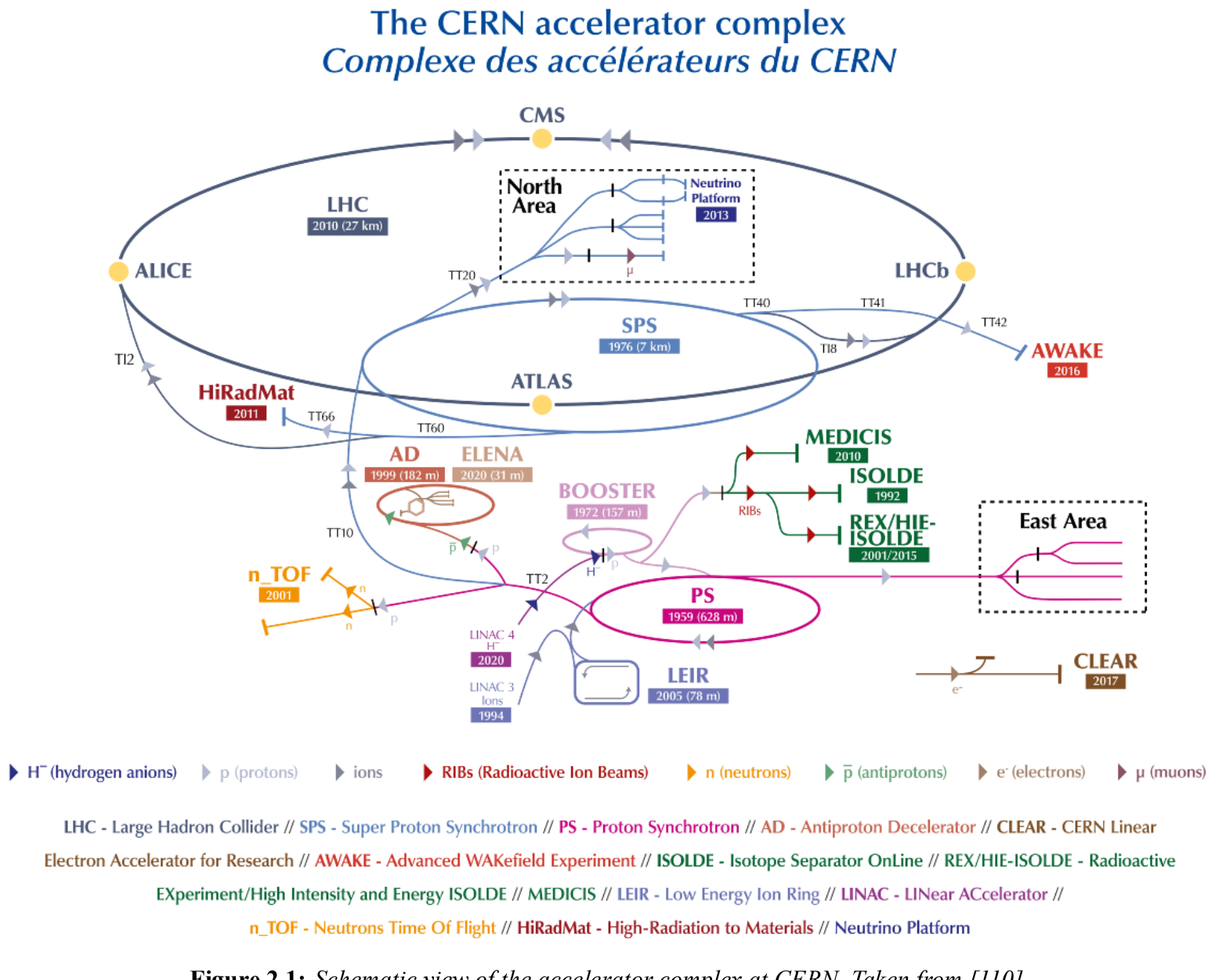

Figure 2.1: *Schematic view of the accelerator complex at CERN. Taken from [110].*

2.2 A Large Ion Collider Experiment (ALICE)

The ALICE Experiment, an acronym for A Large Ion Collider Experiment, is located at Interaction Point 2 of the Large Hadron Collider at CERN. The technical design and the performance of the ALICE detector can be found in [111–114]. The schematic view of the numerous sub-detectors comprising ALICE during Run 2, when the data for this analysis were collected, is depicted in Fig. 2.2. Run 2 spanned from 2015 to 2018, after which ALICE underwent several upgrades to its various sub-detector systems in anticipation of Run 3, during a lengthy shutdown period referred to as Long Shutdown 2 (LS2).

This section will only concentrate on the detectors directly pertinent to this dissertation, namely the Inner Tracking System (ITS), Time-Projection Chamber (TPC), VZERO (V0) system, and Zero-Degree Calorimeters (ZDC). The description of these detectors will be presented in the present tense, based on their Run 2 conditions. All of these detectors adopt a consistent coordinate system, which is a right-handed Cartesian system oriented such that the x-axis points towards the centre of the LHC, while the y-axis points straight up and the z-axis is aligned parallel to the beam axis. The standard conversion from the 3D – Cartesian coordinate system (x, y, z) to the Spherical coordinate system (r, ϕ, θ) is employed, where r is the radial distance, ϕ is the azimuthal angle around the beam axis and θ is the polar angle denoting the angle of a particle w.r.t. the z-axis. The particles recorded by the detectors are characterised by their four-vectors $p^{\mu} = (E, p_x, p_y, p_z)$, from which the commonly used quantities such as transverse momentum p_{T}, rapidity y, and pseudorapidity η are accordingly defined as:

$$p_{\mathrm{T}} = \sqrt{p_x^2 + p_y^2}, \quad y = \frac{1}{2} \ln\left(\frac{E + p_z}{E - p_z}\right), \quad \eta = -\ln\left(\tan\left(\frac{\theta}{2}\right)\right), \tag{2.2.1}$$

respectively. Instead of using angles directly, which are not additive under Lorentz transformation, the rapidity y is a convenient quantity, where its difference is invariant with respect to Lorentz boosts along the beam axis. The pseudorapidity η, used more widely in experimental fields, is a simpler quantity to calculate and measure than rapidity, and is equivalent to the rapidity in the limit of massless particles, which is a valid approximation in high-energy collisions at the LHC. It is also important to note that the production of particles is relatively constant as a function of rapidity or pseudorapidity in the range of around $|\eta| < 2$ (the Inner Tracking System and the Time-Projection Chamber have an acceptance range of $|\eta| < 0.9$) [115], making this quantity even more convenient.

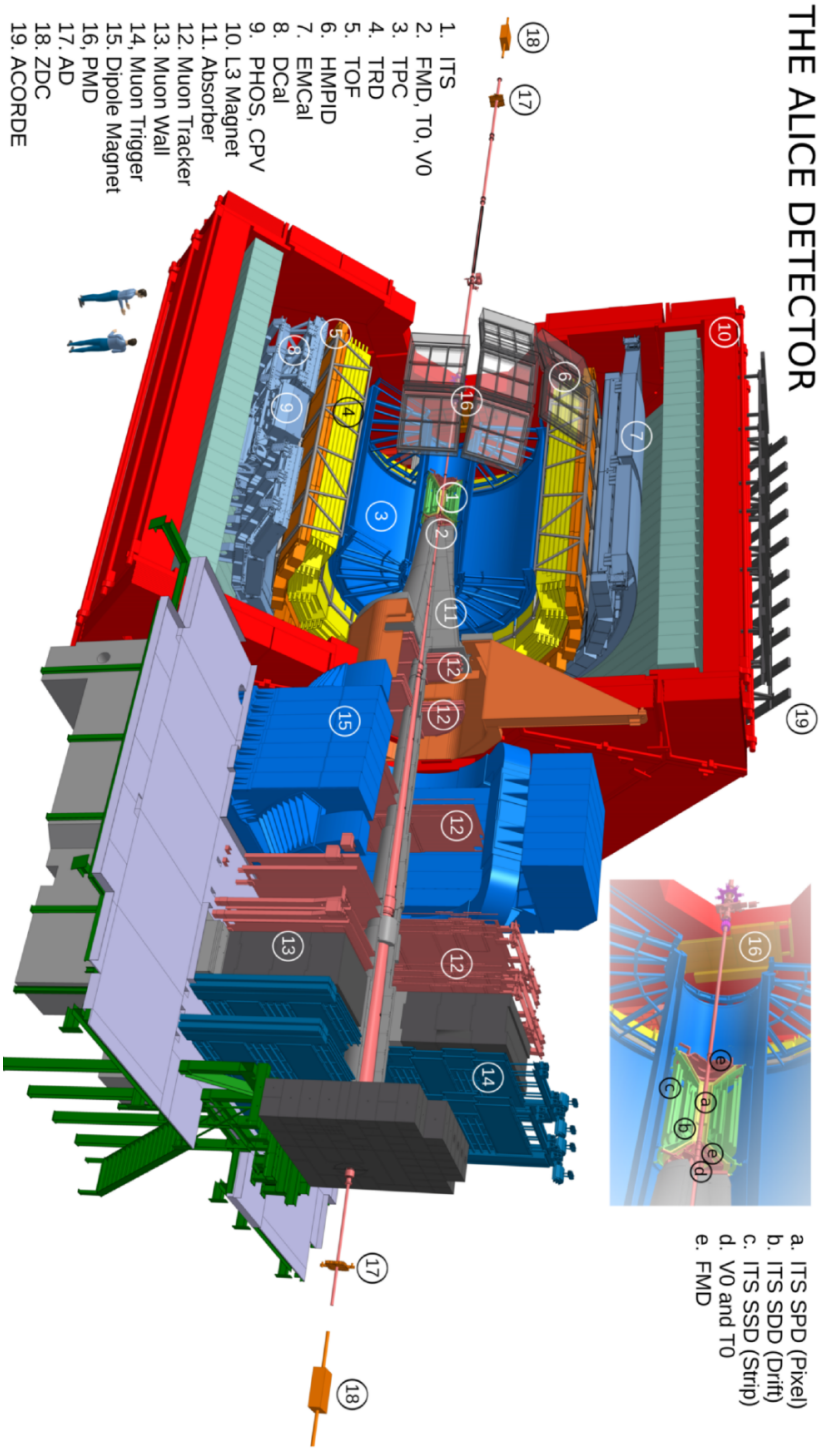

Figure 2.2: *Schematic view of the ALICE detector during LHC Run 2 (2015-2018).*

2.2.1 Inner Tracking System (ITS)

The ITS is the detector situated nearest to the beam pipe, composed of six concentric cylindrical layers of silicon detectors, possessing minimum and maximum diameters of 3.9 and 43 cm, respectively [116]. A silicon detector detects the tracks of charged particles by measuring tiny electrical signals generated by the drifting of electron-hole pairs under an internal electric field. These pairs are formed when charged particles traverse doped silicon, causing the ionisation of the material in their trajectory. The various layers employ different technologies tailored to the anticipated track densities. As depicted in Fig. 2.3, the two innermost layers use Silicon Pixel Detectors (SPD), while the middle layers rely on Silicon Drift Detectors (SDD), and the two outermost layers utilise Silicon Strip Detectors (SSD).

The ITS is primarily used to track the trajectories of charged particles and to reconstruct primary vertices, with a resolution better than 100 μm [117], and secondary vertices. The ITS provides phase space coverage for transverse momentum in the range of $0.1 < p_{\mathrm{T}} < 3$ GeV/c, with a relative momentum resolution of better than 2% for pions in this range [111]. For $p_{\mathrm{T}} > 3$ GeV/c, the ITS is used to improve the transverse momentum resolution for tracks also traversing the TPC. The ITS covers a full range of azimuthal angles (ϕ) and a pseudorapidity region of $|\eta| < 0.9$.

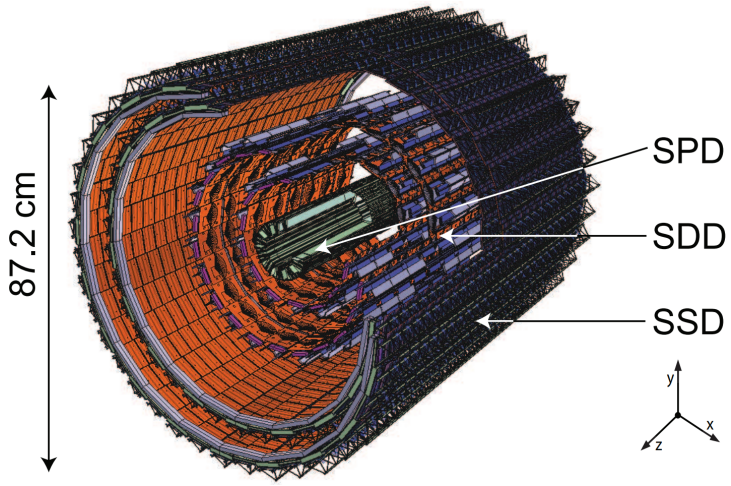

Figure 2.3: *Schematic view of the ITS detector, includes Silicon Pixel Detector (SPD), Silicon Drift Detector (SDD) and Silicon Strip Detector (SSD). This figure is adopted from [117].*

2.2.2 Time-Projection Chamber (TPC)

The TPC detector is one of the largest and most significant components of the ALICE system. A schematic view of the design of the TPC is shown in Fig. 2.4 [118]. It consists of two cylindrical volumes separated by a cathode, providing complete azimuthal angle coverage (ϕ) and a pseudorapidity range of $|\eta| < 0.9$. The cathode generates an electrostatic field of approximately 400 V/cm along the z-axis, thereby producing a maximum drift time of approximately 90 μs. The TPC extends radially from 84.1 cm to 246.6 cm and spans a total length of 5 m. It is a cylindrical gas detector filled with a 90 m^3 gas mixture of Neon and CO_2, ionised when charged particles traverse it. An avalanche reaction is generated, with the drifting electrons ionising additional gas molecules before being absorbed by the multi-wire proportional chambers situated at the end plates. The electric signal induced by freed ions is directly proportional to the

number of electrons that initiate the avalanche. The drift time information is used to determine the z coordinate, while the r and ϕ coordinates are obtained from the end plates' position. The TPC end plates are composed of 18 trapezoidal sectors, distributed evenly around the detector. Each end plate is partitioned into two chambers with 159 pads that form the cathode plane of the multi-wire proportional chambers, as mentioned above, in the radial direction. A *cluster* refers to the charge signals detected in a pad row when a charged particle traverses. Typically, the quality of the track reconstruction improves with an increase in the number of clusters, with a maximum of 159 clusters.

The TPC provides high-quality measurements of charged particle momentum (p_{T} from 0.1 GeV/c to 100 GeV/c) and the position of charged tracks with a resolution of 800-1100 μm in $r\phi$ and 1100-1250 μm in z. The energy loss (dE/dx) of the charged particles is determined through the amount of ionisation per unit length in the gas of the TPC, which allows for particle identification via the Bethe-Bloch formula. Additionally, the TPC is used to support the ITS in determining collision vertices in heavy-ion collisions. Notably, the TPC is also an estimator of collision centrality (see Sec. 3.3 for the definition of centrality), exhibiting a high level of accuracy, ranging from 0.5% in central collisions to 2% in peripheral collisions [119]. In this dissertation, the TPC is primarily used to obtain the azimuthal angle and p_{T} of charged particles. The participant planes reconstructed using the TPC are also used in the analysis for a consistency check, but they are not chosen to be presented in the final result as explained in Sec. 2.2.3 below.

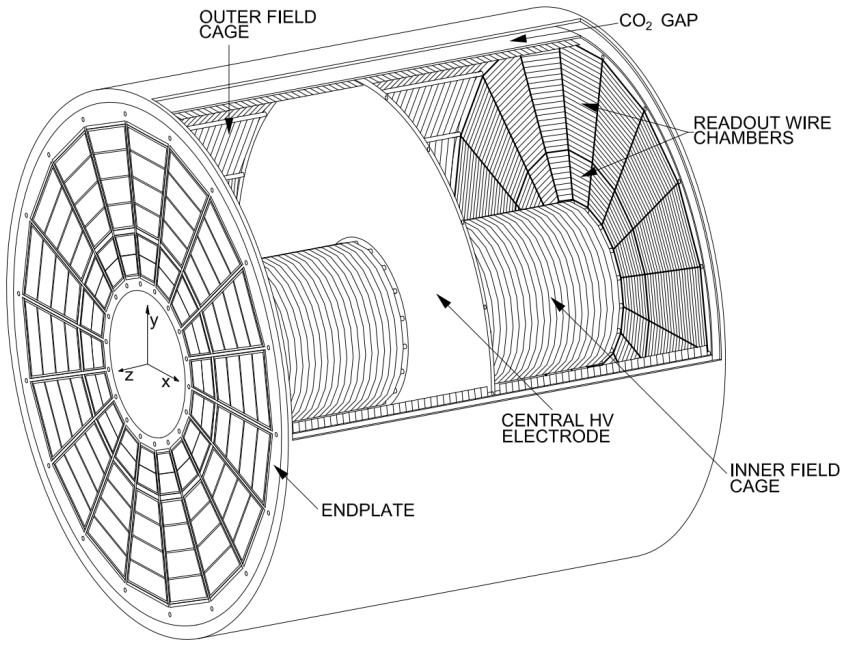

Figure 2.4: *Schematic view of the TPC detector, includes Silicon Pixel Detector (SPD), Silicon Drift Detector (SDD), and Silicon Strip Detector (SSD). This figure is adopted from [120].*

2.2.3 VZERO (V0) system

The VZERO system is comprised of two arrays of scintillator counters, namely V0-A and V0-C, which provide coverage of the pseudorapidity ranges of $2.8 < \eta < 5.1$ and $-3.7 < \eta < -1.7$, respectively [121, 122]. The VZERO-A is positioned at a distance of 329 cm from the nominal vertex on the side opposite to the muon spectrometer, as illustrated in Fig. 2.5a. The VZERO-C

is 90 cm away from the nominal vertex, fixed on the front surface of the hadronic absorber. Each of the VZERO arrays is further segmented into four rings in the radial direction, with each ring being divided into eight sections in the azimuthal direction, as illustrated in Fig. 2.5b.

Several crucial purposes are served by the VZERO system, including triggering (minimum bias or centrality trigger); separating beam–beam interactions from background events through the timing of the signals; monitoring beam luminosity; centrality determination through measuring charged particle multiplicity; and measuring the azimuthal distribution of charged particles in each collision. The minimum bias triggering and the centrality information used in the default selections of the analysis in this dissertation are based on the VZERO system. The last stated purpose allows the estimation of participant planes, which is used in the presentation of my final result. The advantage of using the VZERO system rather than the TPC is that the existence of a natural large gap in η between TPC and V0 reduces the contributions of any short-range correlation (e.g. jet fragmentation and resonance decays) unrelated to the participant planes.

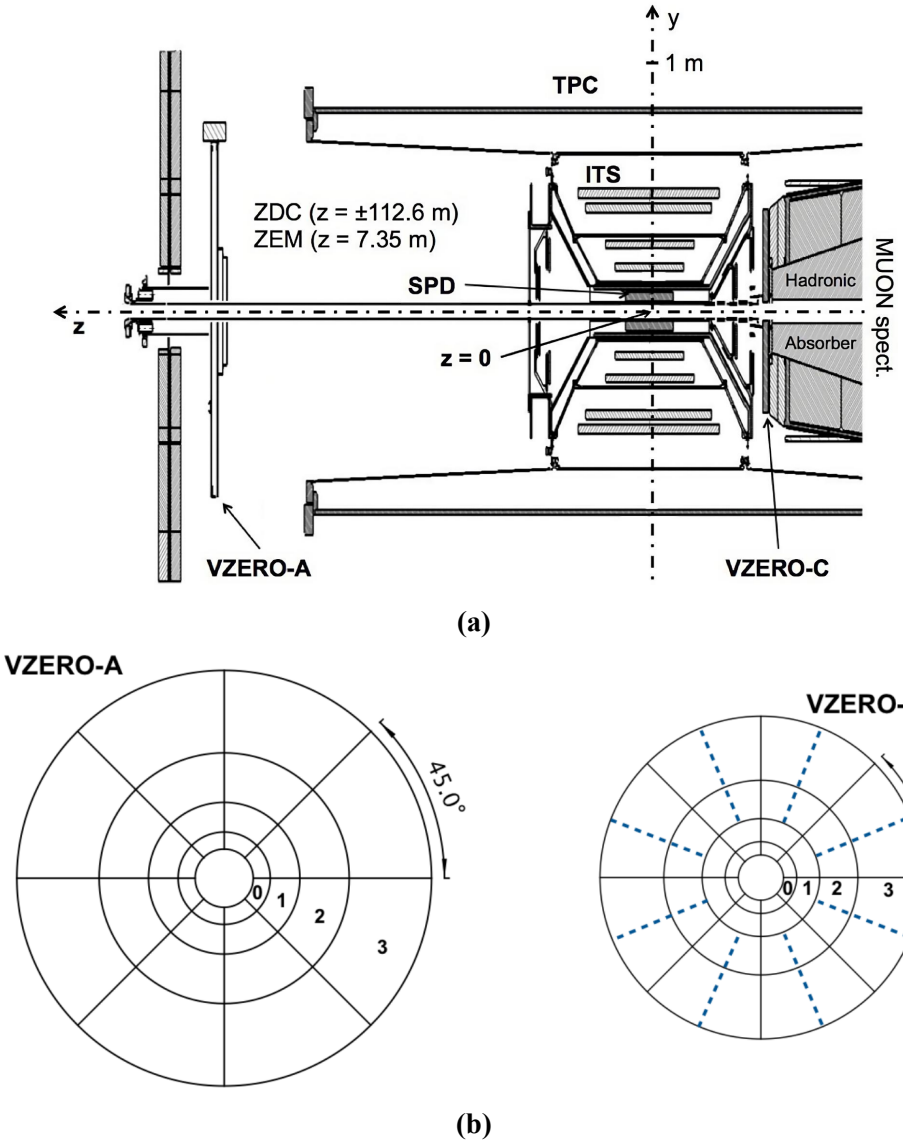

Figure 2.5: *(a) Schematic view of the position of two VZERO arrays within the overall layout of the ALICE experiment. (b) Sketches of the segmentation of VZERO-A and VZERO-C.*

2.2.4 Zero Degree Calorimeter (ZDC)

The Zero Degree Calorimeters (ZDC) for the ALICE experiment are dedicated to measuring spectator nucleons that ”miss” the collisions, flying past each other rather than colliding with almost no interaction between the spectator matter and the participant matter, and exiting from the interaction region in the same direction as the beam direction, in the off-central heavy-ion collisions. The ZDC system consists of two identical sets of hadronic calorimeters located at opposite sides (A and C side, respectively) around 116 meters away from the nominal collision vertex [123, 124]. Each side of the ZDC has two distinct detectors: a proton calorimeter (ZP) and a neutron calorimeter (ZN), placed externally to the beam pipes and between the beam pipes as shown in Fig. 2.6. The separation dipole magnet (D1) deviates proton spectators from the ion beams towards ZP, while neutron spectators are not affected, flying in the same direction at zero degree towards ZN. Then, the recombination dipole magnet (D2) guides the beams to two separated vacuum chambers. In this dissertation, only the neutron ZDCs, labelled as ZNC and ZNA for the C and A side, respectively, are used. In each neutron ZDC, the silica optical fibres as active material are embedded in a dense absorber (tantalum). When incoming neutrons collide with the dense absorber, a cascade of charged particles (shower) is generated. Cherenkov light is further produced when the shower’s charged particles propagate in the fibres. Optical fibres guide the Cherenkov light to photo-multiplier tubes (PMT) where signals can be read out. The transverse area of the neutron ZDC covered by the optic fibres is divided into four segments (or towers) equally, as shown in Fig. 2.7. One in two fibres from all towers is sent to a single PMT (PMT c), known as the common tower, providing a separate measurement of the total energy deposited in each neutron ZDC. The remaining ones are connected to four different PMTs (PMT 1-4), which collect the light from each tower, respectively.

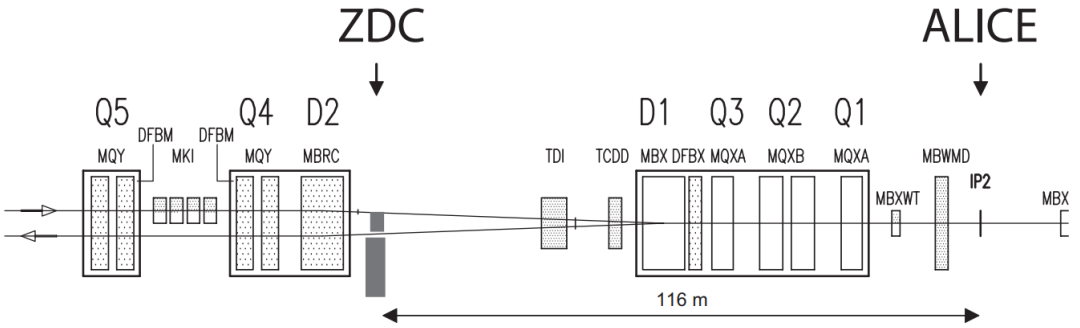

Figure 2.6: *Schematic view of the ZDC location relative to the interaction point 2 (IP2). D1 and D2 refer to the separation and recombination dipole magnets used to direct the beams from IP2 into two distinct vacuum chambers. TDI is a large absorber, complemented by an additional shielding element (TCDD), which serves to protect the cold elements in the event of an injection failure. Q1-Q5 are individually powered magnets, where their specific purposes can be found in [125]. Two DFBMs denote the local current feed box, which provides power to the magnet systems. The cryogenic feed-box DFBX provides both power and a link to the cryogenic distribution line. The injection kicker MKI kicks the injected beam in the vertical plane, directing it towards the closed orbit of the circulating beam. Figure adopted from [126].*

The neutron ZDCs are designed to contain 80% of the shower generated by spectator neutrons [123]. The energy deposited in each neutron ZDC fluctuates event by event, but the average is proportional to the number of absorbed nucleons, equivalent to the energy of the spectator

nucleons. One of the primary goals of neutron ZDCs is to provide a direct determination of the impact parameter and the centrality of the collisions. In addition, neutron ZDCs are also used as an LHC luminosity monitor during operation with heavy-ion beams. Lastly, since each neutron ZDC has four towers, it is possible to determine the central positions of the showers generated by two beams of spectators flying in opposite directions. Ideally, the central position of the shower from spectator neutrons on each side of the neutron ZDC forms a plane with the beam axis, which gives a direct measurement of the spectator plane. In reality, the reconstructed angle from each side of the ZDC does not agree well with each other, and a detailed study on reconstructing the spectator plane with neutron ZDCs will be further discussed in Section 3.7.

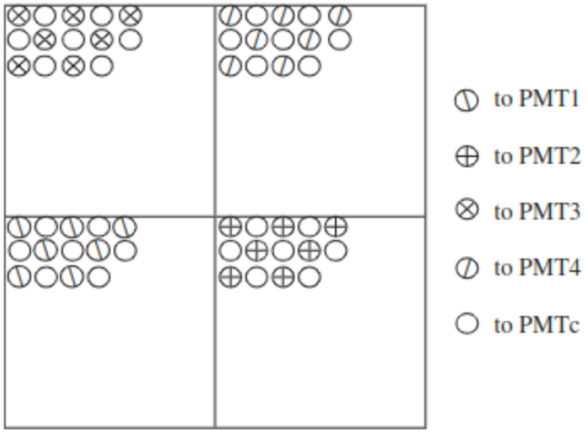

Figure 2.7: *Schematic connection of the fibres to the PMs of the neutron calorimeter. Figure adopted from [127].*

Chapter 3

Data Analysis

3.1 Data Set

The full data sample of Pb–Pb collisions at $\sqrt{s_{NN}} = 5.02$ TeV collected by the ALICE detector in 2018 (LHC18q and LHC18r) during Run 2, consisting of a total of 4.34×10^7 (2.57×10^7 and 1.77×10^7, respectively) minimum-biased collisions in the centrality range 10-50%, is used in this dissertation. The experimental data is partitioned into discrete intervals labelled by "run numbers," each of which encompasses a period of continuous data acquisition by the ALICE detector. Interspersed among these runs are interludes of downtime, which are brought about by one of two factors: the dump of LHC beams, mainly due to unstable beams and a drop in beam intensity over time, or detector-related concerns, such as the need for calibration or repair due to malfunctioning. A total of 125 and 89 run numbers are included in the LHC18q and LHC18r data set, respectively.

3.2 Event selection

Each recorded collision at the interaction point is denoted as an *event*. The ALICE detector has a limited readout rate of 500 Hz for Pb-Pb collisions in Run 2, determined by the rate of the slowest detector, the TPC. An appropriate selection of events is required to effectively differentiate inelastic hadronic nucleus-nucleus collisions constituting the entire hadronic cross-section from various kinds of events, such as electromagnetic interactions, beam-gas interactions, and pile-ups, which are more frequent and uninteresting for this analysis.

The event selection is performed both *online*, during the recording of events, and *offline*, through the analysis of recorded data. The online selection needs to be very fast, which is based on the trigger decision made by the Central Trigger Processor (CTP) on the simultaneous occurrence of detected signals in multiple detectors. For the Run 2 data set, the online trigger conditions require a minimum signal in V0C and V0A detectors simultaneously. The minimum detected signal in the V0 detector is determined based on the energy deposition of a minimum ionising particle in each V0 tile. The events collected with these online trigger requirements are called the *Minimum Bias* (MB) events, which constitute the entire hadronic cross-section. In the analysis framework, each online trigger class is associated with an offline trigger mask, as defined in `AliVEvent::EOfflineTriggerTypes`. There are two trigger types used in this analysis: kINT7 and kSemiCentral, where kINT7 refers to events passing minimum bias selection

criteria and kSemiCentral refers to events with threshold signals detected in V0A and V0C detectors corresponding to semi-central collisions. The kSemiCentral trigger provides around 2.5 and 4 times more events in semi-central collisions compared to kINT7 and has a flat acceptance in the centrality range of 30-50% (as shown in Fig. **??**). The purpose of using the kSemiCentral trigger is to combine with minimum bias events to reduce the statistical uncertainty in the analysis.

The triggered events are contaminated by events from two sources which are checked in offline event selection. The first source is machine-induced background due to the interaction between one of the beams and the residual gas present within the beam-pipe, as well as interactions between ions in the beam halo and mechanical structures within the machine. In addition, ions "jumping" from their own bunch position into one of the empty neighbouring buckets cause collisions well outside the fiducial region $|z_{\rm vtx}| \lesssim 10$ cm, which also contribute to the machine-induced background. The second source is the electromagnetic interactions (photo-production and photo-nuclear interactions) induced by the EM fields of relativistic heavy ions. The removal of these spurious events is done offline with several selection criteria:

- constraints on the signal arrival time at each of the V0A and V0C detectors;
- consistency in the arrival time recorded by each of the neutron ZDCs;
- the neutron ZDC signal being three standard deviations higher than the single neutron peak;

This is followed by a standard ALICE procedure to remove pile-up events, which can come from multiple collisions occurring in the same bunch crossing (*same-bunch-crossing pile-up*) or one (or more) collisions taking place in bunch crossings other than the one that triggered the acquisition (*out-of-bunch pile-up*). These selection criteria can be briefly summarised as:

- checking for the existence of multiple primary vertices determined from reconstructed TPC+ITS tracks;
- consistency check of the convergence point of SPD tracklets.

The full details of the standard pile-up selection in Run 2 can be found in [112, 128]. It should be noted that the selection procedures described above have been taken care of by the ALICE data preparation group and the well-reconstructed events are finally stored in the Analysis Object Data (AOD), which is the most lightweight data format in ALICE for most physics analyses to use.

A few additional event selection criteria are applied to the AOD events to further eliminate contamination. This includes a clean-up procedure on the pile-up events implemented separately on LHC18q and LHC18r by applying a 5σ cut on the centrality estimated by the V0M (V0A+V0C) and CL0 (1st layer of ITS, see Sec. 3.3 for centrality determination), and multiplicities obtained from the TPC and V0 detectors. Furthermore, the longitudinal position of the reconstructed primary vertex is required to be within $|v_{\rm z}| < 10$ cm. The necessity is related to ensuring the high quality of reconstruction of tracks in the central barrel and is dependent on the detector's acceptance in the pseudorapidity region.

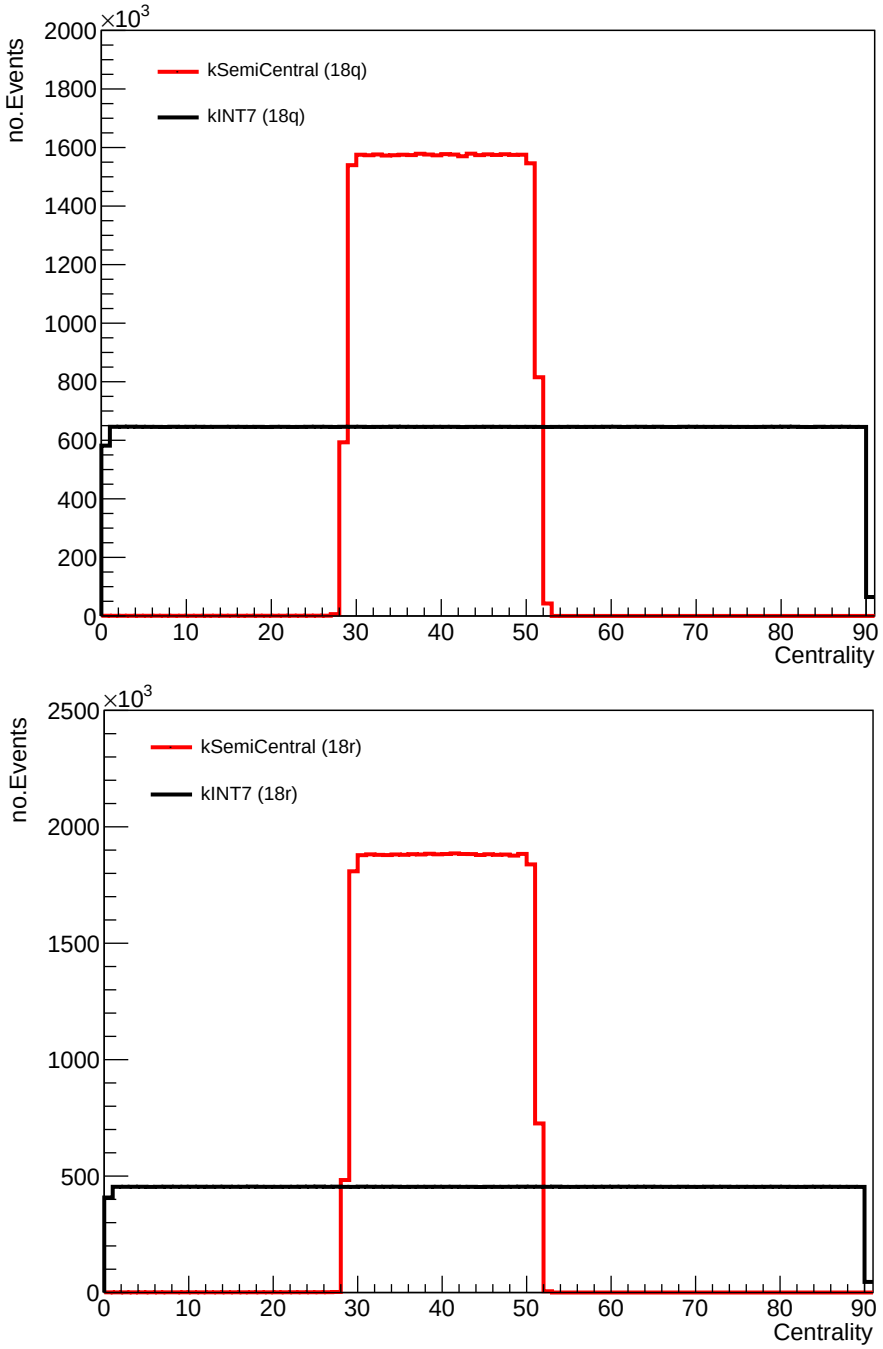

Figure 3.1: *Comparison of the event number distribution vs. centrality in LHC18q (left) and LHC18r (right) data sets for events that pass the kINT7 (black curve) and kSemiCentral (red curve) trigger, respectively.*

3.3 Centrality determination

The concept of centrality in heavy ion physics is proposed to represent the amount of the initial overlap region of the two colliding nuclei, quantified by the percentage of the total nuclear interaction cross section σ_{tot}, with 0% indicating a head-on collision with full overlap and 100% signifying no overlap between the nuclei [43]. The initial overlap region is directly related to the impact parameter b, which is the distance between the centres of two colliding nuclei projected onto the plane perpendicular to the beam axis. For an A-A collision with a particular impact parameter b, the centrality c is theoretically defined as the integration of the impact parameter distribution $d\sigma/db'$:

$$c_{\text{th}} = \frac{1}{\sigma_{\text{tot}}} \int_0^b \frac{d\sigma}{db'} db' \tag{3.3.1}$$

Neither the impact parameter nor the initial overlap region characterised by the number of participants in a collision are experimentally measurable quantities. However, they are directly connected to the average charged-particle multiplicity N_{ch} and the energy of spectators deposited in the ZDCs, E_{ZDC}. The expected number of charged particles $\langle N_{\text{ch}} \rangle$ decreases monotonically with increasing impact parameter, while E_{ZDC} is directly related to the expected number of spectator nucleons $\langle N_{\text{spec}} \rangle$, which increases with increasing impact parameter. It should be noted that E_{ZDC} loses its monotonic dependence on the impact parameter in peripheral collisions because the nucleons bound in nuclear fragments are large enough to exhibit similar magnetic rigidity as the beam nuclei, which remain inside the beam pipe and escape detection by the ZDCs. In ALICE, centrality is conveniently defined based on N_{ch} and E_{ZDC} as

$$c_{\text{exp}} \approx \frac{1}{\sigma_{\text{tot}}} \int_{N_{\text{ch}}^{\text{thr}}}^{\infty} \frac{d\sigma}{dN_{\text{ch}}} dN_{\text{ch}} \approx \frac{1}{\sigma_{\text{tot}}} \int_0^{E_{\text{ZDC}}^{\text{thr}}} \frac{d\sigma}{dE'_{\text{ZDC}}} dE'_{\text{ZDC}}, \tag{3.3.2}$$

where $N_{\text{ch}}^{\text{thr}}$ and $E_{\text{ZDC}}^{\text{thr}}$ aare a given minimum threshold of charged-particle multiplicity and a given maximum value of $E_{\text{ZDC}}^{\text{thr}}$ for the monotonic relation between E_{ZDC} and b to hold, respectively [129]. The absolute scale used in experimental measurements is determined by the *anchor point*, which is identified as the N_{ch} equivalent to 90% of the hadronic cross section. This value can be derived through either of two approaches. The first approach accesses the anchor point through a real multiplicity distribution obtained via careful simulation of hadronic and electromagnetic processes, accounting for detector response and reconstruction efficiency. The second approach involves fitting a simulated N_{ch} distribution (e.g., via the Glauber Monte Carlo model in conjunction with a simple particle production model) to the experimental data and treating the location of the discrepancy between the data and simulation as the anchor point. The default centrality estimator used in ALICE is the sum of the amplitudes in V0C and V0A detectors, which is proportional to N_{ch}. The number of clusters in the first (CL0) and outer layer (CL1) of the SPD, the number of reconstructed tracks in the TPC, and the energy deposited in the neutron ZDCs can also be used to estimate the centrality. Overall, the default estimator provides the best centrality resolution ranging from 0.5% in central to 2% in peripheral collisions, due to its large η coverage.

3.4 Track selection

The reconstruction of the charged tracks in the ALICE central barrel follows an inward–outward–inward scheme, which is described in detail in [112–114]. In brief, the first inward step com-

mences with building the track seeds from a distant radius in the TPC with two TPC clusters and the vertex point reconstructed from charged clusters in two SPD layers. The seeds are progressively advanced inward and are updated at each stage with the closest cluster, provided that it meets the prescribed proximity criteria. The reconstructed tracks from the TPC are utilised as the initial seeds for track finding in the outermost layer of the ITS. These seeds are propagated inwards, and at each ITS layer, they are updated by all clusters within a proximity cut. After the completion of the reconstruction process in the ITS, all tracks are extrapolated to their respective points of closest approach to the preliminary primary vertex. The second procedure starts from the SPD clusters and propagates outward through the TPC and further to outer detectors (e.g. Transition Radiation Detector and Time-Of-Flight detector) by refitting with the Kalman filter using the clusters found previously. In the final track reconstruction stage, all tracks are re-examined and refitted again using the previously determined clusters and propagate from the outer radius of the TPC towards the centre of the ITS.

In the Analysis Object Data (AOD) files, the reconstructed tracks are associated with different filter-bit (FB) masks corresponding to different sets of cuts. In this dissertation, the global hybrid tracks with FB768 are used in the default selection of the analysis. The concept of hybrid tracks was initially introduced in the 2010 Pb-Pb data set (LHC10h) to account for a hole in the azimuthal distribution resulting from inactive modules in the innermost two SPD layers. The filter bit 768 comprises two types of tracks: global hybrid tracks (FB256) and global constrained hybrid tracks (FB512). For the systematic uncertainty study, an alternative filter bit of 96 is used, which consists of tracks passing standard cuts with a tight Distance of Closest Approach (DCA)[1] cut (FB32), along with additional tracks that pass standard cuts with tight DCA but also require the first SDD cluster instead of an SPD cluster (FB64). The primary distinguishing feature between the default FB768 and the alternative FB96 concerns the cut value for DCA. Specifically, the hybrid track implementation utilises more permissive cut values of 2.4 and 3.2 cm in xy and z, respectively, while FB96 employed tighter DCA cuts with a p_{T} dependent cut value and 2.0 cm in xy and z, respectively. With tighter DCA cuts, the tracks tagged with FB96 include fewer secondary particles than hybrid tracks.

In addition, all primary charged tracks are accepted within the kinematic range $0.2 < p_{\mathrm{T}} < 3.0$ GeV/c and $|\eta| < 0.8$. The minimum number of TPC clusters and the average χ^2 of the track fit per TPC space points (χ^2_{TPC}) are required to be 70 and $0.1 < \chi^2_{\mathrm{TPC}} < 4.0$, respectively. The number of shared clusters for each track is required to be less than 40% of the number of clusters recorded in the TPC.

3.5 Q-vector

Before illustrating the calibration work for the TPC, ZDC and V0 detectors, it is important to introduce the notion of Q-vector, which is widely used in this dissertation. The concept of the Q-vector (also known as the flow vector) is first introduced in [130]. The specific definition of the Q-vector varies slightly based on the type of detector utilised in the analysis. In the case of fully reconstructed tracks, such as those obtained from the ITS and TPC, the Q-vector is defined

[1] In the context of particle physics, DCA really represents the distance of closest approach from the trajectory of a charged particle to the primary vertex.

as

$$Q_n = \frac{1}{\sqrt{\sum_{j=1}^{M} w_j}} \sum_{j=1}^{M} w_j e^{in\varphi_j}, \tag{3.5.1}$$

where M represents the track multiplicity, n corresponds to the harmonic order, and the particle weight w_j typically encompasses corrections from non-uniform acceptance and reconstruction efficiency. The pre-factor $1/\sqrt{\sum_{j=1}^{M} w_j}$, as explained in [131], is crucial for suppressing trivial contributions from multiplicity fluctuations in each centrality bin. In other words, Eq. 3.5.1 can be thought of as a random walk of $1/\sqrt{\sum_{j=1}^{M} w_j}$ unit steps, thereby possessing an expected distance of the walker from the origin as $\sqrt{\sum_{j=1}^{M} w_j}$, which cancels out with the factor in front. Note that the power on the weight introduced in [132] is outdated. There is no compelling reason or significant benefit to applying non-linear weights to particle tracks. In the Generic Framework developed in [133], linear weights ($m = 1$) are consistently used. For the V0 or the ZDC system, consisting of segments of calorimeter, the particle weight is replaced by the energy E_j in the j^{th} segment, and the corresponding definition will be introduced in Sections 3.7 and 3.8.

3.6 TPC Reconstruction Efficiency

The TPC does not have perfect efficiency for reconstructing charged primary tracks nor a uniform azimuthal acceptance. It is therefore important to correct for it by applying track weights to the observable. In this dissertation, only the reconstruction efficiency has been estimated because the analysis method utilises a mathematical technique known as the non-isotropic correction to ensure that the non-uniform azimuthal acceptance is corrected. Without using this technique, one has to compute the acceptance correction from real data as:

$$w_{\text{acc}} = \frac{\langle dN(\varphi, x, y...)/d\varphi dx dy d... \rangle_{\varphi}}{dN(\varphi, x, y...)/d\varphi dx dy d...}, \tag{3.6.1}$$

where $x, y, ...$ can be all dependent variables such as η, v_z, centrality, and run number. The average track density, denoted as $\langle dN(\varphi, x, y...)/d\varphi dx dy d... \rangle_{\varphi}$, is integrated over $0 < \varphi < 2\pi$ in each interval of other dependent variables.

The reconstruction efficiency is expected to be mainly dependent on p_{T}, while the sign of the charge and the centrality dependence are also taken into account. The p_{T} dependence can generally be attributed to the tracking process. Specifically, charged tracks with very low p_{T} values experience significant bending from the magnetic field and may not traverse the full length of the TPC, resulting in a reduced number of TPC clusters and consequently, a lower momentum resolution. The weight should also include a correction for the contamination from secondary interactions of two types: interactions with the detector material and weak decays, where both can lead to secondary charged tracks passing the track selection criteria. These effects are studied with an available Monte Carlo sample (LHC20e3a_AOD243) produced by the ALICE collaboration containing 3.2 million Pb-Pb collision events anchored to LHC18q and LHC18r data sets. The collision events are simulated by the Heavy-Ion Jet Interaction Generator (HIJING) [134] and generated tracks are propagated through the detector simulation (interaction of tracks with detectors and detector materials) using GEANT3 [135]. The correction factor

(weight) due to detector reconstruction efficiency and secondary interactions is defined as

$$w_{\text{eff}}(p_{\text{T}}) = \frac{1-c}{\epsilon} \tag{3.6.2}$$

where c and ϵ are the fraction of contamination from secondaries and single particle tracking efficiency given by

$$c = \frac{N_{\text{sec}}(p_{\text{T}})}{N_{\text{tot}}(p_{\text{T}})}, \text{ and } \epsilon = \frac{N_{\text{rec}}(p_{\text{T}})}{N_{\text{gen}}(p_{\text{T}})}, \tag{3.6.3}$$

respectively. In the expression of c, N_{sec} and N_{tot} are the number of secondary charged particles from both weak decays and detector material interactions, and total charged particles (secondaries and primaries), respectively. N_{gen} and N_{rec} in the expression of ϵ correspond to the number of charged particles at the event generator level and after reconstruction, respectively. The efficiency and contamination correction are shown in Fig. 3.2 in several centrality classes: 0-5%, 10-20%, 30-40%, 40-50%, and separately for positively and negatively charged particles. It is noted that the reconstruction efficiency increases with increasing centrality and is higher for positively charged particles than for negatively charged particles within the same centrality class, while the contamination is uniform for different centrality classes and the sign of charge.

One should bear in mind that the method used to estimate the reconstruction efficiency has its own limitations. Firstly, the detector may exhibit varying efficiencies in reconstructing different species of particles. However, estimating the reconstruction efficiency for each particle species requires special care because the reconstructed p_{T} spectra generated by the Monte Carlo simulator may not align well with real data. Furthermore, the contamination only takes into account secondary particles from weak decays and material interactions, which may not encompass all potential sources. Generally, these two considerations have only minor effects on the final result of the CME analysis.

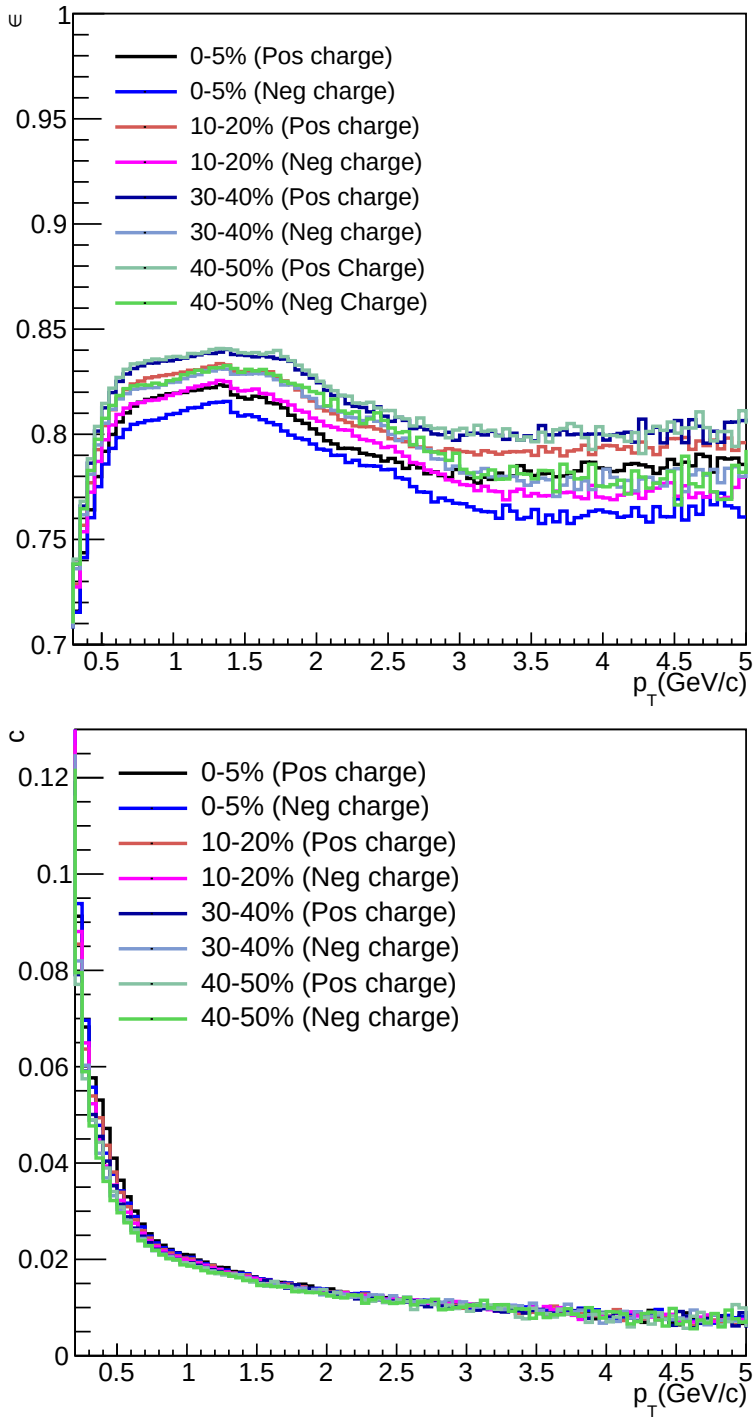

Figure 3.2: *Efficiency (left) and contamination (right), in several centrality bins, estimated from the Monte Carlo sample LHC20e3a_AOD243 anchored to the LHC18q and LHC18r data sets.*

3.7 ZDC calibration

For the ZDC detectors, described in Sec. 2.2.4, the standard procedure for calibration has been previously laid out in the ALICE studies involving ZDC detectors based on the study conducted in [126]. In this section, the standard procedure will be described first, followed by discussions on potential flaws in the standard procedure. The new calibration procedure will be introduced afterwards, and its performance will be compared with the standard procedure.

3.7.1 Standard ZDC calibration procedure

The standard ZDC calibration procedure is performed in two sequential steps: gain equalisation and re-centring, where the former one intends to compensate for the non-uniformity of the response of each tower to the same signal and the latter one corrects for detector misalignment.

Standard ZDC gain equalisation

The standard gain equalisation (based on [126]) assumes that each tower should have the same average response, equalling 1/4 of the average signal in the common tower (PMT c) of ZNC and ZNA, denoted as $\langle E_{\text{com}} \rangle$. The correction factor ξ under this assumption is defined as

$$\xi_j = \frac{\langle E_{\text{com}} \rangle / 4}{\langle E_j \rangle}, \tag{3.7.1}$$

where E_j is the deposited energy in the j-th tower, j runs from 1 to 4 representing each of the four towers in either ZNC or ZNA, and $\langle E_j \rangle$ denotes the average signal of the j$^{\text{th}}$ tower during the run period. The corrected energy of the j-th tower, E', is given by

$$E'_j = \xi_j \cdot E_j. \tag{3.7.2}$$

It is easy to see that with this gain equalisation procedure, the average deposited energy in each tower of either side of the neutron ZDCs is forced to be the same as 1/4 of $\langle E_{\text{com}} \rangle$. The results of the standard gain equalisation can be found in many analysis notes and documents, e.g. Sec. 3.4 in [136]. However, it is not a very realistic assumption, as the sum of towers 1 to 4 does not exactly equal the common tower before calibration, especially for ZNA, as shown in the correlation plot (Fig. 3.3) of both A and C sides for run 296547 in the LHC18q data set recorded by the ALICE detector in Pb-Pb collisions at $\sqrt{s_{NN}} = 5.02$ TeV as an example. The possible causes of this can come from the beam position not being exactly in the centre of the neutron ZDCs; differences in the efficiency of the light transmission in each tower; tolerances on the sizes of the towers. A similar correlation pattern is observed in all run numbers in the whole LHC18q and LHC18r data sets. The possible reason for such a difference could be due to small differences in light generation and collection in each tower. A much larger disagreement in ZNA compared to ZNC is speculated to originate from the mis-calibration in ZNA towers, where its tower 2 was malfunctioning (the photo-multiplier tube stopped working) in the 2015 data-taking period and was fixed later in the 2018 period. In addition, the pedestal (offset in the photo-multiplier signal and electronics) of each tower does not necessarily equal each other, so it is careless to simply assume that

$$\begin{aligned} &\langle E'_j \rangle = \langle E'_{j,\text{signal}} + E'_{j,\text{pedestal}} \rangle \stackrel{?}{=} \langle E_{\text{com}} \rangle / 4 \stackrel{?}{=} \langle \sum_j E_j \rangle / 4, \\ &\langle E'_{j,\text{signal}} \rangle \stackrel{?}{=} \langle E'_{k,\text{signal}} \rangle \text{ and } \langle E'_{j,\text{pedestal}} \rangle \stackrel{?}{=} \langle E'_{k,\text{pedestal}} \rangle. \end{aligned} \tag{3.7.3}$$

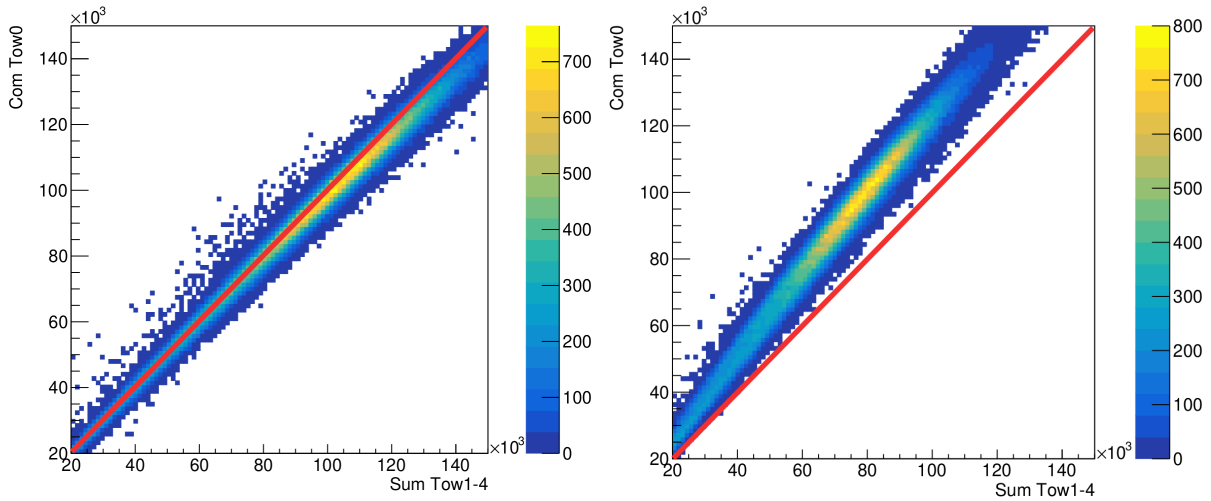

Figure 3.3: *Correlation of the sum energy of towers 1 to 4 and the energy of the common tower for ZNC (left) and ZNA (right), respectively. The red diagonal line is added to guide visually for the deviation from a perfect agreement between the sum energy of towers 1 to 4 and the common tower energy. The data were collected in Pb-Pb collisions at* $\sqrt{s_{NN}} = 5.02$ *TeV by the ALICE detector corresponding to run 296547 in the LHC18q data set.*

Standard re-centring procedure

The standard neutron ZDC Q-vector is defined as

$$Q^{\text{ZNA,ZNC}} = c\frac{\sum_{j=1}^{4} w_j \mathbf{r}_j e^{i\varphi_j}}{\sum_{j=1}^{4} w_j} \tag{3.7.4}$$

where $w_j = E_j^{\alpha}$ is a weight factor depending on the energy. The parameters c and α are determined through fitting to minimise the reconstructed coordinate and the true coordinate based on the model study in [126]. The parameter c is dependent on the neutron multiplicity (n_{neutron}) parameterised as

$$1.89358 - 0.71262/(n_{\text{neutron}} + 0.71789), \tag{3.7.5}$$

and the best-fit value of α is determined as 0.395. $\mathbf{r}_i$ and φ_i are the relative position vector and the azimuthal angle of each tower's centre with respect to the beam axis, respectively. Note that ZNC and ZNA face each other, so that the x-axes of their local coordinates point in the same direction. It is necessary to ensure that ZNC and ZNA have the same global coordinate by having their relative position vector defined as

$$\begin{aligned} &\mathbf{r}_1^{\text{ZNC}} = (-1,-1), \mathbf{r}_2^{\text{ZNC}} = (1,-1), \mathbf{r}_3^{\text{ZNC}} = (-1,1), \mathbf{r}_4^{\text{ZNC}} = (1,1), \text{ and} \\ &\mathbf{r}_1^{\text{ZNA}} = (1,-1), \mathbf{r}_2^{\text{ZNA}} = (-1,-1), \mathbf{r}_3^{\text{ZNA}} = (1,1), \mathbf{r}_4^{\text{ZNA}} = (-1,1). \end{aligned} \tag{3.7.6}$$

The azimuthal angle takes the values of $\varphi_j = \pi/4, 3\pi/4, 5\pi/4, 7\pi/4$. In Fig. 3.4, the distribution of the centre position of the shower in ZNC and ZNA based on the standard definition of the ZDC Q-vector is shown for the LHC18q data set as an example. It can be seen that the contour of the distribution has a squarish shape, which signals that the standard ZDC Q-vector has a potential bias for directions pointing to four corners in the 2018 data set.

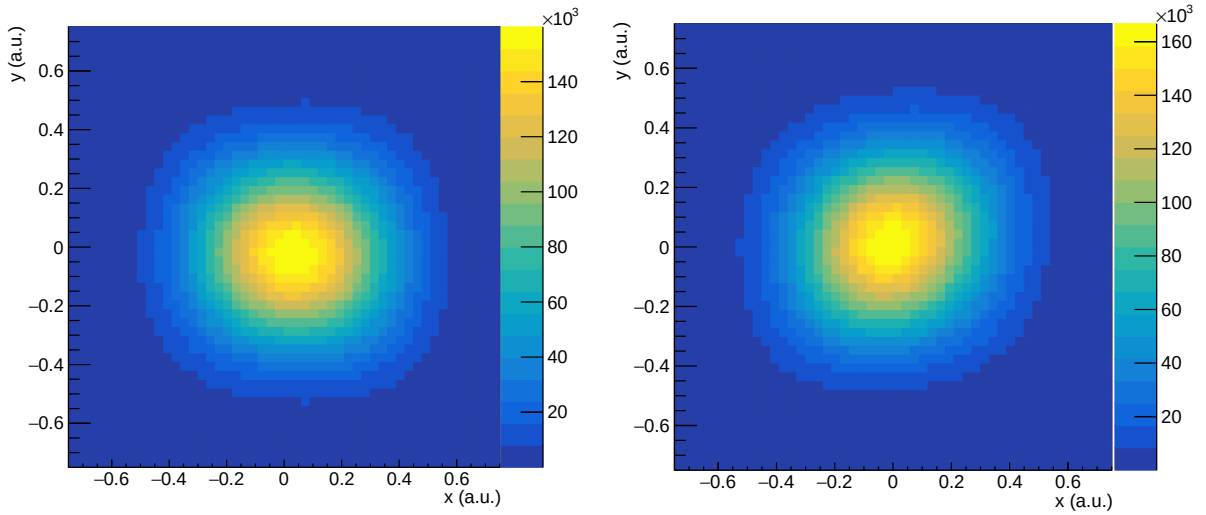

Figure 3.4: *Distribution of the centre position of the shower in ZNC (left) and ZNA (right) based on the standard ZDC Q-vector for the LHC18q data set.*

The re-centring procedure is performed by subtracting the average magnitude of the Q-vector, $\langle Q_x^{\mathrm{ZNk}} \rangle$ and $\langle Q_y^{\mathrm{ZNk}} \rangle$ ($k = A, C$), from different Q-vectors:

$$Q_j'^{\mathrm{ZNk}} = Q_j^{\mathrm{ZNk}} - \langle Q_j^{\mathrm{ZNk}} \rangle. \tag{3.7.7}$$

where $j = x, y$ represents the X and Y component. It is observed that all components of $\langle Q_x^{\mathrm{ZNk}} \rangle$ exhibit a strong dependence on centrality, run number, and all primary vertex coordinates (v_x, v_y, v_z). It was claimed in [136] that there exists "some degree of correlation between all of these", but only a weak correlation between centrality and v_y (slight colour change horizontally) and between v_y and v_z (tilted shape), and a very weak correlation between v_x and v_z (slightly tilted shape) can be observed in the LHC18q and LHC18r data sets, as shown in Fig. 3.5 and 3.6 as an example. The dependence of $\langle Q_j^{\mathrm{ZNk}} \rangle$ on all variables can be recorded in high-dimensional profile histograms. Ideally, the correction should be done simultaneously for all dependent variables, which essentially requires 5-dimensional event variable space. However, the limited amount of data at our disposal prohibits obtaining statistically meaningful averages if the data set is divided to 5-dimension. Instead, the chosen solution is to decompose the correction into three consecutive steps by reducing the dependence to 3 dimensions in each step:

1. re-centre as a function of centrality (1% intervals) and run number;
2. re-centre as a function of centrality (1% intervals) and v_x, v_y, v_z;
3. re-centre as a function of v_x, v_y, v_z and run number.

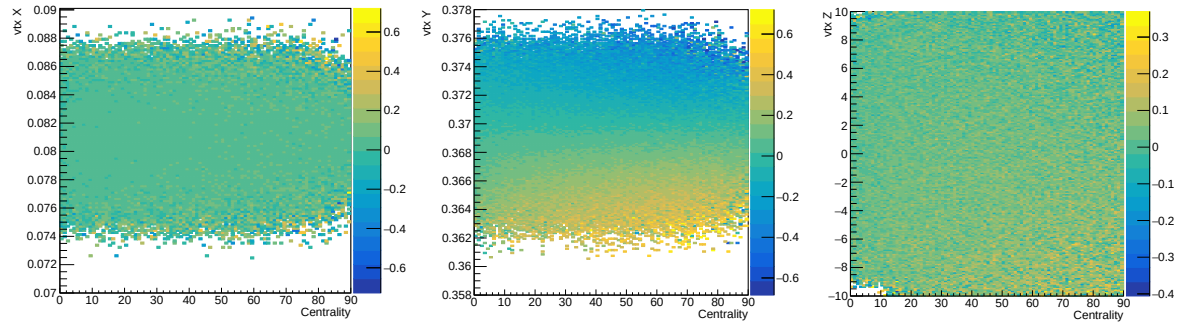

Figure 3.5: *Correlation between centrality and v_x (left), between centrality and v_y (middle), and between centrality and v_z (right) for run 296623 in the LHC18q data set. The colour indicates the value of $\langle Q_x^{ZNC} \rangle$.*

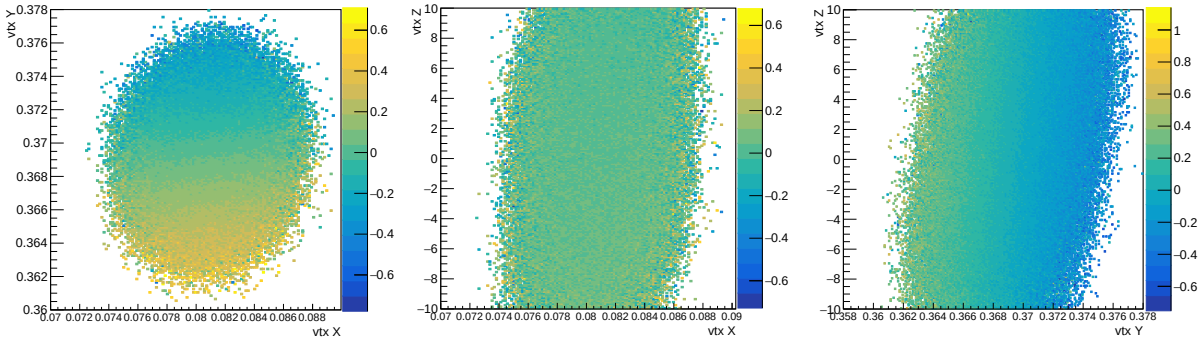

Figure 3.6: *Correlation between v_x and v_y (left), between v_x and v_z (middle), and between v_y and v_z (right) for run 296623 in the LHC18q data set. The color indicates the value of $\langle Q_x^{ZNC} \rangle$.*

In a more recent study using neutron ZDCs [81], it was suggested in their analysis note that the dependent variables of the neutron ZDC Q-vector can be extended to orbit time, which is one of the LHC timing signals to keep track of the time when each collision happens. The reason for this dependence is that the luminosity levelling was switched on in the 2018 run period to maintain constant luminosity during the detection of events. The luminosity levelling can be achieved by changing the offset or the crossing angle between the two colliding beams, and the beam cross-section (β^* levelling) [137]. Since the neutron ZDCs are positioned 116 m away from the collision point, a variation in the polar beam crossing angle of ± 15 μrad leads to a displacement of $\sim$ 2 mm at the ZN surface. It is therefore reasonable to introduce the dependence on time, which is indirectly connected to the changes in the beam condition, especially the crossing angle, due to luminosity levelling. Optimally, the crossing angle would provide a better calibration of ZDC, but this information was not stored in the ALICE 2018 data. In the currently ongoing and future high-luminosity LHC runs, the luminosity levelling is expected to be widely used. Thus, it is essential to store the information of the crossing angle per event to provide extra information on the calibration of ZDC. It should be noted that the standard re-centring procedure also gives rise to a more refined approach in [81]. In this approach, the re-centring is done iteratively by first re-centring with a 4-dimensional dependence on centrality, v_x, v_y, v_z per run in coarse binning. This is followed by five individual 1-dimensional re-centring as a function of centrality, v_x, v_y, v_z, and time in a finer binning, respectively.

It was demonstrated in previous studies that the standard re-center procedure flattens the dependence of Q_j^{ZNk} on event variables. The main drawback of this chosen procedure is that one

has to define the bin width of the profile histograms wisely. It is important to have a significant number of events in each bin of the 3-dimensional histogram to estimate a statistically significant $\langle Q_j^{\mathrm{ZNk}} \rangle$. By changing the bin width, the result of re-centring is also affected, and bias may be introduced.

The performance of calibrated neutron ZDCs was checked with other variables, such as the estimated spectator plane distribution, and the cross-terms of x- and y-components of the Q-vector. The 1st order event plane (spectator plane) can be estimated using either ZNC and ZNA as

$$\Psi_1^{\mathrm{ZNk}} = \mathrm{atan2}\left(\frac{Q_y^{\mathrm{ZNk}}}{Q_x^{\mathrm{ZNk}}}\right). \tag{3.7.8}$$

The effect of the re-centring on the 1st order event plane estimated in ZNA and ZNC detectors is shown in Fig. 3.7. The four peaks shape originates from the bias in four corner directions in the centre position construction.

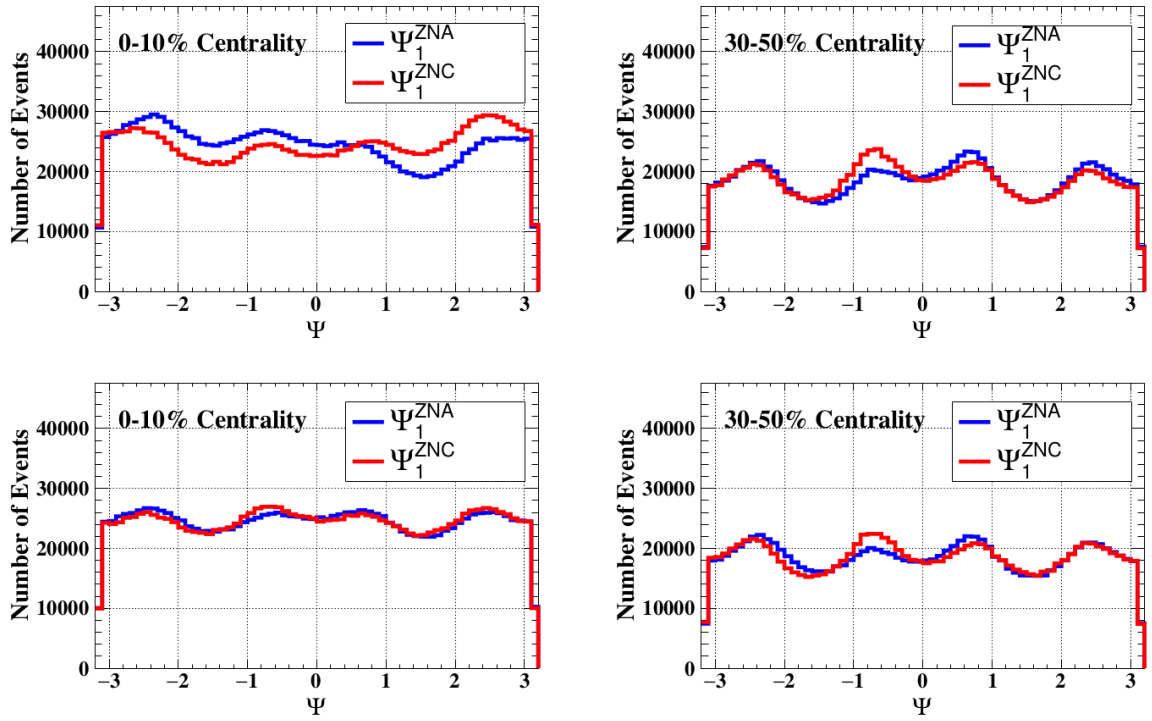

Figure 3.7: *Distribution of the 1st order event plane estimated from ZNA and ZNC (gain equalisation applied) before (upper plots) and after (lower plots) re-centring, selectively shown for centrality classes: 0-10% (left) and 30-50% (right) in the 2018 data set. Figure adopted from the analysis note of [127].*

With proper re-centring, the expected values of each x- and y-component of the Q-vector should be zero, $\langle Q_i^{\mathrm{ZNk}} \rangle = 0$. The cross-terms of the x- and y-components are expected to be zero for $\langle Q_x^{\mathrm{ZNC}} Q_y^{\mathrm{ZNA}} \rangle = \langle Q_y^{\mathrm{ZNC}} Q_x^{\mathrm{ZNA}} \rangle$ and negative for $\langle Q_y^{\mathrm{ZNC}} Q_y^{\mathrm{ZNA}} \rangle = \langle Q_x^{\mathrm{ZNC}} Q_x^{\mathrm{ZNA}} \rangle$. It is easy to see that the former ones are zero because the x- and y-components are orthogonal to each other. The latter ones are negative because the spectator neutrons are deflected oppositely between the A- and C-sides. This means that the $\Psi_{\mathrm{EP}}^{\mathrm{ZNC}}$ is different from $\Psi_{\mathrm{EP}}^{\mathrm{ZNA}}$ by π ideally, resulting in $\langle \cos(\Psi_{\mathrm{EP}}^{\mathrm{ZNC}} - \Psi_{\mathrm{EP}}^{\mathrm{ZNA}}) \rangle < 0$. Since the orthogonal direction should not be correlated ($\langle Q_x^{\mathrm{ZNC}} Q_y^{\mathrm{ZNA}} \rangle = \langle Q_y^{\mathrm{ZNC}} Q_x^{\mathrm{ZNA}} \rangle = 0$), the expansion of the cosine means

that $\langle Q_x^{\mathrm{ZNC}} Q_x^{\mathrm{ZNA}} \rangle = \langle Q_y^{\mathrm{ZNC}} Q_y^{\mathrm{ZNA}} \rangle < 0$. As demonstrated in Fig. 3.8, the cross correlation $\langle Q_x^{\mathrm{ZNC}} Q_y^{\mathrm{ZNA}} \rangle$ and $\langle Q_y^{\mathrm{ZNC}} Q_x^{\mathrm{ZNA}} \rangle$ remain zero over all centrality classes. However, the cross-terms $\langle Q_y^{\mathrm{ZNC}} Q_y^{\mathrm{ZNA}} \rangle$ and $\langle Q_x^{\mathrm{ZNC}} Q_x^{\mathrm{ZNA}} \rangle$ change from negative to positive at around 45% centrality in the LHC18q data set and at 65% centrality in the LHC18r data set, respectively, signalling spurious azimuthal correlations due to detector effects. Such crossing points are also observed in the LHC15o data set (see, e.g. [136]), and originally appear in the LHC11h data set, but they happen at more peripheral collisions (e.g. beyond 60% centrality classes in LHC15o). This problem, however, was mostly absent in the LHC10h data set. The reason can be attributed to that, starting from 2011, the LHC uses a finite beam angle crossing at the interaction point to constrain the spread of the primary vertex positions in the z direction, v_z, by forming a diamond-shaped beam crossing region during interaction, and significantly squeezed the beam cross-section. Neither study can correct for the corresponding detector bias, as the information of the crossing angle is not recorded in the data set and there does not exist a Monte Carlo simulator that can realistically simulate the spectator deflection, the beam conditions, and the response of neutron ZNCs to deconvolute these effects.

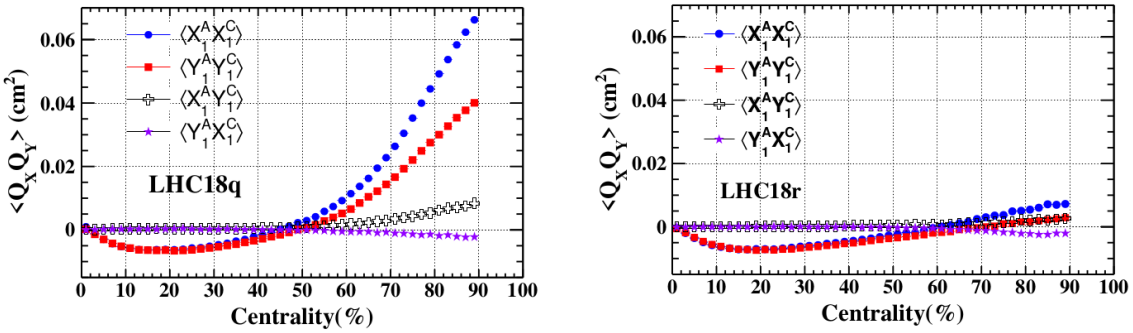

Figure 3.8: *Centrality dependence of the cross-terms of x- and y-components of the Q-vectors constructed using ZNA and ZNC in LHC18q (left) and LHC18r (right) data sets after the standard re-centring procedure. Figure adopted from the analysis note of [127].*

3.7.2 New ZDC calibration procedure

As discussed in the previous section, the standard ZDC calibration procedure possesses a few flaws in its assumptions and has some areas to be improved. In this section, the new ZDC calibration procedure is introduced.

Gain Equalisation using Least Square Fit

The new gain equalisation procedure allows the average deposited energy at each tower of ZNC and ZNA to be flexible. In addition, the sum of the energy of towers 1-4 does not need to be strictly equal to that of the common tower. A least square fit is performed for each run number and each side of the neutron ZNCs, respectively, to find the optimum gain factors, a_i^{ZNk}, and the offset b^{ZNk} that fit the following relation:

$$E_{\mathrm{com}}^{\mathrm{ZNk}} = \left(\sum_{i=1}^{4} a_i^{\mathrm{ZNk}} E_i^{\mathrm{ZNk}} \right) + b^{\mathrm{ZNk}}. \tag{3.7.9}$$

The pedestal is a consequence of the leakage current in the photo-multiplier and potential offset from the electronics. Ideally, all the towers should have their own pedestal terms, but this re-

quires an additional four parameters in the fit, which is impossible given only five input values. It is only possible to determine them separately by measuring directly on the photo-multiplier without the beam. In Fig. 3.9, the correlation between the sum of the energy of towers 1-4 and the energy of the common tower after the standard gain equalisation procedure and the least square fit method are plotted, respectively. It is clear that in this particular run number (296547), the band is much narrower with the new method, indicating a better performance of the gain equalisation. Fig. 3.10 summaries the magnitude of the correlation for ZNC before and after (two methods of) gain equalisation in part of run numbers in LHC18q data set. For brevity, the same plots for ZNA in LHC18q data set and both ZNs in LHC18r data set are shown in Appendix 8.1. In an ideal detector, one would expect a perfect magnitude of correlation of unity. The new method of gain equalisation always leads to a better correlated result, while the old method, most likely due to invalid assumptions, can possibly produce a worse performance even compared to the correlation before gain equalisation in ZNC for LHC18q data set. In both LHC18q and LHC18r data sets, ZNA performs worse than ZNC. The gain factors obtained according to the least square fit generally lie between 0.85 and 1.02 for ZNC in all run numbers, while towers 2 and 3 of ZNA require much higher gains (around 1.3-1.42) than the other two towers (around 1.05-1.2). In addition, it was noted that between run numbers 297595-297441 in LHC18r data set, the gain factor for tower 2 of ZNA required a value of around 1.7, and its value dropped to 1.4 right after. It is not clear what exactly happened that caused these peculiar behaviours in ZNA. A thorough check of e.g. the constructed ZNA event plane distribution and Q-vector cross terms was performed, and nothing peculiar in those quantities was observed, particularly in run numbers 297595-297441. In conclusion, the new method of gain equalisation performs much better than the standard method, and no run number is dropped just based on strangely high gain factors required in two of the towers in ZNA.

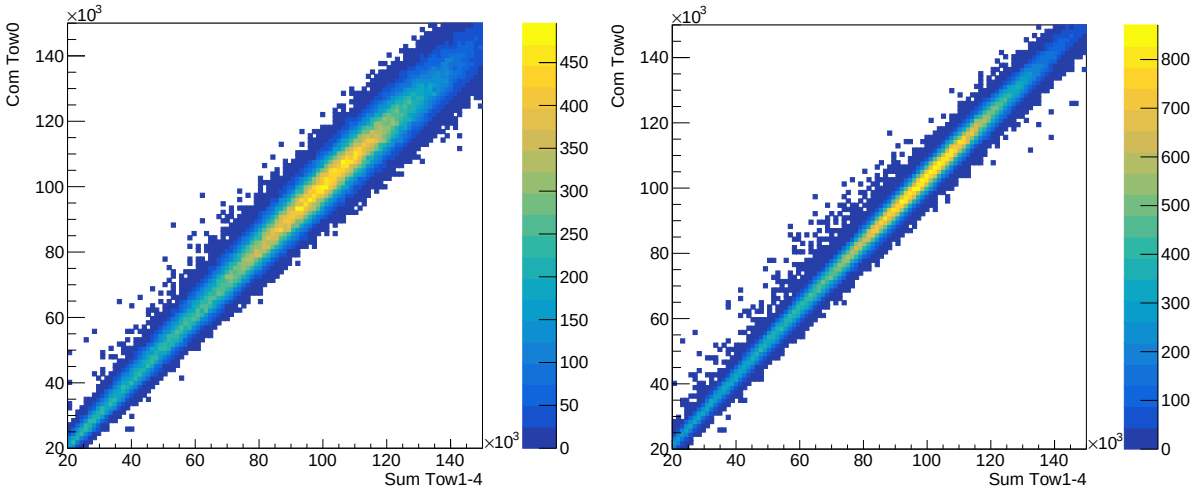

Figure 3.9: *Correlation of the sum energy of tower 1 to 4 and the energy of the common tower for ZNC for run 296547 in LHC18q data set. The left and the right panel show the correlation after the standard gain equalisation procedure and the gain equalisation using least square fit, respectively.*

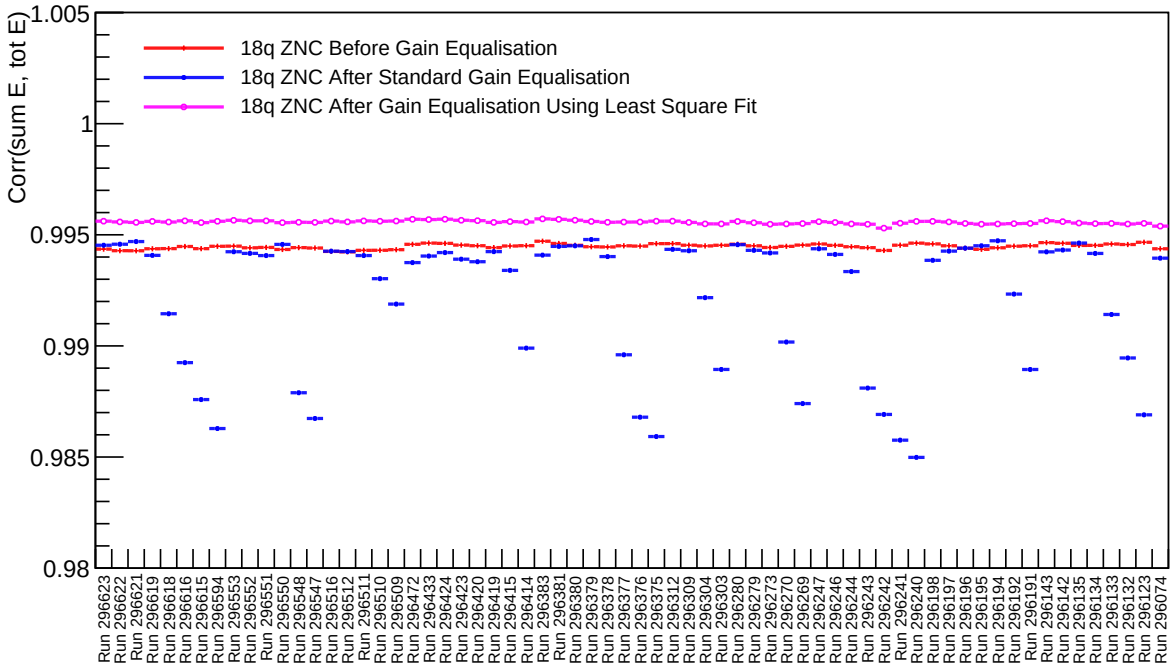

Figure 3.10: *Summary of the magnitude of the correlation between the sum energy of ZNC tower 1 to 4 and the energy of the common ZNC tower before and after (two methods of) gain equalisation in part of the run numbers (too long to show the full data set) in LHC18q data set.*

Reconstructing Centre Position with Logarithmic Weighting

The centre shower position reconstructed from the standard neutron ZDC Q-vector yields a bias in directions of four corners. This lies within the construction of the Q-vector which basically takes the ratio of deposited energies in towers to obtain the relative shower position. The ratio can be extreme when some towers have very low deposited energies. In order to procure a stronger influence of low energy deposit towers, the logarithmic weight is adopted:

$$w_i = \max\left\{\{0; W_0 + \ln\left(\frac{E_i}{E}\right)\right\}, \tag{3.7.10}$$

where W_0 is a free dimensionless parameter depending on the size the towers as well as the energy of incident particles, with its optimum value determined to be 4 for best position reconstruction in [138]. It is easy to see that only towers with an energy deposition higher than Ee^{-W_0} are taking into account. The higher the value of W_0 is, the less favourable the highest energy towers become, which eventually leads to an equal weight to the towers entering the sum. The actual best value of W_0 for the neutron ZDCs is not known and it is hard to obtain it without the existence of a realistic Monte Carlo simulation of the neutron ZDCs, but some variations around 4 are tested and no significant difference in the distribution of the shower centre position is noticed. Thus, the optimum value provided in [138] is adopted in this study. As shown in Fig. 3.11, the contour of the distribution of the shower centre position is more round, agreeing better with the expected shape of randomly Gaussian distributed centre positions around the centre of the detector.

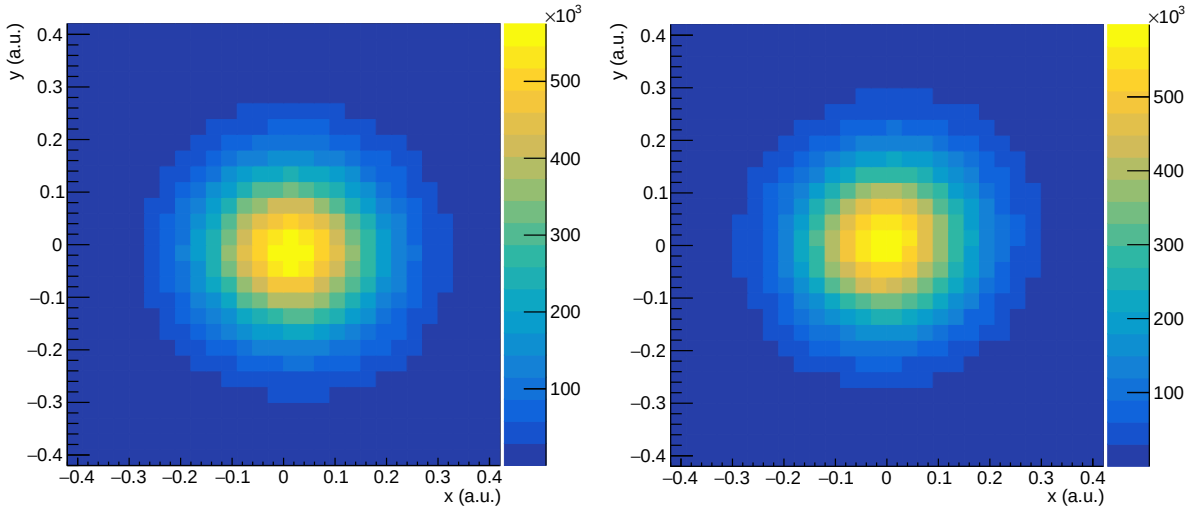

Figure 3.11: *Distribution of the centre position of the shower in ZNC (left) and ZNA (right) reconstructed using logarithmically weighted ZDC Q-vector for LHC18q data set.*

Re-centring using Least Square Fit

In order to preclude the use of high-dimensional histograms for re-centring, which has the issue of introducing biases both due to arbitrary bin sizes and many steps of re-centring required, a least square fit of all dependent variables: centrality, v_x, v_y, v_z, and orbital time is performed for each run number. This also has the advantage of saving CPU time during analysis as the re-centring can be done in one step. In addition, using the input re-centring file that stores all the average Q-vector values in multiple high-dimensional ROOT histograms for each run

number can cause buffer overflow on the ALICE computing grid, as ROOT files are heavily compressed objects when written to disk, but their size in RAM might be very large, especially for high-dimensional histograms.

The determination of the functional form that best fits the x- and y-component of the average Q-vector is done by plotting its dependence on all variables in a one-dimensional histogram, respectively. It is possible to separate each variable without introducing any mixed terms as the correlations between them are very weak and trivial as shown in Fig. 3.5 and 3.6 previously. In general, the dependence on all variables except centrality is linear. The dependence on centrality has been tested with polynomials up to a power of 5. It was found that a 3rd power polynomial is enough to characterise the feature without any noticeable difference in comparison to higher-order polynomials after re-centring. Therefore, the best form of the least square fit is determined as:

$$\langle Q_j^{\mathrm{ZNk}} \rangle = \sum_{i=1}^{3} (a_i)_j^{\mathrm{ZNk}} \cdot \mathrm{cent}^i + (b_1)_j^{\mathrm{ZNk}} \cdot v_x + (b_2)_j^{\mathrm{ZNk}} \cdot v_y + (b_3)_j^{\mathrm{ZNk}} \cdot v_z + c_j^{\mathrm{ZNk}} \cdot \mathrm{OrbitNum} + d_j^{\mathrm{ZNk}}, \tag{3.7.11}$$

where the parameters a_i, b_i ($i = 1, 2, 3$), c, and d are corresponding best fit parameters given by the fit. For each run number, the re-centring is performed as

$$\langle Q_j^{\mathrm{ZNk}} \rangle' = Q_j^{\mathrm{ZNk}} - \langle Q_j^{\mathrm{ZNk}} \rangle \tag{3.7.12}$$

It is worth mentioning that the LHC15o data set has also been studied for ZDC calibration, where one tower (#2) of the ZNA was malfunctioning. In this case, the energy from tower 2 of the ZNA can be obtained through

$$E_2 = E_{\mathrm{com}} - E_1 - E_3 - E_4. \tag{3.7.13}$$

Due to this issue, it is not possible to perform gain equalisation on ZNA for the LHC15o data set. As mentioned in the ZDC gain equalisation section, the gain on each tower is not necessarily close to each other and close to unity. Therefore, using Eq. 3.7.13 does not provide a good approximation, resulting in a highly elliptical distribution of the shower centre position. Consequently, the LHC15o data set is considered unsuitable for this analysis, which necessitates a good measurement of the spectator plane.

3.7.3 ZNA-ZNC cross-terms

The cross-terms, $\langle Q_x^{\mathrm{ZNC}} Q_x^{\mathrm{ZNA}} \rangle$, $\langle Q_y^{\mathrm{ZNC}} Q_y^{\mathrm{ZNA}} \rangle$, $\langle Q_y^{\mathrm{ZNC}} Q_x^{\mathrm{ZNA}} \rangle$, and $\langle Q_x^{\mathrm{ZNC}} Q_y^{\mathrm{ZNA}} \rangle$, after the new re-centring procedure are shown in Fig. 3.12, which are in agreement with the results of the standard calibration procedure shown previously in Fig. 3.8. It is clear that the improved procedure of calibrating neutron ZDCs does not solve the unexpected ZNA-ZNC correlation. This can be possibly reduced with the information of the crossing angle, which is not provided in the AOD. In addition, the non-linearity for small signals in the ZDC (e.g. due to incorrect pedestal) could also contribute to the unexpected correlations. This constrains the maximum usable centrality ranges of ZNA and ZNC being 0-50% and 0-60%, respectively, determined by requiring $\langle Q_x^{\mathrm{ZNC}} Q_x^{\mathrm{ZNA}} \rangle$ and $\langle Q_y^{\mathrm{ZNC}} Q_y^{\mathrm{ZNA}} \rangle$ being anti-correlated (negative).

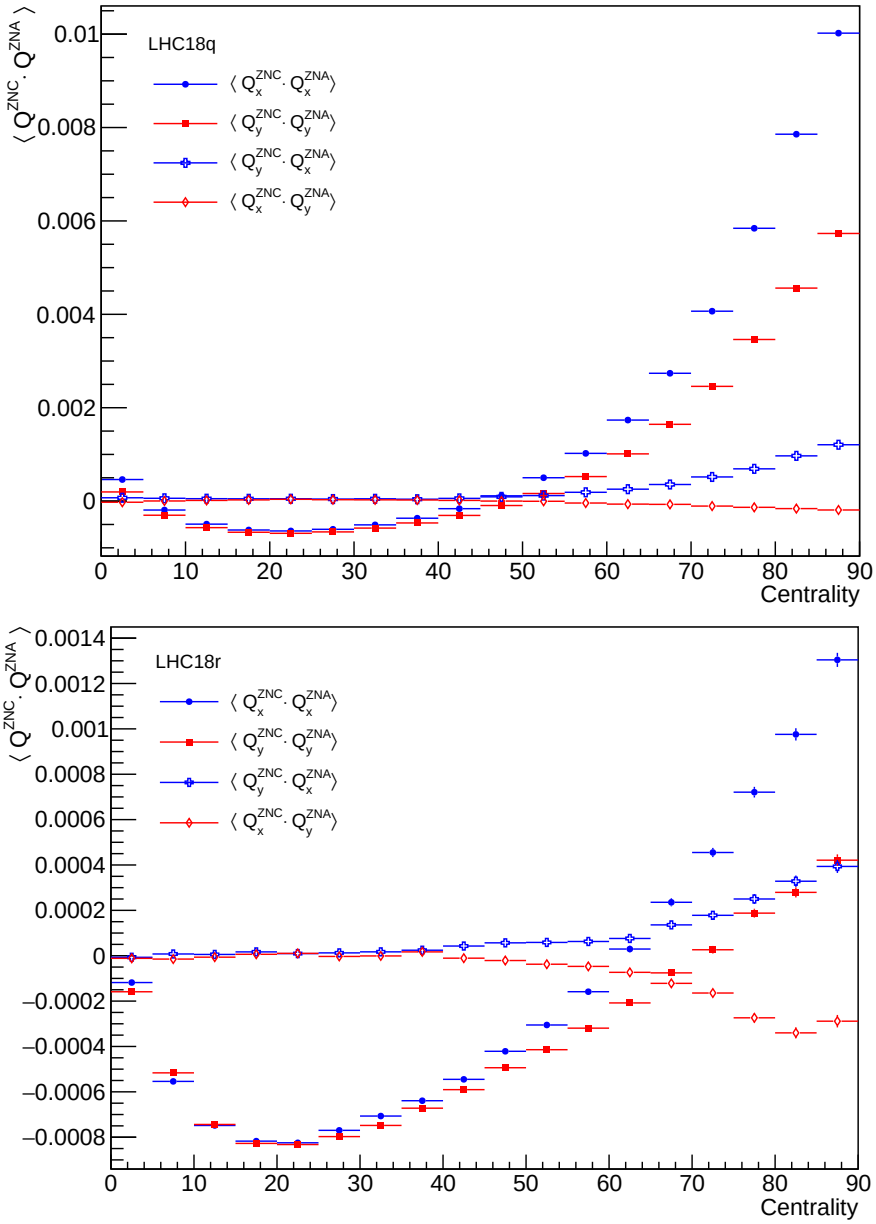

Figure 3.12: *Centrality dependence of the cross-terms of x- and y-components of the Q-vectors constructed using ZNA and ZNC in the LHC18q (left) and LHC18r (right) data sets after re-centring using the least square fit.*

3.7.4 Construction of the 1st Order Event Plane

The 1st order event plane can be constructed using either side of the neutron ZDCs through Eq. (3.7.8). This makes the estimation of the event plane resolution possible, which requires at least two sub-event planes (ZNA and ZNC). The purpose of estimating such a quantity is to take into account the difference between the true participant plane and the corresponding event plane (1st order for ZDC). In the case of neutron ZDCs, such an estimation turns out to be quite tricky, as the positive correlation between ZNA and ZNC at large centrality indicates that the two sub-events are not "equal". To mitigate the problem, a third detector has to be used as described in Eq. (16) of [130]. The 1st order event plane resolution is estimated using the two and three sub-event method for the LHC18 data set in the analysis note of [81], which differs for the LHC18q and LHC18r data set over the entire centrality region. However, the spectator-plane-participant-plane method does not require any estimation of the event plane resolution as such terms cancel out exactly.

Therefore, a better way of estimating the 1st order event plane is realised by combining ZNC and ZNA in the following form:

$$\Psi_1^{\text{ZNC-ZNA}} = \text{atan}\left(\frac{Q_y^{\text{ZNC}} - Q_y^{\text{ZNA}}}{Q_x^{\text{ZNC}} - Q_x^{\text{ZNA}}}\right). \tag{3.7.14}$$

As illustrated in Fig. 3.13, instead of using the azimuthal angle between the x-axis of the neutron ZDCs and the line from the centre of the detector to each of the shower centres in ZNC and ZNA, combining ZNC and ZNA can reduce the fluctuation. In principle, one does not need to re-centre the Q-vector when combining the A- and C-sides, because the shower centre positions will shift in the same direction event by event, and the angle formed by them is not changed. But the test of the final performance shows that re-centring is still necessary to be performed, possibly due to the very same positive ZNA-ZNC correlation, signalling that the shower centre positions do not move together in the expected direction.

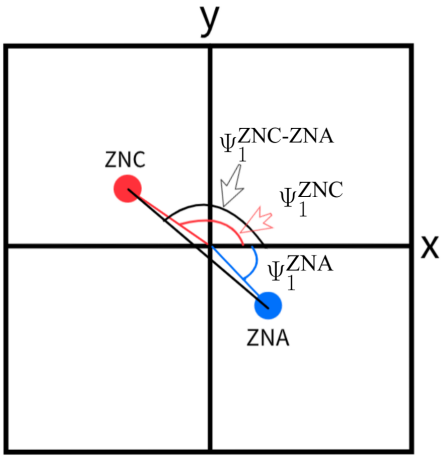

Figure 3.13: *Illustrative diagram of* Ψ_1^{ZNC}, Ψ_1^{ZNA}, *and* $\Psi_1^{ZNC\text{-}ZNA}$.

The 1st order event plane should align approximately with the 2nd order event plane reconstructed using the TPC or V0 detector. It can be clearly seen in Fig. 3.14 that the correlation between $\Psi_1^{\text{ZNC-ZNA}}$ and Ψ_2^{V0C} is much stronger than that between Ψ_1^{ZNC} and Ψ_2^{V0C} in the centrality class 10-50% for the LHC18q data set. The choice of the centrality range shown here will be

explained later. For LHC18r data set, as shown in Fig. 3.15, the same correlation between Ψ_1^{ZNC} and Ψ_2^{V0C} in the same centrality range as LHC18q becomes essentially two vertical lines at -1 to 0 and 2.5-3.5 (the two lines at the edges are considered as one due to periodicity), while combining ZNC and ZNA only leads to a limited improvement. More correlation plots of $\Psi_1^{\mathrm{ZNC\text{-}ZNA}}$ vs. Ψ_2^{V0C} for different centrality classes: $0-10\%, 10-20\%, ..., 80-90\%$ and the correlation plot of Ψ_1^{ZNC} vs. Ψ_1^{ZNA} for the centrality class $10-50\%$ are shown in Appendix 8.2. The different correlation behaviours between LHC18q and LHC18r are hinted at in the distribution of $\Psi_1^{\mathrm{ZNC\text{-}ZNA}}$, as shown in Fig. 3.16, where the distributions of Ψ_1^{ZNC} and Ψ_1^{ZNA} are also shown to illustrate that combining ZNA and ZNC makes the distribution less fluctuating. For the LHC18q data set, the variation of $\Psi_1^{\mathrm{ZNC\text{-}ZNA}}$ after the new procedures of calibration is within 5%, which is much better than the standard method of calibration, as shown in Fig. 3.7. A much wider variation of around 15% (still better than the standard method) is observed in the distribution of $\Psi_1^{\mathrm{ZNC\text{-}ZNA}}$ for the LHC18r dataset with two strongly preferred angles at around 0 and π, which coincides with the bright spots in the corresponding correlation plot. It is concluded that neutron ZNCs perform better in the LHC18q data set, but it is not clear what happens during the LHC18r data-taking period that causes strong preferences in certain angles.

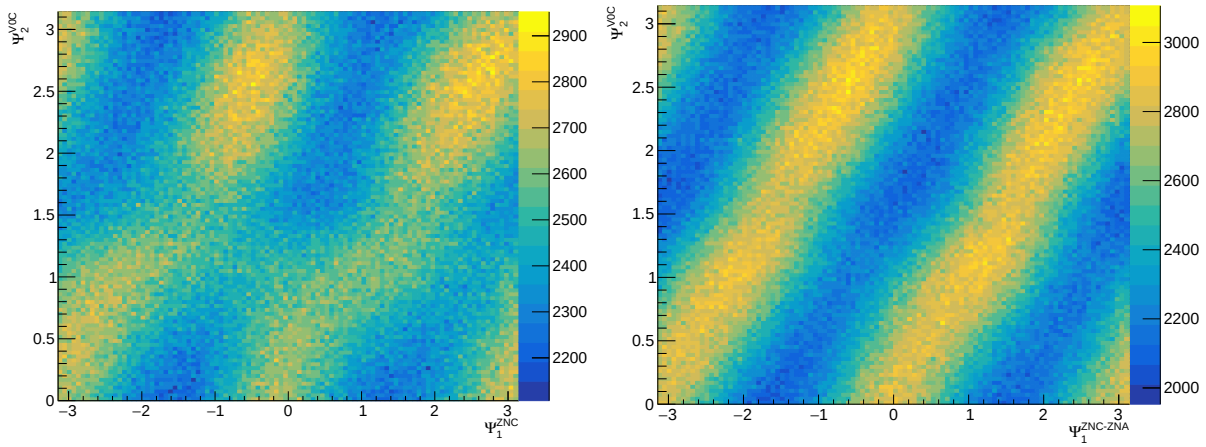

Figure 3.14: *Correlation between Ψ_1^{ZNC} and Ψ_2^{V0C} (left), and between $\Psi_1^{ZNC\text{-}ZNA}$ and Ψ_2^{V0C} (right) in the centrality class 10-50% for LHC18q data set.*

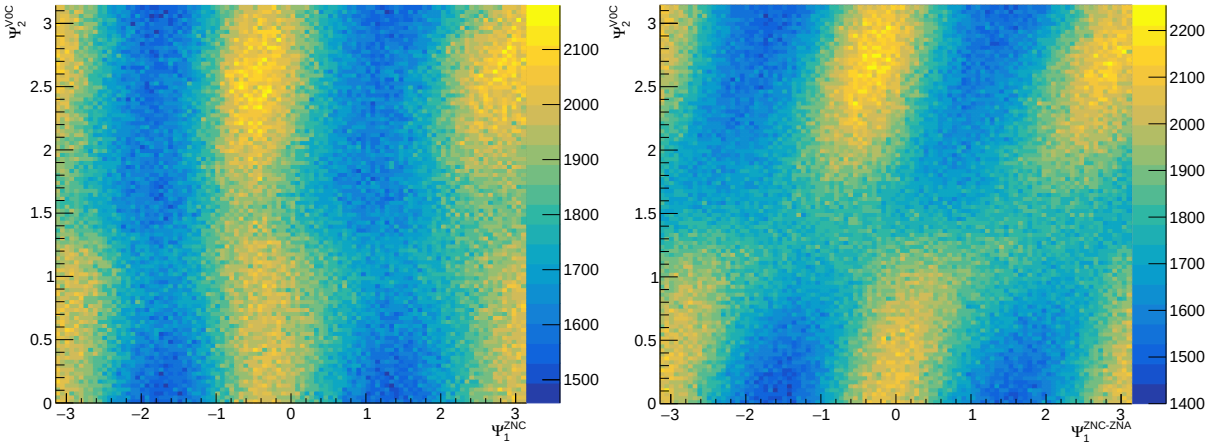

Figure 3.15: *Correlation between Ψ_1^{ZNC} and Ψ_2^{V0C} (left), and between $\Psi_1^{ZNC\text{-}ZNA}$ and Ψ_2^{V0C} (right) in the centrality class 10-50% for LHC18r data set.*

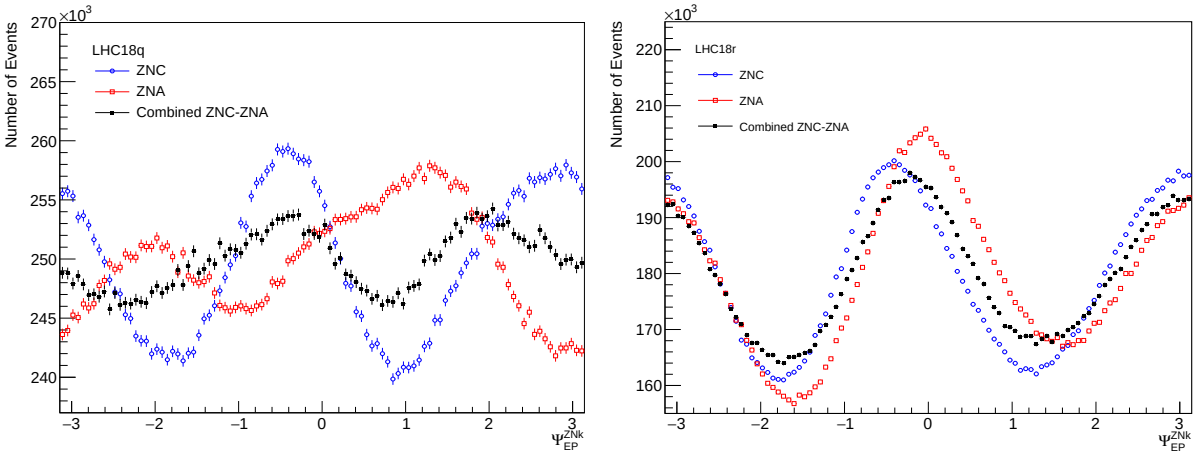

Figure 3.16: *Distribution of Ψ_1^{ZNC}, Ψ_1^{ZNA} and $\Psi_1^{ZNC\text{-}ZNA}$ after new gain equalisation and re-centring procedure in the centrality class 10-50% for LHC18q (left) and LHC18r (right) data sets, respectively.*

Despite the cross-terms, $\langle Q_y^{\mathrm{ZNC}} Q_x^{\mathrm{ZNA}} \rangle$ and $\langle Q_x^{\mathrm{ZNC}} Q_y^{\mathrm{ZNA}} \rangle$, suggesting that the usable centrality range is 0-50% and 0-60% for LHC18q and LHC18r, respectively, the range of centrality that will be used in the data analysis of this dissertation involving neutron ZNCs is chosen to be 10-50% for both LHC18q and LHC18r data sets. This is because the magnitude of the correlation between $\Psi_1^{\mathrm{ZNC\text{-}ZNA}}$ and Ψ_2^{V0C} drops quickly in centrality lower than 10% and above 50%, as shown in Fig. 3.17. At centrality below 10%, where the most central collisions happen, the spectators are much fewer, leading to a more difficult situation in determining the spectator plane. Beyond a centrality of 50%, the residual detector effects due to positive ZNA-ZNC correlation become sizeable.

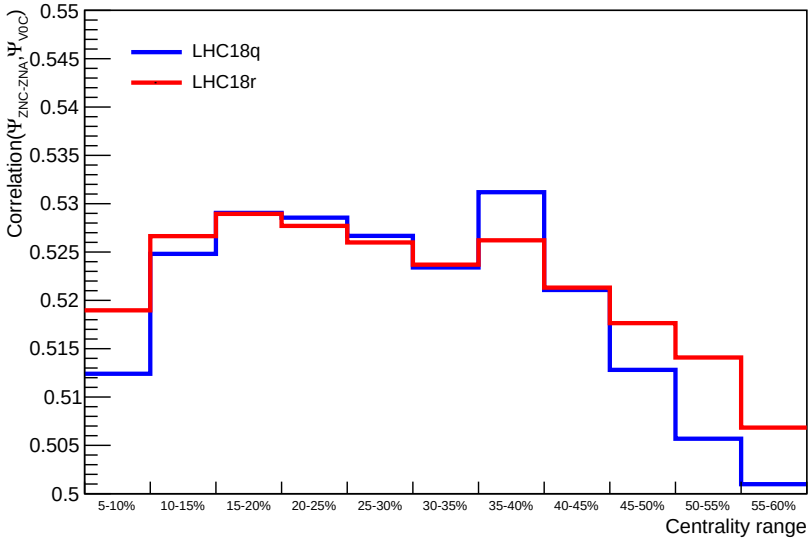

Figure 3.17: *The magnitude of the correlation between $\Psi_1^{ZNC\text{-}ZNA}$ and Ψ_2^{V0C} in each centrality interval of 5% from 5 to 60% for LHC18q (blue) and LHC18r (red) data sets.*

3.8 V0 calibration

The V0 system, described in Sec. 2.2.3, consists of 32 towers on each side and is calibrated in a similar way as the standard calibration procedure used for ZDC calibration. Firstly, all cells have to go through gain equalisation under the assumption that cells from the same ring generate an equal average signal. This assumption has a similar flaw as the assumption made for ZDC towers, which is that cells in the same ring may not necessarily have the same average output signal. However, since the V0 system does not have a common tower (like in the ZDC) that measures the total energy in each ring, it is not possible to use the same ZDC gain equalisation with the least squares fit method. The V0 gain equalisation is performed separately for each run number in both LHC18q and LHC18r data sets. The correction factor for each cell, ξ_j, is given as

$$\xi_j = \frac{\langle E_{i^{\text{th}}\text{ ring}}\rangle/8}{\langle E_j\rangle}, \tag{3.8.1}$$

where $\langle E_{i^{\text{th}}\text{ ring}}\rangle$ is the average signal across the i^{th} ring of each V0 and $\langle E_j\rangle$ is the average signal deposited in the j^{th} cell in the corresponding ring. In Fig. 3.18, the distribution of the average deposited energy in each V0 cell in run number 296547, before and after gain equalization, is shown as an example.

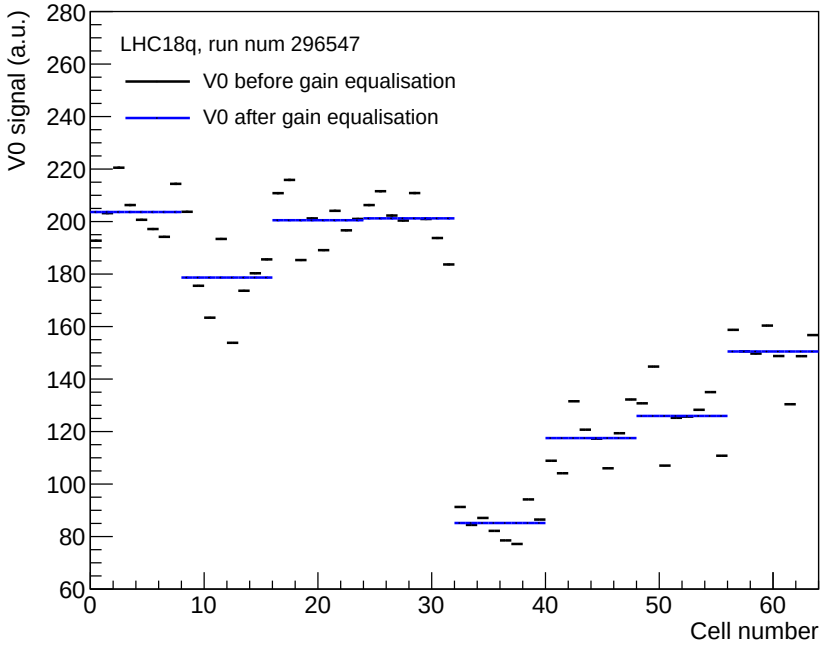

Figure 3.18: *The distribution of the average signal from the V0 cells (1-32 for V0C and 33-64 for V0A) in run number 296547, before (black) and after (blue) gain equalisation.*

The second step of V0 calibration is the re-centring of the Q-vector of the V0 system, defined as

$$Q_n^{\text{V0C,V0A}} = \frac{\sum_{j=1}^{32} \xi_j E_j e^{in\varphi_j}}{\sum_{j=1}^{32} \xi_j E_j}, \tag{3.8.2}$$

where E_j is the deposited energy measured in each V0 cell, n is the order of the Q-vector, and

φ_j is the azimuthal angle of the centre of the j^{th} cell, given by

$$\varphi_j = \frac{\pi}{4}\left(\frac{1}{2} + j\%8\right), \tag{3.8.3}$$

where % is the modulus operator that yields the remainder after integer division. Similar to the re-centring procedure of the neutron ZDCs, the re-centring procedure for the V0 system is performed for each run number by subtracting the average magnitude of the X and Y components of the Q-vector, $\langle Q^{\text{V0k}}_{n,x}\rangle$ and $\langle Q^{\text{V0k}}_{n,y}\rangle$, where k = A,C, from the corresponding Q-vector:

$$Q'^{\text{V0k}}_{n,j} = Q^{\text{V0k}}_{n,j} - \langle Q^{\text{V0k}}_{n,j}\rangle. \tag{3.8.4}$$

Similar to the re-centring of the neutron ZDCs, $\langle Q^{\text{V0k}}_{n,j}\rangle$ can be obtained by either filling the event-by-event value of $Q^{\text{V0k}}_{n,j}$ into histograms with dimensions determined by the number of dependent variables. The same least square fit method as adopted in the ZDC re-centring has been explored, with the best form of the least square fit determined as

$$\langle Q^{\text{V0k}}_{n,j}\rangle = \sum_{i=1}^{3}(a_i)^{\text{V0k}}_j \cdot \text{cent}^i + (b_1)^{\text{V0k}}_j \cdot v_x + (b_2)^{\text{V0k}}_j \cdot v_y + (b_3)^{\text{V0k}}_j \cdot v_z + c^{\text{V0k}}_j, \tag{3.8.5}$$

but no significant improvement is noticed. Therefore, the distribution of the X and Y components of the Q-vector depends strongly on centrality but weakly on primary vertex positions in each run number, as the second-order Q-vector shown in Figs. 3.19 and 3.20. Unlike the neutron ZDCs, the V0 system does not depend strongly on time, so the orbit number is not considered. The re-centring procedure with saved $\langle Qn, j^{\text{V0k}}\rangle$ in histograms has been checked using 1D histograms with dependence on centrality only and with dependence on centrality and primary vertex positions, and a negligible difference is found between them. For the least square fit method, the best form of the least square fit is determined based on the shape of $\langle Qn, j^{\text{V0k}}\rangle$ in Figs. 3.19 and 3.20 as:

$$\langle Q^{\text{V0k}}_{n,j}\rangle = \sum_{i=1}^{3}(a_i)^{\text{V0k}}_j \cdot \text{cent}^i + (b_1)^{\text{V0k}}_j \cdot v_x + (b_2)^{\text{V0k}}_j \cdot v_y + (b_3)^{\text{V0k}}_j \cdot v_z + c^{\text{V0k}}_j, \tag{3.8.6}$$

where the parameters a_i, b_i $(i = 1, 2, 3)$, and c are the corresponding best fit parameters.

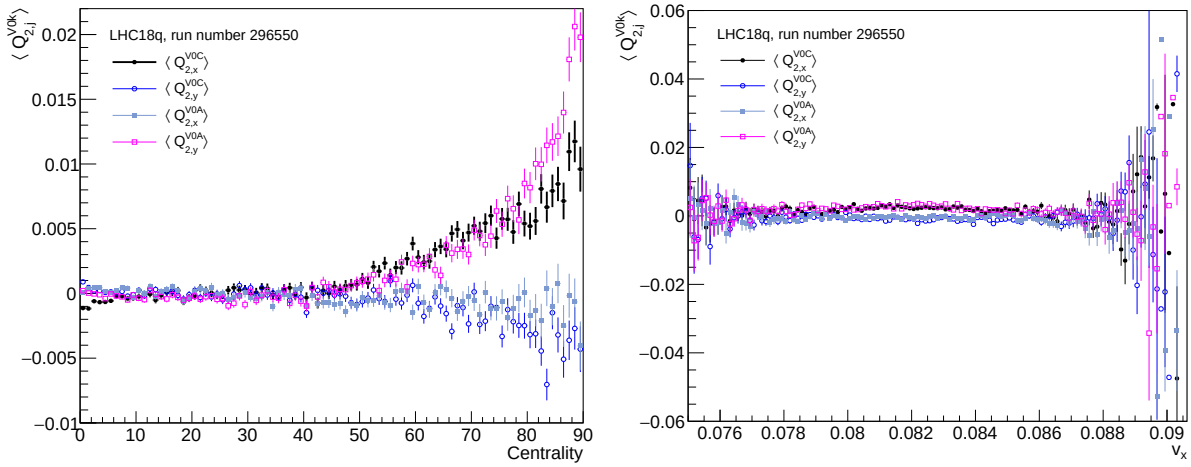

Figure 3.19: *The dependence of $\langle Q^{V0k}_{2,j}\rangle$ on centrality (left) and v_x (right) for run number 296547 in LHC18q data set.*

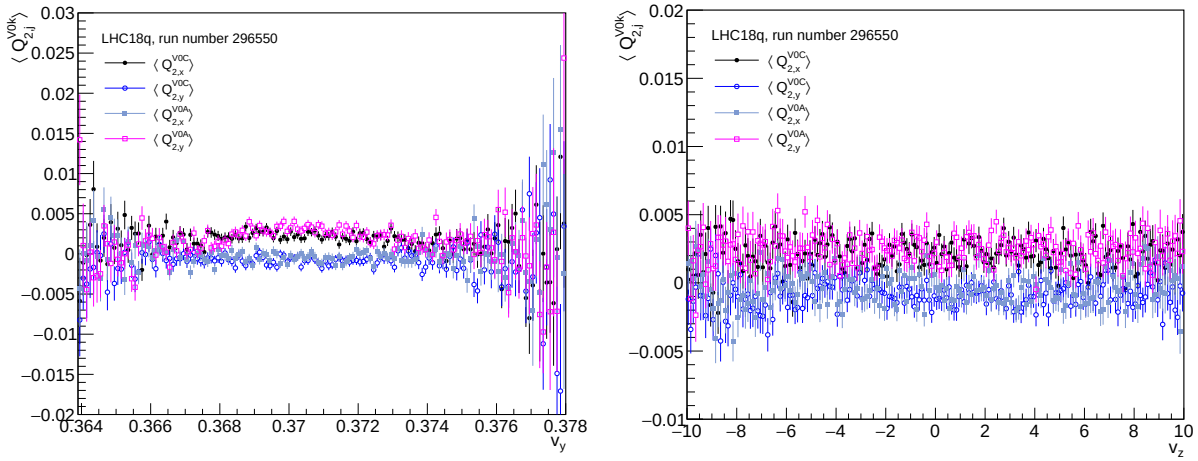

Figure 3.20: *The dependence of $\langle Q_{2,j}^{V0k} \rangle$ on v_y (left) and v_z (right) for run number 296547 in the LHC18q data set.*

The V0 system is used to reconstruct the 2^{nd} order event plane (an approximation for the participant plane) in this dissertation. The reason for being 2^{nd} order is that the V0 system can only determine the inclination of the event plane. More specifically, it cannot distinguish the difference between an angle of a and $a \pm \pi$. The 2^{nd} order event plane is given by

$$\Psi_{2^{\text{nd}}\,\text{EP}}^{\text{V0k}} = \frac{1}{2}\text{atan2}\left(\frac{Q_y^{\text{V0k}}}{Q_x^{\text{V0k}}}\right). \tag{3.8.7}$$

In Fig. 3.21, the distribution of $\Psi_{2^{\text{nd}}\,\text{EP}}^{\text{V0C}}$ before and after re-centring with a 1D histogram (centrality dependence) and with the least square fit method is compared. It is clear that the least square fit method does not improve the performance of the re-centring, and adding the dependence on the primary vertex positions does not make any noticeable difference. Therefore, re-centring with a 1D histogram depending only on centrality is chosen as the final method to re-centre the V0 system in this dissertation. In addition, the four peaks in the distribution of $\Psi_{2^{\text{nd}}\,\text{EP}}^{\text{V0k}}$ are expected and unavoidable due to the fact that each V0 detector is divided into eight individual cells in each ring, which leads to bias in four inclination angles of the event plane.

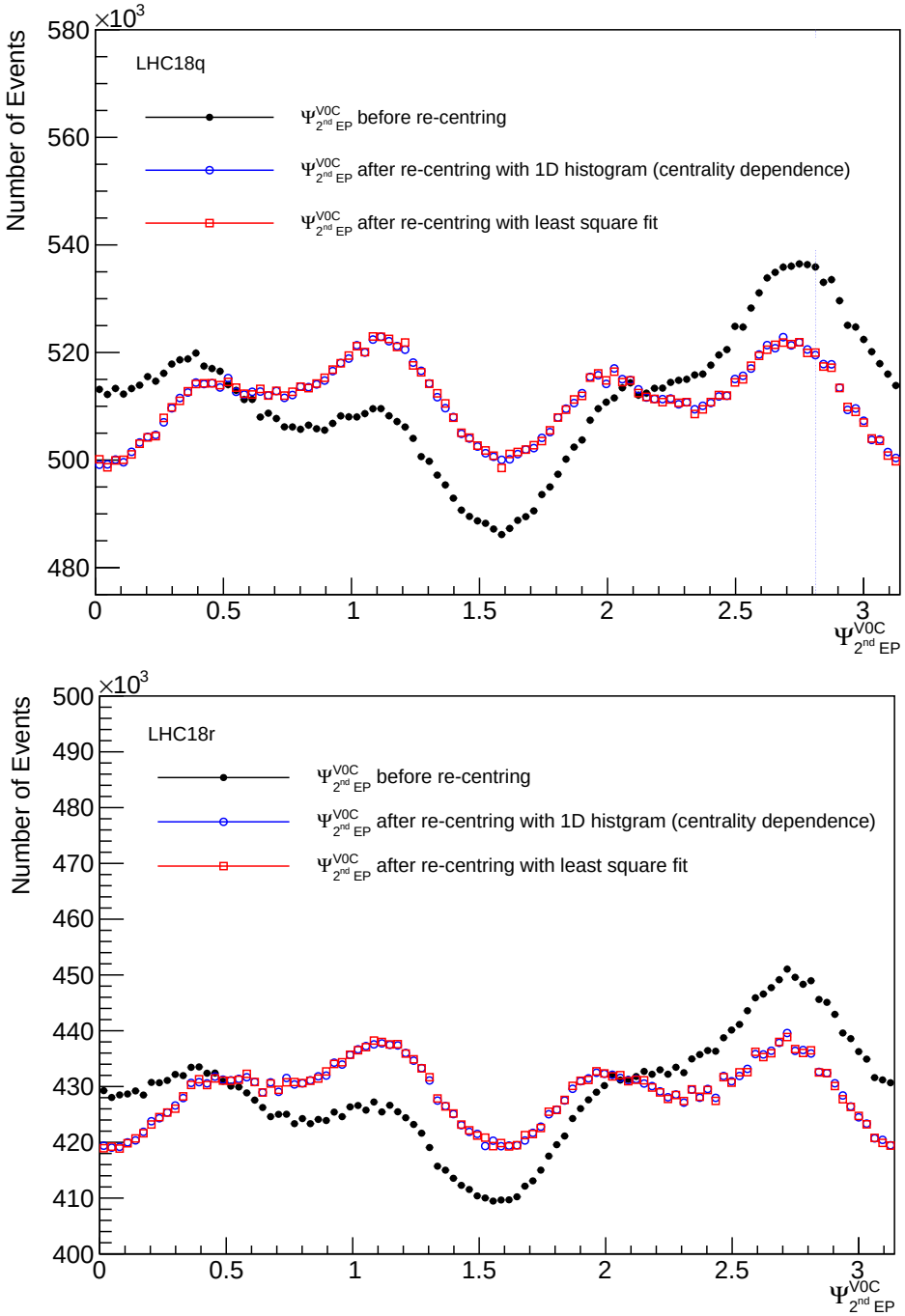

Figure 3.21: *The distribution of $\Psi^{V0C}_{2^{nd}\,EP}$ before (black) and after re-centring with centrality dependent 1D histogram (blue) and with the least square fit method for the LHC18q (left) and LHC18r (right) data sets.*

Chapter 4

Chiral Magnetic Effect measured relative to the participant and spectator flow planes

The possibility of producing metastable bubbles of P- and CP-violation during heavy ion collisions was first proposed in [139, 140]. Later, it was realized that this parity violation would manifest itself through the asymmetry between positively and negatively charged particles with respect to the reaction plane [9]. The orientation of the asymmetry is random event by event, which means that it can only be detected by a correlation study. Based on well-known three-particle correlations already used in anisotropic flow analysis [141], Voloshin proposed that a way to probe the leading order P-odd coefficient in CME is by measuring three-particle charge-dependent azimuthal correlations [86]. In Sec. 4.1, the proposed three-particle charge-dependent azimuthal correlations will be introduced. The two-particle charge-dependent azimuthal correlations, which provide a way to independently evaluate contributions from correlations parallel and perpendicular to the reaction plane, will be presented. However, the observation of quantitative agreement between the same charge-dependent correlation in the LHC and RHIC [87,88], despite different collision energies and collision systems leading to different multiplicity densities and magnetic fields, hints that these correlations are heavily contaminated by background effects. The sources of contamination were identified to be mainly from local charge conservation and transverse momentum conservation coupled to the anisotropic expansion of the system in noncentral collisions [93–95, 142]. Several methods emerged to disentangle the signal and the background in the charge-dependent correlators, including the event shape engineering (ESE) technique [98], the higher harmonic method [90], the two-component model [6], and the spectator-participant plane method [104, 105]. The last method is adopted for my analysis as it is a beautiful idea due to the cancelling of background effects and is proven to be robust in Au-Au collisions at $\sqrt{s_{NN}} = 200$ GeV by the STAR collaboration [103]. In Sec. 4.2, the spectator-participant plane method will be presented. This is followed by the detailed analysis procedure and the estimation of systematic uncertainties. The extraction of the fraction of CME in the three-particle charge-dependent correlator is going to be presented in detail, followed by a discussion on the results.

4.1 Charge-dependent azimuthal correlators

4.1.1 Introduction

As introduced previously, the charge separation induced by CME leads to an electric dipole in momentum space, and the dipole vector (the orientation of the charge separation), denoted as $\vec{d}$, which can be either parallel or anti-parallel to the magnetic field $\vec{B}$. This means that the event-by-event electric dipole is potentially measurable, but it is not possible to directly average over all events to achieve statistical significance as the expectation value of $\langle\vec{d}\rangle = \langle\vec{B}\cdot\vec{d}\rangle = 0$. However, the expectation value of the variance of the dipole vector is non-vanishing, $\langle\vec{d}^2\rangle \neq 0$, which naturally leads to the consideration of two-particle correlations. Voloshin proposed to study the two-particle charge-dependent correlation with respect to the reaction plane, which is sensitive to charge separation with respect to the reaction plane. This proposed correlation is known as the three-particle charge-dependent azimuthal correlator, also known as the $\gamma_{1,1}$ correlator, wherein two particles are correlated with the reaction plane determined independently from another set of particles. It is defined as

$$\begin{aligned}\gamma_{1,1} &= \langle\cos\left(\varphi_\alpha + \varphi_\beta - 2\Psi_{\text{RP}}\right)\rangle = \langle\cos\left[(\varphi_\alpha - \Psi_{\text{RP}}) + (\varphi_\beta - \Psi_{\text{RP}})\right]\rangle \\ &= \langle\cos\left(\Delta\varphi_\alpha + \Delta\varphi_\beta\right)\rangle = \langle\cos\Delta\varphi_\alpha\cos\Delta\varphi_\beta\rangle - \langle\sin\Delta\varphi_\alpha\sin\Delta\varphi_\beta\rangle \\ &= \langle v_{1,\alpha}v_{1,\beta}\rangle + B_{\text{in}} - \langle a_{1,\alpha}a_{1,\beta}\rangle - B_{\text{out}},\end{aligned} \tag{4.1.1}$$

where φ represents the azimuthal angle of a track while α and β indicate either same or opposite charge combinations. For convenience, we use particle type a to denote the same set of particles as α and β. Note that the notation $\langle ...\rangle$ is a bit sloppy, as the calculation of azimuthal correlations involves two distinct averaging procedures: averaging over all tracks within a given event, as well as averaging over all events. In principle, the single angular bracket should be substituted with double angular brackets, $\langle\langle ...\rangle\rangle$, to signify these two separate averaging processes. However, for the sake of simplicity in the equations, the single angular bracket is employed. The decomposed terms $\langle\cos\Delta\varphi_\alpha\cos\Delta\varphi_\beta\rangle$ and $\langle\sin\Delta\varphi_\alpha\sin\Delta\varphi_\beta\rangle$, equivalent to the variance of the x- and y-component of the dipole vector, quantify the correlations with respect to the in- and out-of-plane directions, respectively. The last line is detailed explained in [143], and we discuss it later when introducing $\Delta\gamma_{1,1}$ and $\Delta\delta_1$. It is also possible to replace the event plane Ψ_{RP} with one particle, and it is related to the expression above as

$$\langle\cos\left(\varphi_\alpha + \varphi_\beta - 2\varphi_c\right)\rangle = \langle\cos\left(\varphi_\alpha + \varphi_\beta - 2\Psi_{\text{RP}}\right)\rangle v_{2,c}, \tag{4.1.2}$$

where $v_{2,c} = \langle\cos\left(2\varphi_c - 2\Psi_{\text{RP}}\right\rangle$ is the elliptic flow of particle c. Particles of type c have no choice in the sign of their charge and can be identical to particle type a as long as the auto-correlation (i.e., when φ_c comes from the same track as either φ_α or φ_β) is properly taken into account. It should be noted that auto-correlation also exists in Eq. 4.1.1. If track α or β are used in the process of constructing Q-vectors for reconstructing the reaction plane Ψ_{RP}, the contribution from either α or β to Ψ_{RP} has to be excluded when calculating $\cos\left(\varphi_\alpha + \varphi_\beta - 2\Psi_{\text{RP}}\right)$.

According to the prediction of the CME, when it comes to same-charge (SS) pairs, they are likely to have both angles, φ_α and φ_β, preferably on the same side of the reaction plane, so that $\langle\sin\Delta\varphi_\alpha\sin\Delta\varphi_\beta\rangle > 0$. On the other hand, for opposite-charge (OS) pairs, φ_α and φ_β are more likely to be on the opposite sides of the reaction plane, leading to $\langle\sin\Delta\varphi_\alpha\sin\Delta\varphi_\beta\rangle < 0$. The CME does not contribute to the in-plane correlations, which means that $\langle\cos\Delta\varphi_\alpha\cos\Delta\varphi_\beta\rangle$

is approximately zero for both same and opposite charges. As a summary of the CME alone situation, we have

$$\begin{aligned}\gamma_{1,1}(\text{CME, SS}) &\simeq -\langle \sin\Delta\varphi_{\pm}\sin\Delta\varphi_{\pm}\rangle < 0,\\ \gamma_{1,1}(\text{CME, OS}) &\simeq -\langle \sin\Delta\varphi_{\pm}\sin\Delta\varphi_{\mp}\rangle > 0.\end{aligned} \tag{4.1.3}$$

However, there is some ambiguity in the $\gamma_{1,1}$ correlator when it comes to same-charge out-of-plane same-side correlations (e.g. black plus signs in Fig. 4.1) and same-charge in-plane back-to-back correlations (e.g. red plus signs in Fig. 4.1). Similarly, the $\gamma_{1,1}$ correlator is also ambiguous about opposite-charge out-of-plane back-to-back correlations and opposite-charge in-plane same-side correlations.

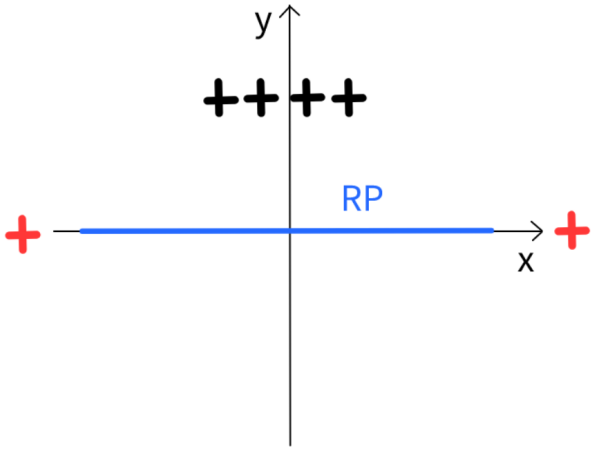

Figure 4.1: *Schematic illustration of the ambiguity of the $\gamma_{1,1}$ correlator in distinguishing out-of-plane same-side correlations and in-plane back-to-back correlations for the case of same charges.*

To break the ambiguity, a genuine two-particle correlation, known as the δ correlator, without dependence on any symmetry plane is introduced:

$$\begin{aligned}\delta_1 &= \langle\cos(\varphi_\alpha-\varphi_\beta)\rangle = \langle\cos[(\varphi_\alpha-\Psi_{\text{RP}})-(\varphi_\beta-\Psi_{\text{RP}})]\rangle\\ &= \langle\cos(\Delta\varphi_\alpha-\Delta\varphi_\beta)\rangle = \langle\cos\Delta\varphi_\alpha\cos\Delta\varphi_\beta\rangle + \langle\sin\Delta\varphi_\alpha\sin\Delta\varphi_\beta\rangle\\ &= \langle v_{1,\alpha}v_{1,\beta}\rangle + B_{\text{in}} + \langle a_{1,\alpha}a_{1,\beta}\rangle + B_{\text{out}},\end{aligned} \tag{4.1.4}$$

which allows the extraction of in-plane and out-of-plane correlations as

$$\begin{aligned}\langle\cos\Delta\varphi_\alpha\cos\Delta\varphi_\beta\rangle &= \frac{1}{2}(\gamma_{1,1}+\delta_1)\ \text{in-plane},\\ \langle\sin\Delta\varphi_\alpha\sin\Delta\varphi_\beta\rangle &= \frac{1}{2}(-\gamma_{1,1}+\delta_1)\ \text{out-of-plane}.\end{aligned} \tag{4.1.5}$$

Both the ALICE and STAR collaborations measured the same- and opposite-charge correlators [87–90], and the results indicated that the $\langle\cos\Delta\varphi_\alpha\cos\Delta\varphi_\beta\rangle_{\text{SS}}$ significantly deviated from 0 and $\langle\cos\Delta\varphi_\alpha\cos\Delta\varphi_\beta\rangle_{\text{OS}} \approx \langle\sin\Delta\varphi_\alpha\sin\Delta\varphi_\beta\rangle_{\text{OS}}$, as shown in Fig. 4.2. It is evident that the observed results do not align with the anticipated outcomes only from the CME. In particular, the same-charge in-plane correlations exhibit significantly high correlation strength, which is puzzling in the context of CME-only predictions. The in- and out-of-plane correlations for opposite-charge pairs exhibit almost the same magnitude, which is also hard to comprehend as

both collision systems have sizeable elliptic flow. The difference in the magnitude of in- and out-of-plane correlations between Au-Au and Pb-Pb collisions has not been offered a quantitative explanation, but the studies at both collision systems suggest that the short- and long-range correlations are different at different collision energies [144–146]. In addition, the Hanbury Brown–Twiss (HBT) radii (the homogeneity length of the particle-emitting system) grow with collision energies, leading to more small-angle emissions in Pb-Pb collisions at higher energies [147, 148]. In each type of heavy-ion collisions, the sources of background contributing to the $\gamma_{1,1}$ and δ_1 correlators include, but are not limited to, transverse-momentum conservation (TMC) [93, 149, 150] and local charge conservation (LCC) [93–95, 150], where the first factor is charge-independent and the second factor is charge-dependent. In peripheral collisions, the TMC effect tends to negatively shift both same-charge and opposite-charge correlations. These shifts are proportional to the elliptic flow v_2 and inversely proportional to the multiplicity of particles [151]. On the other hand, the LCC effect causes charges to be neutralized within small regions (fluid cells) at the surface of the freeze-out, which results in such spatial correlations being translated through the collective flow into final momentum correlations for opposite-charge pairs. Moreover, the elliptic flow introduces in-plane/out-of-plane differences (more opposite-charged pairs, due to the LCC effect, emitted in the reaction plane than in the direction orthogonal to it), leading to a positive contribution to $\gamma_{\rm OS}$, but no contribution to $\gamma_{\rm SS}$ [151]. The alterations to charge-dependent correlations caused by TMC are approximately a factor of 2 smaller than what is required to account for the observed STAR data, as concluded by an AMPT study [142]. The LCC is the dominant source of the background originating from the majority of quarks produced in local phase-space ($\phi, \eta, p_{\rm T}$) with their electric charge conserved during the evolution of the system through multiple parton-parton interactions [93, 94, 150]. Correlations between n-tuples of oppositely charged quarks (with $n = 2, 4, 6...$) are expected due to the common origin of such n-tuples. These correlations are altered by the collective evolution of the system and hadronization but are mostly transferred to the final-state particles. Monte Carlo event generators, such as HIJING [134] and AMPT [152], are insufficient to provide realistic estimations and subtract the LCC background since their accuracy in reproducing this mechanism is not enough for practical purposes. This is evident in the poor performance of HIJING and AMPT in reproducing balance functions measured by RHIC [144, 145] and LHC [146], which are sensitive to the magnitude of correlations induced by LCC.

In the last line of Eq. 4.1.1 and 4.1.4, the in- and out-of-plane correlations are split into two parts. The terms $\langle v_{1,\alpha} v_{1,\beta} \rangle$ (related to directed flow) and $\langle a_{1,\alpha} a_{1,\beta} \rangle$ (being the main target of the CME search) reflect the correlations along the axis in the reaction plane (directed flow) and the axis perpendicular to the reaction plane (P-odd terms), respectively. It is expected that $\langle v_{1,\alpha} v_{1,\beta} \rangle$ is charge-independent and has no relation to the electromagnetic field [70, 143]. The parity-conserving correlations projected onto the in- and out-of-plane directions are denoted as $B_{\rm in}$ and $B_{\rm out}$, respectively, representing other possible background correlations in and out of the flow plane. By taking the difference of opposite- and same-charge ($\gamma_{1,1}$ and δ_1) correlators

$$\begin{aligned} \Delta\gamma &= \gamma_{1,1}(\mathrm{OS}) - \gamma_{1,1}(\mathrm{SS}) \\ \Delta\delta &= \delta_1(\mathrm{OS}) - \delta_1(\mathrm{SS}), \end{aligned} \tag{4.1.6}$$

the $\langle v_{1,\alpha} v_{1,\beta} \rangle$, which has negligible charge dependence, and the charge-independent part of parity-conserving correlations cancel out. The charge-dependent correlations in $(B_{\rm in} - B_{\rm out})$ for $\Delta\gamma_{1,1}$ and $(B_{\rm in} + B_{\rm out})$ for $\Delta\delta 1$ constitute the primary background source and do not cancel out. These correlations exist at a magnitude proportional to the elliptic flow, with the primary source, as previously noted, expected to originate from local charge conservation.

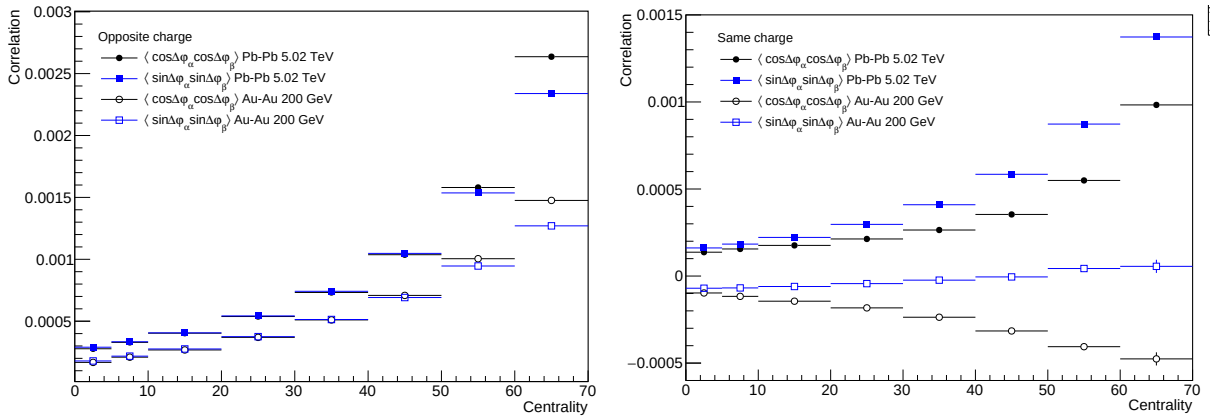

Figure 4.2: *In-* $(\langle \cos\Delta\varphi_\alpha \cos\Delta\varphi_\beta \rangle)$ *and out-of-plane* $(\langle \sin\Delta\varphi_\alpha \sin\Delta\varphi_\beta \rangle)$ *correlations for same- (blue) and opposite-charge (black) pairs in Pb-Pb collisions at* $\sqrt{s_{NN}} = 5.02$ *TeV measured by the ALICE collaboration [90] and in Au-Au collisions at* $\sqrt{s_{NN}} = 200$ *GeV measured by the STAR collaboration [87, 88].*

4.1.2 Calculation of δ and γ correlators

Direct calculation with nested loops

The δ_1 and $\gamma_{1,1}$ correlators can be calculated in various ways. The most direct way is to use nested loops, which typically requires two layers of nested loops to compute the gamma correlator in the form of Eq. 4.1.1. In addition, if the participant plane $\Psi_{\rm PP}$ is reconstructed with TPC tracks, the contributions from φ_α or φ_β have to be subtracted from Q-vectors for each combination to avoid auto-correlation. If one desires to compute the γ correlator in the form of Eq. 4.1.2, the expansion of the cosine function is required (see Eq. **??**), as three layers of nested loops result in excessive computational time. It was discussed in Sections 3.7 and 3.8 that the distribution of the azimuthal angle has to be flattened. The reconstructed charged tracks accepted by the TPC also need similar acceptance correction. The direct calculation requires applying non-uniform acceptance corrections, denoted as $w_j(\eta, \varphi)$, for each track from real data as a function of η, φ, and other related variables individually for each run number, centrality interval, sign of charge, and v_z as

$$w_j(\eta, \varphi, ...) = \frac{\langle dN(\eta, \varphi, ...)/d\eta d\varphi ... \rangle_\varphi}{dN(\eta, \varphi ...)/d\eta d\varphi}, \tag{4.1.7}$$

where $\langle dN(\eta, \varphi, ...)/d\eta d\varphi ... \rangle_\varphi$ denotes the average track density over $0 < \varphi < 2\pi$ in each interval of η. This method is very tedious as the correction factor has to be regenerated whenever the event or track selection is changed. The choice of bin size can also affect the final magnitudes of correlators.

Multi-particle Cumulants

The second approach is utilized in the work of this dissertation. The idea is based on the generalized cumulants expansion method introduced by Kubo [153], which was later introduced to flow analysis by Borghini *et al.* in [131]. The concept of cumulant is widely used in statistics and is usually introduced together with the moment of the distribution of a random variable x. The $n^{\rm th}$ moment is defined as the expectation value of x^n, namely $m_n = \langle x^n \rangle$, which can be obtained by taking the $n^{\rm th}$ derivative of the moment generating function, $M_x(t) = \langle e^{tx} \rangle$, with respect to t

at $t = 0$. The cumulant also has its corresponding generating function defined as the logarithm of the moment generating function, $K_x(t) = \ln M_x(t)$. From the generating functions, one can obtain the relationship between cumulants and moments:

$$\begin{aligned}
\langle x\rangle_c &= \langle x\rangle, \\
\langle x^2\rangle_c &= \langle x^2\rangle - \langle x\rangle, \\
\langle x^3\rangle_c &= \langle x^3\rangle - 3\langle x^2\rangle\langle x\rangle + 2\langle x\rangle^3, \\
\langle x^4\rangle_c &= \langle x^4\rangle - 4\langle x^3\rangle\langle x\rangle - 3\langle x^2\rangle^2 + 12\langle x^2\rangle\langle x\rangle^2 - 6\langle x\rangle^4.
\end{aligned} \tag{4.1.8}$$

The expressions above are very abstract, but the n^{th} moment can be visually represented as the sum of all possible ways of dividing n points into smaller groupings of connected or disconnected clusters (see e.g. [154] for more information):

$\langle x\rangle$ =  $= \langle x\rangle_c$,

$\langle x^2\rangle$ = 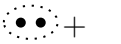 $= \langle x^2\rangle_c + \langle x\rangle_x^2$,

$\langle x^3\rangle$ = 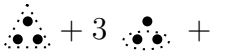 $= \langle x^3\rangle_c + 3\langle x^2\rangle_c\langle x\rangle_c + \langle x\rangle_c^3$,

$\langle x^4\rangle$ = 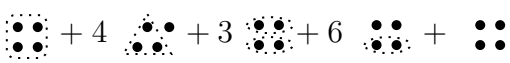

$= \langle x^4\rangle_c + 4\langle x^3\rangle_c\langle x\rangle_c + 3\langle x^2\rangle_c^2 + 6\langle x^2\rangle_c\langle x\rangle_c^2 + \langle x\rangle_c^4$.

One can easily see that the n^{th} cumulant, defined in Eq. 4.1.8, represents the genuine correlation (fully connected cluster) between n points, and it can be obtained by subtracting all other partially connected and fully disconnected contributions (lower-order moments) from the n^{th} moment. With more than one random variable, the graphical relationship discussed above remains valid, except that the combination of multiple variables has to be considered. For example, in the case of two variables, x_1 and x_2, the moment of the form $\langle x_1^2 x_2\rangle$ has to consider the correlations between each of x_1 and x_2, and between two x_1s, respectively:

$\langle x_1^2 x_2\rangle$ = 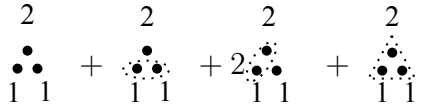

$= \langle x_1\rangle_c^2\langle x_2\rangle_c + \langle x_1^2\rangle_c\langle x_2\rangle_c + 2\langle x_1 x_2\rangle_c\langle x_1\rangle_c + \langle x_1^2 x_2\rangle_c$

The δ and γ correlator simply correspond to $\langle x_1 x_2 \rangle_c$ and $\langle x_1 x_2 x_3 \rangle_c$, respectively, which can be immediately written down with cumulants as:

$$\begin{aligned}
\delta_{1,1} &= \langle \cos(\varphi_\alpha - \varphi_\beta) \rangle_c \\
&= \langle \cos(\varphi_\alpha - \varphi_\beta) \rangle - (\langle \cos(\varphi_\alpha) \rangle \langle \cos(\varphi_\beta) \rangle + \langle \sin(\varphi_\alpha) \rangle \langle \sin(\varphi_\beta) \rangle) \\
\gamma_{11,2} &= \langle \cos(\varphi_\alpha + \varphi_\beta - 2\varphi_c) \rangle_c \\
&= \langle \cos(\varphi_\alpha + \varphi_\beta - 2\varphi_c) \rangle \\
&\quad - [\langle \cos\varphi_\alpha \rangle \langle \cos(\varphi_\beta - 2\varphi_c) \rangle - \langle \sin\varphi_\alpha \rangle \langle \sin(\varphi_\beta - 2\varphi_c) \rangle \\
&\quad + \langle \cos\varphi_\beta \rangle \langle \cos(\varphi_\alpha - 2\varphi_c) \rangle - \langle \sin\varphi_\beta \rangle \langle \sin(\varphi_\alpha - 2\varphi_c) \rangle \\
&\quad + \langle \cos 2\varphi_c \rangle \langle \cos(\varphi_\alpha + \varphi_\beta) \rangle + \langle \sin 2\varphi_c \rangle \langle \sin(\varphi_\alpha + \varphi_\beta) \rangle] \\
&\quad + 2\langle \cos(2\varphi_c) \rangle [\langle \cos(\varphi_\alpha) \rangle \langle \cos(\varphi_\beta) \rangle - \langle \sin(\varphi_\alpha) \rangle \langle \sin(\varphi_\beta) \rangle] \\
&\quad + 2\langle \sin(2\varphi_c) \rangle [\langle \cos(\varphi_\alpha) \rangle \langle \sin(\varphi_\beta) \rangle - \langle \sin(\varphi_\alpha) \rangle \langle \cos(\varphi_\beta) \rangle].
\end{aligned} \tag{4.1.9}$$

All of the terms except for $\langle \cos(\varphi_\alpha + \varphi_\beta - 2\varphi_c) \rangle$ can be calculated with one or two nested loops. The expression $\langle \cos(\varphi_\alpha + \varphi_\beta - 2\varphi_c) \rangle$ can be evaluated by expanding the cosine function using trigonometric identities while considering all auto-correlations as follows:

$$\begin{aligned}
\langle \cos(\varphi_\alpha + \varphi_\beta - 2\varphi_c) \rangle &= \langle w_i w_j \cos(\varphi_{\alpha,i} + \varphi_{\beta,j}) \rangle \langle w_k \cos(2\varphi_{c,k}) \rangle \\
&\quad + \langle w_i w_j \sin(\varphi_{\alpha,i} + \varphi_{\beta,j}) \rangle \langle w_k \sin(2\varphi_{c,k}) \rangle \\
&\quad - \langle w_i^2 w_j \cos(\varphi_{\alpha,i} - \varphi_{\beta,j}) \rangle - \langle w_i w_j^2 \cos(\varphi_{\alpha,i} - \varphi_{\beta,j}) \rangle,
\end{aligned} \tag{4.1.10}$$

where the terms $\langle w_i^2 w_j \cos(\varphi_{\alpha,i} - \varphi_{\beta,j}) \rangle$ and $\langle w_i w_j^2 \cos(\varphi_{\alpha,i} - \varphi_{\beta,j}) \rangle$ come from the auto-correlation when $\varphi_{\alpha,i} = \varphi_{c,k}$ and $\varphi_{\beta,j} = \varphi_{c,k}$, respectively. Interested readers can refer to [155] for a more concise representation of all these equations in the language of Q-vector. In Eq. 4.1.9, the terms following $\langle \cos(\varphi_\alpha - \varphi_\beta) \rangle$ and $\langle \cos(\varphi_\alpha + \varphi_\beta - 2\varphi_c) \rangle$ are commonly referred to as the non-isotropic terms. Each component within the non-isotropic terms is saved separately and subtracted subsequently to ensure an unbiased calculation of the δ and γ correlators. For $\langle \cos(\varphi_\alpha + \varphi_\beta - 2\Psi_{\mathrm{V0k}}) \rangle$ (k=A or C) and $\langle \cos(\varphi_\alpha + \varphi_\beta - 2\Psi_{\mathrm{ZNC\text{-}ZNA}}) \rangle$, the azimuthal angle φ_c is replaced by Ψ_{V0} and $\Psi_{\mathrm{ZNC\text{-}ZNA}}$, respectively, and the non-isotropic terms involving $\langle \cos(2\varphi_c) \rangle$ and $\langle \sin(2\varphi_c) \rangle$ vanish due to recentring of V0 and ZDC detectors. The comparison between applying and without applying non-isotropic corrections for Ψ_{V0} and $\Psi_{\mathrm{ZNC\text{-}ZNA}}$ serves as a good check to test the significance of non-isotropic corrections after recentring. As shown in Fig. 4.3, such differences are negligible for both same- and opposite-charge γ correlator involving V0C and neutron ZDC, which validates the recentring works well from another perspective.

Furthermore, it is evident that the non-uniform acceptance correction factors, as described in Eq. 4.1.7, applied to tracks essentially render the non-isotropic terms negligible or approaching zero. Therefore, applying non-isotropic corrections is equivalent to applying nonuniform acceptance correction factors. Actually, it has been demonstrated to be a superior method, as investigated in [132, 155], yielding results closer to the true values provided by Monte Carlo simulations.

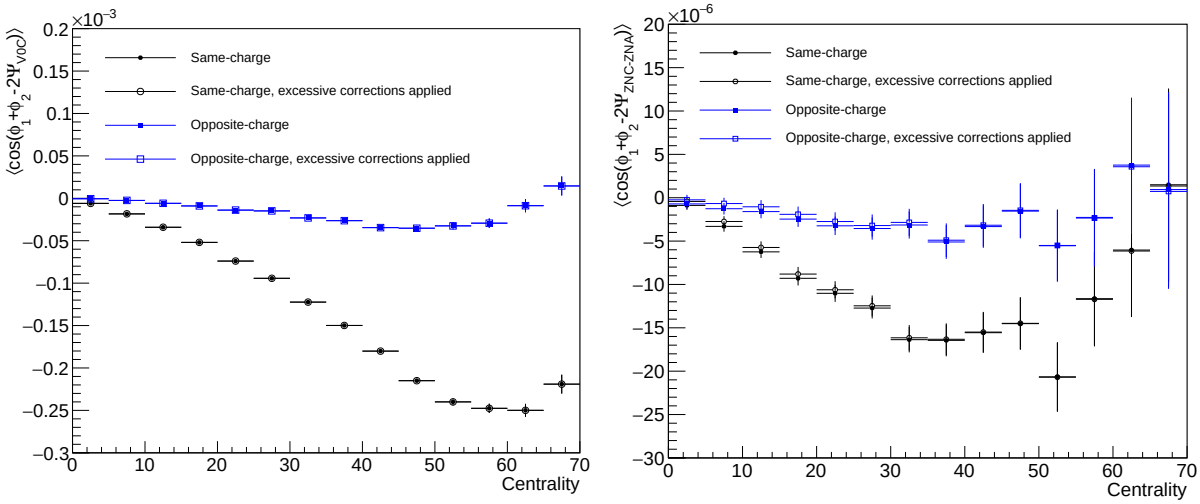

Figure 4.3: *The comparison between applying and not applying non-isotropic corrections for* $\langle\cos(\varphi_\alpha + \varphi_\beta - 2\Psi_{V0C})\rangle_{SS/OS}$ *(left) and* $\langle\cos(\varphi_\alpha + \varphi_\beta - 2\Psi_{ZNC\text{-}ZNA})\rangle_{SS/OS}$ *(right).*

4.2 Spectator-participant plane method

4.2.1 Introduction

The spectator- and participant-plane (SP/PP) method, proposed by [104,105], is an experimental technique designed to cancel out the background in $\Delta\gamma$ by taking the ratio of the $\Delta\gamma$ correlator measured with respect to the spectator- and participant-plane, respectively. The introduction of the SP/PP method is based on [105]. This method starts with a rather safe assumption: as the correlation between the CME signal and background in $\Delta\gamma$ is small, these two parts can be separated as

$$\Delta\gamma = \Delta\gamma^{\mathrm{BG}} + \Delta\gamma^{\mathrm{CME}}, \tag{4.2.1}$$

without considering any potential interactions between the two effects. As discussed in the previous section, the main background contribution to $\Delta\gamma$ is from LCC, which essentially means that both particles α and β are emitted from the same local phase-space (cluster). The background component can be written as:

$$\begin{aligned}\Delta\gamma^{\mathrm{BG}} &= \Delta\langle\cos(\varphi_\alpha + \varphi_\beta - 2\Psi)\rangle = \Delta\langle\cos(\varphi_\alpha + \varphi_\beta - 2\phi_{\mathrm{clust}})\rangle\langle\cos(2\phi_{\mathrm{clust}} - 2\Psi)\rangle_{\alpha,\beta\in\mathrm{clust}},\\ &= \Delta\langle\cos(\varphi_\alpha + \varphi_\beta - 2\phi_{\mathrm{clust}})\rangle\tilde{v}_{2;\mathrm{clust}} \propto \Delta\langle\cos(\varphi_\alpha + \varphi_\beta - 2\phi_{\mathrm{clust}})\rangle v_2,\end{aligned} \tag{4.2.2}$$

where ϕ_{clust} is the cluster emission angle, $\Delta\langle\cos(\varphi_\alpha + \varphi_\beta - 2\phi_{\mathrm{clust}})\rangle$ varies with ϕ_{clust}, and the second component in the factorisation $\langle\cos(2\phi_{\mathrm{clust}} - 2\Psi)\rangle = \tilde{v}_{2;\mathrm{clust}}$ represents the elliptic flow of the cluster. Although the individual contribution of each component in the factorisation remains uncertain, their combined effect typically accounts for the LCC background. To approximate and simplify the contribution of each component, a few assumptions are made:

- $\Delta\gamma^{\mathrm{BG}} \propto \tilde{v}_{2;\mathrm{clust}} \propto v_2$, where the first and the second proportionality assumes linear dependence of $\Delta\gamma^{\mathrm{BG}}$ on $\tilde{v}_{2;\mathrm{clust}}$ and the elliptic flow of the cluster being proportional to the elliptic flow of charged particles. This leads to one final assumption $\Delta\gamma^{\mathrm{BG}} = bv_2$, where b is the proportionality constant. Note that if Ψ in $\Delta\gamma$ is replaced by one particle (see Eq. 4.1.2), we have $\Delta\gamma^{\mathrm{BG}} = bv_2^2$ instead.

Because of variations in the initial state, measurements of the elliptic flow and its corresponding fluctuations relative to various flow symmetry planes differ, as confirmed by observations in [156]. It is therefore necessary to adapt the correlator by computing $\Delta\gamma/v_2$ (or $\Delta\gamma/v_2^2$ if one particle is used instead of Ψ) with v_2 calculated in a similar manner as the numerator:

$$\Delta\gamma/v_2 = \frac{\Delta\langle\cos\left(\varphi_\alpha + \varphi_\beta - 2\Psi\right)\rangle}{\langle\cos\left(2\varphi_a - 2\Psi\right)\rangle}, \tag{4.2.3}$$

where φ_a represents the same group of particles as α and β. It should be noted that the normalisation of $\Delta\gamma$ by v_2 also has the benefit of cancelling the reaction plane resolution, which is present in any azimuthal correlations to compensate for the limited resolution in the measured event plane angle caused by the finite number of detected particles [130]. The reaction plane resolution is typically estimated from the correlation of the planes in multiple sub-events. In the case of using three sub-events, the resolution is given as:

$$\text{Res}(\Psi_2) = \langle\cos\left(n(\Psi_2^a - \Psi_r)\right)\rangle = \sqrt{\frac{\langle\cos\left(n\Psi_2^a - \Psi_2^b\right)\rangle\langle\cos\left(n\Psi_2^a - \Psi_2^c\right)\rangle}{\langle\cos\left(n\Psi_2^b - \Psi_2^c\right)\rangle}}, \tag{4.2.4}$$

where Ψ_r denotes the true reaction plane angle and a, b, c denote each sub-event measured by different (parts of) detectors. The cancellation is crucial for this method to work for the whole analysis on the LHC18q and LHC18r data sets as the resolution of the spectator plane is difficult to estimate due to the spurious ZNA-ZNC correlation. When extracting the fraction of CME in the $\Delta\gamma$ correlator, the resolution of the spectator plane is needed for calculating $v_{2,\text{SP}}$. It will be explained later that assumptions are made to obtain $v_{2,\text{SP}}$ for Pb-Pb collisions at 5.02 TeV based on published results at 2.76 TeV.

In the zero CME-signal scenario ($\Delta\gamma = \Delta\gamma^{\text{BG}}$), the ratio above is simply:

$$\Delta\gamma/v_2 = \frac{bv_2}{v_2} = b. \tag{4.2.5}$$

The essence of this method is to calculate the ratio (Eq. 4.2.3) using the spectator- ($\Psi_{1,\text{SP}}$) and participant-plane ($\Psi_{2,\text{PP}}$ or one particle φ_c), respectively. By decomposing the $\Delta\gamma$ correlator measured relative to φ_c and $\Psi_{1,\text{SP}}$, it can be clearly seen that the background contributions are the same after dividing by v_2 (or v_2^2) and the CME signal contributions differ between two types of planes:

$$\begin{aligned}\Delta\langle\cos\left(\varphi_\alpha + \varphi_\beta - 2\varphi_c\right)\rangle &= \langle\cos\left(\varphi_\alpha + \varphi_\beta - 2\varphi_c\right)\rangle^{\text{BG}} + \langle\cos\left(\varphi_\alpha + \varphi_\beta - 2\varphi_c\right)\rangle^{\text{CME}} \\ &= b\langle\cos\left(2\varphi_a - 2\varphi_c\right)\rangle + \\ &\quad + \langle\cos\left(\varphi_\alpha + \varphi_\beta - 2\Psi_{\text{B}}\right)\rangle^{\text{CME}}\langle\cos\left(2\varphi_c - 2\Psi_{\text{B}}\right)\rangle \\ &= b\langle v_{2,\text{PP}}^2\rangle + \Delta\gamma^{\text{CME}} v_{2,\Psi_{\text{B}}}\end{aligned} \tag{4.2.6}$$

$$\begin{aligned}\Delta\langle\cos\left(\varphi_\alpha + \varphi_\beta - 2\Psi_{1,\text{SP}}\right)\rangle &= b\langle\cos\left(2\varphi_a - 2\Psi_{1,\text{SP}}\right)\rangle + \\ &\quad + \langle\cos\left(\varphi_\alpha + \varphi_\beta - 2\Psi_{\text{B}}\right)\rangle^{\text{CME}}\langle\cos\left(2\Psi_{1,\text{SP}} - 2\Psi_{\text{B}}\right)\rangle \\ &= bv_{2,\text{SP}} + \Delta\gamma^{\text{CME}}\langle\cos\left(2\Psi_{1,\text{SP}} - 2\Psi_{\text{B}}\right)\rangle,\end{aligned} \tag{4.2.7}$$

where Ψ_{B} denotes the orientation of the plane perpendicular to the magnetic field, but it is not measurable in the experiment as the early magnetic fields dissipate extremely fast and last for a timescale of order ~ 1 fm or even less [64–66]. The charge separation driven by the magnetic

field is expected to be maximized with respect to Ψ_{B}, which also maximises the potential CME signal in $\Delta\gamma$. It is assumed that Ψ_{B} coincides with the spectator plane since the magnetic field is directly created by the spectators ($\Psi_{\mathrm{B}} = \Psi_{1,\mathrm{SP}}$). On the other hand, $\Delta\gamma$ measured with respect to $\Psi_{2,\mathrm{PP}}$ is expected to maximise the contribution from flow and the contribution from the CME signal is weaker as $v_{2,\Psi_{\mathrm{B}}} < \langle\cos\left(2\Psi_{1,\mathrm{SP}} - 2\Psi_{\mathrm{B}}\right)\rangle$. It is therefore natural to consider the double ratio

$$\begin{aligned}
\frac{(\Delta\gamma/v_2)_{\mathrm{SP}}}{(\Delta\gamma/v_2)_{\mathrm{c}}} &= \frac{b + \Delta\gamma^{\mathrm{CME}}\frac{\langle\cos\left(2\Psi_{1,\mathrm{SP}}-2\Psi_{\mathrm{B}}\right)\rangle}{v_{2,\mathrm{SP}}}}{b + \Delta\gamma^{\mathrm{CME}}\frac{v_{2,\Psi_{\mathrm{B}}}}{\langle v_{2,\mathrm{PP}}^2\rangle}} \\
&= \frac{b\langle v_{2,\mathrm{PP}}^2\rangle}{b\langle v_{2,\mathrm{PP}}^2\rangle + \Delta\gamma^{\mathrm{CME}}v_{2,\Psi_{\mathrm{B}}}} + \frac{\Delta\gamma^{\mathrm{CME}}\frac{\langle\cos\left(2\Psi_{1,\mathrm{SP}}-2\Psi_{\mathrm{B}}\right)\rangle}{v_{2,\mathrm{SP}}}}{b + \Delta\gamma^{\mathrm{CME}}\frac{v_{2,\Psi_{\mathrm{B}}}}{\langle v_{2,\mathrm{PP}}^2\rangle}} \\
&= \frac{\Delta\langle\cos\left(\varphi_\alpha + \varphi_\beta - 2\varphi_c\right)\rangle - \Delta\langle\cos\left(\varphi_\alpha + \varphi_\beta - 2\varphi_c\right)\rangle^{\mathrm{CME}}}{\Delta\langle\cos\left(\varphi_\alpha + \varphi_\beta - 2\varphi_c\right)\rangle} + \\
&\quad + \frac{\Delta\gamma^{\mathrm{CME}}v_{2,\Psi_{\mathrm{B}}}\frac{\langle\cos\left(2\Psi_{1,\mathrm{SP}}-2\Psi_{\mathrm{B}}\right)\rangle}{v_{2,\mathrm{SP}}}}{(bv_{2,\mathrm{PP}^2} + \Delta\gamma^{\mathrm{CME}}v_{2,\Psi_{\mathrm{B}}})\frac{v_{2,\Psi_{\mathrm{B}}}}{\langle v_{2,\mathrm{PP}}^2\rangle}} \\
&= 1 - f_{\mathrm{PP}}^{\mathrm{CME}} + f_{\mathrm{PP}}^{\mathrm{CME}}\frac{\langle\cos\left(2\Psi_{1,\mathrm{SP}} - 2\Psi_{\mathrm{B}}\right)\rangle\langle v_{2,\mathrm{PP}}^2\rangle}{v_{2,\mathrm{SP}}\cdot v_{2,\Psi_{\mathrm{B}}}} \\
&= 1 + f_{\mathrm{PP}}^{\mathrm{CME}}\left(\frac{\langle\cos\left(2\Psi_{1,\mathrm{SP}} - 2\Psi_{\mathrm{B}}\right)\rangle\langle v_{2,\mathrm{PP}}^2\rangle}{v_{2,\mathrm{SP}}\cdot v_{2,\Psi_{\mathrm{B}}}} - 1\right) \\
&= 1 + f_{\mathrm{PP}}^{\mathrm{CME}}\left(\frac{\langle\cos\left(2\Psi_{1,\mathrm{SP}} - 2\Psi_{\mathrm{B}}\right)\rangle\langle v_{2,\mathrm{PP}}^2\rangle}{v_{2,\mathrm{SP}}\cdot v_{2,\Psi_{\mathrm{B}}}} - 1\right),
\end{aligned} \tag{4.2.8}$$

where

$$f_{\mathrm{PP}}^{\mathrm{CME}} = \frac{\Delta\langle\cos\left(\varphi_\alpha + \varphi_\beta - 2\varphi_c\right)\rangle^{\mathrm{CME}}}{\Delta\langle\cos\left(\varphi_\alpha + \varphi_\beta - 2\varphi_c\right)\rangle} \tag{4.2.9}$$

is the CME signal fraction in $\Delta\gamma$ correlator measured with respect to the participant plane. Using the assumption that $\Psi_{\mathrm{B}} = \Psi_{1,\mathrm{SP}}$, Eq. 4.2.8 can be further simplified to

$$\frac{(\Delta\gamma/v_2)_{\mathrm{SP}}}{(\Delta\gamma/v_2)_{\mathrm{c}}} = 1 + f_{\mathrm{PP}}^{\mathrm{CME}}\left(\frac{\langle v_{2,\mathrm{PP}}^2\rangle}{v_{2,\mathrm{SP}}^2} - 1\right), \tag{4.2.10}$$

which can be rearranged to factor out $f_{\mathrm{PP}}^{\mathrm{CME}}$:

$$f_{\mathrm{PP}}^{\mathrm{CME}} = \frac{A/a - 1}{1/a^2 - 1}, \tag{4.2.11}$$

where

$$A = \frac{\Delta\gamma_{\mathrm{SP}}}{\Delta\gamma_{\mathrm{PP}}} \quad \text{and} \quad a = \frac{v_{2,\mathrm{SP}}}{v_{2,\mathrm{PP}}}. \tag{4.2.12}$$

In the numerator, A/a is simply the double ratio coming from the analysis described previously. To obtain the value of a in the denominator, it is necessary to calculate $v_{2,\mathrm{PP}}$ and $v_{2,\mathrm{SP}}$, which requires the estimation of the participant plane and spectator plane resolution, respectively. However, estimating the resolution of the spectator plane is particularly challenging in the 2018 data set due to the presence of spurious ZNA-ZNC correlation. To calculate $v_{2,\mathrm{SP}}$ for

the LHC18q and LHC18r data sets, using both the standard and new ZDC calculation, Eq. 11 in the reference [157] is followed. The results are depicted in Figure 4.4, showing significant deviations from the published $v_{2,\mathrm{SP}}$ for LHC10h in Pb-Pb collisions at $\sqrt{s_{\mathrm{NN}}} = 2.76$ TeV [157] and the published $v_2\{2\}$ for LHC15o data set in Pb-Pb collisions at $\sqrt{s_{\mathrm{NN}}} = 5.02$ TeV [158]. In order to proceed with this method, it is assumed that the ratio a is independent of collision energies:

$$a = \frac{v_{2,\mathrm{SP}}(5.02\,\mathrm{TeV})}{v_{2,\mathrm{PP}}(5.02\,\mathrm{TeV})} = \frac{v_{2,\mathrm{SP}}(2.76\,\mathrm{TeV})}{v_{2,\mathrm{PP}}(2.76\,\mathrm{TeV})}. \tag{4.2.13}$$

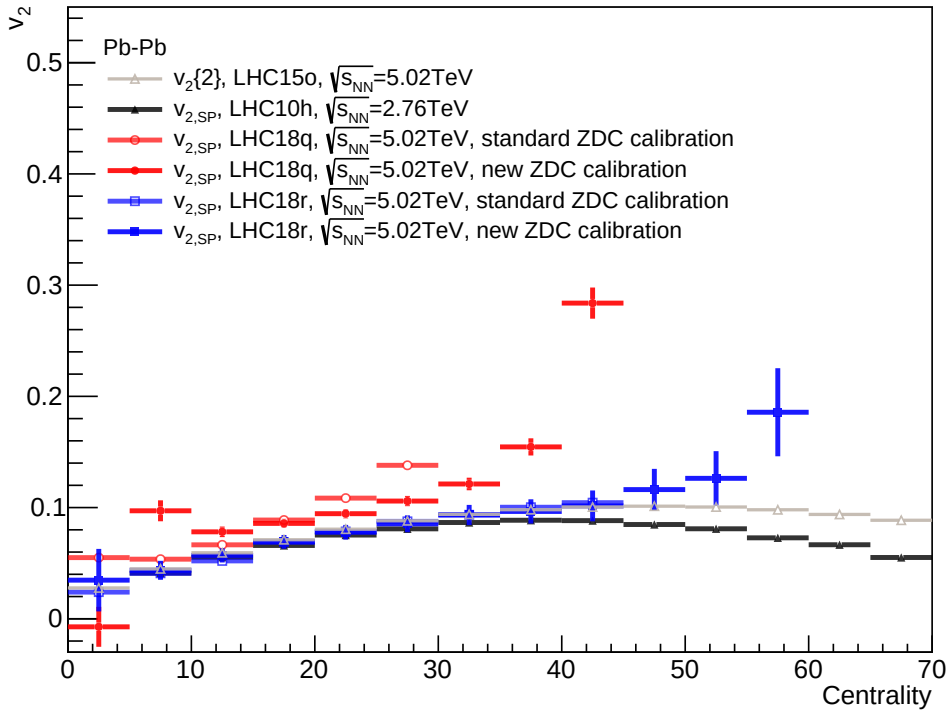

Figure 4.4: *Comparison of the calculation of $v_{2,SP}$ for LHC18q and LHC18r data sets using standard and new ZDC calculation with the published $v_{2,SP}$ for LHC10h data set at $\sqrt{s_{NN}} = 2.76$ TeV [157] and the published $v_2\{2\}$ for LHC15o data set at $\sqrt{s_{NN}} = 5.02$ TeV [158].*

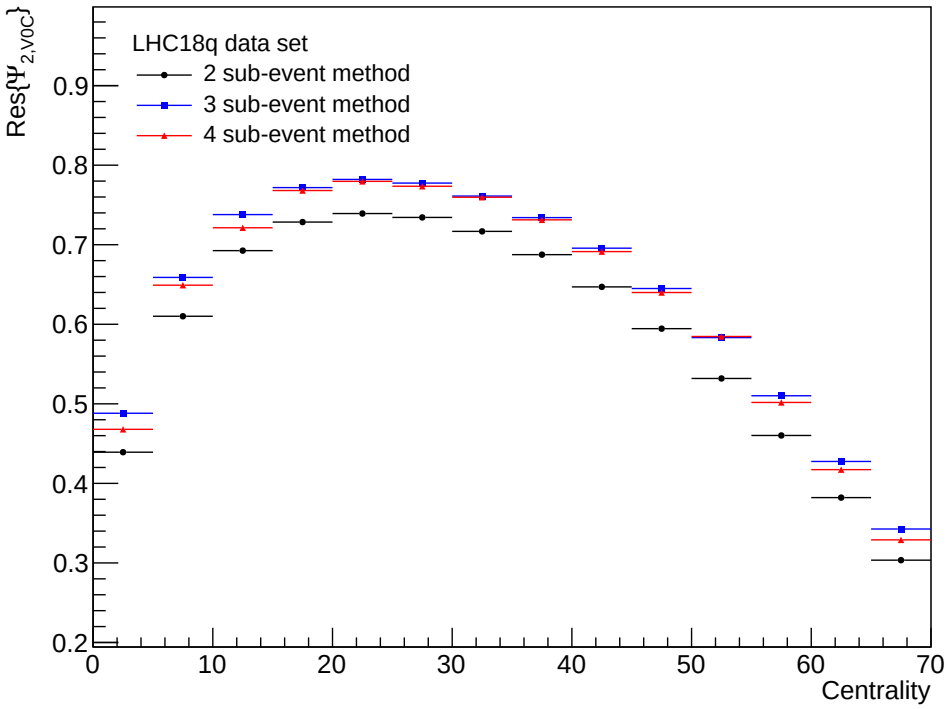

Figure 4.5: *Event plane resolution of $\Psi_{2,V0C}$ calculated using 2, 3 and 4 sub-events method for LHC18q data set.*

In the final result of the double ratio, the second-order event plane reconstructed by the V0C detector is adopted. This choice has the major benefit that a large gap is present between TPC and V0 system so that the non-flow effect is largely suppressed. However, no published result of $v_{2,\mathrm{V0C}}$ is available and the calculation of $v_{2,\mathrm{V0C}}$, which relies on the conventional event plane method, is typically biased due to its susceptibility to correlations that are unrelated to the genuine correlation of all particles with the actual reaction plane [155]. In Fig. 4.5, event plane resolution of $\Psi_{2,\mathrm{V0C}}$ calculated using 2, 3, and 4 sub-events method for LHC18q data set is shown as an example to illustrate the bias introduced due to different choices of the number of sub-events. Therefore, the published $v_2\{2\}$ calculated using the Q-cumulant method with a large η gap applied ($\Delta\eta > 1$) is utilised to approximate $v_{2,\mathrm{V0C}}$ [158], leading to using only published results to estimate a (see Fig. 4.9 for values of a)

$$a = \frac{v_{2,\mathrm{SP}}(2.76\,\mathrm{TeV})}{v_{2,\mathrm{PP}}(2.76\,\mathrm{TeV})} = \frac{v_{2,\mathrm{SP}}(2.76\,\mathrm{TeV})}{v_{2,\mathrm{V0C}}(2.76\,\mathrm{TeV})} \approx \frac{v_{2,\mathrm{SP}}(2.76\,\mathrm{TeV})}{v_2\{2\}(\Delta\eta > 1,\ 2.76\,\mathrm{TeV})}. \tag{4.2.14}$$

4.2.2 Obtaining the statistical uncertainty with subsampling method

The statistical uncertainty in the double ratio can be obtained through the propagation of uncertainty. However, it is easy to make mistakes due to complicated non-isotropic corrections. Therefore, the subsampling method is used to obtain the statistical uncertainty. The brief description of the procedure is provided here, based on the statistical uncertainties section in [155]. Consider each measured value of the double ratio (Eq. 4.2.8) from a total of N events in each centrality bin as a random observable x sampled from a probability density function (PDF) $f(x)$. The mean of x is denoted as μ_x, and its variance is denoted as σ_x^2 (or equivalently, $V[x]$). The

expressions for the mean and variance of x are given as follows:

$$\mu_x = E[x] = \int_{-\infty}^{\infty} x f(x) dx, \tag{4.2.15}$$

$$\sigma_x^2 = V[x] = E[(x - E[x])^2] = \int_{-\infty}^{\infty} (x - \mu_x)^2 f(x) dx, \tag{4.2.16}$$

where $E[x]$ represents the expectation value of x. Imagine splitting N events into k groups with approximately the same number of events n_i. We can use the measured average value x_i from the i^{th} group to estimate the mean and variance of our observable x. The unbiased estimator, denoted as s_x^2, for the variance σ_x^2 is given by

$$\sigma_{x,\text{unbiased}}^2 = s_x^2 = \left[\frac{\sum_{i=1}^{k} n_i (x_i - \langle x \rangle)^2}{\sum_{i=1}^{k} n_i} \right] \times \left[\frac{1}{1 - \frac{\sum_{i=1}^{k} n_i^2}{\left[\sum_{i=1}^{k} n_i\right]^2}} \right], \tag{4.2.17}$$

where $\langle x \rangle$ is the unbiased estimator for the mean μ_x given by

$$\langle x \rangle = \frac{\sum_{i=1}^{k} n_i x_i}{\sum_{i=1}^{k} n_i}. \tag{4.2.18}$$

Therefore, the final central value and the statistical uncertainty of the double ratio in each centrality bin can be written as:

$$\langle x \rangle \pm V[\langle x \rangle]^{1/2}. \tag{4.2.19}$$

The variance of the sample mean is related to the variance of the sample as

$$V[\langle x \rangle] = \frac{\sum_{i=1}^{k} n_i^2}{\left[\sum_{i=1}^{k} n_i\right]^2} V[x]. \tag{4.2.20}$$

To evenly distribute the run numbers into k groups with a similar total number of events, a straightforward bin-packing algorithm is written [159]. This automated approach ensures that each group has a slight variation, typically a few percent, in the total number of events.

It is worth noting that errors are typically assumed to be symmetrical, but this assumption may not always hold true, especially when considering the ratios of multiple quantities. This implies that even though the errors associated with each individual quantity ($\Delta\gamma$ and v_2) are symmetric, the error of $\Delta\gamma/v_2$ may not be symmetric. This is checked by plotting the distribution of the mean of the double ratio for each subsample within different centrality ranges. Figure 4.6 illustrates distributions for the centrality ranges of 10-15% and 15-20%, serving as an example. Upon observation, it is found that the distributions generally conform well to a normal distribution, except for collisions occurring at the more peripheral centralities, as shown in Fig. 4.7). Consequently, there is no significant concern in treating the statistical uncertainty of the double ratio as symmetric. Note that the error bars in Fig. 4.7 are calculated by filling each bin with the centre value of each subsample, applying the event number as the weight.

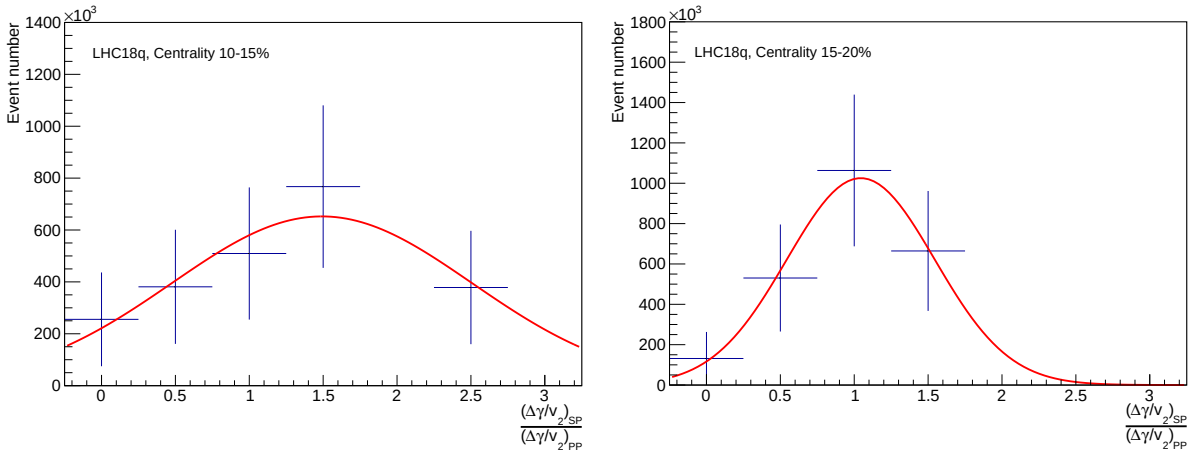

Figure 4.6: *Distribution of the mean of the double ratio for each subsample in centrality range 10-15% and 15-20% from LHC18q data set, respectively.*

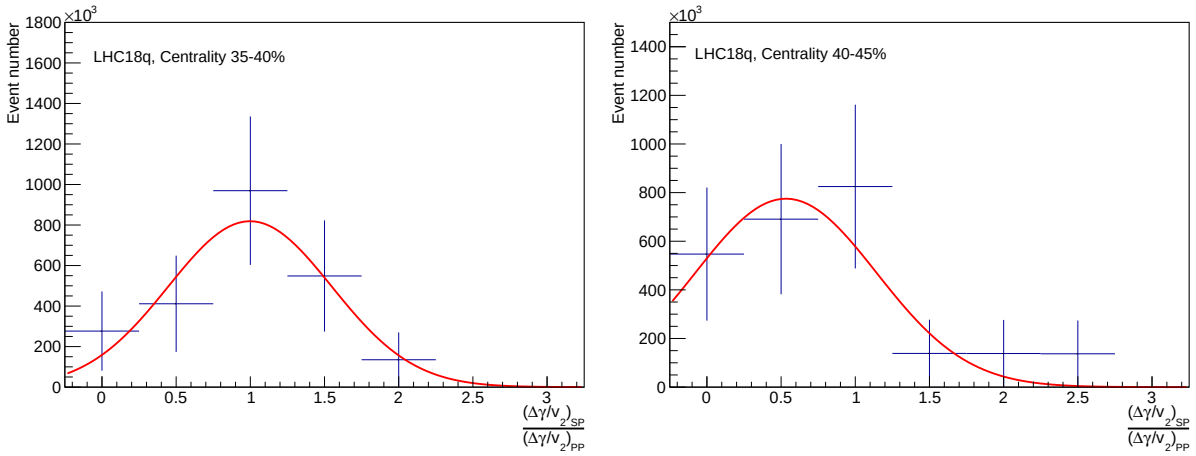

Figure 4.7: *Distribution of the mean of the double ratio for each subsample in centrality range 35-40% and 40-45% from LHC18q data set, respectively.*

4.3 Systematic uncertainties

4.3.1 Systematic uncertainty of the double ratio

The systematic uncertainties (σ_{syst}) of the double ratio have contributions from multiple sources. To account for systematic uncertainties, each potential source undergoes variation of its corresponding parameters (such as track selection criteria, detector calibration parameters, etc.) within a reasonable range. If the difference between these results is determined to be statistically significant using the Barlow ratio estimation [160], it is considered as a source of the systematic uncertainty. In order to evaluate the statistical significance of the systematic variations, we calculate the differences between the results obtained with default cuts and various systematic variations. These differences are then utilised to estimate the Barlow ratio, as defined by:

$$B = \frac{x_{\text{def}} - x_{\text{var}}}{\sqrt{|\sigma^2_{\text{def}} \pm \sigma^2_{\text{var}}|}}, \tag{4.3.1}$$

where x_{def} and x_{var} are the double ratio results obtained with default and varied cuts with σ_{def} and σ_{var} as the corresponding statistical uncertainties. The sign in the denominator is positive when comparing two independent samples, such as comparing results from different runs. Conversely, the sign is negative when comparing a subset of data to a larger sample, for example, when using more stringent or looser track or event selection criteria. In cases where the samples fall between these extremes, a conservative approach is taken. The Barlow ratio essentially tells the number of σ that the difference between two central values deviates from the total statistical uncertainties of two central values. The Barlow ratio is calculated individually for each source within each centrality bin. Then, the total Barlow ratio for each source is calculated as the quadrature sum of the Barlow ratios across all centrality bins normalised by the number of centrality bins:

$$B_{\text{total,each source}} = \sqrt{\sum_{i=1}^{N_{\text{cent bins}}} B_i^2 / N_{\text{cent bins}}}. \tag{4.3.2}$$

As suggested by Barlow[1], if the value of B is less than 2 σ, the deviation is considered insignificant. Between 2 and 4 σ, the source has to be examined and the analyser needs to make a judgement. For deviation above 4 σ, this systematic uncertainty source should be considered. The contributions from different sources are combined in quadrature to estimate the total systematic uncertainty:

$$\sigma_{\text{total syst}} = \sqrt{\sum_i \sigma_{\text{syst,i}}^2} \tag{4.3.3}$$

The list of all possible systematic variations of the parameters along with the default values are given below:

- event selection criteria:
  - pile-up cuts (no pile-up cuts applied)
  - primary vertex z range (-7 to 7 cm)
  - centrality determination (CL1)
  - ALICE dipole magnet polarity (LHC18q and LHC18r have opposite magnetic field polarities)
- track quality variables:
  - the number of minimum TPC clusters required for reconstructed tracks (> 90 TPCnCluster)
  - the maximum percentage of shared clusters between two tracks ($< 20\%$ of TPC clusters are shared)
- particle charge (using either positive-positive or negative-negative pairs for same-charge correlations)
- reconstruction efficiency (no reconstruction efficiency applied)
- compatibility between kINT7 and kSemiCentral triggers in centrality range 30-50%

[1] See the presentation by Barlow [161].

- V0 calibration (varying binning in recentring histograms)
- ZDC calibration (varying gain equalisation and recentring parameters by corresponding uncertainties of best-fit parameters)
- ZDC cross correlation (explained in details later)

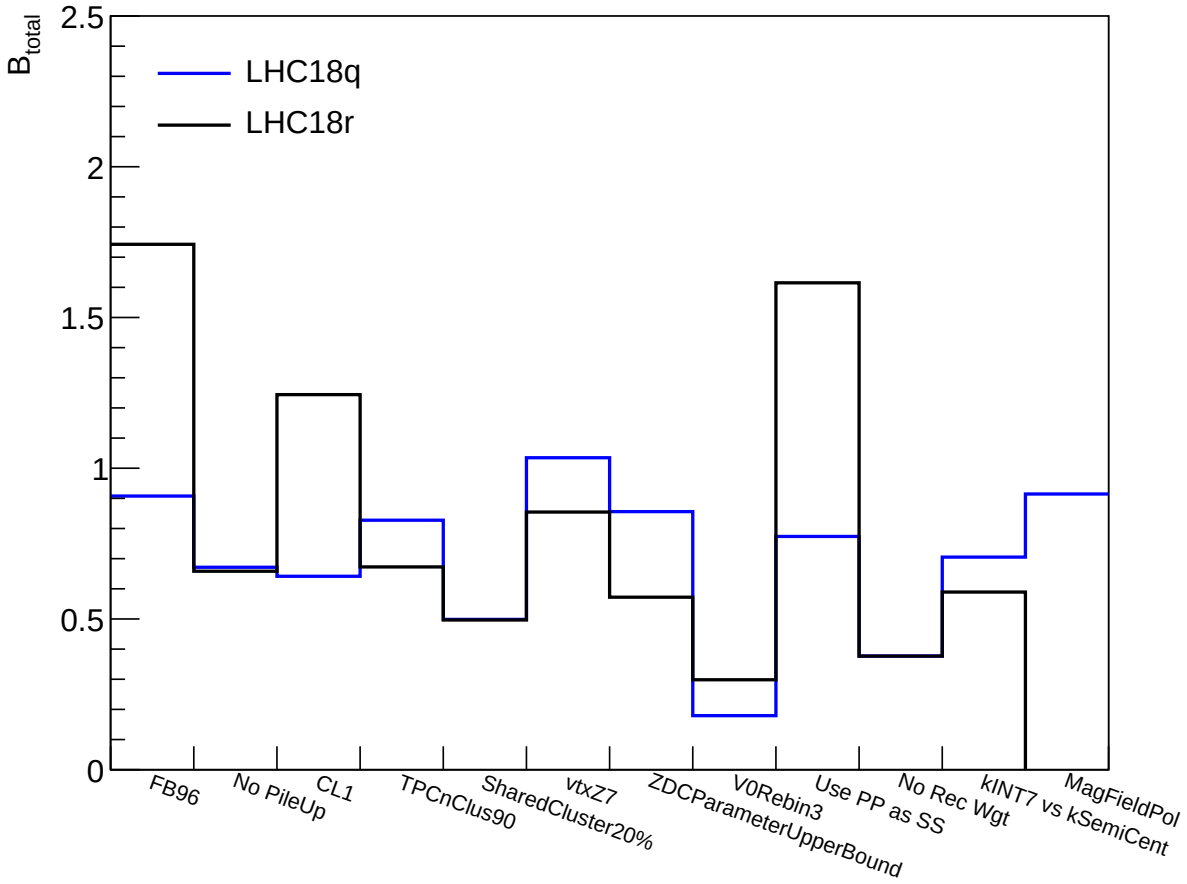

Figure 4.8: *The magnitude of B_{total} for each systematic variation affecting the value of $(\Delta\gamma/v_2)_{ZDC}/(\Delta\gamma/v_2)_{V0C}$, except for the ZDC cross-correlation, in the LHC18q (blue) and LHC18r (black) dataset. The last bin (magnetic field polarisation) only has a blue line plotted because it is the Barlow ratio calculated using the LHC18r dataset as the variation from the LHC18q dataset.*

In all of these variations, except for the ZDC cross correlation, the denominator in Eq. 4.3.2 is chosen to have a negative sign. This choice is based on the fact that the data set remains the same for each variation. Ideally, one would vary the parameter gradually, such as changing the primary vertex z range gradually from -5 to 5 cm to -12 to 12 cm. This approach allows for a clear distinction between measurements that change with a trend (indicating correlated errors) and measurements that change without a trend (indicating uncorrelated errors). However, it is not practically feasible to perform such a gradual variation using the ALICE computing grid, as it would require significant computational resources to analyse the large data set repeatedly.

As mentioned previously, the detector used to reconstruct $\Psi_{\rm PP}$ in the double ratio is chosen to be V0C so that we have the ratio in the form of $(\Delta\gamma/v_2)$ZDC$/(\Delta\gamma/v_2)$V0C. The value of

B_{total} for each systematic variation, except for the ZDC cross-correlation, is shown in Fig. 4.8. Specifically, for the Barlow test of kINT7 and kSemiCentral triggers, the centrality range is restricted to 30-50% because the valid centrality range for the kSemiCentral trigger is limited to that specific range. Since the magnitude of B_{total} for every source is below 2 σ, all of the variations pass the Barlow test. Other possible choices of detectors that can be used to reconstruct Ψ_{PP}, including V0A and TPC, have also been calculated. The difference in the double ratio is very small as the participant plane reconstructed by TPC, V0C, and V0A agrees well with each other. The results of the Barlow test for ZDC/V0A and ZDC/TPC are presented in the Appendix 8.3.

ZDC cross correlation

The neutron ZDC has its own systematic uncertainty due to a noticeable correlation that remains between the $\langle XY\rangle$ ($\langle Q_x^{\text{ZNC}} Q_y^{\text{ZNA}}\rangle$) and $\langle YX\rangle$ ($\langle Q_y^{\text{ZNC}} Q_x^{\text{ZNA}}\rangle$) components even after recentring, which affects the values of $\cos\left(n\Psi_{\text{ZNC-ZNA}}\right)$ and $\sin\left(n\Psi_{\text{ZNC-ZNA}}\right)$. Unlike other sources of systematic uncertainty, this source does not need a Barlow test, as it is irrelevant to the variation of selections or detector calibrations. To evaluate the potential impact on $\Delta\gamma_{\text{SP}}$ and $v_{2,\text{SP}}$, the idea used in [156] is adopted, where the values of these observables are scaled by a fraction to estimate any residual effects:

$$\sigma_{\text{syst}}(\Delta\gamma_{\text{SP}}) = \Delta\gamma_{\text{SP}} \times \sqrt{\frac{\langle Q_x^{\text{ZNC}} Q_y^{\text{ZNA}}\rangle\langle Q_y^{\text{ZNC}} Q_x^{\text{ZNA}}\rangle}{\langle Q_x^{\text{ZNC}} Q_x^{\text{ZNA}}\rangle\langle Q_y^{\text{ZNC}} Q_y^{\text{ZNA}}\rangle}} \tag{4.3.4}$$

and

$$\sigma_{\text{syst}}(v_{2,\text{SP}}) = v_{2,\text{SP}} \times \sqrt{\frac{\langle Q_x^{\text{ZNC}} Q_y^{\text{ZNA}}\rangle\langle Q_y^{\text{ZNC}} Q_x^{\text{ZNA}}\rangle}{\langle Q_x^{\text{ZNC}} Q_x^{\text{ZNA}}\rangle\langle Q_y^{\text{ZNC}} Q_y^{\text{ZNA}}\rangle}}. \tag{4.3.5}$$

This fraction assumes that any parasitic correlations responsible for the nonzero correlations $\langle XY\rangle$ and $\langle YX\rangle$ could potentially affect the correlations in $\langle XX\rangle$ ($\langle Q_x^{\text{ZNC}} Q_x^{\text{ZNA}}\rangle$) and $\langle YY\rangle$ ($\langle Q_y^{\text{ZNC}} Q_y^{\text{ZNA}}\rangle$). The magnitude of this effect can be estimated by considering the ratio of $\langle XY\rangle\langle YX\rangle$ to $\langle XX\rangle\langle YY\rangle$ and taking the geometric mean. The same fraction can be applied to both $\Delta\gamma_{\text{SP}}$ and $v_{2,\text{SP}}$ because, after expanding without considering non-isotropic terms, the same components $\langle\cos\left(2\Psi_{2,\text{SP}}\right)\rangle$ and $\langle\sin\left(2\Psi_{2,\text{SP}}\right)\rangle$ can be factored out, similar to $v_{2,\text{SP}}$:

$$\begin{aligned}\Delta\gamma_{\text{SP}} &= \langle\cos\left(\varphi_\alpha + \varphi_\beta - 2\Psi_{2,\text{SP}}\right)_{\text{OS}}\rangle - \langle\cos\left(\varphi_\alpha + \varphi_\beta - 2\Psi_{2,\text{SP}}\right)_{\text{SS}}\rangle \\ &= \left[\langle\cos\left(\varphi_\alpha + \varphi_\beta\right)\rangle_{\text{OS}} - \langle\cos\left(\varphi_\alpha + \varphi_\beta\right)\rangle_{\text{SS}}\right]\langle\cos\left(2\Psi_{2,\text{SP}}\right)\rangle \\ &\quad + \left[\langle\sin\left(\varphi_\alpha + \varphi_\beta\right)\rangle_{\text{OS}} - \langle\sin\left(\varphi_\alpha + \varphi_\beta\right)\rangle_{\text{SS}}\right]\langle\sin\left(2\Psi_{2,\text{SP}}\right)\rangle\end{aligned} \tag{4.3.6}$$

Since the ZDC cross-correlation contributes to both $\Delta\gamma_{\text{SP}}$ and $v_{2,\text{SP}}$ in the same way, these two errors are considered to be fully correlated when taking the ratio $\Delta\gamma_{\text{SP}}/v_{2,\text{SP}}$. The following equation is used to deal with the completely correlated error of a ratio:

$$f = \frac{E_A}{E_B}, \quad \sigma_f = \frac{E_A}{E_B}\sqrt{\frac{\sigma_A^2}{E_A^2} + \frac{\sigma_B^2}{E_B^2} - \frac{2}{E_A E_B}\sigma_A^2}. \tag{4.3.7}$$

As previously shown in Figure 3.12, the correlations $\langle XX\rangle$ and $\langle YY\rangle$ for the LHC18q data set are more negative than those for the LHC18r data set in the centrality range of 0-50%. Consequently, the ZDC cross-correlation fraction is larger in the LHC18q data set. It is worth noting

that this estimation has a "drawback" (particularly in our case): the $\langle XX \rangle$ and $\langle YY \rangle$ correlations approach zero at a centrality around 50%, causing the fraction to diverge. Eqs. 4.3.4 and 4.3.5 do make sense as the $\langle XX \rangle$ and $\langle YY \rangle$ correlations being zero means that the ZDC detector has no resolution at all, which implies that the systematic uncertainty should be very large. Additionally, the mixed event correlation of the neutron ZDC, where Q_a^{ZNC} and Q_b^{ZNA}, $a, b = X$ or Y, are from different events, has been studied, but has a negligible effect.

4.3.2 Systematic uncertainty in the fraction of CME

The fraction of CME, f_{CME}, is calculated from Eq. 4.2.11, which implies that the systematic uncertainty of $a = v_{2,\mathrm{SP}}/v_{2,\mathrm{PP}}$ in the denominator must also be taken into account for the final result. As previously assumed in Eq. 4.2.14, the ratio a is approximated as $a = v_{2,\mathrm{SP}}(2.76\mathrm{TeV})/v_2\{2\}(\Delta\eta > 1, 2.76\mathrm{TeV})$. The statistical and systematic uncertainties in both v_2 values are provided in publications and are used to represent our ignorance of the value of a. The fully uncorrelated error propagation is then performed to obtain the final error in f_{CME}. It is worth discussing the error propagation further. In our case, the value of a in the denominator is obtained from the LHC10h data set at a different energy. Therefore, the systematic uncertainties can be treated as uncorrelated with the double ratio in the numerator. However, if a can be measured with the LHC18q or LHC18r data set, the error propagation becomes more complicated because it may be naive to argue that the systematic uncertainty of A/a in the numerator and a in the denominator are fully correlated and estimating their covariance is challenging.

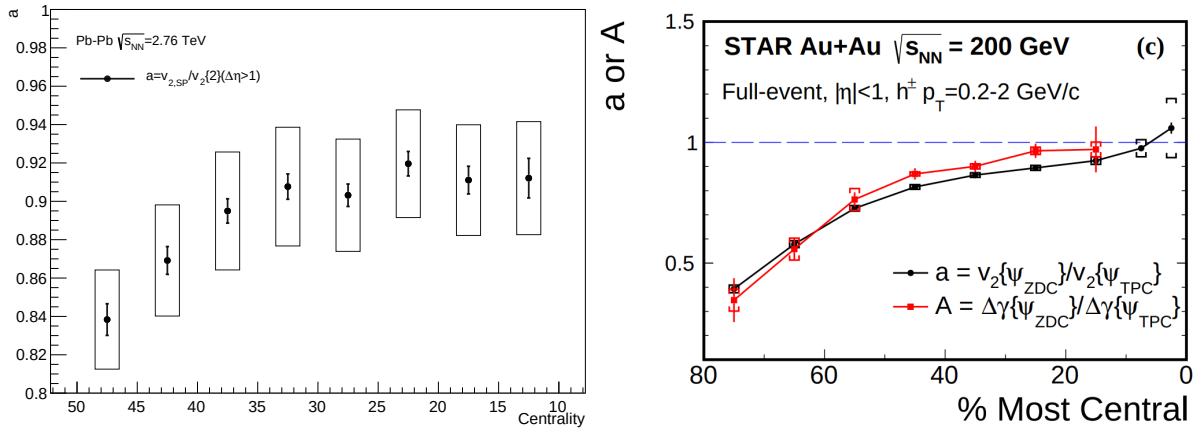

Figure 4.9: *In the left panel, $a = v_{2,SP}/v_{2,PP}$ obtained from published $v_{2,SP}$ and $v_{2,PP}$ in Pb-Pb collisions at $\sqrt{s_{NN}} = 2.76$ TeV is plotted with respect to the centrality. Both statistical and systematic uncertainties are calculated using standard error propagation, represented by a solid line and a hollow box, respectively. The total error for a will be calculated as $\sigma_{tot} = \sqrt{\sigma^2_{stat.} + \sigma^2_{syst.}}$. In the right panel, the same a from Au-Au collisions at $\sqrt{s_{NN}} = 200$ GeV measured by the STAR collaboration is shown [103].*

The left panel of Fig. 4.9 shows the magnitude of a as a function of centrality with the error bars indicating the combined statistical and systematic uncertainties. It exhibits a trend that agrees with the a measured by the STAR collaboration in Au-Au collisions [103], as shown in the right subfigure. It is also noticed that the final extracted fraction of CME is not significantly affected by the error of a as the numerator $(A/a - 1)$ is much smaller than 1 and the denominator

$(1/a^2 - 1)$. This can be clearly seen from the error propagation for a simple ratio A/B,

$$\sigma(A/B) = \sqrt{\left(\frac{\sigma(A)}{B}\right)^2 + \left(\frac{A}{B^2}\sigma(B)\right)^2}. \tag{4.3.8}$$

In our case, $1/B \gg A/B^2$ so that the first term in the square root dominates.

4.4 Results

4.4.1 Measurements of γ/v_2

For the completeness of the results, the measurements of γ/v_2 are shown firstly. The V0C detector has been chosen to reconstruct Ψ_{PP} and to combine the ZNC and ZNA detectors to reconstruct Ψ_{SP}. Fig. 4.10 shows the centrality dependence of $\gamma_{\alpha\beta}(\Psi_{\mathrm{V0C}})/v_2(\Psi_{\mathrm{V0C}})$ and $\gamma_{\alpha\beta}(\Psi_{\mathrm{ZNC\text{-}ZNA}})/v_2(\Psi_{\mathrm{ZNC\text{-}ZNA}})$, where pairs of particles in $\gamma_{\alpha\beta}$ are either of the same charge or opposite charge, for the LHC18q and LHC18r data sets, respectively. Note that only statistical uncertainties are shown here because systematic uncertainties are estimated directly in the double ratio to avoid error propagation. Estimating the correlation between the errors in $\gamma_{\alpha\beta}(\Psi_{\mathrm{V0C}})/v_2(\Psi_{\mathrm{V0C}})$ and $\gamma_{\alpha\beta}(\Psi_{\mathrm{ZNC\text{-}ZNA}})/v_2(\Psi_{\mathrm{ZNC\text{-}ZNA}})$ is very difficult, as naive error propagation assuming uncorrelated errors tends to result in overestimation.

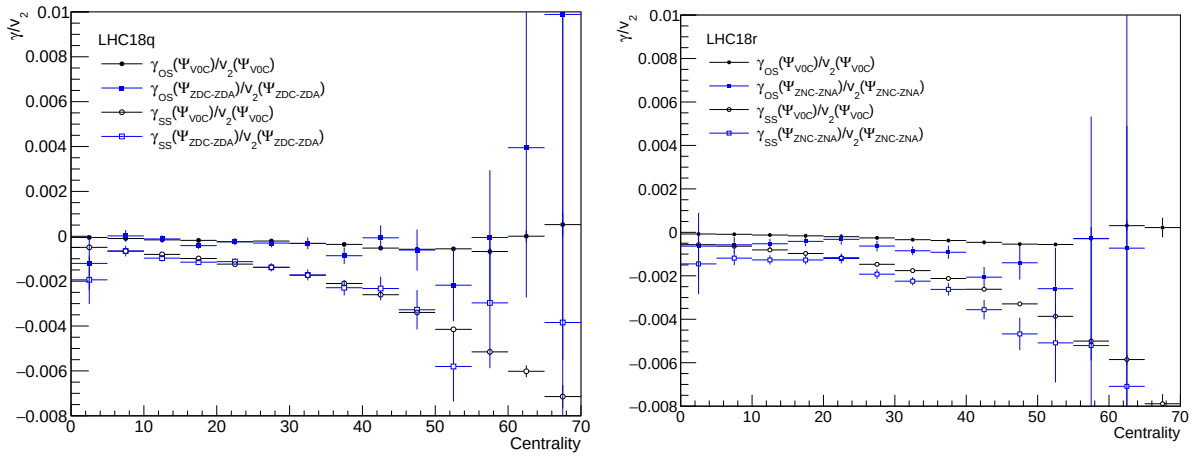

Figure 4.10: *Centrality dependence of $\gamma_{\alpha\beta}(\Psi_{V0C})/v_2(\Psi_{V0C})$ (black) and $\gamma_{\alpha\beta}(\Psi_{ZNC\text{-}ZNA})/v_2(\Psi_{ZNC\text{-}ZNA})$ (blue), where pairs of particles in $\gamma_{\alpha\beta}$ are either the same charge or opposite charge, for the LHC18q (left) and LHC18r (right) data sets.*

4.4.2 Double ratio

The result of the double ratio for the LHC18q and LHC18r data sets is shown in Fig. 4.12. Clearly, the statistical uncertainties in LHC18r are much larger than in LHC18q, which is not due to the number of events but mainly arises from the significantly worse correlation between $\Psi_{\mathrm{ZNC\text{-}ZNA}}$ and Ψ_{V0C}, as previously demonstrated in Fig. 3.15. The systematic uncertainties in LHC18r are much smaller than in LHC18q, originating from the fact that the ZDC cross-correlation fraction is much smaller in the LHC18r data set. It should be noted that the data points in the centrality range of 10-30% are measured with the kINT7 trigger, while those in

the 30-50% centrality range are measured with the kSemiCentral trigger. As shown in Fig. 3.1, the number of events recorded with the kSemiCentral trigger is around 2.8 and 4.7 times higher than that recorded with the kINT7 trigger for the LHC18q and LHC18r data sets, respectively. It has been verified by comparing kINT7 and kSemiCentral results in the 30-50% centrality that the statistical uncertainties of the double ratio data points decrease approximately as $1/\sqrt{N}$, as shown in Fig. 4.11.

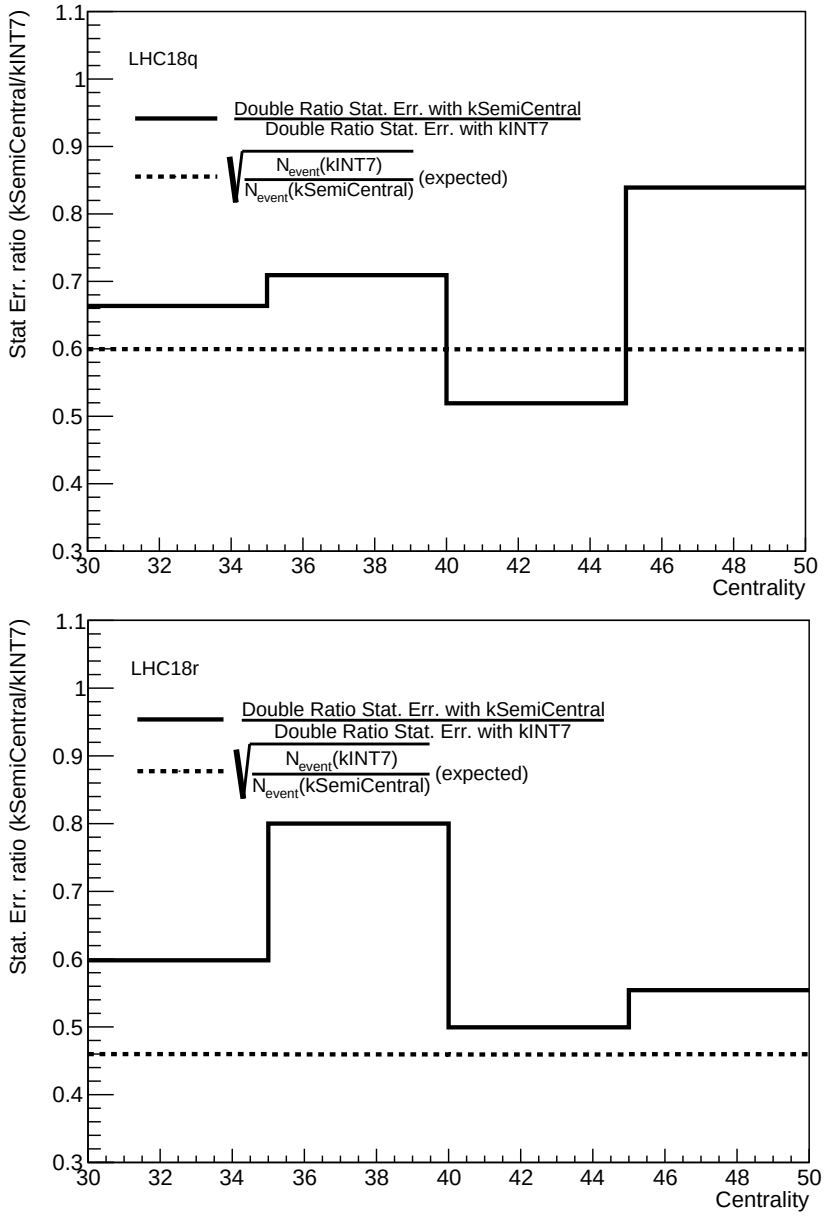

Figure 4.11: *Comparison of the reduction in statistical uncertainties for the double ratio data points using the kSemiCentral trigger with the expected reduction based on* $1/\sqrt{N}$ *for LHC18q (upper panel) and LHC18r (lower panel), respectively.*

A constant line is fitted to the double ratio data points in Fig. 4.12 with only statistical uncertainties considered at this moment in the centrality range of 10-50%, and the results of the fit for the LHC18q and LHC18r data sets are summarised in Table 4.1 below:

Data set	Double ratio (ZDC/V0C)	χ^2	NDf
LHC18q	0.990 ± 0.030	4.58	7
LHC18r	1.000 ± 0.069	3.76	7

Table 4.1: *Summary of the results of the constant line fit to the double ratio data points from LHC18q and LHC18r data sets.*

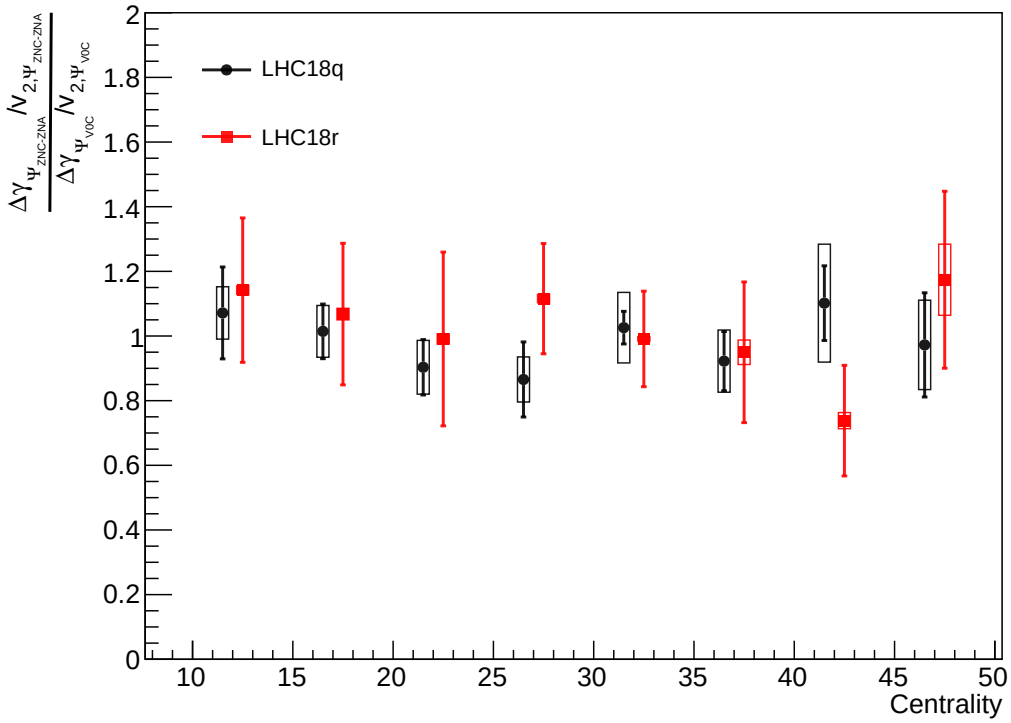

Figure 4.12: *The double ratio of the LHC18q and LHC18r data sets. The blue line represents the baseline scenario (double ratio equalling 1) with zero CME signal.*

The participant plane reconstructed using V0A and TPC has also been studied, and the results of the double ratio are consistent with those obtained using the V0C detector. In Fig. 4.13, the double ratio of ZDC/V0C and ZDC/V0A for the LHC18q data set is shown as an example.

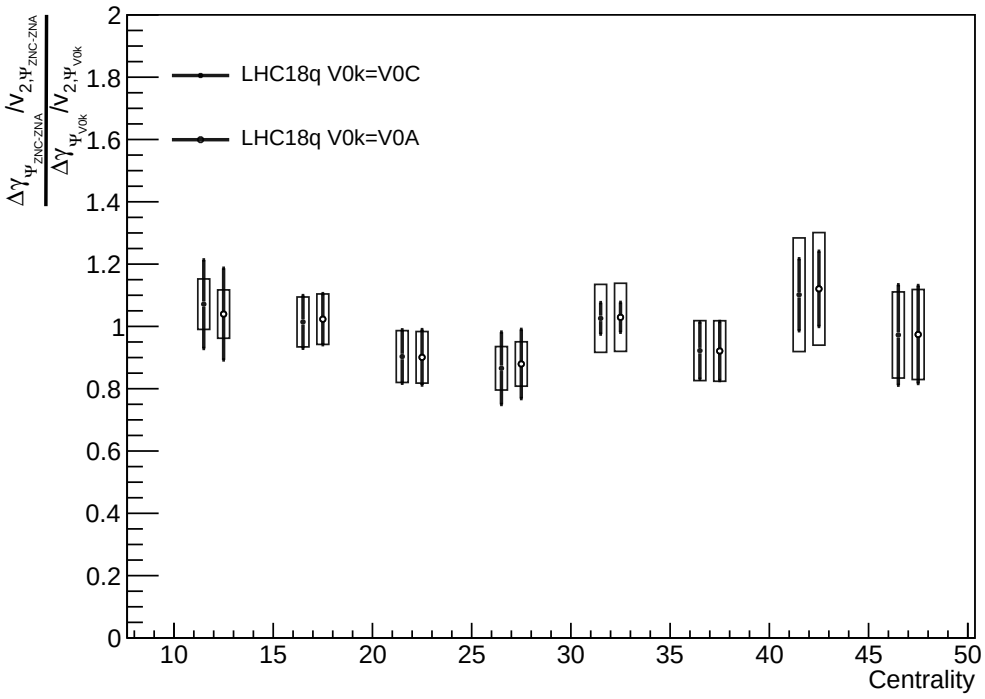

Figure 4.13: *Comparison of the double ratio of ZDC/V0C and ZDC/V0A for the LHC18q data set.*

4.4.3 Constraint on the fraction of CME

The fraction of CME in the $\Delta\gamma$ correlator measured with respect to the participant plane is determined through Eq. 4.2.11. The total error ($\sqrt{\sigma^2_{\text{stat.}} + \sigma^2_{\text{sys.}}}$) in the numerator (double ratio) and the denominator ($v_{2,\text{SP}}/v_{2,\text{PP}}$) are propagated as uncorrelated errors to f_{CME}. Fig. 4.14 shows the extracted f_{CME} as a function of centrality from LHC18q and LHC18r data sets, respectively, where error bars in this figure represent the combined statistical and systematic uncertainties.

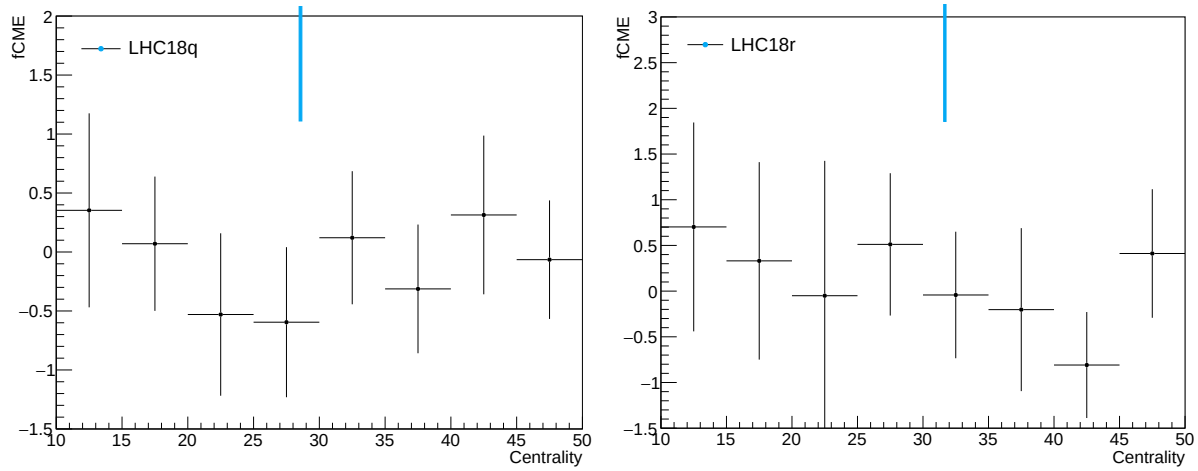

Figure 4.14: *Extracted f_{CME} as a function of centrality from LHC18q (left) and LHC18r (right) data sets. The error bars in this plot represent the total error $\sqrt{\sigma^2_{stat.} + \sigma^2_{sys.}}$. The blue line at $f_{CME} = 0$ represents the zero CME signal scenario.*

A constant line is fitted to f_{CME} in the centrality range of 10-50%, and the results of the fit for the LHC18q and LHC18r data sets are summarised in Table 4.2 below:

Data set	f_{CME}	χ^2	NDf
LHC18q	-0.096 ± 0.214	2.08	7
LHC18r	-0.023 ± 0.288	3.24	7

Table 4.2: *Summary of the results of the constant line fit to f_{CME} in the LHC18q and LHC18r data sets.*

At a 95% confidence level (CL), the limit of f_{CME} is less than 33.2% and 55.3% for the LHC18q and LHC18r data sets, respectively. Clearly, the LHC18q data set provides a tighter limit on f_{CME}. Attempts have been made to combine the double ratio results from both data sets. When combining measurements $(p_1, p_2, ...)$ from N data sets, the combined central value ($\bar{P}$) is determined by weighting each central value by the inverse of the squared statistical uncertainties of the corresponding measurement, followed by normalising as follows:

$$\bar{P} = \frac{\sum_{i=1}^{N} p_i/\sigma^2_{p_i,\text{stat.}}}{\sum_{i=1}^{N} 1/\sigma^2_{p_i,\text{stat.}}}. \tag{4.4.1}$$

The combined statistical uncertainties of $\bar{P}$ are given by

$$\sigma_{\bar{P},\text{stat.}} = \frac{\prod_{i=1}^{N} \sigma_{p_i,\text{stat.}}}{\sqrt{\sum_{i=1}^{N} \sigma^2_{p_i,\text{stat.}}}}. \tag{4.4.2}$$

The systematic uncertainty cannot be combined in any form of error propagation as it is only introduced by repeatable processes inherent to the system. A conservative approach is to adopt whichever systematic uncertainties are the largest among multiple data sets. In this case, the systematic uncertainties from the LHC18q data set should be adopted as the "combined" systematic uncertainty. In Fig. 4.15, the extracted f_{CME} as a function of centrality from the combination of both the LHC18q and LHC18r data sets is shown. The fit with a constant line leads to $f_{\text{CME}} = -0.054 \pm 0.200$, with $\chi^2/NDF = 1.45/7 = 0.21$. No significant improvement is noticed in the combined result, and the reduction in χ^2 suggests that the errors, particularly the inheritance of systematic uncertainties from the LHC18q data set, could be an overestimation and work against the combined result. Therefore, based on the facts that the correlation between $\Psi_{\text{ZNC-ZNA}}$ and Ψ_{V0C} is much worse in the LHC18r data set and the combined results have to inherit larger systematic uncertainties from the LHC18q data set, the limit on f_{CME} reported as the final result only uses the LHC18q data set.

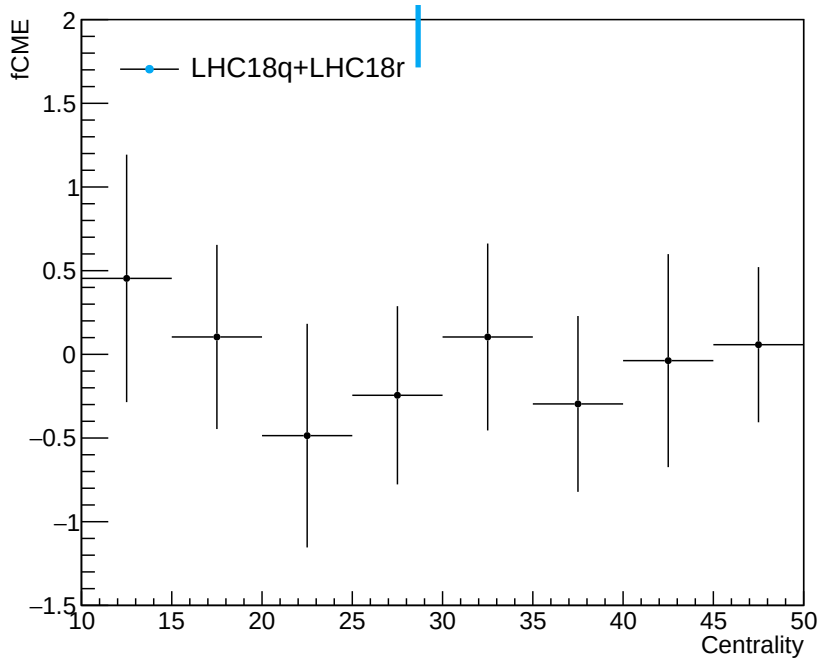

Figure 4.15: *Extracted f_{CME} as a function of centrality from the combination of LHC18q and LHC18r data sets. The error bars in this plot represent the total error $\sqrt{\sigma^2_{stat.} + \sigma^2_{sys.}}$. The blue line at $f_{CME} = 0$ represents the zero CME signal scenario.*

4.4.4 Discussion

The limit for the fraction of CME measured using 3-particle charge-dependent azimuthal correlators, relative to the participant and spectator flow planes, is determined to be 33.2% at a 95% CL. This result is consistent with the previously shown limits in Fig. 1.12. However, due to the limitation of the ZDC, this limit does not provide a tighter constraint compared to other published results. This analysis relies on a key assumption that the flow background is proportional to the final-state hadron v_2 [105]. By using the V0C detector to reconstruct the participant plane, the non-flow effects, which could impose a positive effect on f_{CME} due to an increase of $v_2(\Psi_{\mathrm{PP}})$ from two-particle correlations and a negative effect on f_{CME} due to an increase of $\Delta\gamma(\Psi_{\mathrm{PP}})$ from three-particle (e.g., dijet) correlations, are suppressed. It should be noted that this 95% CL limit is directly determined by adding the central value with two standard deviations. Since the central value of the line of best fit for f_{CME} is negative, which is nonphysical, it is not strictly rigorous in the context of Bayesian statistics. In principle, one should determine the posterior probability that characterises the epistemic uncertainty concerning f_{CME}, given a set of observed data. In other words, a prior reflecting the degree of belief in f_{CME} driven by theoretical prediction is needed. In terms of Bayesian probability for (particle) physics (as discussed in [162]), it can be written as

$$P(\text{parameter}|\text{data}) \propto P(\text{data}|\text{parameter}) \cdot P(\text{parameter}), \tag{4.4.3}$$

where $P(\text{data}|\text{parameter})$ is the likelihood, denoting the probability of observing the data points given this specific parameter of f_{CME}, $P(\text{parameter})$ represents the degree of belief of f_{CME} (the prior probability), and $P(\text{parameter}|\text{data})$ is the probability of f_{CME} given the observed data (the posterior probability). Despite theoretical progress, it is not yet possible to provide independent quantitative theoretical predictions on the magnitude of CME in heavy ion collisions due to the following limitations:

- the sphaleron transition rate depending on the magnitude of the energy barrier separating different QCD vacua and the ambient thermal energy to excite sphalerons;
- uncertainty in the magnitude and the duration of the B-field created by spectators;
- limited understanding of background sources, e.g. local charge conservation.

Therefore, there is no prior provided from the pure theory side except for a flat prior that f_{CME} should be in the range of 0 to 100%.

A flat prior is not a good representation of our knowledge of f_{CME} as a large CME signal would enable a statistically significant measurement by current experimental searches. In particular, it is anticipated that a significance of 3 standard deviations would arise if the CME fraction in isobar (Zr-Zr and Ru-Ru) collisions at RHIC is 10% [163, 164]. Nevertheless, no evidence of the CME has been detected, indicating that the CME fraction in isobar collisions is considerably smaller than 10%. The recent study, combining insights from theoretical simulations based on the event-by-event anomalous-viscous fluid dynamics (EBE-AVFD) framework and the result of the isobar experiment, concludes that the $\Delta\gamma$ correlation measurements are consistent with a finite CME signal contribution in Ru-Ru of $6.8 \pm 2.6\%$ [165]. As suggested in [166], the CME signal in Au-Au collisions at RHIC is estimated to be approximately doubled. This increase is attributed to a stronger magnetic field under the assumption that the QCD vacuum transition probability and axial charge per entropy density are independent of collision systems. In Pb-Pb collisions at LHC energies, the current published limit on f_{CME} ranges from 18-33%. It has been modelled that the initial magnetic field exhibits a much stronger peak magnitude compared to RHIC energies, but it also decreases more rapidly, possibly even vanishing before the formation of the QGP [65, 67]. In the absence of any electric conductivity in the QGP, by a time of 0.1 fm/c, the remaining magnetic field at LHC energies is typically lower than that at RHIC energies by two orders of magnitude. Consequently, one can expect a smaller Chiral Magnetic Effect (CME) at LHC energies compared to RHIC energies. In the absence of any electric conductivity in the QGP, by a time of 0.1 fm/c, the remaining magnetic field at LHC energies is typically lower than that at RHIC energies by two orders of magnitude. Consequently, the CME signal at LHC energies is expected to be smaller compared to RHIC energies.

It is possible to derive a model-dependent prior for f_{CME} using the EBE-AVFD framework. However, I will only describe the procedure instead of conducting the detailed study, as it would not yield significantly more insights beyond providing a slightly lower model-dependent limit. The key point is to use the EBE-AVFD framework to extract the optimum values of the percentage of axial charge per entropy (n_5/s) and the background using the EBE-AVFD framework that provides a quantitative description of the centrality dependence of the experimental measurements. In Chapter 5, the systematic study of such extraction for both Pb-Pb and Xe-Xe collisions will be presented. The obtained results can then be translated to the prior on f_{CME} by simulating a sample with zero signal ($n_5/s = 0$) but the same background input values in order to calculate the background only $\Delta\gamma$ (denoted as $\Delta\gamma_{\text{bkg only}}$). A proxy estimator for the prior on

$$f_{\text{CME}} = 1 - \frac{\Delta\gamma_{\text{bkg only}}}{\Delta\gamma}. \tag{4.4.4}$$

Finally, it is clear that this measurement is dominated by the systematic uncertainty of the ZDCs. According to the upgrade strategy of the ZDCs, only the readout system will be updated in Run 3 to accommodate the tenfold increase in luminosity delivered by the LHC during heavy ion collisions, as well as the continuous acquisition strategy being adopted by ALICE [167].

Without a significant improvement in the performance of ZDCs (e.g. finer segmentation) for reconstructing the spectator plane, an enhancement in statistics will unlikely lead to a substantially lower limit or a potential discovery of the CME signal using the SP/PP method in Run 3. Therefore, there is a strong need to upgrade the current ZDCs in ALICE. The decrease in the error bars in $f_{\rm CME}$ not only benefits the significance of the final result but also helps to study the possible centrality dependence of $f_{\rm CME}$. As discussed in [151], the $\Delta\gamma$ correlator can be decomposed into two independent sources: a linear dependence on v_2 and a quadratic dependence on

$$\Delta\gamma = \kappa f v_2 - h\langle (e\mathbf{B})^2 \cos\left[2(\Psi_B - \Psi_{2,\rm EP}\right]\rangle, \tag{4.4.5}$$

where $f = F_{\rm OS} - F_{\rm SS}$ is the flow-driven contribution, with $F_{\rm OS}$ and $F_{\rm SS}$ representing the v_2-related backgrounds in $\gamma_{\rm OS}$ and $\gamma_{\rm SS}$, respectively, and κ is a factor unimportant for the discussion here. The CME signal primarily stems from $\mathbf{B}^2$, which should increase with centrality, as demonstrated in Figs. 5.1 and 5.13. Nevertheless, the magnitude of $f_{\rm CME}$ is also inversely influenced by the relative size of the flow-driven backgrounds, which could potentially become the dominant factor. A definitive assessment of the centrality dependence of $f_{\rm CME}$ by future measurements would be valuable in comprehending the interplay between the CME signal and the background effect.

Chapter 5

Studying Pb-Pb and Xe-Xe measurements with AVFD

In this section, the study that leads to our phenomenology paper [168] and the model interpolation of the CME measurements in Xe-Xe collisions [6] will be presented. Some parts of the text will have significant overlap with these two publications. We follow a different approach to extract the CME signal by performing a systematic study of the correlators used in CME searches for Pb–Pb and Xe–Xe collisions at $\sqrt{s_{\rm NN}} = 5.02$ TeV (for Pb ions) [90, 169] and at $\sqrt{s_{\rm NN}} = 5.44$ TeV (for Xe ions) [92] with the Anomalous-Viscous Fluid Dynamics (AVFD) framework [170–172]. The goal of this study is to extract the relevant values that govern the CME signal and the background in the AVFD model that will allow for a quantitative description of the centrality dependence of the charge-dependent correlations measured in various colliding systems and energies at the LHC. In Sec. 5.1, the AVFD framework will be briefly introduced together with the key parameters used to control the CME signal and the background. Then, the model calibration to reproduce the transverse momentum spectra and v_2 and the parametrization of the key parameters will be presented. The final results of the extracted CME signal (axial charge density) and the background parameter will be presented in Sec. 5.3, followed by a discussion on the results in these two papers: the extracted CME signal from AVFD and the fraction of CME in the $\Delta\gamma$ correlator extracted by collaborators using the two-component method.

5.1 AVFD framework

5.1.1 Introduction

The AVFD framework is a state-of-the-art model that describes the fluctuating initial states of the collision using a Glauber prescription (superMC generator [173]), and accounts for the development of the early-stage electromagnetic fields as well as for the propagation of anomalous fermion currents. The calculation of the early-stage electromagnetic field at the initial time ($t = 0$) takes into account the contribution from all protons in the two incoming nuclei, irrespective of whether they participate in binary collisions or not:

$$B(x, y, 0) = \sum_i B_{\rm t}(x - x_i, y - y_i, 0 - z_i) + \sum_j B_{\rm p}(x - x_j, y - y_j, 0 - z_j), \qquad (5.1.1)$$

where B_t and B_p represent the magnetic field generated by a proton centred at $(x_{i/j}, y_{i/j}, z_{i/j})$ in the two incoming nuclei (conventionally named the target and projectile in nuclear physics), respectively. The electric charge density of a proton is assumed to be Gaussian. With the known speed of the projectile and target based on the collision energy, B_t and B_p can be calculated with ease, allowing the total B field to be computed. Depending on different initial conditions (e.g. the transverse profile of heavy nuclei, deformation parameters), the magnetic field at the initial time is affected. Fig. 5.1 shows the centrality dependence of the average value of the magnetic field perpendicular to the reaction plane ($\mathbf{B}_y$) calculated by the AVFD framework for Pb–Pb and Xe–Xe collisions at $\sqrt{s\mathrm{NN}} = 5.02$ and $\sqrt{s_{\mathrm{NN}}} = 5.44$ TeV, respectively. The increasing trend with respect to centrality is attributed to the fact that in more peripheral collisions, a greater number of (spectator) nucleons do not participate in the collision, resulting in the creation of a larger magnetic field. The values for both systems reach, and for some centralities even exceed, 10^{16} T. In addition, the magnitude of **B** for a given centrality interval in Pb–Pb collisions is larger than the corresponding value in Xe–Xe collisions by a factor that reflects the ratio of the atomic numbers of the two nuclei (82 for Pb and 54 for Xe).

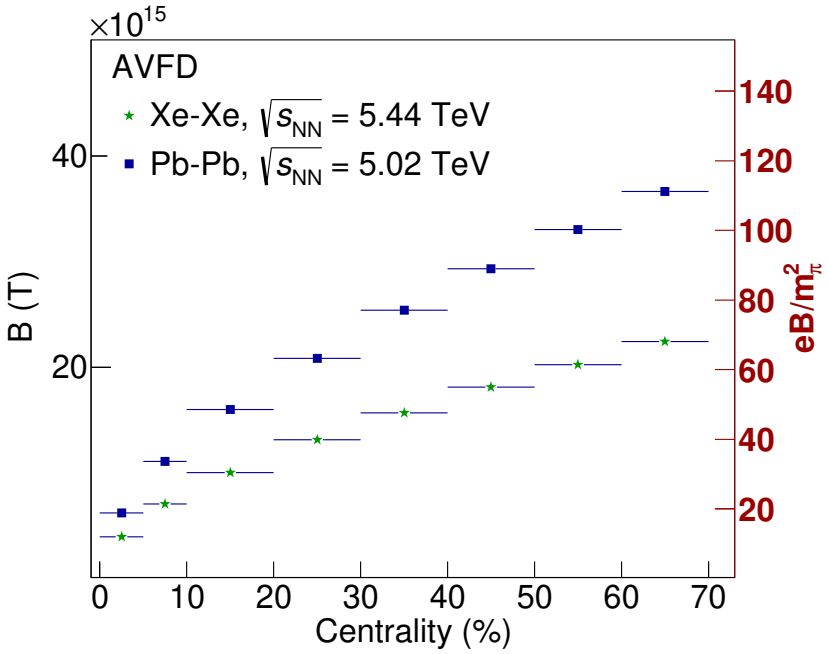

Figure 5.1: *The dependence of the average value of the magnetic field perpendicular to the reaction plane ($\mathbf{B}_y$) on centrality for Pb–Pb and Xe–Xe collisions at $\sqrt{s_{\mathrm{NN}}} = 5.02$ and $\sqrt{s_{\mathrm{NN}}} = 5.44$ TeV, respectively.*

The time evolution of the magnetic field in the QGP is still an open question due to the fact that the properties of the QGP, such as its electrical conductivity and chiral magnetic conductivity, remain largely uncertain. Despite numerous efforts to compute the time dependence of the magnetic field, the results vary significantly among different studies (see e.g. [66, 69, 174, 175]). In AVFD, the default time evolution is given by a modified form of the exponential decay model for the magnetic field equation

$$\mathbf{B} = \frac{B_0}{1 + \tau^2/\tau_B^2}\hat{\mathbf{y}} \tag{5.1.2}$$

where τ_B stands for the lifetime of the magnetic field, with its value setting to 0.2 fm/c as a rather conservative choice for both collision systems[1]. Fig. 5.2 shows the time evolution of the average value of the magnetic field perpendicular to the reaction plane (**B**) for an indicative centrality interval i.e. 40-50% for both Pb–Pb (solid line) and Xe–Xe collisions (dashed line).

The expanding medium is treated via a 2+1 dimensional viscous hydrodynamics (VISH2+1) code [173], which solves the fluid dynamical equations governing the overall bulk fluid evolution with chiral fermion currents (representing the right- and left-handed currents for u and d favours, respectively) as perturbations added on top. This is the most distinctive feature of the AVFD framework, where the chiral fermion currents are driven by the magnetic field, evolving in an asymmetric and opposite manner.

Upon completing the fluid evolution, the QGP undergoes hadronization at a distinct temperature known as the freeze-out temperature T_f. Subsequently, the final hadrons are generated within each fluid cell situated on the freeze-out hyper-surface with a local thermal-equilibrium distribution following the Cooper-Frye freeze-out formula (see Eq. 71 in [173]), which essentially gives the probability of emitting a particle from that fluid cell with a specified momentum. This is taken care of by the ISS module, which finally gives a collection of hadrons on the hyper-surface. Each hadron is characterised by its production time, location (position on the hyper-surface), momentum, flavour type, mass, and quantum numbers.

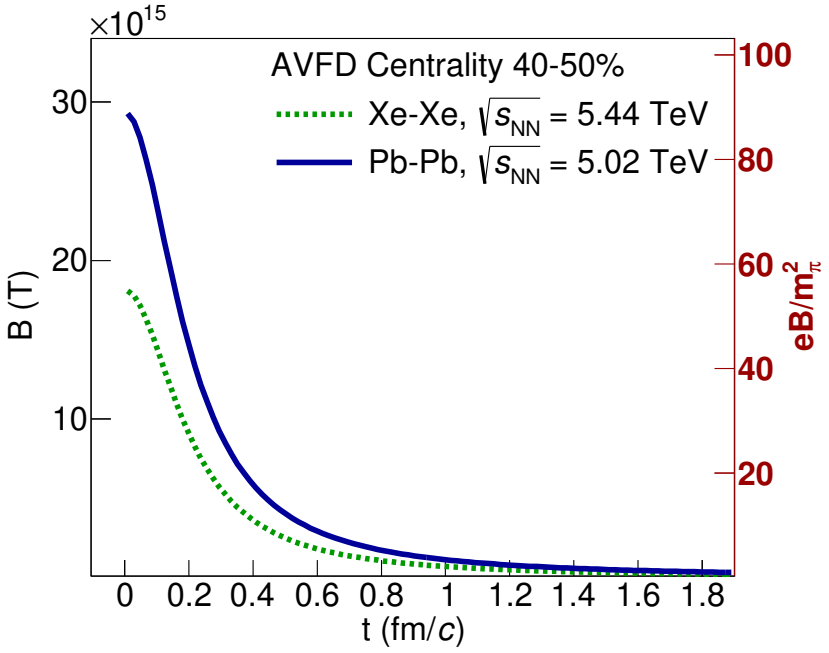

Figure 5.2: *The time evolution of the average value of the magnetic field perpendicular to the reaction plane (**B**) for the 40%-50% centrality interval in Pb–Pb and Xe–Xe collisions at* $\sqrt{s_{\rm NN}} = 5.02$ *and* $\sqrt{s_{\rm NN}} = 5.44$ *TeV, respectively.*

The hadron information is used as an initial condition for the hadron cascade model: Ultra-relativistic Quantum Molecular Dynamics (UrQMD) [176]. The UrQMD model evolves the

[1]This value was decided based on the discussion with Dr. Panos Christakoglou and Dr. Jinfeng Liao. The lifetime should be very short so that it is less than the duration of the pre-equilibrium stage [66].

system's hadrons through a series of binary collisions and 2 − N-body decays to produce the distribution function of all hadrons following the Boltzmann equation. A total of 53 different baryon species and 24 different meson species can be produced in the process of string decays, s-channel collisions, or resonance decays.

5.1.2 Key parameters in AVFD

In the AVFD framework, two key parameters, n_5/s and LCC, are used to control the CME signal and the background, respectively. The former (n_5/s) represents the axial charge density, where n_5 is the amount of axial charge representing the imbalance between left- and right-handed fermions induced in the initial stage of each event, and s represents the entropy density, which, in turn, is related to the temperature and energy density of the system. It has been discussed in [170] that the vector charge density, representing the collective number density of all quark species, including both the right- and left-handed sectors, does not significantly influence the final charge separation. It is expected that the CME current (the final charge separation) should be linearly proportional to the amount of initial axial charge, $J^{\mu}_{\rm CME} = C_A \mu_5 B^{\mu} \propto n_5/s$, and this linear dependence has been verified in the simulation of Au-Au collisions by the AVFD framework, as shown in Fig. 5.3.

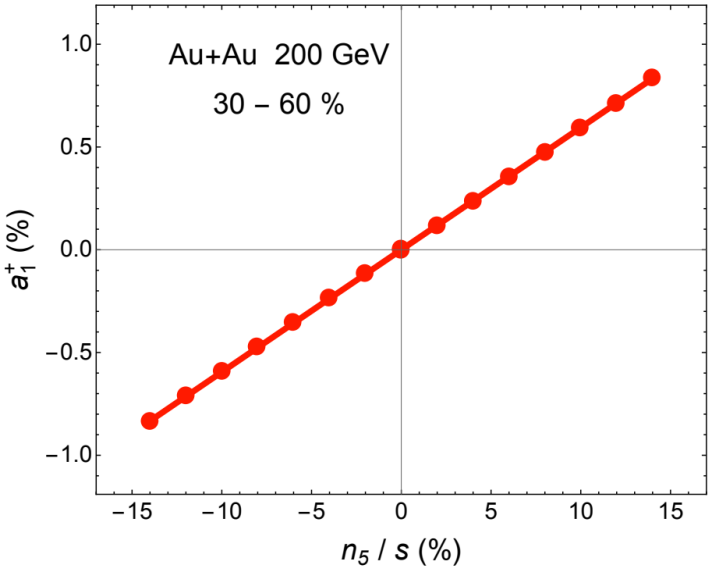

Figure 5.3: *Plot of charge separation (a_1) as a function of the initial axial charge density per flavour. Figure adopted from [170].*

The parameter which controls the background is the percentage of local charge conservation (LCC) within an event. This number can be considered as the amount of positive and negative charged partners emitted from the same fluid element at the freeze-out, relative to the total multiplicity of the event. As mentioned in Sec. 4.1.1, the LCC is the dominant source of the background.

5.2 Model calibration and parametrisation

The goal of this study is to extract the values that control the CME signal and the background in the AVFD model, allowing for a quantitative, simultaneous description of the centrality dependence of the charge-dependent correlations, i.e. $\Delta\delta_1$ and $\Delta\gamma_{1,1}$ measured in Pb-Pb collisions at $\sqrt{s_{\rm NN}} = 5.02$ TeV [90, 169] and in Xe-Xe collisions at $\sqrt{s_{\rm NN}} = 5.44$ TeV [92]. Here, $\Delta\delta_1$ and $\Delta\gamma_{1,1}$ denote the difference of δ_1 and $\gamma_{1,1}$ between opposite- and same-sign pairs. Our goal is to utilise AVFD to parameterise the dependence of $\Delta\delta_1$ and $\Delta\gamma_{1,1}$ at each chosen centrality bin with respect to the axial charge density and the percentage of local charge conservation, respectively. The parametrisation allows us to find the optimum values of n_5/s and LCC to best describe simultaneously the centrality dependence of the charge-dependent correlations, $\Delta\delta$ and $\Delta\gamma$, measured in both Pb-Pb and Xe-Xe collisions.

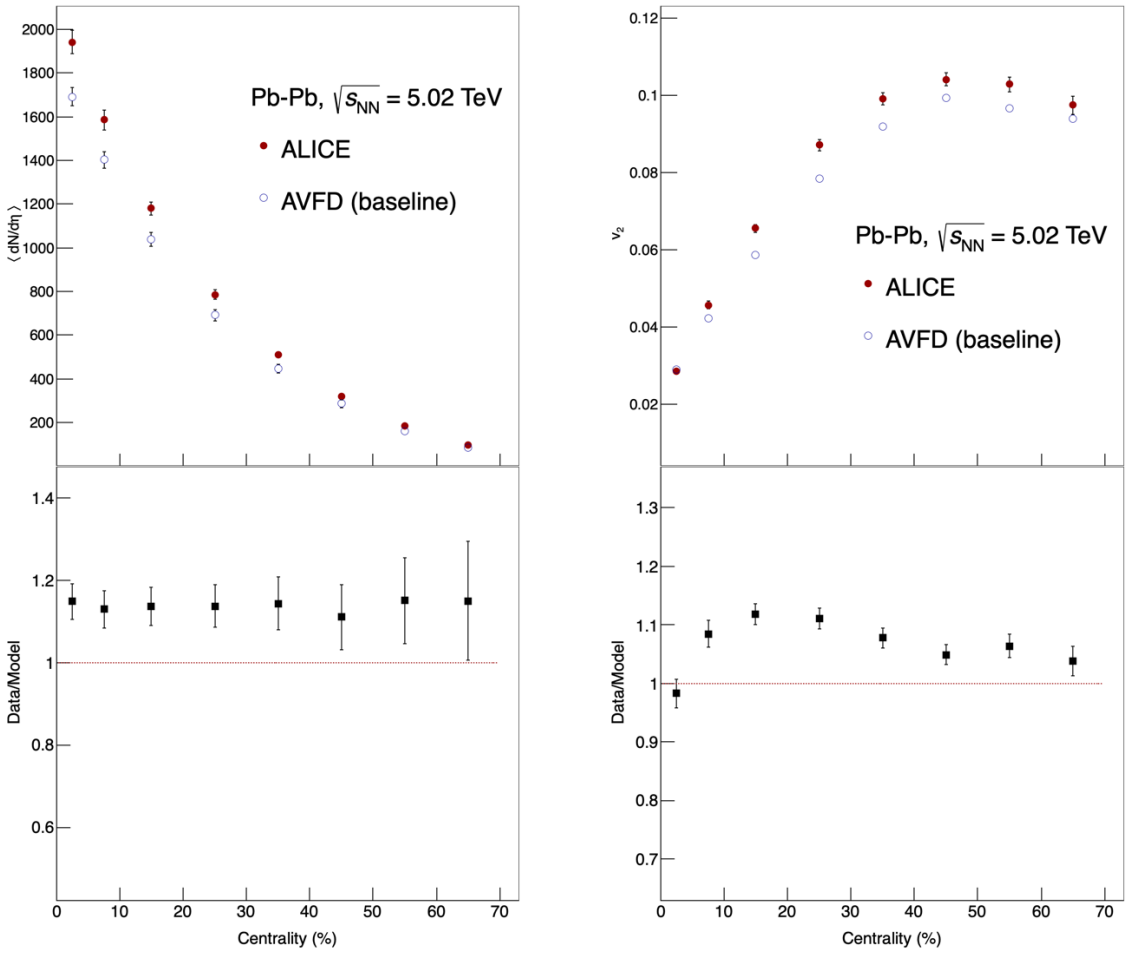

Figure 5.4: *Comparison of the centrality dependence of the charged particle multiplicity density (left) and the centrality dependence of v_2 (right) in Pb-Pb collisions at $\sqrt{s_{NN}} = 5.02$ TeV between the ALICE data (black dots) and the AVFD baseline simulation (hollow blue dots).*

The first step in the whole procedure was to calibrate the model without the inclusion of any CME or LCC effects, in what will be referred to in the rest of the text as "baseline". This involved tuning the input parameters to describe the centrality dependence of bulk measurements, such

as the charged particle multiplicity density $dN/d\eta$ [177–179] and v_2 [180–182] in Pb–Pb and Xe–Xe collisions at LHC energies. Overall, the model was able to describe the experimental measurements within 15%, as shown in Figs. 5.4 and 5.5. Finally, we also checked that the slopes of the transverse momentum (p_T) spectra of pions, kaons, and protons in the baseline sample of AVFD have a similar centrality dependence as reported by ALICE in Refs. [183–185].

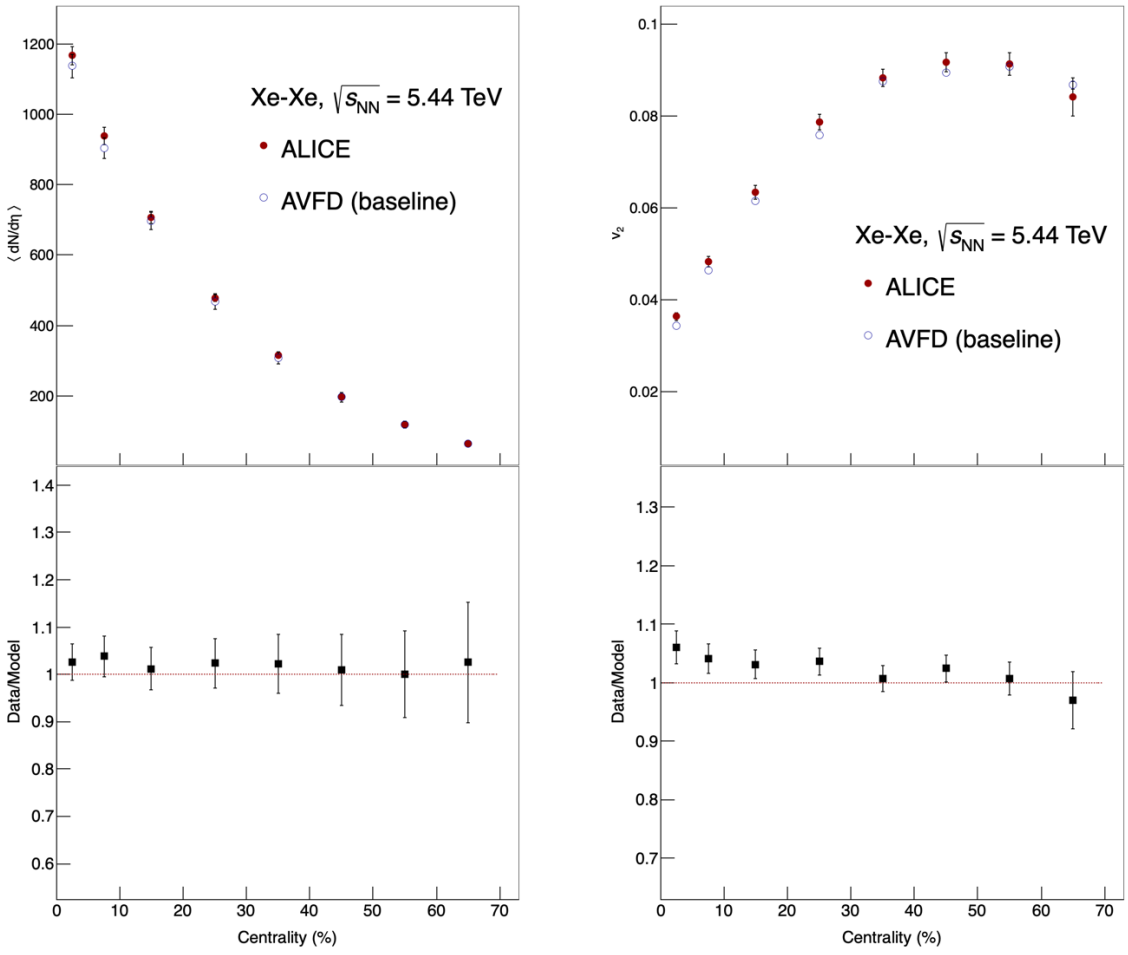

Figure 5.5: *Comparison of the centrality dependence of the charged particle multiplicity density (left) and the centrality dependence of v_2 (right) in Xe-Xe collisions at $\sqrt{s_{NN}} = 5.44$ TeV between the ALICE data (black dots) and the AVFD baseline simulation (hollow blue dots).*

New AVFD samples were produced for centralities ranging from 0 to 70 with 7 equal intervals, for both systems and energies. The baseline sample has n_5/s and LCC both set to zero. Then, the amount of CME-induced signal was incremented, i.e. using $n_5/s = 0.05, 0.07$, and 0.1, while the percentage of LCC was fixed at zero at the same time. To gauge the dependence of both correlators on the background, a similar amount of events was generated for two levels of the percentage of LCC, using 33% and 50% for the Pb-system and 15% and 30% for the Xe-system, but fixing n_5/s at zero this time.

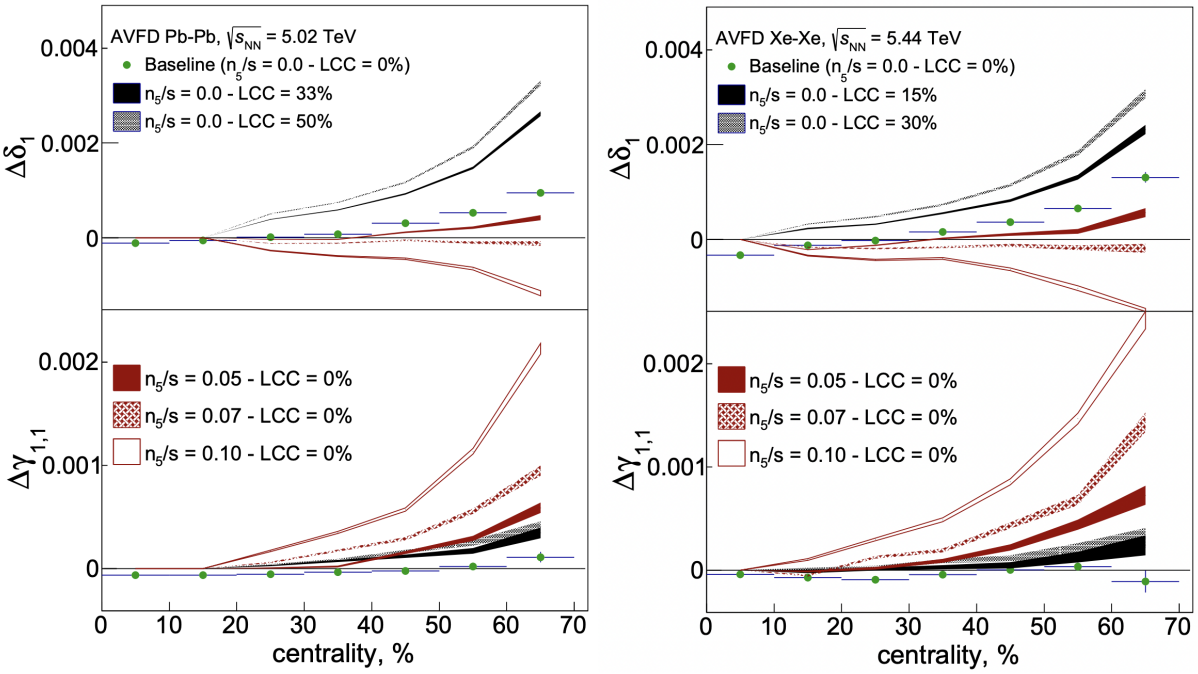

Figure 5.6: *The centrality dependence of $\Delta\delta_1$ (upper panel) and $\Delta\gamma_{1,1}$ (lower panel) in Pb-Pb collisions at $\sqrt{s_{NN}} = 5.02$ TeV (left) and in Xe-Xe collisions at $\sqrt{s_{NN}} = 5.44$ TeV (right), respectively. The results from the analysis of the baseline sample are represented by the green markers. The various bands show the AVFD expectations for $\Delta\delta_1$ and $\Delta\gamma_{1,1}$ for various values of n_5/s (red bands) and percentage of LCC (blue bands).*

FFig. 5.6 shows the centrality dependence of $\Delta\delta_1$ (upper panel) and $\Delta\gamma_{1,1}$ (lower panel) in Pb-Pb collisions at $\sqrt{s_{NN}} = 5.02$ TeV (left) and in Xe-Xe collisions at $\sqrt{s_{NN}} = 5.44$ TeV (right), respectively. In the case of Pb-Pb collisions, the baseline curves of two correlators, $\Delta\delta_1$ and $\Delta\gamma_{1,1}$, represented by green markers, exhibit non-zero values for the majority of the centrality intervals in both collision systems. These non-zero values are due to the existence of hadronic resonances in the model, whose decay products are affected by both radial and elliptic flows. Moreover, the same plots illustrate the change in magnitude of these correlators for various values of the axial current density n_5/s, represented by the red bands. It is conspicuous that in both Pb-Pb and Xe-Xe collisions, the increase of n_5/s leads to opposite trends in the two correlators: a decrease in the values of $\Delta\delta_1$ and a rise in the values of $\Delta\gamma_{1,1}$. This is an expected behaviour as a consequence of the different sign in front of the CME-induced contribution, $\langle a_{1,\alpha}a_{1,\beta}\rangle$, in Eqs. 4.1.1 and 4.1.4, respectively. Finally, when the value of n_5/s is fixed at zero and the percentage of LCC in the sample is progressively increased (represented by the black curves in the left panel of Fig. 5.6), both $\Delta\delta_1$ and $\Delta\gamma_{1,1}$ values increase. However, the latter correlator shows reduced sensitivity compared to $\Delta\delta_1$ to the background due to its construction as the difference in the magnitude of background effects between the in-plane and out-of-plane directions (see Eq. 4.1.1).

In Xe-Xe collisions, as shown in the right panel of Fig. 5.6, the results for the baseline AVFD sample are represented with the green markers, while the red and black bands correspond to samples with progressively increasing values of n_5/s and the percentage of LCC, respectively. The same qualitative observations are also found in this system: the baseline sample exhibits non-zero values for both $\Delta\delta_1$ and $\Delta\gamma_{1,1}$, these two correlators have opposite trends with increasing n_5/s and $\Delta\delta_1$ exhibits bigger sensitivity on the LCC percentage than $\Delta\gamma_{1,1}$.

To directly compare the values of $\Delta\delta_1$ and $\Delta\gamma_{1,1}$ between these two collision systems, the results are organized based on the input parameters used: zero n_5/s but various choices of LCC, and non-zero n_5/s but LCC fixed to zero. Fig. 5.7 summaries the centrality dependence of the results for $\Delta\delta_1$ and $\Delta\gamma_{1,1}$.

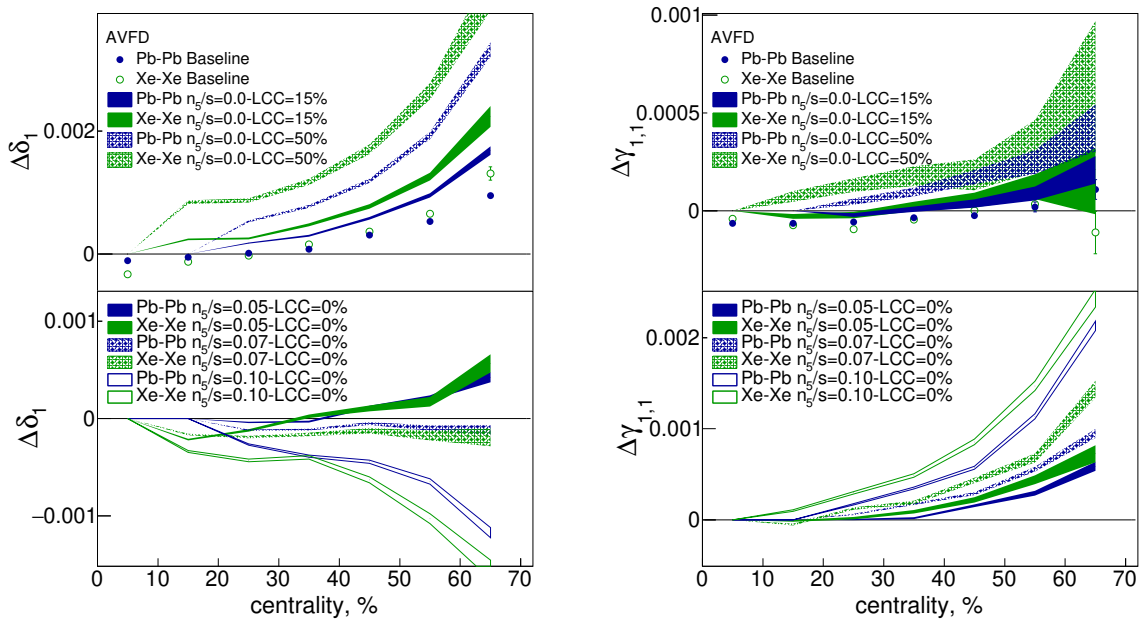

Figure 5.7: *The centrality dependence of $\Delta\delta_1$ (left) and $\Delta\gamma_{1,1}$ (right) grouped in two scenarios: zero n_5/s but various choices of LCC (upper panel) and non-zero n_5/s but LCC fixed to zero (lower panel). The various bands show the AVFD expectations for $\Delta\delta_1$ (left) and $\Delta\gamma_{1,1}$ (right) for Pb–Pb collisions and Xe–Xe collisions, with blue and green bands, respectively. The results of the baseline sample are represented by the filled and open markers.*

In Fig. 5.7a, the baseline and LCC being 15% and 50% for Pb–Pb collisions at $\sqrt{s_{NN}} = 5.02$ TeV and for Xe–Xe collisions at $\sqrt{s_{NN}} = 5.44$ TeV are chosen. The upper panel illustrates that for a fixed LCC percentage, the values of $\Delta\delta_1$ are higher for the Xe–Xe than for the Pb–Pb samples. For a fixed centrality, while the effect of radial flow between these two systems is similar [185], the charged particle multiplicity in Pb–Pb is 60–70% higher than the corresponding value in Xe–Xe collisions [178, 179]. This could lead to a faster dilution of the correlations induced by the LCC mechanism in the larger system, reflected in this difference in $\Delta\delta_1$. At the same time, the upper panel of Fig. 5.7b shows that the values of $\Delta\gamma_{1,1}$ for the two systems do not exhibit any significant difference. This is in line with the expectation that the sensitivity of $\Delta\gamma_{1,1}$ to the background is significantly reduced compared to $\Delta\delta_1$.

In the second case of non-zero axial current density, the samples containing $n_5/s = 0.05, 0.07,$ and 0.10 are chosen. The lower panel of Fig. 5.7a shows that $\Delta\delta_1$ is similar between the two systems since it is primarily affected by background contributions. This correlator needs higher values of n_5/s (e.g. $n_5/s = 0.1$ in the plot) to start observing some differences. Finally, the lower panel of Fig. 5.7b illustrates that the magnitude of $\Delta\gamma_{1,1}$ is higher in the Xe–Xe than in the Pb–Pb samples. Although the value of the magnetic field is higher for the larger Pb-system,

as shown in Fig. 5.1, the significantly larger multiplicity that this system has, leads to a larger dilution effect reflected in the ordering of the corresponding curves in the plot.

The previous results for each colliding system and energy can be grouped in a different way that allows to parametrise the dependence of each of the correlators on the LCC percentage and on n_5/s. Fig. 5.8 and 5.9 present how $\Delta\delta_1$ and $\Delta\gamma_{1,1}$ develop as a function of the LCC percentage and n_5/s, respectively. Results for the 40–50% centrality interval of Pb–Pb at $\sqrt{s_{\mathrm{NN}}} = 5.02$ TeV and Xe–Xe collisions at $\sqrt{s_{\mathrm{NN}}} = 5.44$ TeV are indicatively chosen to illustrate the procedure. An identical protocol was used for all centrality intervals of both colliding systems. One can see that both $\Delta\delta_1$ and $\Delta\gamma_{1,1}$ exhibit a linear dependence on the percentage of LCC, with the latter being less sensitive and thus having a smaller slope. Finally, these two correlators exhibit a quadratic dependence on n_5/s with an opposite trend, originating from the dependence of δ_1 and $\gamma_{1,1}$ on $\langle a_{1,\alpha}a_{1,\beta}\rangle$ and $-\langle a_{1,\alpha}a_{1,\beta}\rangle$ in Eqs. 4.1.1 and 4.1.4, respectively. This a_1 coefficient has been shown in Fig. 5.3 to be proportional to the value of n_5/s.

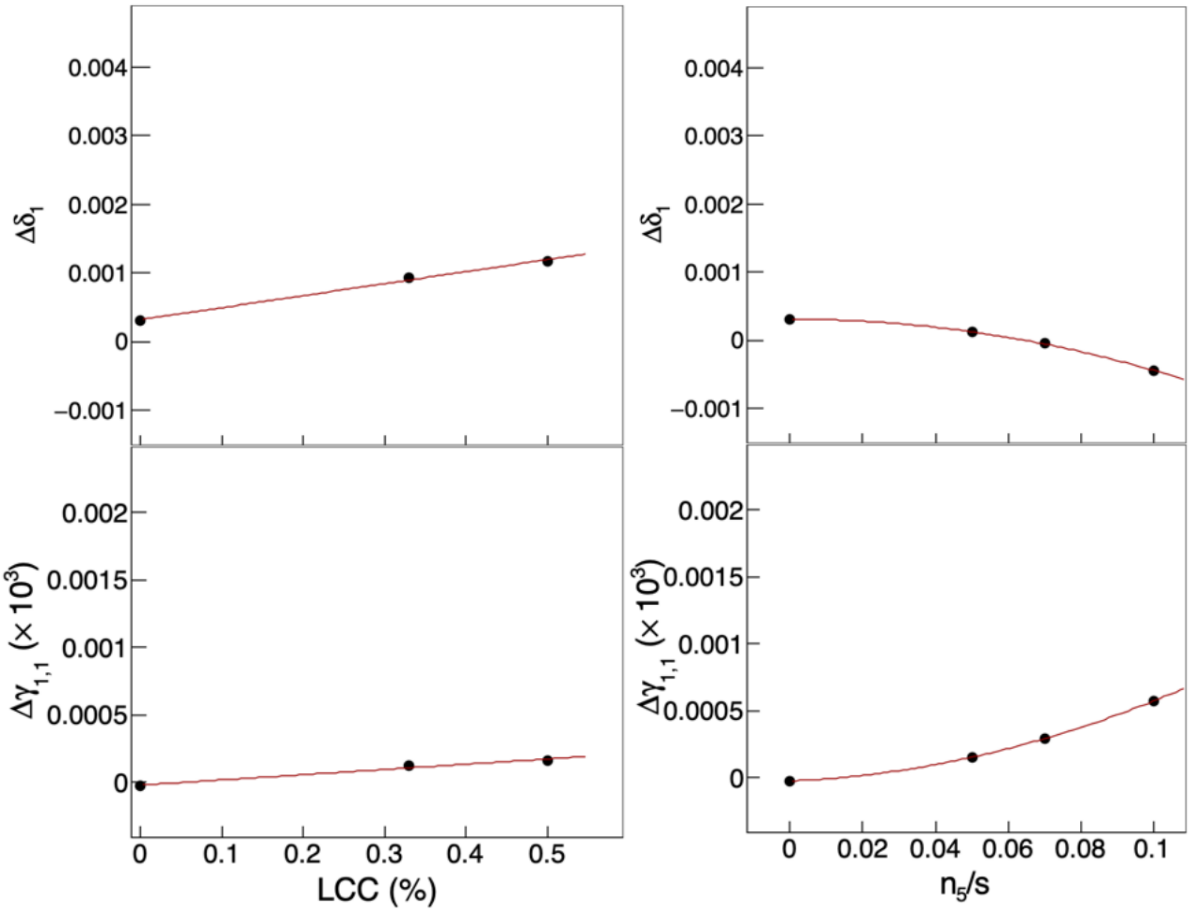

Figure 5.8: *The dependence of $\Delta\delta_1$ and $\Delta\gamma_{1,1}$ in the upper and lower panels, respectively, on the percentage of LCC (left) and the axial current density n_5/s (right) in the analysed samples of Pb-Pb collisions at $\sqrt{s_{NN}} = 5.02$ TeV for the 40%-50% centrality interval. The black curves are the lines of parametrisation.*

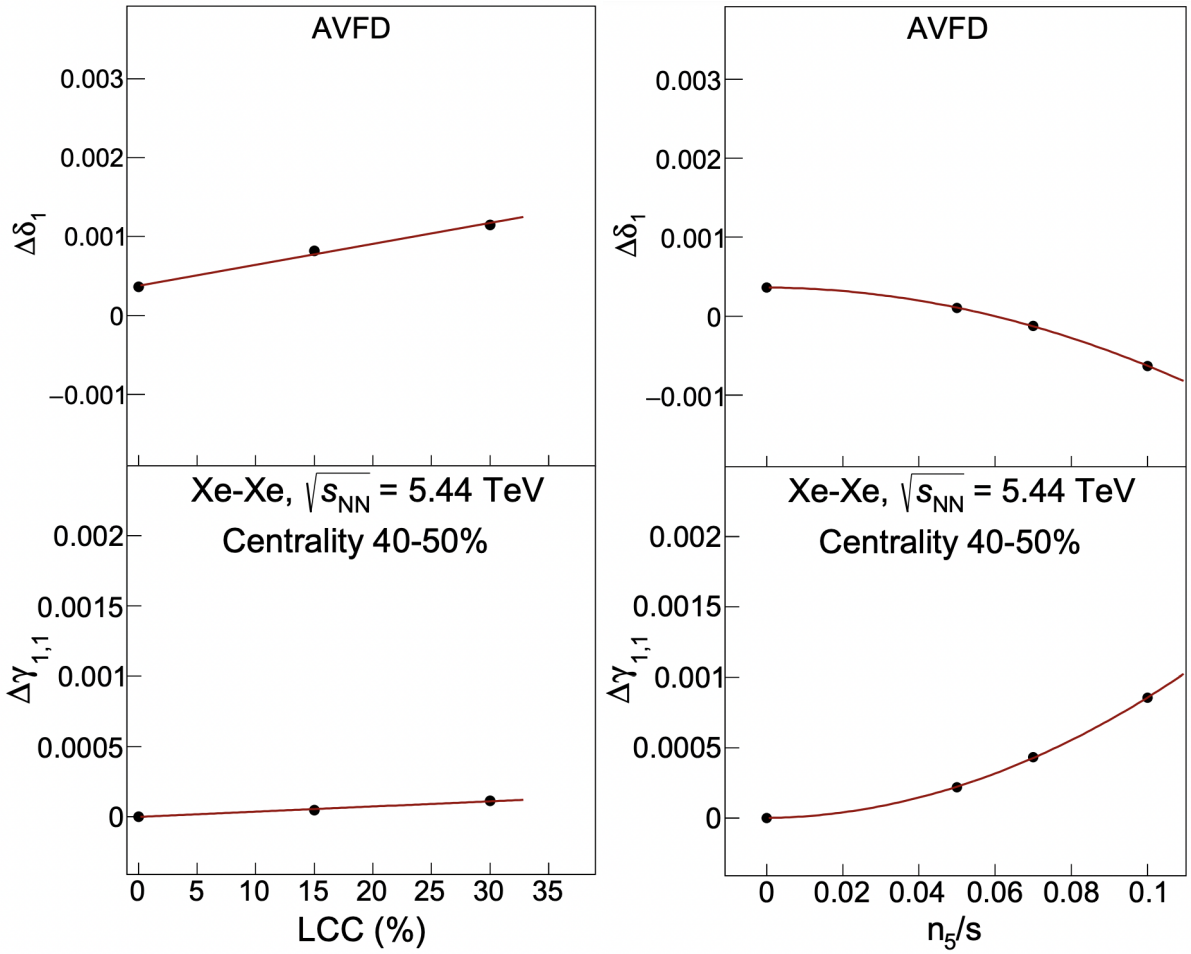

Figure 5.9: *The dependence of $\Delta\delta_1$ and $\Delta\gamma_{1,1}$ in the upper and lower panels, respectively, on the percentage of LCC (left) and the axial current density n_5/s (right) in the analysed samples of Xe-Xe collisions at $\sqrt{s_{NN}} = 5.44$ TeV for the 40%-50% centrality interval. The black curves are the lines of parametrisation.*

Following this procedure, one is able to parameterise the dependence of $\Delta\delta_1$ and $\Delta\gamma_{1,1}$ according to

$$\begin{aligned} \Delta\delta_1 &= c_2 \cdot (n_5/s)^2 + c_1 \cdot (n_5/s) + b_1 \cdot (LCC) + b_0, \\ \Delta\gamma_{1,1} &= e_2 \cdot (n_5/s)^2 + e_1 \cdot (n_5/s) + d_1 \cdot (LCC) + d_0, \end{aligned} \tag{5.2.1}$$

where $e_2, e_1, d_1, d_0, c_2, c_1, b_1$, and b_0 are real numbers constrained by the simultaneous fit of the corresponding dependencies of $\Delta\delta_1$ and $\Delta\gamma_{1,1}$ for each centrality interval of every collision system and energy. The parameterisation of Eqs. 4.1.1 and 4.1.4 assumes that the two components that control the CME signal and the background are not correlated. This is a reasonable assumption considering that LCC and the generation of axial current density are two independent processes happening at different stages of heavy-ion collisions.

5.3 Results

Having the dependence of both $\Delta\delta_1$ and $\Delta\gamma_{1,1}$ on n_5/s and LCC parameterised from Eq. 5.2.1, one can deduce the values of these two parameters that govern the CME signal and the back-

ground for each centrality, colliding system, and energy that allows, at the same time, for a quantitative description of the measured centrality dependence of $\Delta\delta_1$ and $\Delta\gamma_{1,1}$ at LHC energies.

Fig. 5.10 presents the results of such procedure for Pb–Pb collisions at $\sqrt{s_{\rm NN}} = 5.02$ TeV. The data points, extracted from Ref. [90] for both correlators are described fairly well by the tuned model. A similarly satisfactory description is also achieved for the results of Xe–Xe collisions at $\sqrt{s_{\rm NN}} = 5.44$ TeV [6], as shown in Fig. 5.11.

Fig. 5.12 presents the final result of the whole procedure. The plots show the centrality dependence of the pairs of LCC percentage (upper panel) and n_5/s (lower panel) that are needed to describe with AVFD the experimental measurements of $\Delta\delta_1$ and $\Delta\gamma_{1,1}$. The different markers represent results for different collision systems and energies. It can be seen that all systems can be described by large values of LCC that range from 40% for peripheral up to around 60% for more central Pb–Pb collisions. There is no significant difference observed in these values among the two sets of results.

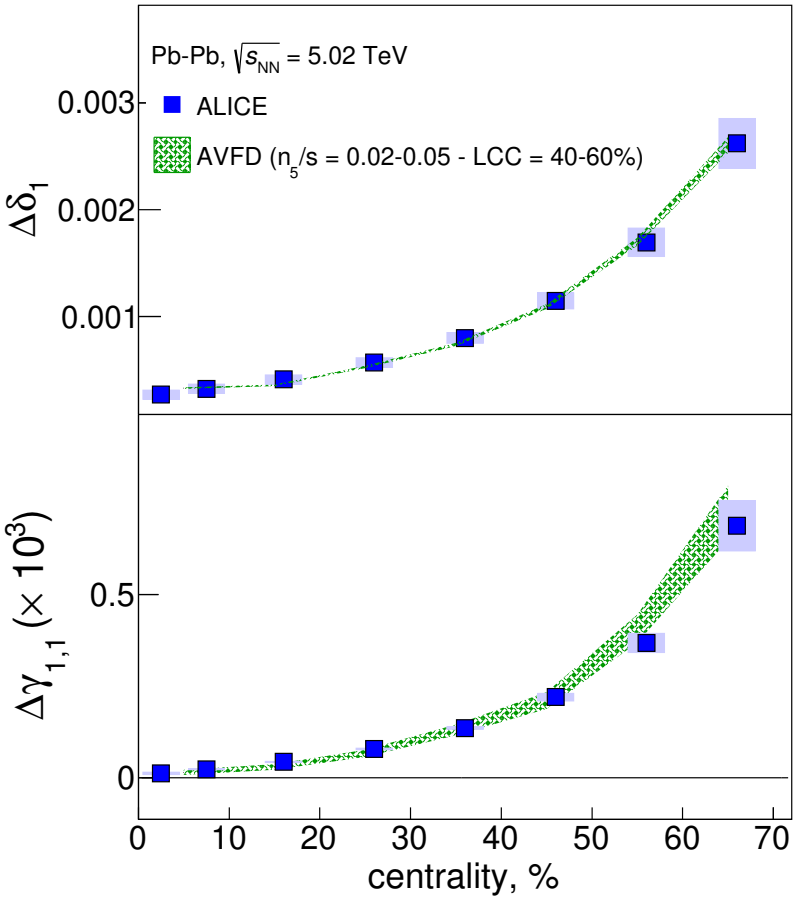

Figure 5.10: *The centrality dependence of $\Delta\delta_1$ and $\Delta\gamma_{1,1}$ in the upper and lower panels, respectively. The data points represent the experimental measurements in Pb–Pb collisions at $\sqrt{s_{\rm NN}} = 5.02$ TeV [90]. The green band shows the results obtained from the tuned AVFD sample (see text for details).*

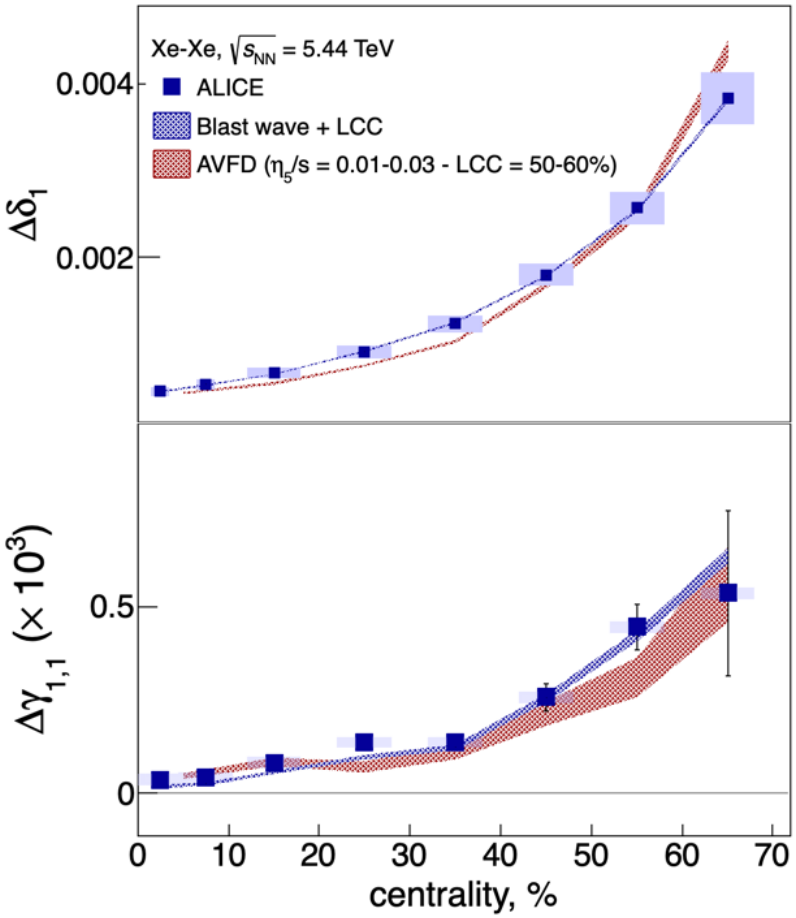

Figure 5.11: *The centrality dependence of $\Delta\delta_1$ and $\Delta\gamma_{1,1}$ in the upper and lower panels, respectively. The data points represent the experimental measurements in Xe–Xe collisions at $\sqrt{s_{\rm NN}} = 5.44$ TeV [6]. The green band shows the results obtained from the tuned AVFD sample (see text for details).*

Furthermore, the lower panel of Fig. 5.12 illustrates that there is no significant centrality dependence of n_5/s. However, there is a dependence on the colliding system. More particularly, the experimental results from the analysis of Xe–Xe collisions lead to a value of n_5/s which is compatible with zero within the uncertainties for all centrality intervals. A fit with a constant function results in values of 0.011 ± 0.005. This naturally results in a CME fraction which is compatible with zero. At the same time, the results for Pb–Pb collisions can be described by non-zero values of axial current densities, again for the entire centrality region studied. The corresponding fit leads to a value of 0.034 ± 0.003, i.e., significantly above the background-only scenario. The numerical values of the extracted n_5/s and LCC are summarised in Table 5.1 and 5.2 for Xe-Xe and Pb-Pb collisions, respectively.

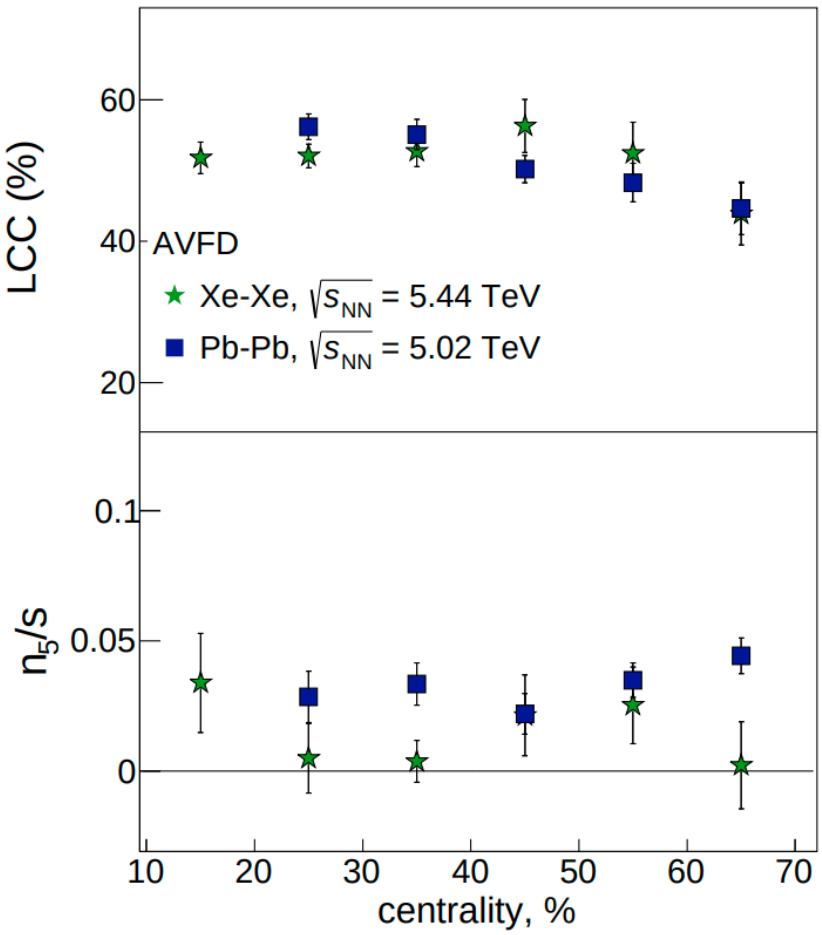

Figure 5.12: *The centrality dependence of the LCC percentage (upper panel) and the axial current density n_5/s that allow one to describe simultaneously the experimentally measured dependencies of $\Delta\delta_1$ and $\Delta\gamma_{1,1}$ on n_5/s [6, 90, 92] in all collision systems and at all energies studied in this article.*

Centrality	n_5/s	LCC (%)
10-20%	0.034 ± 0.019	51.8 ± 2.1
20-30%	0.005 ± 0.014	52.1 ± 1.7
30-40%	0.004 ± 0.008	52.7 ± 2.2
40-50%	0.021 ± 0.015	56.4 ± 3.6
50-60%	0.025 ± 0.015	52.5 ± 4.3
60-70%	0.002 ± 0.016	43.9 ± 4.4

Table 5.1: *Summary of optimum values of n_5/s and LCC percentage extracted for each centrality interval of Xe-Xe collisions at $\sqrt{s_{NN}} = 5.44$ TeV.*

Centrality	n_5/s	LCC (%)
20-30%	0.028 ± 0.010	56.2 ± 1.8
30-40%	0.034 ± 0.008	55.2 ± 1.9
40-50%	0.022 ± 0.007	50.3 ± 1.9
50-60%	0.035 ± 0.006	48.3 ± 2.7
60-70%	0.045 ± 0.006	44.7 ± 3.6

Table 5.2: *Summary of optimum values of n_5/s and LCC percentage extracted for each centrality interval of Pb-Pb collisions at $\sqrt{s_{NN}} = 5.02$ TeV.*

5.4 Discussion

The systematic study of charge dependent azimuthal correlations in Pb–Pb collisions at $\sqrt{s_{\rm NN}} = 5.02$ TeV, as well as in Xe–Xe collisions at $\sqrt{s_{\rm NN}} = 5.44$ TeV to probe the CME using the AVFD framework is presented. Through parametrising the dependence of both $\Delta\delta_1$ and $\Delta\gamma_{1,1}$ on the LCC percentage, the main contribution to the background, and the axial current density n_5/s which dictates the amount of CME signal, the measurements in Xe–Xe are consistent with a background only scenario, with values of n_5/s compatible with zero. On the other hand, the results of Pb–Pb collisions require n_5/s with significantly non-zero values.

This result is consistent with the expectation that the CME signal is greater in Pb–Pb collisions compared to Xe–Xe collisions, due to the relatively lower magnetic field strength and the increased decorrelation between Ψ_B and $\Psi_{2,\rm EP}$ in Xe–Xe collisions. As described in [6], the fraction of CME ($f_{\rm CME}$) in the $\Delta\gamma$ correlator is extracted using the two-component method, based on the assumption that both CME and the background scale with $dN_{\rm ch}/d\eta$. The γ correlators are decomposed similarly to previously introduced Eq. 4.4.5, as described below:

$$\begin{aligned} \gamma_{\alpha\beta}^{\text{Xe-Xe}} dN_{\rm ch}^{\text{Xe-Xe}}/d\eta &= sB^{\text{Xe–Xe}} + bv_2^{\text{Xe–Xe}} \\ \gamma_{\alpha\beta}^{\text{Pb-Pb}} dN_{\rm ch}^{\text{Pb-Pb}}/d\eta &= sB^{\text{Pb–Pb}} + bv_2^{\text{Pb–Pb}}, \end{aligned} \tag{5.4.1}$$

where $B = \langle (e\mathbf{B})^2 \cos\left[2(\Psi_B - \Psi_{2,\rm EP}\right]\rangle$ is simulated using the MC Glauber model (see e.g. [**?**]) for Pb-Pb and Xe-Xe collisions, respectively, as shown in Fig. 5.13. The s and b parameters quantify the signal and background contributions, respectively, and do not depend on the collision system as a result of the assumption that both scale with $dN_{\rm ch}/d\eta$. After obtaining the optimum values of s and b, $f_{\rm CME}$ can be calculated through

$$f_{\rm CME} = \frac{sB}{sB + bv_2}. \tag{5.4.2}$$

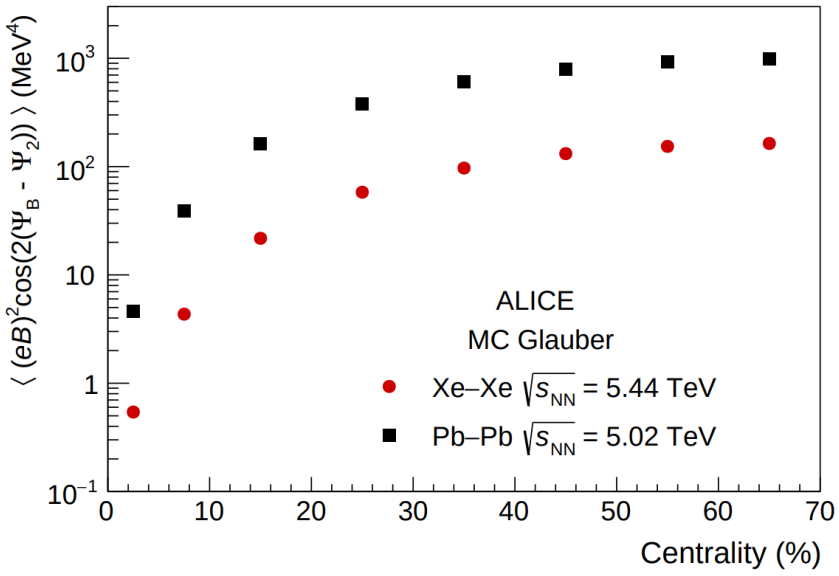

Figure 5.13: *The expected CME signal as a function of centrality from MC Glauber simulations for Xe–Xe and Pb–Pb collisions. Figure taken from [6].*

The centrality dependence of the f_{CME} in Xe–Xe and Pb–Pb collisions for the two models used in this study are shown in Fig. 5.14. For both systems, the f_{CME} remains compatible with zero up to 30% centrality and then becomes positive for midcentral and peripheral collisions, with larger values observed in Pb–Pb compared to Xe–Xe. Fitting the data points in the centrality range 0–70% with a constant function neglecting any centrality dependence shows that f_{CME} is consistent with zero in Xe-Xe collisions and gives an upper limits on f_{CME} of 2% (3%) and 25% (32%) at 95% (99.7%) confidence level for MC Glauber (TRENTo) initial conditions in Xe–Xe and Pb–Pb collisions, respectively.

It is clear that the conclusions from the AVFD study and the two-component method are consistent, but there are some subtleties to bear in mind. The fraction of CME extracted by the two-component method is expected to be the combined effect of the initial chirality imbalance and the magnetic field created by the spectators. However, the conclusion from the AVFD study shows that the axial charge density is consistent with zero in Xe-Xe collisions, taking the consideration of the magnetic field difference into account. The initial axial charge density (n_5/s) is defined as

$$n_5/s = \frac{\int_V \sqrt{\langle n_5^2 \rangle}}{\int_V s}, \tag{5.4.3}$$

where the axial charge density fluctuations $\sqrt{\langle n_5^2 \rangle}$ is given by

$$\sqrt{\langle n_5^2 \rangle} = [...] \times \sqrt{N_{\mathrm{tube}}} \times \frac{\pi \rho_{\mathrm{tube}}^2}{A_{\mathrm{overlap}}}, \tag{5.4.4}$$

with [...] representing the complicated expression of the axial charge density within a single glasma flux tube [170]. The total number of glasma flux tubes N_{tube} is proportional to the number of binary collisions N_{coll} [186]. The last term gives a smoothed and averaged axial charge density over the entire transverse area of the fireball, considering the contributions from individual flux tubes, which is given by the ratio of the flux tube transverse area $\pi \rho_{\mathrm{tube}}^2$ and the transverse geometric overlapping area of the two colliding nuclei A_{overlap}. Given that the total

entropy $\int_V s$ typically scales with the number of participating nucleons [187], the total entropy in Xe-Xe collisions within the same centrality interval as Pb-Pb collisions should be lower. Therefore, it can be conclusively affirmed that the AVFD framework indicates a significantly lower total average axial charge in Xe-Xe collisions compared to Pb-Pb collisions. According to Eq. 5.4.4, it is evident that $\sqrt{N_{\text{tube}}}$ is lower in Xe-Xe collisions. Currently, there is no clear evidence indicating whether the density of axial charge in a single glasma flux tube or the averaged axial charge density over the overlapped transverse area (significantly) changes in different collision systems.

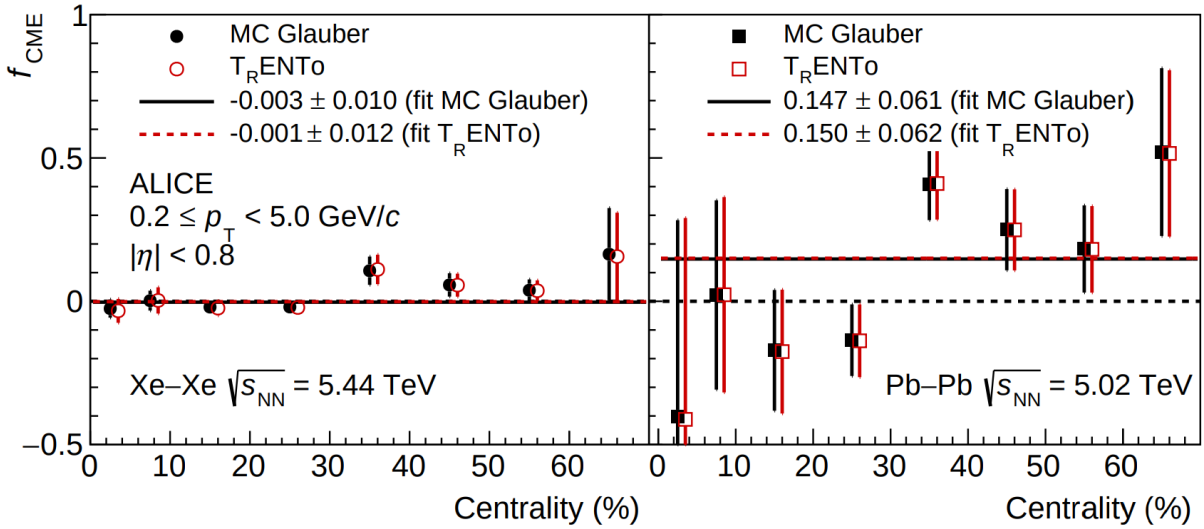

Figure 5.14: *The centrality dependence of the CME fraction, obtained using Eq. 5.4.2, where the expected CME signal (B) is calculated based on MC Glauber (closed markers) and TRENTo models (open markers). Figure taken from [6].*

Chapter 6

Outlook

The heavy-ion collisions provide an excellent environment to search for the chiral magnetic effect (CME). It is a challenging and nontrivial task, given the dominance of background effects in experimental observables. Previous experimental endeavours conducted at LHC and RHIC (e.g. [87–90, 96, 97, 101, 165]), along with the study conducted in this thesis, have used various experimental techniques to separate the signal from the backgrounds. Although valuable insights have been gained in understanding sources of backgrounds in CME observables, no evidence supporting the existence of the CME has been found. Furthermore, the theoretical challenges associated with simulating heavy-ion collisions from first physics principles hinder the realistic and reliable modelling of backgrounds that can be subtracted from experimental observables.

The field of heavy-ion physics at LHC undoubtedly has exciting times ahead in the Run 3 LHC running schedule and beyond. Bolstered by technological advancements, the Inner Tracking System (ITS) of the ALICE detector has been upgraded to achieve a better track reconstruction performance (in particular for low-momentum particles and particle identification capabilities), resulting in an improvement by a factor of approximately three for the impact parameter resolution in the transverse plane [188]. Other detector components, including the readout chamber of Time-Projection Chamber (TPC) and the readout electronics of the Time-Of-Flight (TOF) detector, Muon Spectrometer, and Zero Degree Calorimeter (ZDC), have been upgraded to accommodate higher interaction rates in the Run 3 LHC running schedule [188]. This leads to a change in the data acquisition procedure to a continuous readout mode (trigger-less), enabling an event readout rate of up to 50 kHz (currently at 25 kHz in 2023 [189]) for Pb–Pb collisions (at $\sqrt{s_{\mathrm{NN}}} = 5.36$ TeV in Nov 2023 [189]). This corresponds to an instantaneous luminosity of $\mathcal{L} = 6 \times 10^{27}$ cm^{2}s^{-1}, approximately ten times higher than that achieved in previous LHC Runs. It is anticipated that the quantity of minimum-bias events collected during Run 3 and 4 will be two orders of magnitude larger than that gathered during Run 2 [188]. The recorded number of Pb-Pb collision events until the end of Nov 2023 is around 40 times[1] more than the number of minimum bias events recorded in Run 2, reaching around 11.7 billion events. In addition, a new Muon Forward Tracker (MFT) has been integrated in front of the front absorber of the existing Muon Spectrometer. This addition enhances the tracking precision and the reconstruction of secondary vertices for muon tracks in the forward region ($-3.6 < \eta < -2.5$).

With the recent upgrades at ALICE and the forthcoming plans for the LHC, a pivotal question

[1] The integrated luminosity for Run 3, as provided in [190], can be used to calculate the number of events by multiplying the integrated luminosity by a cross-sectional area of 7.67 barn for ALICE Run 2, assuming no changes [191]. The trigger statistics for minimum bias events in Run 2 are documented in [192].

for the community focused on the study of chiral-related phenomena in heavy-ion collisions arises: Do these upgrades bring significant benefits? From my perspective, the direct search for the CME stands to gain primarily from increased event statistics rather than improvements in detector performance. While the enhanced tracking precision is expected to offer the most advantages for heavy flavor reconstruction, its impact on azimuthal correlations is limited.

It has been discussed that the upper limit of the fraction of CME in the $\Delta\gamma$ correlator obtained with the spectator-participant plane method is significantly influenced by how well the spectator plane can be reconstructed by ZDC. The ZDC performance in Run 2 and its problems have been detailed in Sec. 3.7. With a hundredfold increase in data accumulated during Run 3 and 4, statistical uncertainties are expected to reduce by a factor of 10. However, the general form of the Bienaymé formula says that given a sample of n independent observations $(x_1, ..., x_n)$, the variance of the mean of these measurements $(\bar{x})$ is given by

$$\mathrm{Var}[\bar{x}] = \mathrm{Var}\left[\frac{\sum_{i=1}^{n} x_i}{n}\right] = \frac{\sum_{i=1}^{n} \mathrm{Var}[x_i] + \sum_{\substack{i,j=1 \\ i\neq j}}^{n} \mathrm{Cov}[x_i, x_j]}{n}. \tag{6.0.1}$$

This means that the reduction may be less if the covariance between the spectator plane reconstructed from different events or the covariance between the spectator plane and the second-order symmetry plane reconstructed by V0 or TPC cannot be fully eliminated by detector calibrations. The systematic uncertainties are mainly driven by the ZDC cross correlation (see Sec. 4.3.1), and their origins are speculated to be highly dependent on beam parameters, yet not thoroughly understood. Given that the configuration of the ZDC remains unchanged in Run 3 and 4, these uncertainties are expected to persist as dominant factors. Consequently, the reduction in total uncertainties is going to be quite limited. Other methods to search for the CME, including the event shape engineering and the higher harmonics, rely on the second order symmetry plane reconstructed with V0 or TPC and charged tracks reconstructed with ITS and TPC. While increased event statistics benefit the final extracted upper limits on f_{CME} by reducing statistical uncertainties, systematic uncertainties do not exhibit a similar reduction trend. A representative result of f_{CME}, estimated using the event shape engineering method in centrality 20-30%, has been used to estimate the upper limit of f_{CME} as a function of the number of events (see Fig. 11 in [188]). According to this estimation, the upper limit for the f_{CME} with the null hypothesis ($f_{\mathrm{CME}} = 0$) can be set to below 1% at a 95% confidence level, considering an event count of 10^{10} in centrality 20-30%. However, this estimation suggests a reduction in the upper limit by a factor of around 3.3 for every 10-fold increase in the event count, which appears overly optimistic. This optimism is because that this estimation only accounts for statistical uncertainties, which decrease as $1/\sqrt{N}$. The systematic uncertainties of $\Delta\gamma$, already comparable in size to the statistical uncertainties in the current event shape engineering study using the LHC18q and LHC18r data sets (see this presentation [193]), are likely to dominate the total uncertainties in Run 3 and 4. In addition, the model uncertainties originated from different initial-state models, which are used in the event shape engineering method to simulate v_2 dependence of the magnetic field for each centrality interval, become relatively large. It is therefore crucial to understand the difference between initial-state models (EKRT [45], KLN [46, 47] and Glauber [43]), as current upper limits provided by different models differ by a few percent [96]. Moreover, it is important to conduct measurements that are sensitive to the early magnetic field. Such measurements are pivotal in establishing concrete evidence for the existence of this field and determining its strength. One of the most sensitive observables is $\Delta v_1(D) = v_1(D^0) - v_1(\bar{D}^0)$ as c quarks in D^0 and $\bar{D}^0$ are predominantly produced through hard binary collisions (having a formation time

of 0.1 fm/c), when the magnetic field is at its maximum. If the slope of $\Delta v_1(D)$ can be precisely measured at ALICE, it would clarify whether there is really a difference in the previously observed slopes of $\Delta v_1(D)$ between ALICE [77] and STAR [79]. The precise measurement of this gradient will provide important constraints to theoretical calculations concerning the interplay of various effects in the early stages of the collision (refer to Fig. 1.8). Furthermore, it will help significantly constrain theoretical predictions regarding the magnitude of the CME signal.

Apart from using established techniques to search for CME, a new method inspired by the event shape engineering method could benefit significantly from more event statistics. The Zero Proton Calorimeter (ZPC) directly measures the spectator protons, which is related to the strength of the early magnetic field. By selecting events with not only low eccentricity to minimise flow background but also large ZPC signals (E_{ZPC}) to maximise CME signal strength, the sensitivity of the $\Delta\gamma$ correlator can be maximised. Given that the $\Delta\gamma$ correlator exhibits a linear dependence on v_2 and a quadratic dependence on the magnetic field (see Eq. 4.4.5), the observation of a quadratic relationship of $\Delta\gamma$ (with the flow background suppressed through selecting on low-eccentricity events) as a function of E_{ZPC} would serve as a strong indicator of the presence of CME. It is essential to note that the primary challenge associated with this method lies in accurately and unambiguously quantifying the quadratic nature of the relationship.

Our AVFD study concludes that the analysis of Xe–Xe collisions yields values of axial current densities (n_5/s) compatible with zero within uncertainties for all centrality intervals. In contrast, the results for Pb–Pb collisions can be described by non-zero values of n_5/s. This is compatible with the conclusion from the two-component method using Xe-Xe and Pb-Pb collisions data as detailed in Sec. 5.4. This suggests that heavier nuclei are preferred when searching for CME. The $^{96}_{44}$Ru and $^{96}_{40}$Zr used in the isobar study by STAR are lighter than $^{129}_{54}$Xe and much lighter than $^{208}_{82}$Pb collided at the LHC. Despite a relatively larger difference in the proton number of $^{96}44$Ru and $^{96}40$Zr, resulting in a greater difference in their magnetic fields, the induced axial current densities may be too small for any CME signal to be created. Future isobar collisions should consider heavier isobar pairs. Identifying optimal candidates necessitates a comprehensive understanding of the nuclear structure and careful validation with simulations. Promising candidates could include Pb and Hg. While the optimal mass number has not been specifically studied, it has been demonstrated in the model study that the v_2 of the isobar pair Pb and Hg is expected to be similar (see Fig. 9 in [194]).

Chapter 7

Summary

In this thesis, we have presented two studies focused on the chiral magnetic effect (CME) in relativistic heavy-ion collisions. The first study uses the spectator-participant method to search for CME in Pb-Pb collisions at $\sqrt{s_{\rm NN}} = 5.02$ TeV collected by the ALICE experiment at the LHC in 2018. Chapter 3 details the dataset, event and track selection, and the calibration processes for the Time Projection Chamber (TPC), V0 detector, and Zero Degree Calorimeter. Notably, we redesign the calibration procedures for neutron ZDCs, addressing issues in the standard ALICE calibration method. This is important as neutron ZDCs play a pivotal role in measuring the spectator plane. The redesigned procedures enhance the performance of neutron ZDCs, as evidenced by various comparisons, such as the correlation of the sum energy of towers 1 to 4 and the energy of the common tower (Fig. 3.9), the distribution of the shower centre position (Figs. 3.4 and 3.11), and the distribution of the spectator plane angle (Figs. 3.7 and 3.16). However, the new procedures do not resolve the unexpected ZNA-ZNC correlation (Fig. 3.12), which is also present in the standard calibration procedure. This correlation may be mitigated by using information on the crossing angle in the recentring process.

The spectator-participant-plane method employs the ratio of the three-particle charge-dependent azimuthal correlator, $\Delta\gamma$, measured with respect to the second-order symmetry plane and the spectator plane to search for CME. We apply the non-isotropic correction technique to account for detector acceptance non-uniformity. Systematic uncertainties are primarily driven by the bias induced by the unexpected ZNA-ZNC correlation. Our conclusion is that no significant contribution of CME is evident in the observable, and we quantify this statement with an upper limit of 33.2% at a 95% confidence level.

The second study adopts a different approach, systematically examining the measured charge-dependent correlations ($\Delta\gamma$ and $\Delta\delta$) in experimental CME searches through the Anomalous-Viscous Fluid Dynamics (AVFD) framework. We extract optimal values for axial current densities governing the CME signal and percentages of local charge conservation governing the background across various centrality intervals in the AVFD model. This allows a quantitative description of the centrality dependence of charge-dependent correlations observed in Pb–Pb collisions at $\sqrt{s_{\rm NN}} = 5.02$ TeV and Xe–Xe collisions at $\sqrt{s_{\rm NN}} = 5.44$ TeV at the LHC. We conclude that the analysis of Xe–Xe collisions yields axial current density values (n_5/s) compatible with zero within uncertainties for all centrality intervals. In contrast, results for Pb–Pb collisions can be characterized by non-zero values of axial charge densities, consistent with the conclusions drawn from the two-component method using Xe-Xe and Pb-Pb collision data.

Altogether, the work presented in this thesis contributes to the journey of the ALICE collab-

oration towards a better understanding of Quantum Chromodynamics in relativistic heavy-ion collisions. Future studies in Run 3 and beyond will improve our understanding of CME and the early magnetic field influencing the CME signal. A definitive answer regarding the existence of CME may even be attainable.

Chapter 8

Appendix

8.1 Additional plots demonstrating the effect of the new gain equalisation method

This appendix shows the magnitude of the correlation for ZNA in a subset of run numbers in the LHC18q data set and ZNC and ZNA in a subset of run numbers in the LHC18r data set before and after (using two methods of) gain equalisation. The purpose is to show that the gain equalisation using a least square fit always leads to a better correlated result for both ZNC and ZNA in LHC18q and LHC18r data set, as claimed in Sec. 3.7.2.

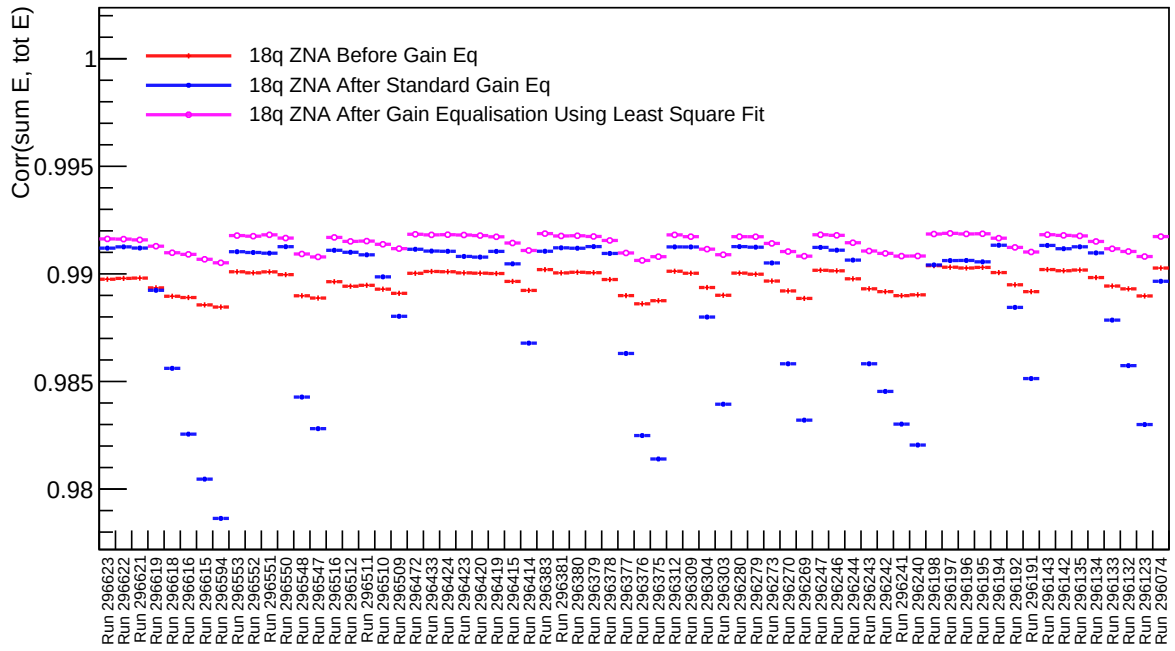

Figure 8.1: *Summary of the magnitude of the correlation between the sum energy of ZNC tower 1 to 4 and the energy of the common ZNA tower before and after (two methods of) gain equalisation in part of the run numbers (too long to show the full data set) in the LHC18q data set.*

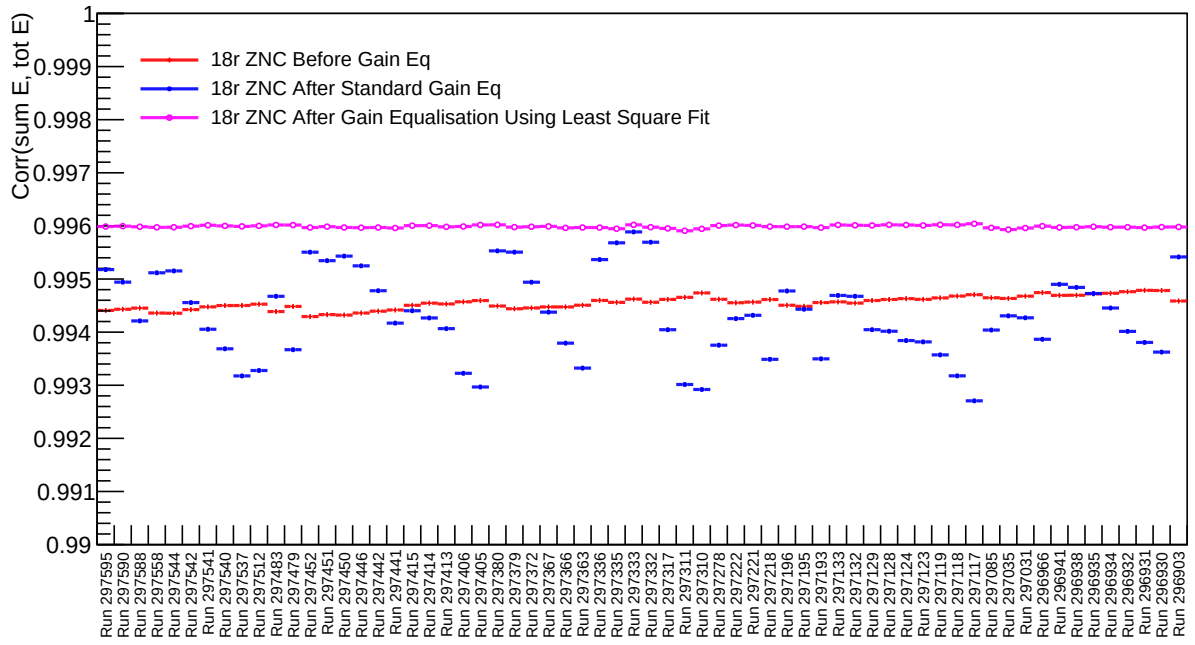

Figure 8.2: *Summary of the magnitude of the correlation between the sum energy of ZNC tower 1 to 4 and the energy of the common ZNC tower before and after (two methods of) gain equalisation in part of the run numbers (too long to show the full data set) in the LHC18r data set.*

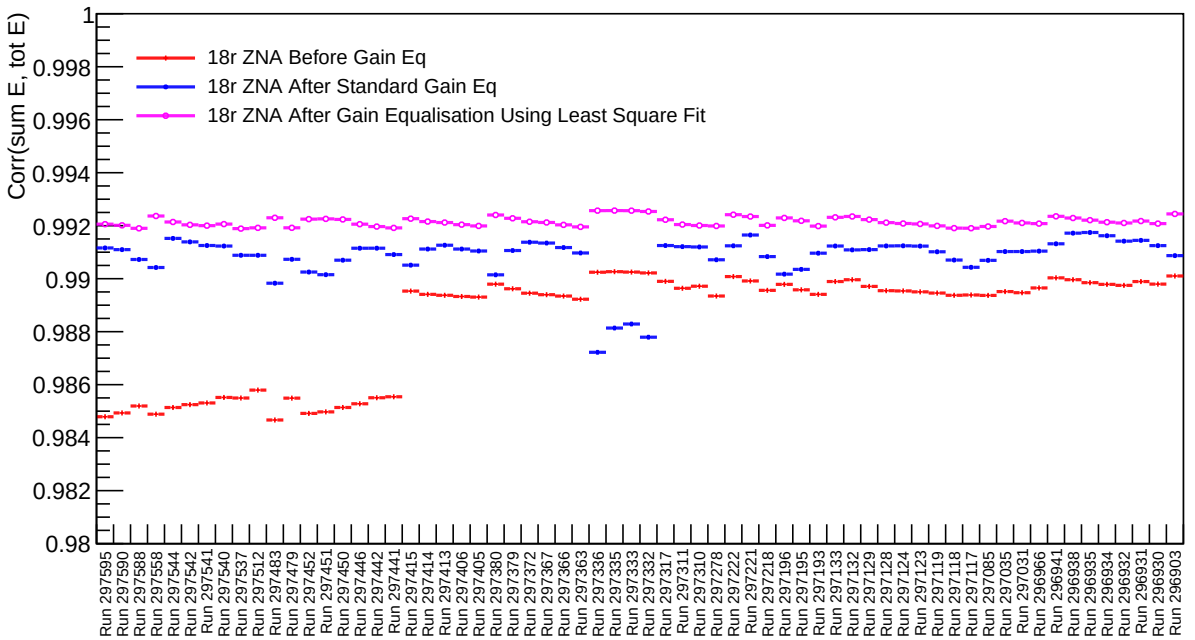

Figure 8.3: *Summary of the magnitude of the correlation between the sum energy of ZNC tower 1 to 4 and the energy of the common ZNA tower before and after (two methods of) gain equalisation in part of the run numbers (too long to show the full data set) in the LHC18r data set.*

8.2 Additional correlation plots for $\Psi_1^{\text{ZNC-ZNA}}$ vs. Ψ_2^{V0C} and Ψ_1^{ZNC} vs. Ψ_1^{ZNA}

This appendix lists the correlation between $\Psi_1^{\text{ZNC-ZNA}}$ and Ψ_2^{V0C} in centrality classes: $0-10\%$, $10-20\%$, $\ldots$, $80-90\%$ for the LHC18q and LHC18r datasets (Fig. 8.4 - 8.12). Additionally, Fig. 8.13 presents the correlation between Ψ_1^{ZNC} and Ψ_1^{ZNA} in the centrality class $10-50\%$ for both the LHC18q and LHC18r data sets. Notably, the Ψ_1^{ZNC} vs. Ψ_1^{ZNA} correlation in the LHC18r data set exhibits an interference-like pattern, the cause of which is not well understood.

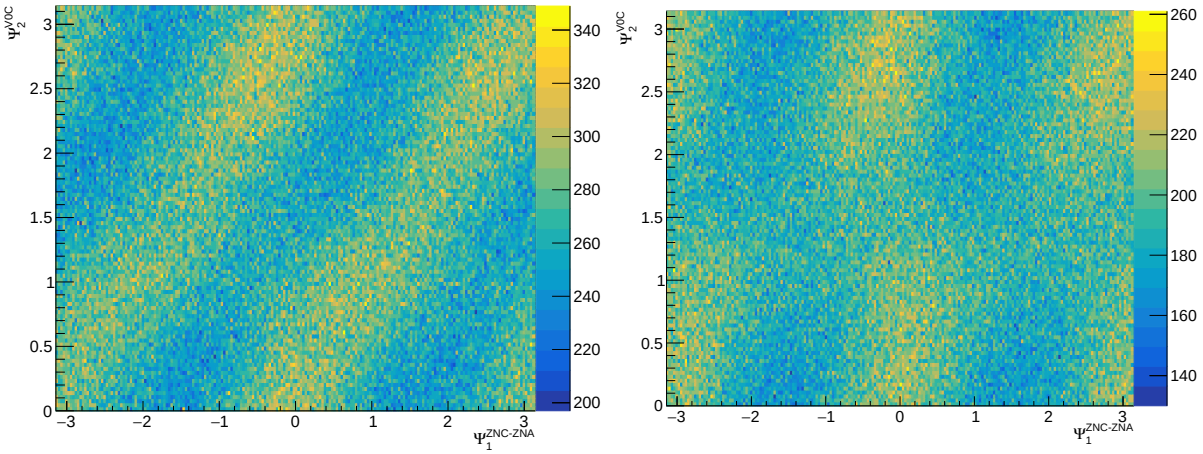

Figure 8.4: *Correlation between $\Psi_1^{ZNC-ZNA}$ and Ψ_2^{V0C} in the centrality class 0-10% for the LHC18q (left) and LHC18r (right) data sets.*

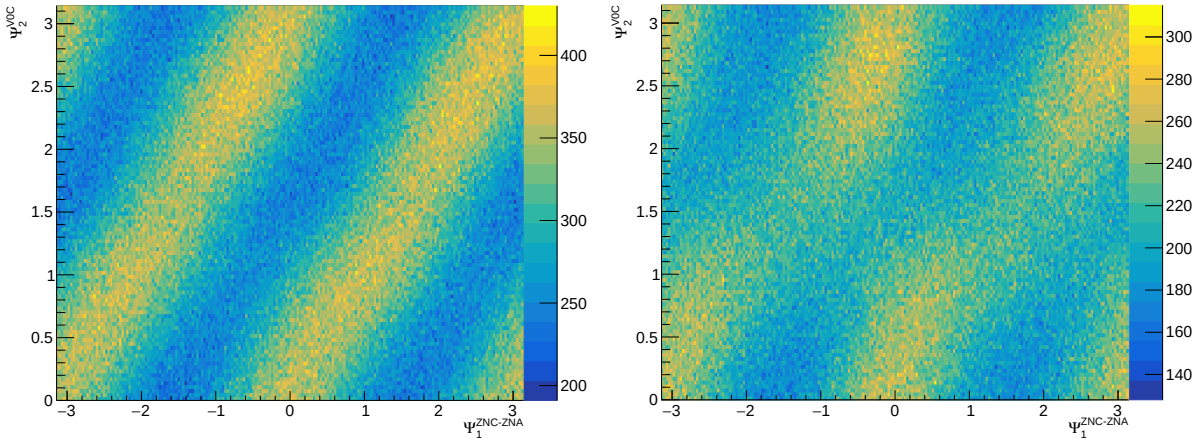

Figure 8.5: *Correlation between $\Psi_1^{ZNC-ZNA}$ and Ψ_2^{V0C} in the centrality class 10-20% for the LHC18q (left) and LHC18r (right) data sets.*

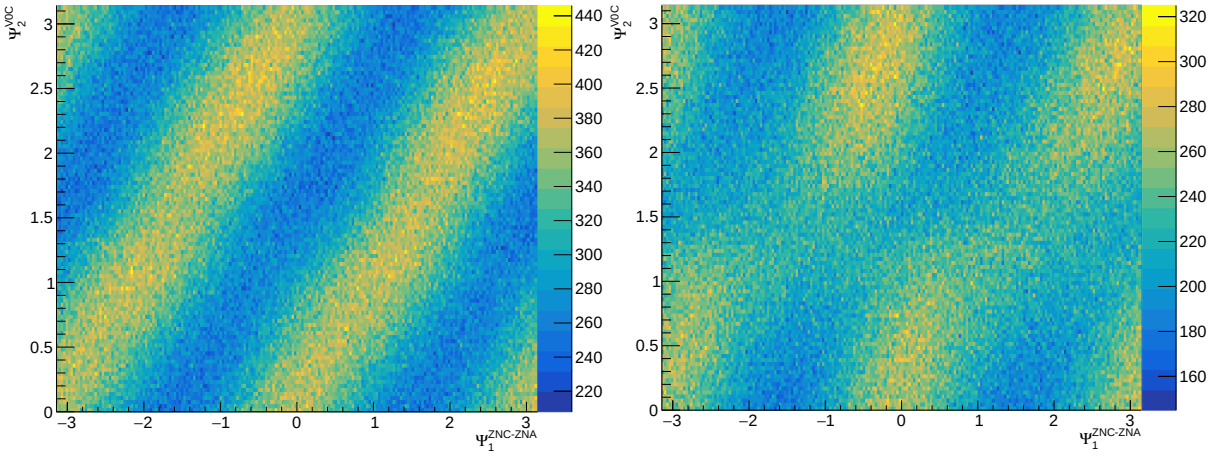

Figure 8.6: *Correlation between $\Psi_1^{ZNC-ZNA}$ and Ψ_2^{V0C} in the centrality class 20-30% for the LHC18q (left) and LHC18r (right) data sets.*

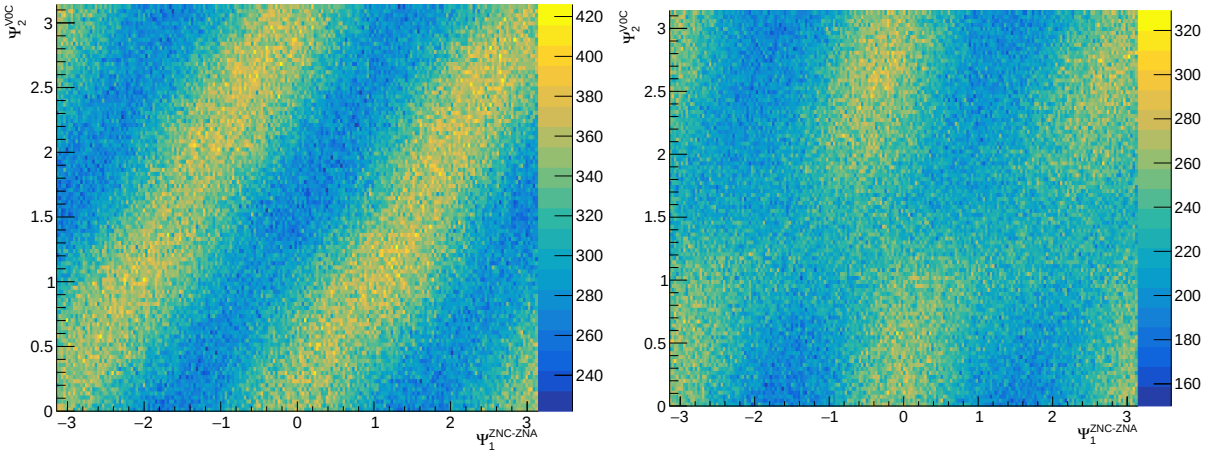

Figure 8.7: *Correlation between $\Psi_1^{ZNC-ZNA}$ and Ψ_2^{V0C} in the centrality class 30-40% for the LHC18q (left) and LHC18r (right) data sets.*

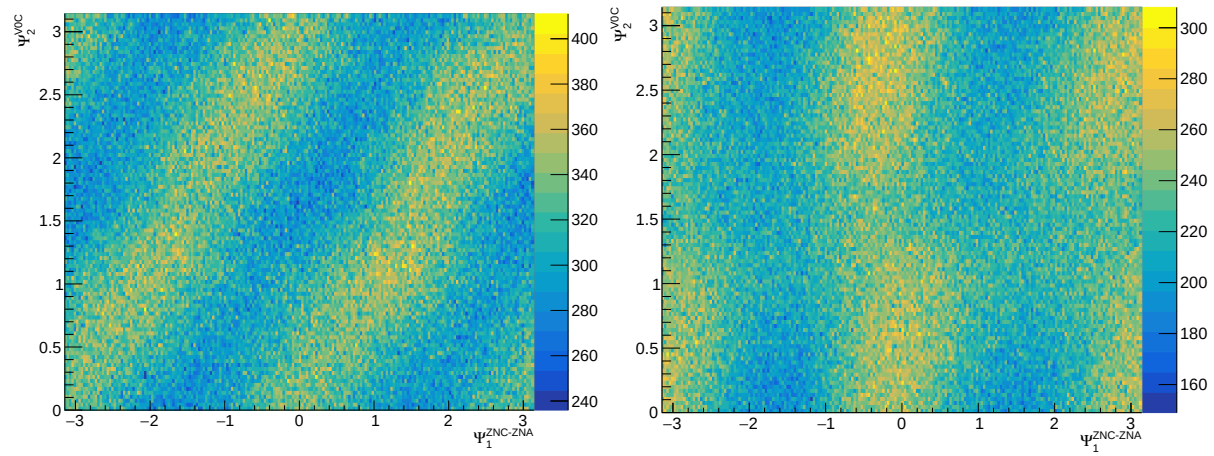

Figure 8.8: *Correlation between $\Psi_1^{ZNC-ZNA}$ and Ψ_2^{V0C} in the centrality class 40-50% for the LHC18q (left) and LHC18r (right) data sets.*

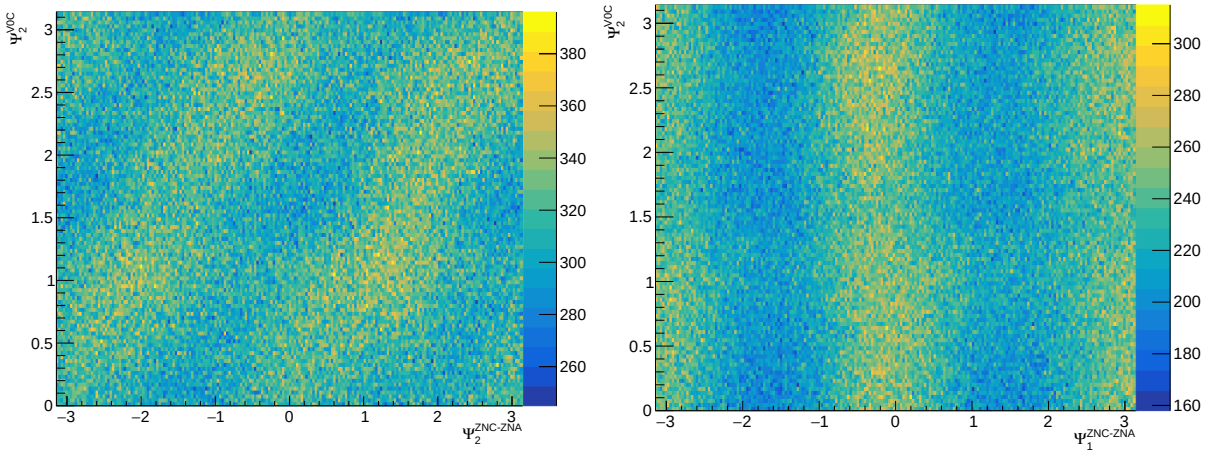

Figure 8.9: *Correlation between $\Psi_1^{ZNC-ZNA}$ and Ψ_2^{V0C} in the centrality class 50-60% for the LHC18q (left) and LHC18r (right) data sets.*

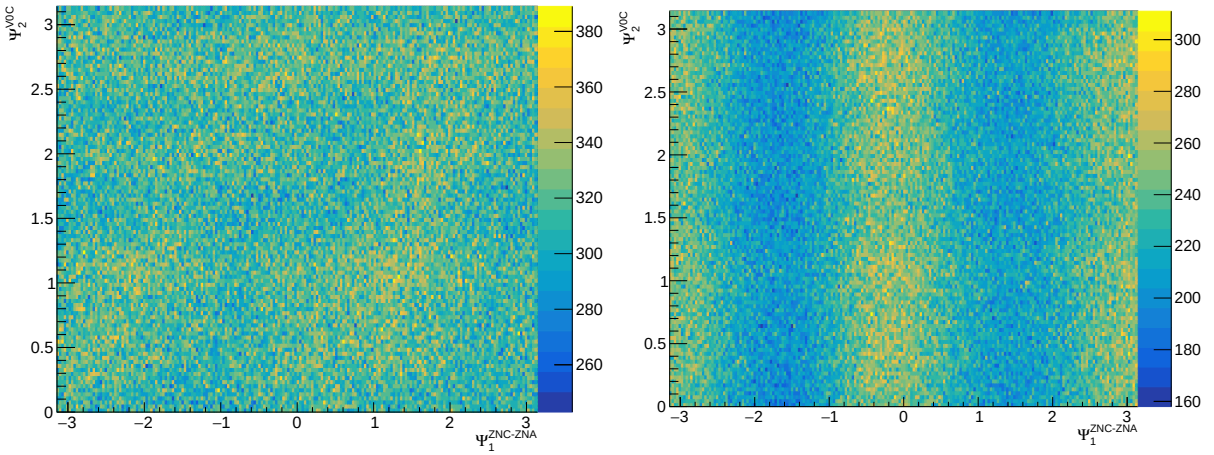

Figure 8.10: *Correlation between $\Psi_1^{ZNC-ZNA}$ and Ψ_2^{V0C} in the centrality class 60-70% for the LHC18q (left) and LHC18r (right) data sets.*

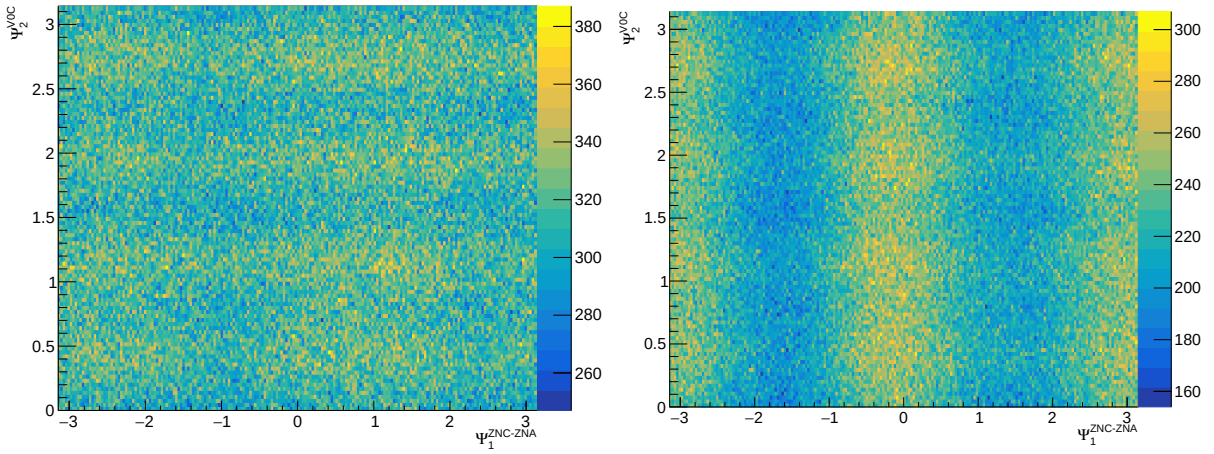

Figure 8.11: *Correlation between $\Psi_1^{ZNC-ZNA}$ and Ψ_2^{V0C} in the centrality class 70-80% for the LHC18q (left) and LHC18r (right) data sets.*

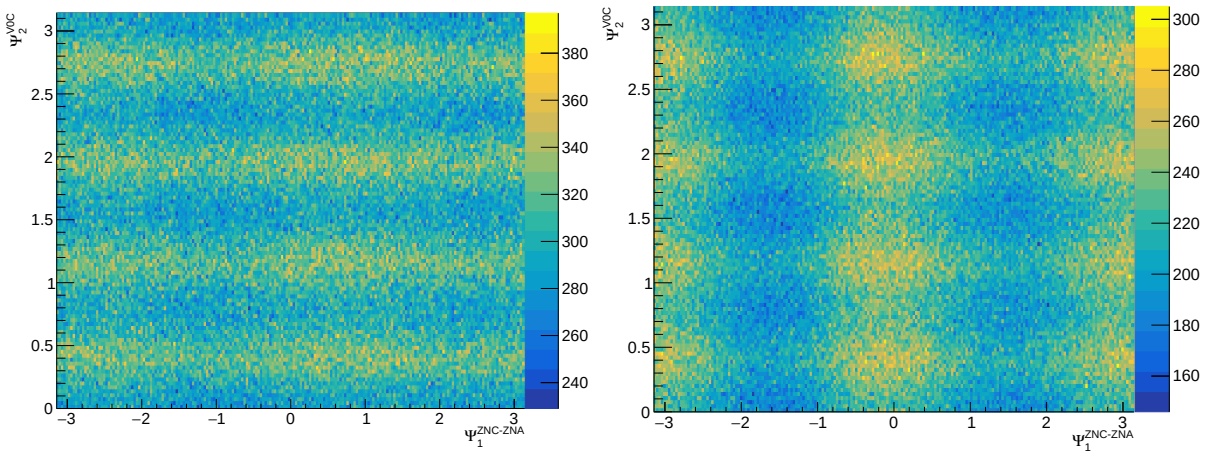

Figure 8.12: *Correlation between $\Psi_1^{ZNC\text{-}ZNA}$ and Ψ_2^{V0C} in the centrality class 80-90% for the LHC18q (left) and LHC18r (right) data sets.*

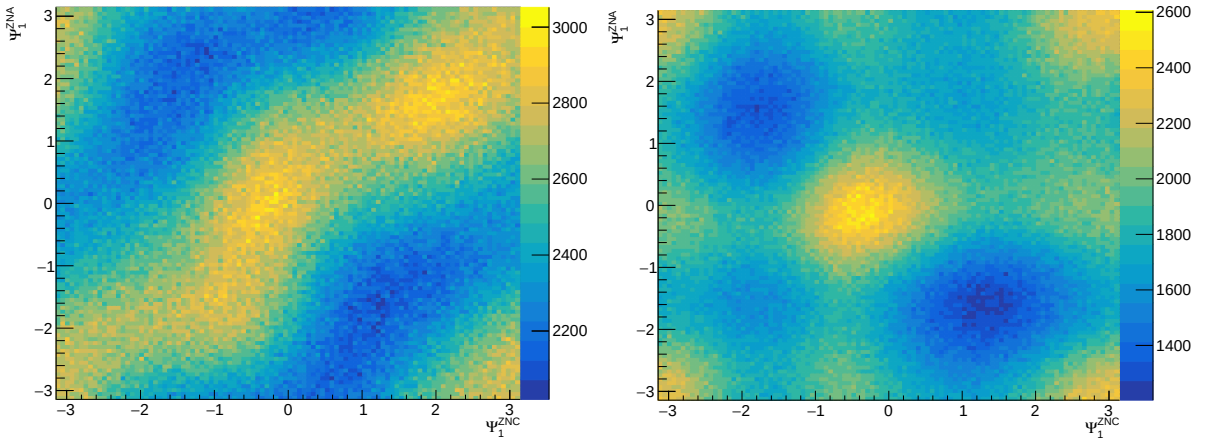

Figure 8.13: *Correlation between Ψ_1^{ZNC} and Ψ_1^{ZNA} in the centrality class 10-50% for the LHC18q (left) and LHC18r (right) data sets.*

8.3 Systematic uncertainty of other two choices of double ratio: ZDC/V0A and ZDC/TPC

This appendix shows the value of B_{total} for each systematic variation, except for ZDC cross correlation, for the other two choices of double ratio: ZDC/V0A and ZDC/TPC.

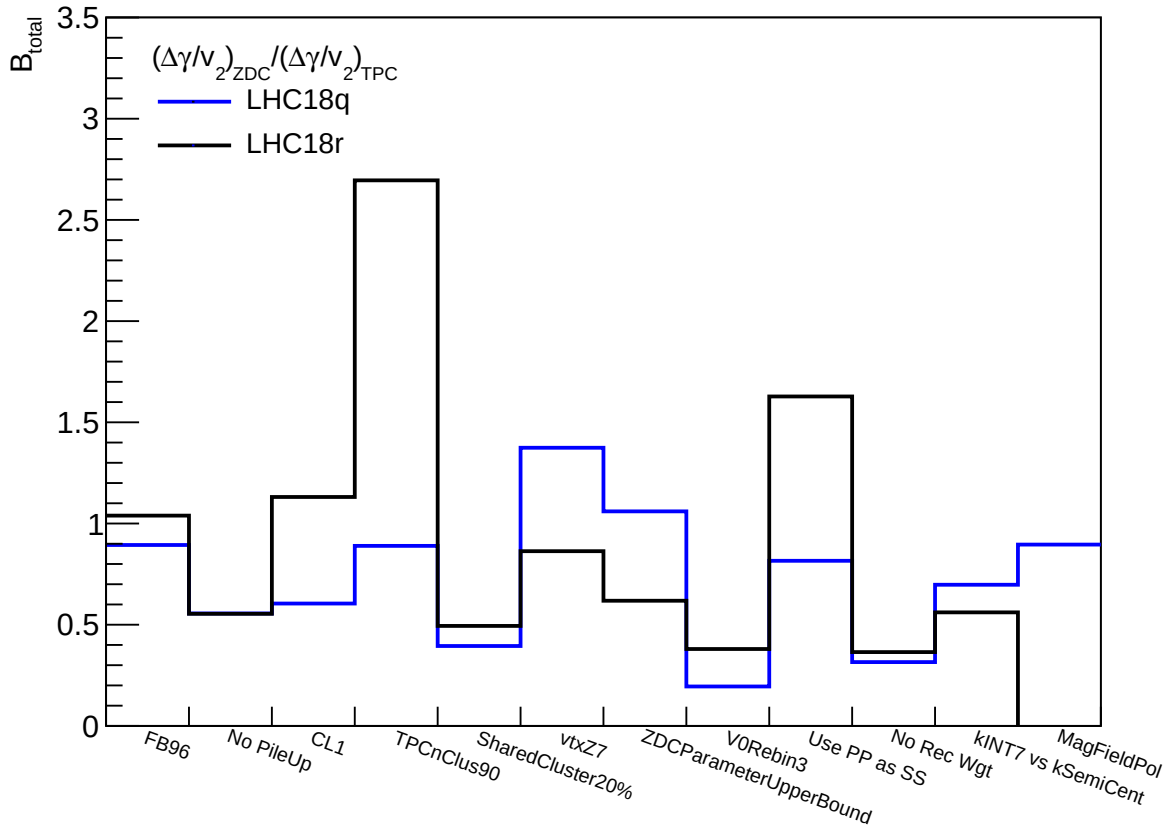

Figure 8.14: *The magnitude of B_{total} for each systematic variation affecting the value of $(\Delta\gamma/v_2)_{ZDC}/(\Delta\gamma/v_2)_{TPC}$, except for ZDC cross correlation, in the LHC18q (blue) and LHC18r (black) data sets.*

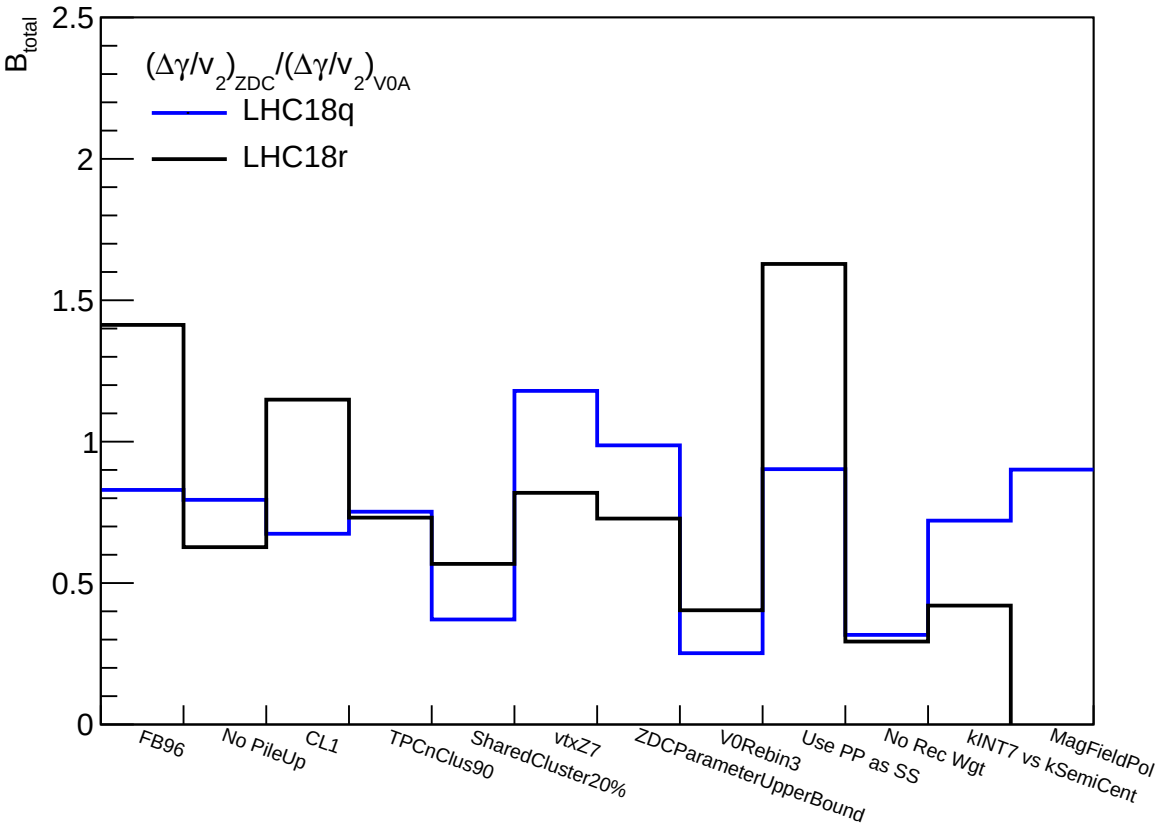

Figure 8.15: *The magnitude of B_{total} for each systematic variation affecting the value of $(\Delta\gamma/v_2)_{ZDC}/(\Delta\gamma/v_2)_{V0A}$, except for ZDC cross correlation, in the LHC18q (blue) and LHC18r (black) data sets.*

Bibliography

[1] P. Skands, "Introduction to QCD," in *Theoretical Advanced Study Institute in Elementary Particle Physics: Searching for New Physics at Small and Large Scales*, pp. 341–420. 2013. arXiv:1207.2389 [hep-ph].

[2] D. Griffiths, *Introduction to elementary particles*. 2008.

[3] R. K. Ellis, W. J. Stirling, and B. R. Webber, *QCD and collider physics*, vol. 8. Cambridge University Press, 2, 2011.

[4] E. D. Bloom *et al.*, "High-Energy Inelastic e p Scattering at 6-Degrees and 10-Degrees," *Phys. Rev. Lett.* **23** (1969) 930–934.

[5] M. Breidenbach, J. I. Friedman, H. W. Kendall, E. D. Bloom, D. H. Coward, H. C. DeStaebler, J. Drees, L. W. Mo, and R. E. Taylor, "Observed behavior of highly inelastic electron-proton scattering," *Phys. Rev. Lett.* **23** (1969) 935–939.

[6] **ALICE** Collaboration, "Search for the Chiral Magnetic Effect with charge-dependent azimuthal correlations in Xe-Xe collisions at $\sqrt{s_{\rm NN}} = 5.44$ TeV," arXiv:2210.15383 [nucl-ex].

[7] G. Eichmann, "http://cftp.ist.utl.pt/~gernot.eichmann/2014-hadron-physics/hadron-part-1.pdf," 2014.

[8] D. Tong, *Lectures on Gauge Theory*. 2018.

[9] D. Kharzeev, "Parity violation in hot QCD: Why it can happen, and how to look for it," *Phys. Lett. B* **633** (2006) 260–264, arXiv:hep-ph/0406125.

[10] D. E. Kharzeev, "Topologically induced local P and CP violation in QCD x QED," *Annals Phys.* **325** (2010) 205–218, arXiv:0911.3715 [hep-ph].

[11] H. Forkel, "A Primer on instantons in QCD," arXiv:hep-ph/0009136.

[12] D. E. Kharzeev, L. D. McLerran, and H. J. Warringa, "The Effects of topological charge change in heavy ion collisions: 'Event by event P and CP violation'," *Nucl. Phys. A* **803** (2008) 227–253, arXiv:0711.0950 [hep-ph].

[13] G. 't Hooft, "Computation of the Quantum Effects Due to a Four-Dimensional Pseudoparticle," *Phys. Rev. D* **14** (1976) 3432–3450. [Erratum: Phys.Rev.D 18, 2199 (1978)].

[14] T. Schäfer and E. V. Shuryak, "Instantons in QCD," *Rev. Mod. Phys.* **70** (1998) 323–426, arXiv:hep-ph/9610451.

[15] R. Jackiw and C. Rebbi, "Vacuum Periodicity in a Yang-Mills Quantum Theory," *Phys. Rev. Lett.* **37** (1976) 172–175.

[16] K. Huang, *QUARKS, LEPTONS AND GAUGE FIELDS*. World Scientific, 1992.

[17] R. Rajaraman, *SOLITONS AND INSTANTONS. AN INTRODUCTION TO SOLITONS AND INSTANTONS IN QUANTUM FIELD THEORY*. 1982.

[18] G. 't Hooft, "Monopoles, instantons and confinement," in *National Summer School for Graduate Students: We-Heraeus Doktorandenschule Saalburg: Grundlagen und Neue Methoden der Theoretischen Physik*. 9, 1999. arXiv:hep-th/0010225.

[19] S. Amoroso, D. Kar, and M. Schott, "How to discover QCD Instantons at the LHC," *Eur. Phys. J. C* **81** no. 7, (2021) 624, arXiv:2012.09120 [hep-ph].

[20] C. A. Baker *et al.*, "An Improved experimental limit on the electric dipole moment of the neutron," *Phys. Rev. Lett.* **97** (2006) 131801, arXiv:hep-ex/0602020.

[21] D. Kharzeev and A. Zhitnitsky, "Charge separation induced by P-odd bubbles in QCD matter," *Nucl. Phys. A* **797** (2007) 67–79, arXiv:0706.1026 [hep-ph].

[22] R. D. Peccei and H. R. Quinn, "Constraints Imposed by CP Conservation in the Presence of Instantons," *Phys. Rev. D* **16** (1977) 1791–1797.

[23] J. E. Kim, "Weak Interaction Singlet and Strong CP Invariance," *Phys. Rev. Lett.* **43** (1979) 103.

[24] M. A. Shifman, A. I. Vainshtein, and V. I. Zakharov, "Can Confinement Ensure Natural CP Invariance of Strong Interactions?," *Nucl. Phys. B* **166** (1980) 493–506.

[25] A. R. Zhitnitsky, "On Possible Suppression of the Axion Hadron Interactions. (In Russian)," *Sov. J. Nucl. Phys.* **31** (1980) 260.

[26] M. Dine, W. Fischler, and M. Srednicki, "A Simple Solution to the Strong CP Problem with a Harmless Axion," *Phys. Lett. B* **104** (1981) 199–202.

[27] A. A. Belavin, A. M. Polyakov, A. S. Schwartz, and Y. S. Tyupkin, "Pseudoparticle Solutions of the Yang-Mills Equations," *Phys. Lett. B* **59** (1975) 85–87.

[28] N. S. Manton, "Topology in the Weinberg-Salam Theory," *Phys. Rev. D* **28** (1983) 2019.

[29] F. R. Klinkhamer and N. S. Manton, "A Saddle Point Solution in the Weinberg-Salam Theory," *Phys. Rev. D* **30** (1984) 2212.

[30] G. 't Hooft, "Symmetry Breaking Through Bell-Jackiw Anomalies," *Phys. Rev. Lett.* **37** (1976) 8–11.

[31] S. R. Coleman, "The Uses of Instantons," *Subnucl. Ser.* **15** (1979) 805.

[32] H. J. Warringa, "Implications of CP-violating transitions in hot quark matter on heavy ion collisions," *J. Phys. G* **35** (2008) 104012, arXiv:0805.1384 [hep-ph].

[33] Y. Sakai, H. Kouno, T. Sasaki, and M. Yahiro, "Theta vacuum effects on QCD phase diagram," *Phys. Lett. B* **705** (2011) 349–355, arXiv:1105.0413 [hep-ph].

[34] L. D. McLerran, E. Mottola, and M. E. Shaposhnikov, "Sphalerons and Axion Dynamics in High Temperature QCD," *Phys. Rev. D* **43** (1991) 2027–2035.

[35] G. D. Moore, "Computing the strong sphaleron rate," *Phys. Lett. B* **412** (1997) 359–370, arXiv:hep-ph/9705248.

[36] G. D. Moore, C.-r. Hu, and B. Muller, "Chern-Simons number diffusion with hard thermal loops," *Phys. Rev. D* **58** (1998) 045001, arXiv:hep-ph/9710436.

[37] G. D. Moore, "Do we understand the sphaleron rate?," in *4th International Conference on Strong and Electroweak Matter*, pp. 82–94. 6, 2000. arXiv:hep-ph/0009161.

[38] M. Mace, S. Schlichting, and R. Venugopalan, "Off-equilibrium sphaleron transitions in the Glasma," *Phys. Rev. D* **93** no. 7, (2016) 074036, arXiv:1601.07342 [hep-ph].

[39] J. Brewer, A. Mazeliauskas, and W. van der Schee, "Opportunities of OO and pO collisions at the LHC," in *Opportunities of OO and pO collisions at the LHC*. 3, 2021. arXiv:2103.01939 [hep-ph].

[40] W. Busza, K. Rajagopal, and W. van der Schee, "Heavy Ion Collisions: The Big Picture, and the Big Questions," *Ann. Rev. Nucl. Part. Sci.* **68** (2018) 339–376, arXiv:1802.04801 [hep-ph].

[41] **ALICE** Collaboration, "The ALICE experiment – A journey through QCD," arXiv:2211.04384 [nucl-ex].

[42] J. J. Ethier and E. R. Nocera, "Parton Distributions in Nucleons and Nuclei," *Ann. Rev. Nucl. Part. Sci.* **70** (2020) 43–76, arXiv:2001.07722 [hep-ph].

[43] M. L. Miller, K. Reygers, S. J. Sanders, and P. Steinberg, "Glauber modeling in high energy nuclear collisions," *Ann. Rev. Nucl. Part. Sci.* **57** (2007) 205–243, arXiv:nucl-ex/0701025.

[44] B. Schenke, P. Tribedy, and R. Venugopalan, "Fluctuating Glasma initial conditions and flow in heavy ion collisions," *Phys. Rev. Lett.* **108** (2012) 252301, arXiv:1202.6646 [nucl-th].

[45] H. Niemi, K. J. Eskola, and R. Paatelainen, "Event-by-event fluctuations in a perturbative QCD + saturation + hydrodynamics model: Determining QCD matter shear viscosity in ultrarelativistic heavy-ion collisions," *Phys. Rev. C* **93** no. 2, (2016) 024907, arXiv:1505.02677 [hep-ph].

[46] H.-J. Drescher and Y. Nara, "Eccentricity fluctuations from the color glass condensate at RHIC and LHC," *Phys. Rev. C* **76** (2007) 041903, arXiv:0707.0249 [nucl-th].

[47] J. L. ALbacete and A. Dumitru, "A model for gluon production in heavy-ion collisions at the LHC with rcBK unintegrated gluon densities," arXiv:1011.5161 [hep-ph].

[48] **HotQCD** Collaboration, A. Bazavov *et al.*, "Equation of state in (2+1)-flavor QCD," *Phys. Rev. D* **90** (2014) 094503, arXiv:1407.6387 [hep-lat].

[49] P. Romatschke and U. Romatschke, "Viscosity Information from Relativistic Nuclear Collisions: How Perfect is the Fluid Observed at RHIC?," *Phys. Rev. Lett.* **99** (2007) 172301, arXiv:0706.1522 [nucl-th].

[50] J. E. Bernhard, J. S. Moreland, S. A. Bass, J. Liu, and U. Heinz, "Applying Bayesian parameter estimation to relativistic heavy-ion collisions: simultaneous characterization of the initial state and quark-gluon plasma medium," *Phys. Rev. C* **94** no. 2, (2016) 024907, arXiv:1605.03954 [nucl-th].

[51] D. H. Rischke, S. Bernard, and J. A. Maruhn, "Relativistic hydrodynamics for heavy ion collisions. 1. General aspects and expansion into vacuum," *Nucl. Phys. A* **595** (1995) 346–382, arXiv:nucl-th/9504018.

[52] D. H. Rischke, Y. Pursun, and J. A. Maruhn, "Relativistic hydrodynamics for heavy ion collisions. 2. Compression of nuclear matter and the phase transition to the quark - gluon plasma," *Nucl. Phys. A* **595** (1995) 383–408, arXiv:nucl-th/9504021. [Erratum: Nucl.Phys.A 596, 717–717 (1996)].

[53] E. Shuryak, "Why does the quark gluon plasma at RHIC behave as a nearly ideal fluid?," *Prog. Part. Nucl. Phys.* **53** (2004) 273–303, arXiv:hep-ph/0312227.

[54] Y. Aoki, G. Endrodi, Z. Fodor, S. D. Katz, and K. K. Szabo, "The Order of the quantum chromodynamics transition predicted by the standard model of particle physics," *Nature* **443** (2006) 675–678, arXiv:hep-lat/0611014.

[55] J. Cleymans and K. Redlich, "Unified description of freezeout parameters in relativistic heavy ion collisions," *Phys. Rev. Lett.* **81** (1998) 5284–5286, arXiv:nucl-th/9808030.

[56] A. Andronic, P. Braun-Munzinger, K. Redlich, and J. Stachel, "Decoding the phase structure of QCD via particle production at high energy," *Nature* **561** no. 7723, (2018) 321–330, arXiv:1710.09425 [nucl-th].

[57] V. Greco, C. M. Ko, and P. Levai, "Parton coalescence and anti-proton / pion anomaly at RHIC," *Phys. Rev. Lett.* **90** (2003) 202302, arXiv:nucl-th/0301093.

[58] R. J. Fries, V. Greco, and P. Sorensen, "Coalescence Models For Hadron Formation From Quark Gluon Plasma," *Ann. Rev. Nucl. Part. Sci.* **58** (2008) 177–205, arXiv:0807.4939 [nucl-th].

[59] R. Pasechnik and M. Šumbera, "Phenomenological Review on Quark–Gluon Plasma: Concepts vs. Observations," *Universe* **3** no. 1, (2017) 7, arXiv:1611.01533 [hep-ph].

[60] **ALICE** Collaboration, S. Acharya *et al.*, "Symmetry plane correlations in Pb-Pb collisions at $\sqrt{s_{\rm NN}} = 2.76$TeV," *Eur. Phys. J. C* **83** no. 7, (2023) 576, arXiv:2302.01234 [nucl-ex].

[61] **JETSCAPE** Collaboration, D. Everett *et al.*, "Multisystem Bayesian constraints on the transport coefficients of QCD matter," *Phys. Rev. C* **103** no. 5, (2021) 054904, arXiv:2011.01430 [hep-ph].

[62] G. Nijs, W. van der Schee, U. Gürsoy, and R. Snellings, "Bayesian analysis of heavy ion collisions with the heavy ion computational framework Trajectum," *Phys. Rev. C* **103** no. 5, (2021) 054909, arXiv:2010.15134 [nucl-th].

[63] J. E. Parkkila, A. Onnerstad, S. F. Taghavi, C. Mordasini, A. Bilandzic, M. Virta, and D. J. Kim, "New constraints for QCD matter from improved Bayesian parameter estimation in heavy-ion collisions at LHC," *Phys. Lett. B* **835** (2022) 137485, arXiv:2111.08145 [hep-ph].

[64] V. Skokov, A. Y. Illarionov, and V. Toneev, "Estimate of the magnetic field strength in heavy-ion collisions," *Int. J. Mod. Phys. A* **24** (2009) 5925–5932, arXiv:0907.1396 [nucl-th].

[65] Y. Zhong, C.-B. Yang, X. Cai, and S.-Q. Feng, "A systematic study of magnetic field in Relativistic Heavy-ion Collisions in the RHIC and LHC energy regions," *Adv. High Energy Phys.* **2014** (2014) 193039, arXiv:1408.5694 [hep-ph].

[66] G. Inghirami, M. Mace, Y. Hirono, L. Del Zanna, D. E. Kharzeev, and M. Bleicher, "Magnetic fields in heavy ion collisions: flow and charge transport," *Eur. Phys. J. C* **80** no. 3, (2020) 293, arXiv:1908.07605 [hep-ph].

[67] W. Li and G. Wang, "Chiral Magnetic Effects in Nuclear Collisions," *Ann. Rev. Nucl. Part. Sci.* **70** (2020) 293–321, arXiv:2002.10397 [nucl-ex].

[68] A. Dubla, U. Gürsoy, and R. Snellings, "Charge-dependent flow as evidence of strong electromagnetic fields in heavy-ion collisions," *Mod. Phys. Lett. A* **35** no. 39, (2020) 2050324, arXiv:2009.09727 [hep-ph].

[69] U. Gursoy, D. Kharzeev, and K. Rajagopal, "Magnetohydrodynamics, charged currents and directed flow in heavy ion collisions," *Phys. Rev. C* **89** no. 5, (2014) 054905, arXiv:1401.3805 [hep-ph].

[70] U. Gürsoy, D. Kharzeev, E. Marcus, K. Rajagopal, and C. Shen, "Charge-dependent Flow Induced by Magnetic and Electric Fields in Heavy Ion Collisions," *Phys. Rev. C* **98** no. 5, (2018) 055201, arXiv:1806.05288 [hep-ph].

[71] H. T. Ding, A. Francis, O. Kaczmarek, F. Karsch, E. Laermann, and W. Soeldner, "Thermal dilepton rate and electrical conductivity: An analysis of vector current correlation functions in quenched lattice QCD," *Phys. Rev. D* **83** (2011) 034504, arXiv:1012.4963 [hep-lat].

[72] A. Francis and O. Kaczmarek, "On the temperature dependence of the electrical conductivity in hot quenched lattice QCD," *Prog. Part. Nucl. Phys.* **67** (2012) 212–217, arXiv:1112.4802 [hep-lat].

[73] A. Amato, G. Aarts, C. Allton, P. Giudice, S. Hands, and J.-I. Skullerud, "Electrical conductivity of the quark-gluon plasma across the deconfinement transition," *Phys. Rev. Lett.* **111** no. 17, (2013) 172001, arXiv:1307.6763 [hep-lat].

[74] P. V. Buividovich, D. Smith, and L. von Smekal, "Electric conductivity in finite-density $SU(2)$ lattice gauge theory with dynamical fermions," *Phys. Rev. D* **102** no. 9, (2020) 094510, arXiv:2007.05639 [hep-lat].

[75] G. Aarts and A. Nikolaev, "Electrical conductivity of the quark-gluon plasma: perspective from lattice QCD," *Eur. Phys. J. A* **57** no. 4, (2021) 118, arXiv:2008.12326 [hep-lat].

[76] S. K. Das, S. Plumari, S. Chatterjee, J. Alam, F. Scardina, and V. Greco, "Directed Flow of Charm Quarks as a Witness of the Initial Strong Magnetic Field in Ultra-Relativistic Heavy Ion Collisions," *Phys. Lett. B* **768** (2017) 260–264, arXiv:1608.02231 [nucl-th].

[77] **ALICE** Collaboration, S. Acharya *et al.*, "Probing the effects of strong electromagnetic fields with charge-dependent directed flow in Pb-Pb collisions at the LHC," *Phys. Rev. Lett.* **125** no. 2, (2020) 022301, arXiv:1910.14406 [nucl-ex].

[78] **STAR** Collaboration, L. Adamczyk *et al.*, "Beam-Energy Dependence of the Directed Flow of Protons, Antiprotons, and Pions in Au+Au Collisions," *Phys. Rev. Lett.* **112** no. 16, (2014) 162301, arXiv:1401.3043 [nucl-ex].

[79] **STAR** Collaboration, J. Adam *et al.*, "First Observation of the Directed Flow of D^0 and $\overline{D^0}$ in Au+Au Collisions at $\sqrt{s_{\rm NN}}$ = 200 GeV," *Phys. Rev. Lett.* **123** no. 16, (2019) 162301, arXiv:1905.02052 [nucl-ex].

[80] F. Becattini, I. Karpenko, M. Lisa, I. Upsal, and S. Voloshin, "Global hyperon polarization at local thermodynamic equilibrium with vorticity, magnetic field and feed-down," *Phys. Rev. C* **95** no. 5, (2017) 054902, arXiv:1610.02506 [nucl-th].

[81] **ALICE** Collaboration, S. Acharya *et al.*, "Global polarization of $\Lambda\bar{\Lambda}$ hyperons in Pb-Pb collisions at $\sqrt{s_{NN}}$ = 2.76 and 5.02 TeV," *Phys. Rev. C* **101** no. 4, (2020) 044611, arXiv:1909.01281 [nucl-ex]. [Erratum: Phys.Rev.C 105, 029902 (2022)].

[82] **STAR** Collaboration, L. Adamczyk *et al.*, "Global Λ hyperon polarization in nuclear collisions: evidence for the most vortical fluid," *Nature* **548** (2017) 62–65, arXiv:1701.06657 [nucl-ex].

[83] S. A. Voloshin, "Vorticity and particle polarization in heavy ion collisions (experimental perspective)," *EPJ Web Conf.* **171** (2018) 07002, arXiv:1710.08934 [nucl-ex].

[84] K. Fukushima, D. E. Kharzeev, and H. J. Warringa, "The Chiral Magnetic Effect," *Phys. Rev. D* **78** (2008) 074033, arXiv:0808.3382 [hep-ph].

[85] D. E. Kharzeev, J. Liao, S. A. Voloshin, and G. Wang, "Chiral magnetic and vortical effects in high-energy nuclear collisions—A status report," *Prog. Part. Nucl. Phys.* **88** (2016) 1–28, arXiv:1511.04050 [hep-ph].

[86] S. A. Voloshin, "Parity violation in hot QCD: How to detect it," *Phys. Rev. C* **70** (2004) 057901, arXiv:hep-ph/0406311.

[87] **STAR** Collaboration, B. I. Abelev *et al.*, "Azimuthal Charged-Particle Correlations and Possible Local Strong Parity Violation," *Phys. Rev. Lett.* **103** (2009) 251601, arXiv:0909.1739 [nucl-ex].

[88] **STAR** Collaboration, B. I. Abelev *et al.*, "Observation of charge-dependent azimuthal correlations and possible local strong parity violation in heavy ion collisions," *Phys. Rev. C* **81** (2010) 054908, arXiv:0909.1717 [nucl-ex].

[89] **ALICE** Collaboration, K. Aamodt *et al.*, "Centrality dependence of the charged-particle multiplicity density at mid-rapidity in Pb-Pb collisions at $\sqrt{s_{NN}} = 2.76$ TeV," *Phys. Rev. Lett.* **106** (2011) 032301, arXiv:1012.1657 [nucl-ex].

[90] **ALICE** Collaboration, S. Acharya *et al.*, "Constraining the Chiral Magnetic Effect with charge-dependent azimuthal correlations in Pb-Pb collisions at $\sqrt{s_{\rm NN}}$ = 2.76 and 5.02 TeV," *JHEP* **09** (2020) 160, arXiv:2005.14640 [nucl-ex].

[91] **CMS** Collaboration, V. Khachatryan *et al.*, "Observation of charge-dependent azimuthal correlations in p-Pb collisions and its implication for the search for the chiral magnetic effect," *Phys. Rev. Lett.* **118** no. 12, (2017) 122301, arXiv:1610.00263 [nucl-ex].

[92] **ALICE** Collaboration, S. Aziz, "Search for the Chiral Magnetic Effect with the ALICE detector," *Nucl. Phys. A* **1005** (2021) 121817, arXiv:2005.06177 [hep-ex].

[93] S. Pratt, S. Schlichting, and S. Gavin, "Effects of Momentum Conservation and Flow on Angular Correlations at RHIC," *Phys. Rev. C* **84** (2011) 024909, arXiv:1011.6053 [nucl-th].

[94] S. Pratt, "Alternative Contributions to the Angular Correlations Observed at RHIC Associated with Parity Fluctuations," arXiv:1002.1758 [nucl-th].

[95] S. Schlichting and S. Pratt, "Charge conservation at energies available at the BNL Relativistic Heavy Ion Collider and contributions to local parity violation observables," *Phys. Rev. C* **83** (2011) 014913, arXiv:1009.4283 [nucl-th].

[96] **ALICE** Collaboration, S. Acharya *et al.*, "Constraining the magnitude of the Chiral Magnetic Effect with Event Shape Engineering in Pb-Pb collisions at $\sqrt{s_{\rm NN}}$ = 2.76 TeV," *Phys. Lett. B* **777** (2018) 151–162, arXiv:1709.04723 [nucl-ex].

[97] **CMS** Collaboration, A. M. Sirunyan *et al.*, "Constraints on the chiral magnetic effect using charge-dependent azimuthal correlations in pPb and PbPb collisions at the CERN Large Hadron Collider," *Phys. Rev. C* **97** no. 4, (2018) 044912, arXiv:1708.01602 [nucl-ex].

[98] J. Schukraft, A. Timmins, and S. A. Voloshin, "Ultra-relativistic nuclear collisions: event shape engineering," *Phys. Lett. B* **719** (2013) 394–398, arXiv:1208.4563 [nucl-ex].

[99] **STAR** Collaboration, M. S. Abdallah *et al.*, "Pair invariant mass to isolate background in the search for the chiral magnetic effect in Au + Au collisions at sNN=200 GeV," *Phys. Rev. C* **106** no. 3, (2022) 034908, arXiv:2006.05035 [nucl-ex].

[100] W.-T. Deng, X.-G. Huang, G.-L. Ma, and G. Wang, "Test the chiral magnetic effect with isobaric collisions," *Phys. Rev. C* **94** (2016) 041901, arXiv:1607.04697 [nucl-th].

[101] **STAR** Collaboration, M. Abdallah *et al.*, "Search for the chiral magnetic effect with isobar collisions at $\sqrt{s_{NN}}$=200 GeV by the STAR Collaboration at the BNL Relativistic Heavy Ion Collider," *Phys. Rev. C* **105** no. 1, (2022) 014901, arXiv:2109.00131 [nucl-ex].

[102] D. E. Kharzeev, J. Liao, and S. Shi, "Implications of the isobar-run results for the chiral magnetic effect in heavy-ion collisions," *Phys. Rev. C* **106** no. 5, (2022) L051903, arXiv:2205.00120 [nucl-th].

[103] **STAR** Collaboration, M. S. Abdallah *et al.*, "Search for the Chiral Magnetic Effect via Charge-Dependent Azimuthal Correlations Relative to Spectator and Participant Planes in Au+Au Collisions at $\sqrt{s_{NN}}$ = 200 GeV," *Phys. Rev. Lett.* **128** no. 9, (2022) 092301, arXiv:2106.09243 [nucl-ex].

[104] H.-j. Xu, J. Zhao, X. Wang, H. Li, Z.-W. Lin, C. Shen, and F. Wang, "Varying the chiral magnetic effect relative to flow in a single nucleus-nucleus collision," *Chin. Phys. C* **42** no. 8, (2018) 084103, arXiv:1710.07265 [nucl-th].

[105] S. A. Voloshin, "Estimate of the signal from the chiral magnetic effect in heavy-ion collisions from measurements relative to the participant and spectator flow planes," *Phys. Rev. C* **98** no. 5, (2018) 054911, arXiv:1805.05300 [nucl-ex].

[106] **ATLAS** Collaboration, G. Aad *et al.*, "The ATLAS Experiment at the CERN Large Hadron Collider," *JINST* **3** (2008) S08003.

[107] **CMS** Collaboration, S. Chatrchyan *et al.*, "The CMS Experiment at the CERN LHC," *JINST* **3** (2008) S08004.

[108] **LHCb** Collaboration, A. A. Alves, Jr. *et al.*, "The LHCb Detector at the LHC," *JINST* **3** (2008) S08005.

[109] "LHC Machine," *JINST* **3** (2008) S08001.

[110] E. Lopienska, "The CERN accelerator complex, layout in 2022. Complexe des accélérateurs du CERN en janvier 2022,". https://cds.cern.ch/record/2800984. General Photo.

[111] **ALICE** Collaboration, K. Aamodt *et al.*, "The ALICE experiment at the CERN LHC," *JINST* **3** (2008) S08002.

[112] **ALICE** Collaboration, B. B. Abelev *et al.*, "Performance of the ALICE Experiment at the CERN LHC," *Int. J. Mod. Phys. A* **29** (2014) 1430044, arXiv:1402.4476 [nucl-ex].

[113] **ALICE** Collaboration, P. Cortese *et al.*, "ALICE: Physics performance report, volume I," *J. Phys. G* **30** (2004) 1517–1763.

[114] **ALICE** Collaboration, C. W. Fabjan *et al.*, "ALICE: Physics Performance Report," *J. Phys. G* **32** (2006) 1295–2040.

[115] **ALICE** Collaboration, J. Adam *et al.*, "Centrality dependence of the pseudorapidity density distribution for charged particles in Pb-Pb collisions at $\sqrt{s_{\rm NN}} = 5.02$ TeV," *Phys. Lett. B* **772** (2017) 567–577, arXiv:1612.08966 [nucl-ex].

[116] **ALICE** Collaboration, G. Dellacasa *et al.*, "ALICE technical design report of the inner tracking system (ITS),".

[117] **ALICE** Collaboration, "Alignment of the ALICE Inner Tracking System with cosmic-ray tracks," *JINST* **5** (2010) P03003, arXiv:1001.0502 [physics.ins-det].

[118] **ALICE** Collaboration, G. Dellacasa *et al.*, "ALICE: Technical design report of the time projection chamber,".

[119] **ALICE** Collaboration, A. Toia, "Bulk Properties of Pb-Pb collisions at $\sqrt{s_{NN}} = 2.76$ TeV measured by ALICE," *J. Phys. G* **38** (2011) 124007, arXiv:1107.1973 [nucl-ex].

[120] J. Alme *et al.*, "The ALICE TPC, a large 3-dimensional tracking device with fast readout for ultra-high multiplicity events," *Nucl. Instrum. Meth. A* **622** (2010) 316–367, arXiv:1001.1950 [physics.ins-det].

[121] **ALICE** Collaboration, P. Cortese *et al.*, "ALICE technical design report on forward detectors: FMD, T0 and V0,".

[122] **ALICE** Collaboration, E. Abbas *et al.*, "Performance of the ALICE VZERO system," *JINST* **8** (2013) P10016, arXiv:1306.3130 [nucl-ex].

[123] **ALICE** Collaboration, G. Dellacasa *et al.*, "ALICE technical design report of the zero degree calorimeter (ZDC),".

[124] R. Arnaldi *et al.*, "The Zero degree calorimeters for the ALICE experiment," *Nucl. Instrum. Meth. A* **581** (2007) 397–401. [Erratum: Nucl.Instrum.Meth.A 604, 765 (2009)].

[125] "LHC Design Report Vol.1: The LHC Main Ring,".

[126] R. Gemme, *Study of the ALICE ZDC detector performance*. PhD thesis, Turin U., 2006.

[127] **ALICE** Collaboration, G. Dellacasa *et al.*, "The neutron zero degree calorimeter for the ALICE experiment," *Nucl. Instrum. Meth. A* **564** (2006) 235–242.

[128] A. D. P. Group, "https://twiki.cern.ch/twiki/bin/view/ALICE/AliDPGtoolsPhysSel," 2021.

[129] **ALICE** Collaboration, B. Abelev *et al.*, "Centrality determination of Pb-Pb collisions at $\sqrt{s_{NN}}$ = 2.76 TeV with ALICE," *Phys. Rev. C* **88** no. 4, (2013) 044909, arXiv:1301.4361 [nucl-ex].

[130] A. M. Poskanzer and S. A. Voloshin, "Methods for analyzing anisotropic flow in relativistic nuclear collisions," *Phys. Rev. C* **58** (1998) 1671–1678, arXiv:nucl-ex/9805001.

[131] N. Borghini, P. M. Dinh, and J.-Y. Ollitrault, "A New method for measuring azimuthal distributions in nucleus-nucleus collisions," *Phys. Rev. C* **63** (2001) 054906, arXiv:nucl-th/0007063.

[132] A. Bilandzic, R. Snellings, and S. Voloshin, "Flow analysis with cumulants: Direct calculations," *Phys. Rev. C* **83** (2011) 044913, arXiv:1010.0233 [nucl-ex].

[133] A. Bilandzic, C. H. Christensen, K. Gulbrandsen, A. Hansen, and Y. Zhou, "Generic framework for anisotropic flow analyses with multiparticle azimuthal correlations," *Phys. Rev. C* **89** no. 6, (2014) 064904, arXiv:1312.3572 [nucl-ex].

[134] M. Gyulassy and X.-N. Wang, "HIJING 1.0: A Monte Carlo program for parton and particle production in high-energy hadronic and nuclear collisions," *Comput. Phys. Commun.* **83** (1994) 307, arXiv:nucl-th/9502021.

[135] R. Brun, F. Bruyant, M. Maire, A. C. McPherson, and P. Zanarini, "GEANT3,".

[136] J. Margutti, *Rotating planes, fluctuating shapes : Anisotropic flow and magnetic fields in heavy-ion collisions*. PhD thesis, Utrecht U., 2018.

[137] B. Muratori and T. Pieloni, "Luminosity levelling techniques for the LHC," in *ICFA Mini-Workshop on Beam-Beam Effects in Hadron Colliders*, pp. 177–181. 2014. arXiv:1410.5646 [physics.acc-ph].

[138] M. G. Bekishev and V. N. Ivanchenko, "A Method of electromagnetic shower identification and measuring of its position in segmented calorimeters," *Nucl. Instrum. Meth. A* **361** (1995) 138–148.

[139] D. Kharzeev and R. D. Pisarski, "Pionic measures of parity and CP violation in high-energy nuclear collisions," *Phys. Rev. D* **61** (2000) 111901, arXiv:hep-ph/9906401.

[140] D. Kharzeev, R. D. Pisarski, and M. H. G. Tytgat, "Possibility of spontaneous parity violation in hot QCD," *Phys. Rev. Lett.* **81** (1998) 512–515, arXiv:hep-ph/9804221.

[141] N. Borghini, P. M. Dinh, and J. Y. Ollitrault, "Analysis of directed flow from elliptic flow," *Phys. Rev. C* **66** (2002) 014905, arXiv:nucl-th/0204017.

[142] G.-L. Ma and B. Zhang, "Effects of final state interactions on charge separation in relativistic heavy ion collisions," *Phys. Lett. B* **700** (2011) 39–43, arXiv:1101.1701 [nucl-th].

[143] S. Choudhury *et al.*, "Investigation of experimental observables in search of the chiral magnetic effect in heavy-ion collisions in the STAR experiment *," *Chin. Phys. C* **46** no. 1, (2022) 014101, arXiv:2105.06044 [nucl-ex].

[144] **PHENIX** Collaboration, A. Adare *et al.*, "Dihadron azimuthal correlations in Au+Au collisions at $\sqrt{s_{NN}} = 200$ GeV," *Phys. Rev. C* **78** (2008) 014901, arXiv:0801.4545 [nucl-ex].

[145] **PHOBOS** Collaboration, B. Alver *et al.*, "High transverse momentum triggered correlations over a large pseudorapidity acceptance in Au+Au collisions at s(NN)**1/2 = 200 GeV," *Phys. Rev. Lett.* **104** (2010) 062301, arXiv:0903.2811 [nucl-ex].

[146] **CMS** Collaboration, S. Chatrchyan *et al.*, "Long-range and short-range dihadron angular correlations in central PbPb collisions at a nucleon-nucleon center of mass energy of 2.76 TeV," *JHEP* **07** (2011) 076, arXiv:1105.2438 [nucl-ex].

[147] **ALICE** Collaboration, K. Aamodt *et al.*, "Two-pion Bose-Einstein correlations in central Pb-Pb collisions at $\sqrt{s_{NN}} = 2.76$ TeV," *Phys. Lett. B* **696** (2011) 328–337, arXiv:1012.4035 [nucl-ex].

[148] M. A. Lisa, S. Pratt, R. Soltz, and U. Wiedemann, "Femtoscopy in relativistic heavy ion collisions," *Ann. Rev. Nucl. Part. Sci.* **55** (2005) 357–402, arXiv:nucl-ex/0505014.

[149] A. Bzdak, V. Koch, and J. Liao, "Azimuthal correlations from transverse momentum conservation and possible local parity violation," *Phys. Rev. C* **83** (2011) 014905, arXiv:1008.4919 [nucl-th].

[150] A. Bzdak, V. Koch, and J. Liao, "Charge-Dependent Correlations in Relativistic Heavy Ion Collisions and the Chiral Magnetic Effect," *Lect. Notes Phys.* **871** (2013) 503–536, arXiv:1207.7327 [nucl-th].

[151] J. Bloczynski, X.-G. Huang, X. Zhang, and J. Liao, "Charge-dependent azimuthal correlations from AuAu to UU collisions," *Nucl. Phys. A* **939** (2015) 85–100, arXiv:1311.5451 [nucl-th].

[152] Z.-W. Lin, C. M. Ko, B.-A. Li, B. Zhang, and S. Pal, "A Multi-phase transport model for relativistic heavy ion collisions," *Phys. Rev. C* **72** (2005) 064901, arXiv:nucl-th/0411110.

[153] R. Kubo, "Generalized Cumulant Expansion Method," *Journal of the Physical Society of Japan* **17** no. 7, (1962) 1100–1120, https://doi.org/10.1143/JPSJ.17.1100.

[154] M. Kardar, *Statistical Physics of Particles*. Cambridge University Press, 2007.

[155] A. Bilandzic, *Anisotropic flow measurements in ALICE at the large hadron collider*. PhD thesis, Utrecht U., 2012.

[156] **ALICE** Collaboration, "Elliptic flow of charged particles at midrapidity relative to the spectator plane in Pb-Pb and Xe-Xe collisions," arXiv:2204.10240 [nucl-ex].

[157] **ALICE** Collaboration, "Elliptic flow of charged particles at midrapidity relative to the spectator plane in Pb-Pb and Xe-Xe collisions," arXiv:2204.10240 [nucl-ex].

[158] **ALICE** Collaboration, S. Acharya *et al.*, "Energy dependence and fluctuations of anisotropic flow in Pb-Pb collisions at $\sqrt{s_{\rm NN}} = 5.02$ and 2.76 TeV," *JHEP* **07** (2018) 103, arXiv:1804.02944 [nucl-ex].

[159] B. Korte and J. Vygen, *Combinatorial Optimization: Theory and Algorithms*. Springer Publishing Company, Incorporated, 5th ed., 2012.

[160] R. Barlow, "Systematic errors: Facts and fictions," in *Conference on Advanced Statistical Techniques in Particle Physics*, pp. 134–144. 7, 2002. arXiv:hep-ex/0207026.

[161] R. Barlow, "Systematic errors in particle physics." https://indico.cern.ch/event/591374/contributions/2511753/attachments/1429002/2193943/01_PWA-Barlow.pdf.

[162] L. Lyons, "Discovery or fluke: statistics in particle physics," *Physics Today* **65** no. 7, (2012) 45–51, https://pubs.aip.org/physicstoday/article-pdf/65/7/45/10096162/45_1_online.pdf. https://doi.org/10.1063/PT.3.1642.

[163] V. Koch, S. Schlichting, V. Skokov, P. Sorensen, J. Thomas, S. Voloshin, G. Wang, and H.-U. Yee, "Status of the chiral magnetic effect and collisions of isobars," *Chin. Phys. C* **41** no. 7, (2017) 072001, arXiv:1608.00982 [nucl-th].

[164] W.-T. Deng, X.-G. Huang, G.-L. Ma, and G. Wang, "Test the chiral magnetic effect with isobaric collisions," *Phys. Rev. C* **94** (2016) 041901, arXiv:1607.04697 [nucl-th].

[165] D. E. Kharzeev, J. Liao, and S. Shi, "Implications of the isobar-run results for the chiral magnetic effect in heavy-ion collisions," *Phys. Rev. C* **106** no. 5, (2022) L051903, arXiv:2205.00120 [nucl-th].

[166] Y. Feng, Y. Lin, J. Zhao, and F. Wang, "Revisit the chiral magnetic effect expectation in isobaric collisions at the relativistic heavy ion collider," *Phys. Lett. B* **820** (2021) 136549, arXiv:2103.10378 [nucl-ex].

[167] **ALICE** Collaboration, P. Cortese, "Performance of the ALICE Zero Degree Calorimeters and upgrade strategy," *J. Phys. Conf. Ser.* **1162** no. 1, (2019) 012006.

[168] P. Christakoglou, S. Qiu, and J. Staa, "Systematic study of the chiral magnetic effect with the AVFD model at LHC energies," *Eur. Phys. J. C* **81** no. 8, (2021) 717, arXiv:2106.03537 [nucl-th].

[169] **ALICE** Collaboration, B. Abelev *et al.*, "Charge separation relative to the reaction plane in Pb-Pb collisions at $\sqrt{s_{NN}} = 2.76$ TeV," *Phys. Rev. Lett.* **110** no. 1, (2013) 012301, arXiv:1207.0900 [nucl-ex].

[170] S. Shi, Y. Jiang, E. Lilleskov, and J. Liao, "Anomalous Chiral Transport in Heavy Ion Collisions from Anomalous-Viscous Fluid Dynamics," *Annals Phys.* **394** (2018) 50–72, arXiv:1711.02496 [nucl-th].

[171] S. Shi, Y. Jiang, E. Lilleskov, Y. Yin, and J. Liao, "Quantifying the Chiral Magnetic Effect from Anomalous-Viscous Fluid Dynamics," *Nucl. Phys. A* **967** (2017) 748–751, arXiv:1704.05531 [nucl-th].

[172] S. Shi, H. Zhang, D. Hou, and J. Liao, "Signatures of Chiral Magnetic Effect in the Collisions of Isobars," *Phys. Rev. Lett.* **125** (2020) 242301, arXiv:1910.14010 [nucl-th].

[173] C. Shen, Z. Qiu, H. Song, J. Bernhard, S. Bass, and U. Heinz, "The iEBE-VISHNU code package for relativistic heavy-ion collisions," *Comput. Phys. Commun.* **199** (2016) 61–85, arXiv:1409.8164 [nucl-th].

[174] G. Inghirami, L. Del Zanna, A. Beraudo, M. H. Moghaddam, F. Becattini, and M. Bleicher, "Numerical magneto-hydrodynamics for relativistic nuclear collisions," *Eur. Phys. J. C* **76** no. 12, (2016) 659, arXiv:1609.03042 [hep-ph].

[175] L. McLerran and V. Skokov, "Comments About the Electromagnetic Field in Heavy-Ion Collisions," *Nucl. Phys. A* **929** (2014) 184–190, arXiv:1305.0774 [hep-ph].

[176] S. A. Bass *et al.*, "Microscopic models for ultrarelativistic heavy ion collisions," *Prog. Part. Nucl. Phys.* **41** (1998) 255–369, arXiv:nucl-th/9803035.

[177] **ALICE** Collaboration, E. Abbas *et al.*, "Centrality dependence of the pseudorapidity density distribution for charged particles in Pb-Pb collisions at $\sqrt{s_{\rm NN}}$ = 2.76 TeV," *Phys. Lett. B* **726** (2013) 610–622, arXiv:1304.0347 [nucl-ex].

[178] **ALICE** Collaboration, J. Adam *et al.*, "Centrality dependence of the pseudorapidity density distribution for charged particles in Pb-Pb collisions at $\sqrt{s_{\rm NN}} = 5.02$ TeV," *Phys. Lett. B* **772** (2017) 567–577, arXiv:1612.08966 [nucl-ex].

[179] **ALICE** Collaboration, S. Acharya *et al.*, "Centrality and pseudorapidity dependence of the charged-particle multiplicity density in Xe–Xe collisions at $\sqrt{s_{\rm NN}}$ =5.44TeV," *Phys. Lett. B* **790** (2019) 35–48, arXiv:1805.04432 [nucl-ex].

[180] **ALICE** Collaboration, K. Aamodt *et al.*, "Elliptic flow of charged particles in Pb-Pb collisions at 2.76 TeV," *Phys. Rev. Lett.* **105** (2010) 252302, arXiv:1011.3914 [nucl-ex].

[181] **ALICE** Collaboration, J. Adam *et al.*, "Anisotropic flow of charged particles in Pb-Pb collisions at $\sqrt{s_{\rm NN}} = 5.02$ TeV," *Phys. Rev. Lett.* **116** no. 13, (2016) 132302, arXiv:1602.01119 [nucl-ex].

[182] **ALICE** Collaboration, S. Acharya *et al.*, "Anisotropic flow in Xe-Xe collisions at $\sqrt{\mathbf{s}_{\rm NN}} = \mathbf{5.44}$ TeV," *Phys. Lett. B* **784** (2018) 82–95, arXiv:1805.01832 [nucl-ex].

[183] **ALICE** Collaboration, B. Abelev *et al.*, "Centrality dependence of π, K, p production in Pb-Pb collisions at $\sqrt{s_{NN}}$ = 2.76 TeV," *Phys. Rev. C* **88** (2013) 044910, arXiv:1303.0737 [hep-ex].

[184] **ALICE** Collaboration, S. Acharya *et al.*, "Production of charged pions, kaons, and (anti-)protons in Pb-Pb and inelastic pp collisions at $\sqrt{s_{NN}}$ = 5.02 TeV," *Phys. Rev. C* **101** no. 4, (2020) 044907, arXiv:1910.07678 [nucl-ex].

[185] **ALICE** Collaboration, S. Acharya *et al.*, "Production of pions, kaons, (anti-)protons and ϕ mesons in Xe–Xe collisions at $\sqrt{s_{\rm NN}}$ = 5.44 TeV," *Eur. Phys. J. C* **81** no. 7, (2021) 584, arXiv:2101.03100 [nucl-ex].

[186] Y. Hirono, T. Hirano, and D. E. Kharzeev, "The chiral magnetic effect in heavy-ion collisions from event-by-event anomalous hydrodynamics," arXiv:1412.0311 [hep-ph].

[187] P. Steinberg, "Bulk dynamics in heavy ion collisions," *Nucl. Phys. A* **752** (2005) 423–432, arXiv:nucl-ex/0412009.

[188] **ALICE** Collaboration, S. Acharya *et al.*, "ALICE upgrade physics performance studies for 2018 Report on HL/HE-LHC physics,". https://cds.cern.ch/record/2661798.

[189] A. Ferrero, "Run coordination report." https://indico.cern.ch/event/1202843/contributions/5670809/attachments/2753347/4793717/ALICE-AF-RC-TB-16-11-2023.pdf.

[190] **ALICE** Collaboration, ALICE, "Alice performance: recorded integrated luminosity in pb-pb @ 5.36 tev during 2023." https://alice-figure.web.cern.ch/node/29431.

[191] **ALICE** Collaboration, "ALICE luminosity determination for Pb−Pb collisions at $\sqrt{s_{\mathrm{NN}}} = 5.02$ TeV," arXiv:2204.10148 [nucl-ex].

[192] **ALICE** Collaboration, ALICE, "Alice performance: Run2 trigger statistics in pb-pb." https://alice-figure.web.cern.ch/node/14884.

[193] **ALICE** Collaboration, ALICE, "Search for anomalous chiral effects in heavy-ion collisions with alice." https://indico.cern.ch/event/1139644/contributions/5502913/attachments/2708260/4702209/AnomalousChiralEffect_ALICE_QM23_Chunzheng.pdf.

[194] J. Jia, "Shape of atomic nuclei in heavy ion collisions," *Phys. Rev. C* **105** no. 1, (2022) 014905, arXiv:2106.08768 [nucl-th].

Public Summary

People generally prefer symmetry in diverse aesthetic forms, from painting and sculpture to architecture, music, and sport. This preference is evident in Leonardo Da Vinci's "The Last Supper," the symmetrical design of cathedral vaulted ceilings, the compositions of Bach, and the harmonious movements of synchronised divers. In nature, symmetry is a prevalent feature among various objects. The radial symmetry found in starfish or flower petals, the efficient hexagonal structure of honeycombs, the distinct symmetrical crystal structure of snowflakes or the spherically symmetric planets and suns. Conversely, asymmetry often signals illness or danger.

In the book "The Accidental Universe: The World You Thought You Knew," physicist Alan Lightman writes, "I would claim that symmetry represents order, and we crave order in this strange universe we find ourselves in". Particle physicists' primary interest is not on the fact that objects in nature often exhibit symmetry, but rather on uncovering the remarkable symmetries, and, more astonishingly, the instances of broken symmetry within the fundamental laws that govern the behaviour of particles in the physical world. When a physical law is described as "symmetrical," it implies that the law remains unchanged despite changes in the identity or properties of specific elementary particles, or in the abstract mathematical representations of nature, such as spacetime symmetries, Gauge symmetries, conformal symmetry, and topological invariants. However, symmetry breaking often signals the emergence of new physical phenomena. One of the most notable examples of symmetry breaking is the development of the theory of spontaneous symmetry breaking (a.k.a. the Higgs mechanism) in the early 1960s. Physicists Robert Brout and François Englert, Peter Higgs, and independently, Gerald Guralnik, Carl Richard Hagen, and Tom Kibble, proposed mechanisms where the ground state (or vacuum state) of the Higgs field does not exhibit the symmetry in the Lagrangian for the Higgs field, which describes the dynamics of the Higgs field. This breaking of symmetry through the Higgs mechanism leads to certain particles acquiring mass. Initially, these particles are theorised to be massless, but they gain mass through their interactions with the Higgs field.

The focus of this dissertation is to explore the potential breaking of a specific type of symmetry, known as P (parity) symmetry, through a distinct physics phenomenon, the chiral magnetic effect (CME), occurring within a strongly interacting system, particularly the quark-gluon plasma, as described by quantum chromodynamics (QCD). QCD is the theory that describes the strong interaction between quarks mediated by gluons. The strong force is one of the four fundamental forces, responsible for binding quarks to form subatomic particles like protons and neutrons, and for holding atomic nuclei together. It is noteworthy that CME is known to lead to violations of both P and CP (charge parity) symmetry. This is because the charge symmetry is conserved in CME. If P symmetry is broken by CME, it inherently leads to the simultaneous

breaking of CP symmetry as well. Nonetheless, it is crucial to clarify that the violation of P symmetry does not necessarily lead to the violation of CP symmetry. CP symmetry combines both charge conjugation symmetry (C), which swaps particles with their antiparticles, and parity symmetry (P), which flips spatial coordinates.

The search for P and CP violation in QCD is crucial and could unveil new physics. To date, neither global nor local violations of P or CP symmetry has been observed in the strong interaction. Apart from being theoretically possible, the belief in the possibility of such violations in QCD is backed by the observed violations of both P and CP symmetry within the weak interaction—one of the four fundamental forces known for processes like radioactive decay that transform one type of subatomic particle into another, such as a neutron into a proton. The initial discovery of P symmetry violation, followed by the discovery of CP symmetry violation in weak interaction, came as huge surprises to the physics community and led to two Nobel prizes. It means that our universe has a preference for certain processes in weak interaction over their mirrored or mirrored and charge-conjugated counterparts.

How does local symmetry breaking occur in QCD?

In heavy-ion collisions, a state of strongly interacting matter at extreme temperatures known as the quark-gluon plasma (QGP) is created, where quarks and gluons are only weakly bound, allowing them to move freely. The underlying theory that describes it is QCD, where its vacuum or ground states (states with the minimal amount of energy) have a very rich structure and play a key role in inducing chirality imbalance. There are infinitely many ground states, which are not positioned adjacent to each other (not in a spatial sense), but rather, potential barriers exist between them, as shown in Fig. 8.19. Ground states are labelled with a set of discrete values (0,1,2,...), known as the winding number or the Chern-Simon number (N_{CS}), where each value denotes a distinct field configuration. Transitioning from one ground state to another is a topologically non-trivial process, implying that it is impossible to smoothly and continuously transform from one state to another. Instead, transitions require mechanisms like tunnelling, facilitated by instantons, or crossing over barriers, facilitated by sphalerons, to change the field configuration in a localised domain. An instanton is a pseudoparticle, shown as red points in Fig. 8.19. It is similar in concept to the wave function of an electron in a periodic potential, which has a finite probability to tunnel through the potential barrier between distinct vacuum states. On the other hand, a sphaleron is an unstable pseudoparticle that resides at the saddle point of the potential, shown as blue points in Fig. 8.19. The transition via a sphaleron involves the system gaining enough energy (through thermal or quantum fluctuations) to cross over the barrier, effectively transitioning to a nearby ground state without the need for tunnelling.

The change of the field configuration is related to the axial anomaly, which "flips" the chirality of quarks and results in a chirality imbalance of quarks in the local domain. Chirality is a quantum number that describes whether a particle—such as a quark in our case—is in a right-handed or left-handed state based on its intrinsic properties. An imbalance in chirality occurs when there is a difference between the number of right-handed and left-handed (anti-)quarks in a system.

While chirality is not directly related to parity transformation, the two become related in the context of massless particles. In high-energy heavy-ion collisions at the Large Hadron Collider, the kinetic energy involved is much higher than the rest mass energy of quarks, effectively allowing quarks to be treated as massless. In this massless limit, chirality coincides with helicity, which is defined as the alignment of a particle's spin with its momentum direction. Parity

transformation, which inverts spatial coordinates, also reverses the momentum direction, thus flipping the helicity state of the particle. Consequently, a massless particle's chirality state is flipped under a parity transformation. The chirality imbalance induced by the QCD vacuum non-trivial configuration is directly related to the parity violation in the massless limit.

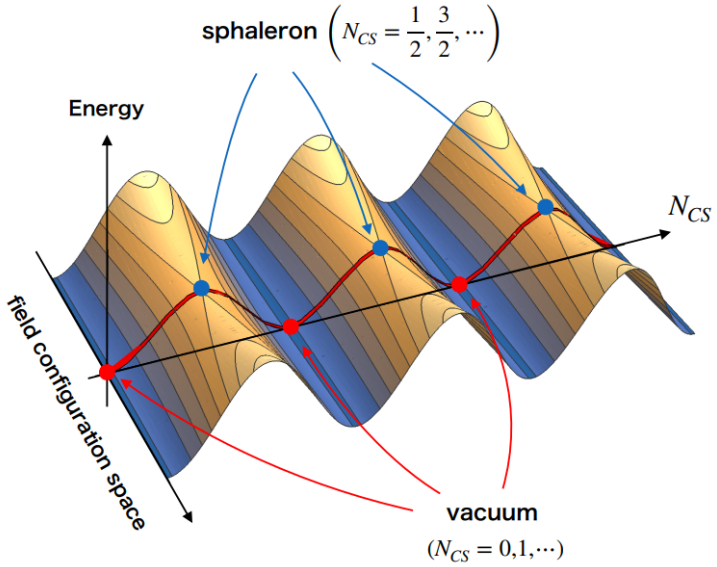

Figure 8.16: *The simplified illustration of the instanton and sphaleron in configuration space. The red points represents the infinitely degenerate vacua, which also correspond to instanton solutions with $N_{CS} = 0, 1, ...$ The blue points denote sphaleron solutions with $N_{CS} = 1/2, 3/2, ...$ Credit: Yu Hamada and Kengo Kikuchi at Kyoto University.*

What is the chiral magnetic effect?

The chiral magnetic effect is predicted to occur in heavy-ion collisions, where an imbalance of the chirality of quarks leads to the generation of an electric current along the direction of an external magnetic field. In the earliest moments after non-central heavy-ion collisions (where two incoming ions do not fully overlap), an extremely strong magnetic field is created by the spectator protons that do not participate in the collision, as shown in Fig. 8.20. The magnitude of the initial magnetic field is estimated to reach up to an order of 10^{15} Tesla. For comparison, a refrigerator magnet has a field strength of about 0.01 Tesla, and the strongest magnetic field ever found in the universe by astronomers is 1.6×10^9 Tesla at the surface of a neutron star. Despite its immense strength, the initial magnetic field is short-lived, dissipating in less than 10^{-23} seconds—a mere ten millionths of a billionth of a billionth of a second.

The particle's spin tends to align either parallel or anti-parallel to the magnetic field depending on its charge, as it is a more energetically favourable state. For example, the spin of u (+2/3 charge) and d (-1/3 charge) quarks align in the same and opposite directions as the magnetic field, respectively. Quarks can change their chirality (helicity) only by reversing their momenta in the presence of a strong magnetic field, as a spin flip is energetically suppressed. This implies that the momenta of positively-charged right-handed quarks and negatively-charged left-handed quarks align in the same direction as $\vec{B}$, while the momenta of positively-charged left-handed quarks and negatively-charged right-handed quarks align anti-parallel to $\vec{B}$. Consequently, in the case of an excess of right-handed quarks, an electric current forms with a net quantity of

positively-charged right-handed quarks moving in the same direction as the magnetic field. This is known as the chiral magnetic effect.

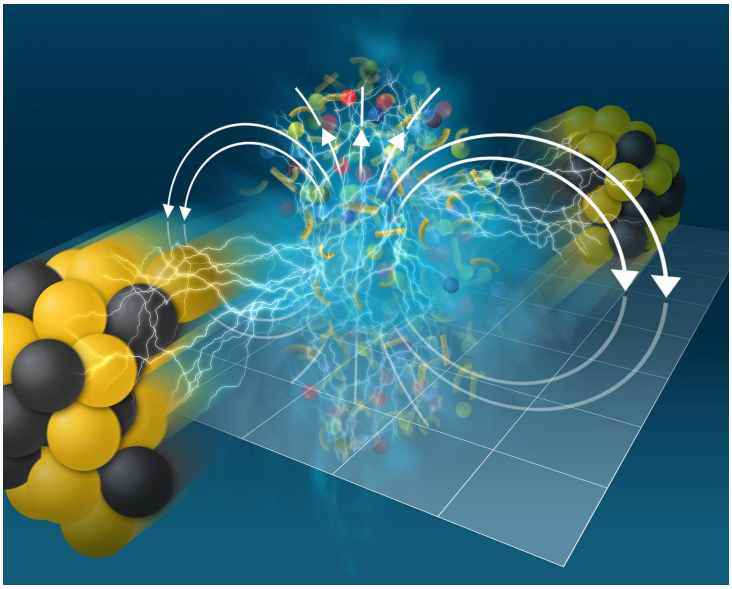

Figure 8.17: *Artistic representation of the magnetic field generated by the heavy-ion collisions. Spectator protons and neutrons are shown as black and yellow spheres, respectively. Credit: Tiffany Bowman and Jen Abramowitz at Brookhaven National Laboratory.*

Searching for the chiral magnetic effect

Heavy-ion collisions provide an ideal laboratory to search for CME. The experimental signature we seek is the charge separation along the magnetic field, e.g. an excess of positively charged particles moving parallel to the magnetic field, and an excess of negatively charged particles moving antiparallel to it. Nonetheless, detecting this signal poses a significant challenge due to its expected minute magnitude and the presence of numerous background effects that overwhelm the real signal.

There are many experimental techniques developed to disentangle the signal and the background. The technique adopted in this dissertation leverages the distinct characteristics of two types of planes: the spectator and participant planes. The spectator plane is defined by spectator nucleons. Given that the magnetic field originates from the charged particles, specifically the protons within these spectator nucleons, it is expected to be perpendicular to the spectator plane, as depicted in Fig. 8.21. Therefore, measuring the charge separation relative to the spectator plane should maximise the contribution of the CME signal. On the other hand, the participant plane is defined by the geometry of the interaction zone—the overlap area of the two colliding nuclei, depicted as the blue shaded region in Fig. 8.21. This plane is influenced by the initial geometric shape of the region and, hence, the magnetic field's orientation is only approximately perpendicular, with fluctuations observed across different collision events. Therefore, the contribution of the CME signal is less when measuring the charge separation with respect to the participant plane. By calculating the ratio of measurements taken with respect to the spectator and participant plane, respectively, the background effects are cancelled out. Importantly, the CME signal remains more pronounced for measurements relative to the spectator plane. A ratio exceeding one indicates the detection of the CME.

Our result, measured with the ALICE detector, one of the four major experiments at the Large Hadron Collider at CERN, shows that the ratio is consistent with one in lead-ion collisions. While this aligns with measurements from various other experimental techniques, none of the results definitively rules out the possibility of the CME. The experimental uncertainties present in all measurements remain sizeable, preventing us from conclusively dismissing the CME's contribution at levels of a few percent or even below one percent. For instance, consider if our result is 1.1 ± 0.1, which will be deemed consistent with one. This could only exclude a potential CME signal that is very large. Should a future experiment offer a more precise measurement, yielding a result of 1.05 ± 0.01, this would then represent a small contribution from the CME signal but a significant deviation from one.

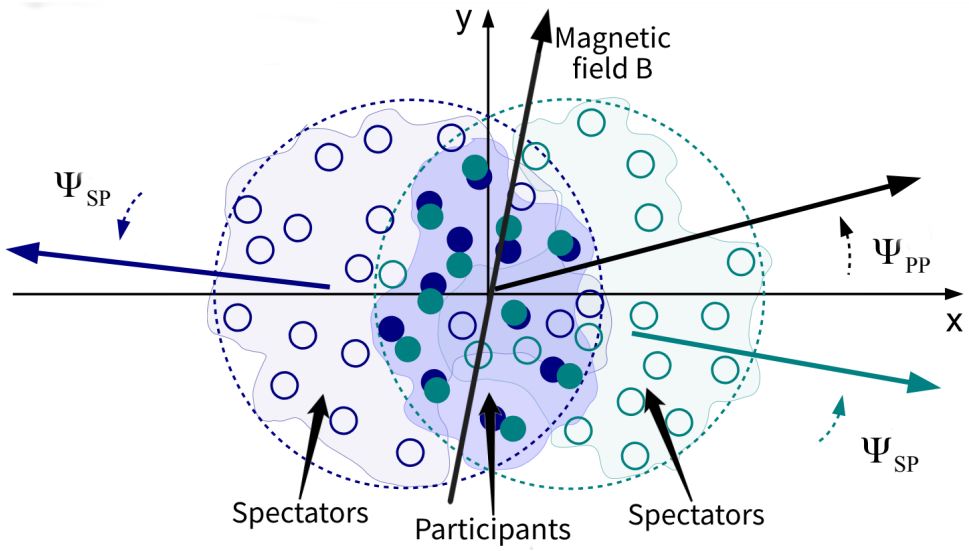

Figure 8.18: *Sketch of a non-central heavy-ion collision. Credit: ALICE collaboration.*

Implications of chiral magnetic effect experimental measurements for theory

With numerous experimental measurements of CME being conducted, it is natural to ask what kind of insights these provide to theory. This question can be approached by differentiating between pure theoretical considerations and the application of theoretical parameters in simulating CME through physics models. For the pure theory, which focuses on the transition rates between different vacuum states by instantons and sphalerons, establishing a direct connection is currently challenging. This difficulty stems from our incomplete knowledge on various factors, such as the strength of the magnetic field, its decay rate within the quark-gluon plasma, and the time at which chirality imbalance is induced after the collision. Regarding the theory underlying CME simulation models, we undertook a study using a state-of-the-art model dedicated to simulating CME in heavy-ion collisions. Through this study, we extracted the optimal theoretical parameters governing the CME signal, namely the percentage of chirality imbalance, and the background. Our findings indicate that to replicate the experimental observations for lead ions, a non-zero input for the CME signal parameter is required. Conversely, for xenon ions, which are significantly smaller than lead ions, the CME signal parameter is effectively zero. This is mainly attributed to the larger magnetic field generated in collisions of heavier ions due to a greater number of protons.

What is next?

The theory behind CME is elegant, yet the experimental search for CME presents formidable challenges. Following a shutdown lasting over 3 years, during which extensive upgrades were made to both the detectors and the accelerator, the LHC restarted at the end of 2022. The ALICE collaboration has an ambitious plan for its Run 3 and Run 4, aiming for a hundredfold increase in data accumulated from lead ion collisions. This significant enhancement is expected to reduce statistical uncertainties by a factor of 10, potentially enabling the discovery of CME signals if they exist at the level of a few percent. With this expanded dataset, the ALICE collaboration also anticipates achieving more precise measurements of the early magnetic field, a crucial factor in CME modelling that has never been unambiguously determined.

Finally, I would like to emphasise that if CME indeed exists, it would undoubtedly leave a significant impact on the advancement of physics. However, if it does not, do not be disheartened. As the legendary physicist Richard Feynman once said, “progress in science comes when experiments contradict theory,” and “if you thought that science was certain - well, that is just an error on your part.”

Openbare Samenvatting

Mensen geven over het algemeen de voorkeur aan symmetrie in diverse esthetische vormen, van schilderkunst en beeldhouwkunst tot architectuur, muziek en sport. Deze voorkeur is evident in Leonardo Da Vinci's "Het Laatste Avondmaal", het symmetrische ontwerp van kathedraalgewelven, de composities van Bach en de harmonieuze bewegingen van gesynchroniseerde duikers. In de natuur is symmetrie een veelvoorkomend kenmerk bij verschillende objecten. De radiale symmetrie gevonden in zeesterren of in bloemblaadjes, de efficiënte hexagonale structuur van honingraten, de kenmerkende symmetrische kristalstructuur van sneeuwvlokken of de bolvormig symmetrische planeten en zonnen. Daartegenover duidt asymmetrie vaak op ziekte of gevaar.

In het boek "The Accidental Universe: The World You Thought You Knew", schrijft de natuurkundige Alan Lightman, "Ik zou beweren dat symmetrie orde vertegenwoordigt, en we verlangen naar orde in dit vreemde universum waarin we ons bevinden". De primaire interesse van deeltjesfysici daarentegen is niet het feit dat objecten in de natuur vaak symmetrie vertonen, maar eerder in het onthullen van de opmerkelijke symmetrieën, en, nog verbazingwekkender, de gevallen van gebroken symmetrie binnen de fundamentele wetten die het gedrag van deeltjes in de fysieke wereld beschrijven. Wanneer een natuurwet als "symmetrisch" wordt beschreven, impliceert dit dat de wet onveranderd blijft ondanks veranderingen in de identiteit of eigenschappen van specifieke elementaire deeltjes, of in de abstracte wiskundige representaties van de natuur, zoals ruimtetijdsymmetrieën, Gauge-symmetrieën, conforme symmetrie en topologische invarianten. Echter, symmetriebreking duidt vaak op het ontstaan van nieuwe fysische fenomenen. Een van de meest opmerkelijke voorbeelden van symmetriebreking is de ontwikkeling van de theorie van spontane symmetriebreking (ook bekend als het Higgs-mechanisme) in het begin van de jaren 1960. Fysici Robert Brout en François Englert, Peter Higgs, en onafhankelijk daarvan, Gerald Guralnik, Carl Richard Hagen en Tom Kibble, stelden mechanismen voor waarbij de grondtoestand (of vacuümtoestand) van het Higgs-veld de symmetrie in de Lagrangiaan voor het Higgs-veld, die de dynamica van het Higgs-veld beschrijft, niet vertoont. Deze breuk van symmetrie door het Higgs-mechanisme leidt ertoe dat bepaalde deeltjes massa verkrijgen. Aanvankelijk werd gedacht dat deze deeltjes massaloos zijn, maar ze krijgen massa door hun interacties met het Higgs-veld.

De focus van dit proefschrift is het verkennen van het potentieel doorbreken van een specifiek type van symmetrie, bekend als P (pariteit) symmetrie, door een kenmerkend natuurkundig fenomeen, het chirale magnetische effect (CME), dat plaatsvindt binnen een sterk wisselwerkend systeem, met name het quark-gluon plasma, dat beschreven wordt door de kwantumchromodynamica (QCD). QCD is de theorie die de sterke wisselwerking tussen quarks beschrijft, overgedragen door gluonen. De sterke kracht is een van de vier fundamentele krachten, verant-

woordelijk voor het binden van quarks om subatomaire deeltjes zoals protonen en neutronen te vormen, en voor het bijeenhouden van atoomkernen. Het is noemenswaardig dat CME bekend staat om te leiden tot schendingen van zowel P als CP (lading-pariteit) symmetrie. Dit komt doordat de ladingssymmetrie bewaard blijft in CME. Als P symmetrie wordt gebroken door CME, leidt dit inherent tot het gelijktijdig breken van CP symmetrie. Desalniettemin is het cruciaal om te verduidelijken dat de schending van P symmetrie niet noodzakelijkerwijs leidt tot de schending van CP symmetrie. CP symmetrie combineert zowel de ladingconjugatiesymmetrie (C), die deeltjes verwisselt met hun antideeltjes, als de pariteitssymmetrie (P), die ruimtelijke coördinaten omkeert.

De zoektocht naar P- en CP-schending in QCD is cruciaal en zou nieuwe natuurkunde kunnen onthullen. Tot op heden zijn noch globale, noch lokale schendingen van P- of CP-symmetrie waargenomen in de sterke wisselwerking. Afgezien van het feit dat het theoretisch mogelijk is, wordt het geloof in de mogelijkheid van dergelijke schendingen in QCD ondersteund door de waargenomen schendingen van zowel P- als CP-symmetrie binnen de zwakke wisselwerking - een van de vier fundamentele krachten bekend om processen zoals radioactief verval die één type subatomair deeltje in een ander subatomair deeltje transformeren, zoals een neutron in een proton. De initiële ontdekking van P-symmetrie schending, gevolgd door de ontdekking van CP-symmetrie schending in zwakke wisselwerking, kwam als enorme verrassingen voor de natuurkundegemeenschap en leidde tot twee Nobelprijzen. Het betekent dat ons universum een voorkeur heeft voor bepaalde processen in de zwakke wisselwerking boven hun gespiegelde of gespiegelde en lading-geconjugeerde tegenhangers.

Hoe vindt lokale symmetriebreking plaats in QCD?

Bij botsingen tussen zware ionen wordt een toestand van sterk interactieve materie bij extreme temperaturen gecreëerd, bekend als het quark-gluon plasma (QGP), waar quarks en gluonen vrij kunnen bewegen. De onderliggende theorie die dit beschrijft is QCD, waar de vacuüm- of grondtoestanden (toestanden met de minimale hoeveelheid energie) een zeer rijke structuur hebben en een sleutelrol spelen bij het induceren van chiraliteitsonevenwicht. Er zijn oneindig veel grondtoestanden, die niet naast elkaar geplaatst zijn (niet in een ruimtelijke zin), maar er bestaan potentiële barrières tussen hen, zoals getoond in Fig. 8.19. Grondtoestanden worden gelabeld met een reeks discrete waarden (0,1,2,...), bekend als het windinggetal of het Chern-Simonsgetal (N_{CS}), waarbij elke waarde een onderscheidende veldconfiguratie aangeeft. De overgang van de ene grondtoestand naar de andere is een topologisch niet-triviaal proces, wat impliceert dat het onmogelijk is om soepel en continu van de ene toestand naar de andere te transformeren. In plaats daarvan vereisen overgangen mechanismen zoals tunnelen, gefaciliteerd door instantonen, of het oversteken van barrières, gefaciliteerd door sphalerons, om de veldconfiguratie in een gelokaliseerd domein te wijzigen. Een instanton is een pseudodeeltje, getoond als rode punten in Fig. 8.19. Het is vergelijkbaar met het concept van de golffunctie van een elektron in een periodieke potentiaal, dat een eindige kans heeft om door de potentiaalbarrière tussen onderscheidende vacuümtoestanden te tunnelen. Aan de andere kant is een sphaleron een instabiel pseudodeeltje dat zich op het zadel punt van het potentiaal bevindt, getoond als blauwe punten in Fig. 8.19. De overgang via een sphaleron houdt in dat het systeem genoeg energie verkrijgt (door thermische of kwantumfluctuaties) om de barrière over te steken, effectief overgaand naar een nabije grondtoestand zonder de noodzaak van tunnelen.

De verandering van de veldconfiguratie is gerelateerd aan de axiale anomalie, die de chiraliteit van quarks “omdraait” en resulteert in een chiraliteitsonevenwicht van quarks in het

lokale domein. Chiraliteit is een kwantumgetal dat beschrijft of een deeltje—zoals een quark in ons geval—zich in een rechtshandige of linkshandige toestand bevindt op basis van zijn intrinsieke eigenschappen. Een onbalans in chiraliteit treedt op wanneer er een verschil is tussen het aantal rechtshandige en linkshandige (anti-)quarks in een systeem.

Hoewel chiraliteit niet direct gerelateerd is aan een pariteitstransformatie, worden de twee gerelateerd in de context van massaloze deeltjes. Bij botsingen van zware ionen met hoge energie in de Large Hadron Collider is de betrokken kinetische energie veel hoger dan de rustmassa-energie van quarks, waardoor quarks effectief als massaloos kunnen worden behandeld. In deze massaloze limiet valt chiraliteit samen met heliciteit, wat gedefinieerd wordt als de uitlijning van de spin van een deeltje met zijn bewegingsrichting. De pariteitstransformatie, die ruimtelijke coördinaten omkeert, keert ook de bewegingsrichting om, waardoor de heliciteitsstaat van het deeltje wordt omgekeerd. Daardoor wordt de chiraliteitsstaat van een massaloos deeltje omgekeerd onder een pariteitstransformatie. De chiraliteitsonbalans, geïnduceerd door de niet-triviale configuratie van het QCD-vacuüm, is direct gerelateerd aan de pariteitsschending in de massaloze limiet.

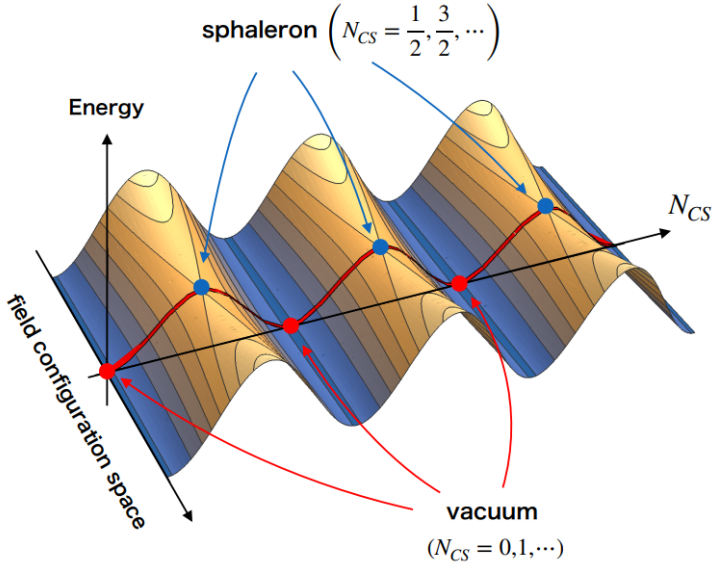

Figure 8.19: *De vereenvoudigde illustratie van de instanton en sphaleron in configuratieruimte. De rode punten vertegenwoordigen de oneindig degenererende vacua, die ook overeenkomen met instanton-oplossingen met $N_{CS} = 0, 1, ...$ De blauwe punten duiden sphaleron-oplossingen aan met $N_{CS} = 1/2, 3/2, ...$ Met dank aan: Yu Hamada en Kengo Kikuchi aan de Universiteit van Kyoto.*

Wat is het chirale magnetische effect?

Het chirale magnetische effect wordt voorspeld op te treden bij botsingen van zware ionen, waar een onbalans in de chiraliteit van quarks leidt tot de generatie van een elektrische stroom langs de richting van een extern magnetisch veld. In de vroegste momenten na niet-centrale zware-ionenbotsingen (waar twee botsende ionen niet volledig overlappen), wordt een extreem sterk magnetisch veld gecreëerd door de toeschouwer protonen die niet deelnemen aan de botsing, zoals getoond in Fig. 8.20. De grootte van het initiële magnetische veld wordt geschat tot een orde van 10^{15} Tesla te bereiken. Ter vergelijking, een koelkastmagneet heeft een veldsterkte

van ongeveer 0,01 Tesla, en het sterkste magnetische veld ooit gevonden in het universum door astronomen is $1,6 \times 10^9$ Tesla aan het oppervlak van een neutronenster. Ondanks zijn immense sterkte is het initiële magnetische veld kortstondig, en verdwijnt in minder dan 10^{-23} seconden - een luttele tien miljoenste van een miljardste van een miljardste van een seconde.

De spin van het deeltje heeft de neiging om zich parallel of antiparallel aan het magnetische veld te oriënteren, afhankelijk van zijn lading, omdat dit een energetisch gunstigere staat is. Bijvoorbeeld, de spin van u (+2/3 lading) en d (-1/3 lading) quarks lijnen zich uit in dezelfde en tegenovergestelde richtingen als het magnetische veld, respectievelijk. Quarks kunnen hun chiraliteit (heliciteit) alleen veranderen door hun momenta om te keren in de aanwezigheid van een sterk magnetisch veld, aangezien een spinflip energetisch onderdrukt wordt. Dit impliceert dat de momenta van positief geladen rechtshandige quarks en negatief geladen linkshandige quarks zich in dezelfde richting als $\vec{B}$ oriënteren, terwijl de momenta van positief geladen linkshandige quarks en negatief geladen rechtshandige quarks antiparallel aan $\vec{B}$ oriënteren. Dientengevolge, in het geval van een overschot aan rechtshandige quarks, vormt zich een elektrische stroom met een netto hoeveelheid van positief geladen rechtshandige quarks die zich in dezelfde richting als het magnetische veld bewegen. Dit staat bekend als het chirale magnetische effect.

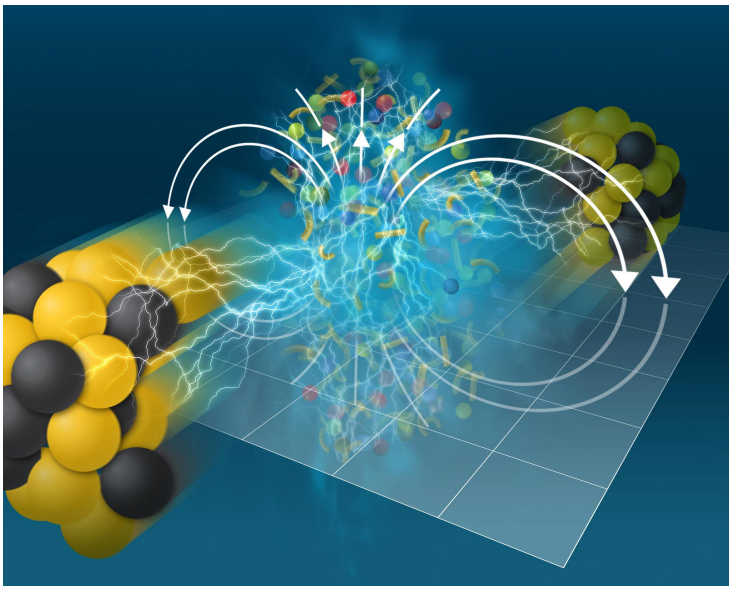

Figure 8.20: *Artistieke weergave van het magnetische veld gegenereerd door botsingen van zware ionen. Toeschouwer protonen en neutronen worden respectievelijk weergegeven als zwarte en gele bollen. Credit: Tiffany Bowman en Jen Abramowitz bij Brookhaven National Laboratory.*

Op zoek naar het chirale magnetische effect

Zware-ionenbotsingen bieden een ideaal laboratorium om te zoeken naar CME. Het experimentele bewijs dat we zoeken is de ladingscheiding langs het magnetische veld, bijvoorbeeld een overschot aan positief geladen deeltjes die parallel bewegen aan het magnetische veld, en een overschot aan negatief geladen deeltjes die antiparallel daaraan bewegen. Desalniettemin vormt het detecteren van dit signaal een aanzienlijke uitdaging vanwege de verwachte geringe grootte en de aanwezigheid van talrijke achtergrondeffecten die het echte signaal overschaduwen.

Er zijn veel experimentele technieken ontwikkeld om het signaal en de achtergrond te ont-

warren. De techniek die in deze dissertatie wordt toegepast, maakt gebruik van de distinctieve kenmerken van twee soorten vlakken: het toeschouwer- en deelnemersvlak. Het toeschouwervlak wordt gedefinieerd door toeschouwernucleonen. Aangezien het magnetische veld afkomstig is van de geladen deeltjes, specifiek de protonen binnen deze toeschouwernucleonen, wordt verwacht dat het loodrecht staat op het toeschouwervlak, zoals afgebeeld in Fig. 8.21. Daarom zou het meten van de ladingscheiding ten opzichte van het toeschouwervlak de bijdrage van het CME-signaal moeten maximaliseren. Aan de andere kant wordt het deelnemersvlak gedefinieerd door de geometrie van de interactiezone - het overlappingsgebied van de twee botsende kernen, afgebeeld als het blauw gearceerde gebied in Fig. 8.21. Dit vlak wordt beïnvloed door de initiële geometrische vorm van het overlappingsgebeid en daar is dus de oriëntatie van het magnetische veld slechts bij benadering loodrecht, met fluctuaties waargenomen bij verschillende botsingen. Daarom is de bijdrage van het CME-signaal minder bij het meten van de ladingscheiding met betrekking tot het deelnemersvlak. Door de verhouding te berekenen van metingen genomen met betrekking tot respectievelijk het toeschouwer- en deelnemersvlak, worden de achtergrondeffecten tenietgedaan. Belangrijk is dat het CME-signaal groter is bij metingen ten opzichte van het toeschouwervlak. Een verhouding die hoger is dan één duidt op de detectie van het CME.

Ons resultaat, gemeten met de ALICE-detector, een van de vier grote experimenten bij de Large Hadron Collider bij CERN, toont aan dat de verhouding consistent is met één bij botsingen van loodionen. Hoewel dit overeenkomt met metingen van verschillende andere experimentele technieken, sluit geen van de resultaten de mogelijkheid van de CME definitief uit. De experimentele onzekerheden die in alle metingen aanwezig zijn, blijven aanzienlijk, waardoor we niet met zekerheid kunnen uitsluiten dat de bijdrage van de CME op niveaus van een paar procent of zelfs onder één procent ligt. Neem bijvoorbeeld aan dat ons resultaat $1,1 \pm 0,1$ is, wat consistent zal worden geacht met één. Dit zou alleen een potentieel CME-signaal kunnen uitsluiten dat zeer groot is. Mocht een toekomstig experiment een nauwkeurigere meting bieden, resulterend in een resultaat van $1,05 \pm 0,01$, dan zou dit een kleine bijdrage van het CME-signaal vertegenwoordigen maar een aanzienlijke afwijking van één.

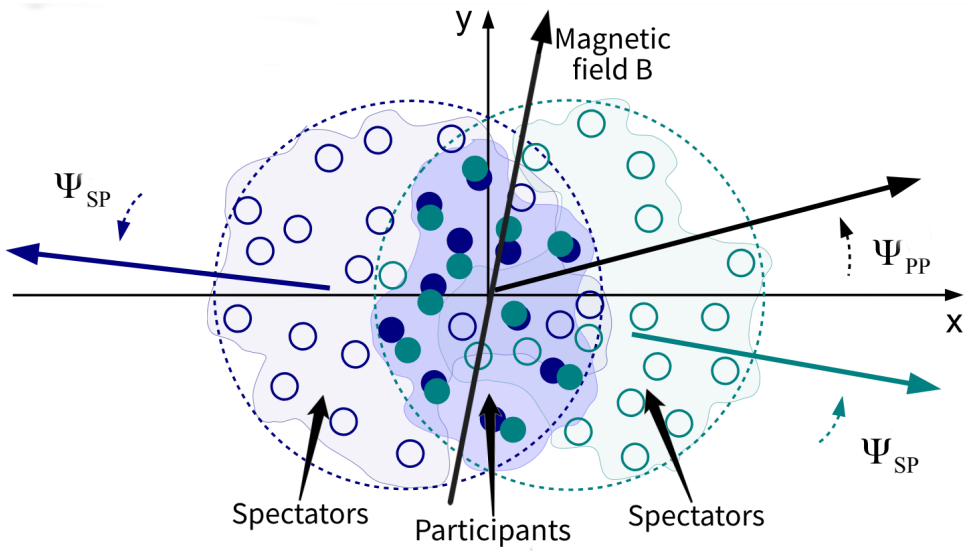

Figure 8.21: *Schets van een niet-centrale zware-ionenbotsing. Met dank aan de ALICE-samenwerking.*

Implicaties van experimentele metingen van het chirale magnetische effect voor de theorie

Met talrijke experimentele metingen van CME die worden uitgevoerd, is het natuurlijk om te vragen welke theoretische inzichten deze bieden. Deze vraag kan beantwoord worden door een onderscheid te maken tussen zuiver theoretische overwegingen en de toepassing van theoretische parameters bij het simuleren van CME door middel van natuurkundige modellen. Voor de zuivere theorie, die zich richt op de overgangssnelheden tussen verschillende vacuümtoestanden door instantonen en sphaleronen, is het op dit moment lastig om een directe verbinding te leggen. Deze moeilijkheid komt voort uit onze onvolledige kennis over verschillende factoren, zoals de sterkte van het magnetisch veld, de vervalssnelheid binnen het quark-gluonplasma en het moment waarop de chiraliteits onbalans wordt geïnduceerd na de botsing. Wat betreft de theorie achter CME-simulatiemodellen, we hebben een studie gedaan met behulp van een state-of-the-art model dat gewijd is aan het simuleren van CME in botsingen van zware ionen. Door middel van deze studie hebben we de optimale theoretische parameters geëxtraheerd die het CME-signaal beheersen, namelijk het percentage van chiraliteitsonbalans, en de achtergrond. Onze bevindingen geven aan dat om de experimentele waarnemingen voor loodionen te repliceren, een niet-nul input voor de CME-signaalparameter vereist is. Daarentegen is voor botsingen met Xenon-ionen, die aanzienlijk kleiner zijn dan lood-ionen, de CME-signaalparameter effectief nul. Dit wordt voornamelijk toegeschreven aan het grotere magnetische veld dat gegenereerd wordt in botsingen van zwaardere ionen vanwege een groter aantal protonen.

Wat is het volgende?

De theorie achter CME is elegant, maar de experimentele zoektocht naar CME presenteert aanzienlijke uitdagingen. Na een pauze van meer dan 3 jaar, waarin uitgebreide upgrades werden uitgevoerd aan zowel de detectoren als de versneller, werd de LHC eind 2022 herstart. De ALICE-collaboratie heeft een ambitieus plan voor Run 3 en Run 4, met als doel een honderdvoudige toename in het aantal gemeten botsingen met loodionen. Deze aanzienlijke verbetering wordt verwacht statistische onzekerheden met een factor 10 te verminderen, wat mogelijk de ontdekking van CME-signalen mogelijk maakt als deze bestaan op het niveau van enkele procenten. Met deze uitgebreide dataset verwacht de ALICE-collaboratie ook nauwkeurigere metingen te bereiken van het vroege magnetische veld, een cruciale factor in het modeleren van CME die nooit ondubbelzinnig is vastgesteld.

Tot slot wil ik benadrukken dat als CME inderdaad bestaat, het ongetwijfeld een aanzienlijke impact zal hebben op de vooruitgang van de natuurkunde. Maar als het niet bestaat, laat je dan niet ontmoedigen. Zoals de legendarische natuurkundige Richard Feynman ooit zei: “vooruitgang in de wetenschap komt wanneer experimenten de theorie tegenspreken,” en “als je dacht dat wetenschap zeker was - nou, dat is gewoon een fout van jouw kant.”

Acknowledgements

It is an intimidating task to adequately thank my promotor Raimond Snellings and my supervisors Paul Kuijer and Panos Christakoglou. I remember four years ago during my interview for this position, Raimond's classic black jacket, broad smile, and friendly wink made me think that he is a nice and cool guy. I was so glad that he offered me this position. Even though, I am now a bit "cynical" about the chance of discovering CME anytime soon, I really enjoyed this topic and appreciated the physics behind it. As the group leader, Raimond is always busy, but I had plenty of opportunities to talk to him about physics and life, both in his office and over drinks. His insight into physics is excellent, and he has a beautiful plan for examining the equation of state in QGP and neutron stars for the future of the GRASP group. This excites me when I think about it.

Paul is exceptionally intelligent, knowledgeable, and inspiring. I must admit that I was initially confused when my daily supervisor, Paul, decided to leave the ALICE group for the gravitational wave group one year into my PhD. Paul primarily supervised me through discussions over coffee and tea, which was a very interesting and unique experience. It was these many discussions with him that led to many great ideas in this dissertation. I feel regretful that one day I will have to leave his supervision and may not have another opportunity to discuss various scientific topics beyond my research scope, global economics, European history, and anecdotes of physicists over afternoon tea. Without his patient guidance and emotional support, I would not have made it through this doctorate.

Panos has always been extremely supportive during my PhD. I am truly grateful for the many insights he provided on my research directions, his guidance on technical details, and the opportunities to be involved in his research on CME. It goes without saying that his passion for physics, and specifically his enthusiasm for CME, has deeply inspired me. I wish I could stay at Nikhef indefinitely and continue doing research with Panos. It is not a sign of Stockholm syndrome. Perhaps that could indeed lead to the discovery of CME and many more interesting physics!

Regarding the service task, which was not mentioned in this dissertation, I am grateful to have worked with Alessandro Grelli and Marcel Rossewij and received substantial support and advice from them. It was a truly enjoyable experience. Beyond performing chip testing at CERN, I will always cherish the memory of going skiing with Marcel driving the Nikhef van, which had a quite visible dent on it left by Alessandro a few days ago accidentally.

Next, my gratitude towards my peers: I extend my heartfelt thanks to Tyson Jones for being an exceptionally intelligent friend, with whom I have had endless discussions about everything. I thank my office mate, Christos Pliatskas, with whom I have shared the last four years in the same office. The final year of the PhD has been quite stressful, hasn't it? I thank Enzo Tapia for

being a delightful friend to be around, sharing many drinks and BBQs together. I thank Maria Bader for her incredible support during my challenging times. I thank Quirijn Meijer, with whom I believe we share some similar interests and ambitions. I thank Henrique for being very helpful in discussing and helping with technical problems about the ALICE computing grid. I would also like to thank Gijs van Weelden, Bas Hofman, Rik Spijkers, Johanna Lömker, Olaf Massen, Joey Staa, Jasper, Noor Koster, Justus Rudolph, and Anna Puecher for all the enjoyable moments we shared. Among these amazing individuals, I specifically want to mention that Bas has a great sense of humour, and Justus, we should have more hotpot gatherings in the future.

Finally, I would like to express my deepest gratitude to my family: my mother, Songwen Tao, for her life wisdom and bringing me into this world; my father, Qimin Qiu, for always believing in my potential for greatness; my aunt, Limin Qiu, for her selflessness, generosity, and support throughout my life in Australia; my grandmothers, Ziying Li and Demei Zhang, for their exceptional care and love. Lastly, I thank my beloved girlfriend, Hua Tu, for her love, support and company over the past two years.

List of publications

Papers

- ALICE collaboration, (to be published soon). Searches for the chiral magnetic effect at the LHC using charge dependent azimuthal correlations with the event shape engineering and with different symmetry planes
- Yelkenci, A., Qiu, S., Rossewij, M.J., Grelli, A., Gajanana, D., and Gromov, V., (2023). Bandgap reference, temperature sensor and low drop-out regulator circuits monolithic sensors in tpsco 65 nm isc technology. Journal of Instrumentation, 18(02):C02017
- ALICE colaboration (2022) Search for the Chiral Magnetic Effect with charge-dependent azimuthal correlations in Xe-Xe collisions at $\sqrt{s_{NN}} = 5.44$ TeV arXiv:2210.15383, submitted to PLB
- Christakoglou, P., Qiu, S., and Staa, J., (2021). Systematic study of the chiral magnetic effect with the avfd model at lhc energies. Eur. Phys. J. C, 81(8):717

Proceedings

- Qiu, S., (2022) Rapidity-dependent charge-dependent flow, global polarisation and chiral magnetic effect in heavy ion collisions. EPJ Web Conf. 274 05001
- Qiu, S., (2022) Studying the Chiral Magnetic Effect in Pb-Pb and Xe-Xe collisions using the AVFD model. EPJ Web Conf. 274 02005